

FINAL TECHNICAL REPORT
SEPTEMBER 15, 1993 TO SEPTEMBER 14, 1996

ARPA ORDER NO: A475
PROGRAM CODE: 3D10

IBM THOMAS J. WATSON RESEARCH CENTER

DATE OF CONTRACT: 9/15/93
DATE OF EXPIRATION: 9/14/96
CONTRACT AMOUNT: \$1,430,643
CONTRACT NO. F49620-93-C-0068,DEF

T.H. PHILIP CHANG
PRINCIPAL INVESTIGATOR
914-945-2720

Dr. GERALD WITT
PROGRAM MANAGER
202-767-4932

MICROCOLUMN ARRAYS FOR NANOLITHOGRAPHY

Sponsored by
ADVANCED RESEARCH PROJECT AGENCY
ARPA Order No. A475
Monitored By AFOSR under Contract No. F49620-93-C-0068,DEF

The views and conclusions contained in this document are those of the authors and should not be interpreted as necessarily representing the official policies or endorsements, either expressed or implied, of the Advanced Research Project Agency or the U.S. Government

Approved for public release,
distribution unlimited

AIR FORCE
NOTED
THIS
APPROPRIATE
DISTRIBUTION
STANDARD

19961122 079

4-12

REPORT DOCUMENTATION PAGE

Form Approved
OMB No. 0704-0188

Public reporting burden for this collection of information is estimated to average 1 hour per response, including the time for reviewing instructions, searching existing data sources, gathering and maintaining the data needed, and completing and reviewing the collection of information. Send comments regarding this burden estimate or any other aspect of this collection of information, including suggestions for reducing this burden, to Washington Headquarters Services, Directorate for Information Operations and Reports, 1215 Jefferson Davis Highway, Suite 1204, Arlington, VA 22202-4302, and to the Office of Management and Budget, Paperwork Reduction Project (0704-0188), Washington, DC 20503.

1. AGENCY USE ONLY (Leave blank) 2. REPORT DATE 3. REPORT TYPE AND DATES COVERED
FINAL REPORT 15 Sep 93 - 14 Sep 96

4. TITLE AND SUBTITLE
MICRO-COLUMN ARRAYS FOR NANOLITHOGRAPHY 5. FUNDING NUMBERS
61101E
A475/03

6. AUTHOR(S)
Dr Chang

7. PERFORMING ORGANIZATION NAME(S) AND ADDRESS(ES)
IBM Research Division
Thomas J. Watson Research Center
P O Box 218
Yorktown Heights, NY 10598 8. PERFORMING ORGANIZATION
REPORT NUMBER
AFOSR-TR-96
0562

9. SPONSORING/MONITORING AGENCY NAME(S) AND ADDRESS(ES)
AFOSR/NE
110 Duncan Avenue Suite B115
Bolling AFB DC 20332-8080 10. SPONSORING/MONITORING AGENCY
REPORT NUMBER
F49620-93-C-0068

11. SUPPLEMENTARY NOTES

12a. DISTRIBUTION/AVAILABILITY STATEMENT
APPROVED FOR PUBLIC RELEASE: DISTRIBUTION UNLIMITED 12b. DISTRIBUTION CODE

13. ABSTRACT (Maximum 200 words)

This program is to explore a novel method, based on arrays of miniaturized electron beam columns operating in parallel (for lithography in the 100 nm and below linewidth regime). It requires no mask and can be extended to the sub-25 nm linewidth regime. It offers the potential of a low cost, high throughput manufacturing process for the new generation of ultradense, ultrafast devices. The objective of the current program is to develop the base technologies for the electron beam microcolumn and the related lithographic processes to allow its feasibility for high throughput multi-beam lithography to be evaluated. This is a joint IBM Research/Cornell University project with IBM focusing on microcolumn development, pattern generation and simple array multi-beam operation, and Cornell on low voltage lithographic processes, aspects of advanced field emission studies, and novel column fabrication techniques. This report covers only the activities at IBM Research.

14. SUBJECT TERMS 15. NUMBER OF PAGES
16. PRICE CODE
DTIC QUALITY INSPECTED 2

17. SECURITY CLASSIFICATION OF REPORT UNCLASSIFIED 18. SECURITY CLASSIFICATION OF THIS PAGE UNCLASSIFIED 19. SECURITY CLASSIFICATION OF ABSTRACT UNCLASSIFIED 20. LIMITATION OF ABSTRACT

Contents:

	page
(1) Summary	2
1.1 The Basic Concept	2
1.2 Progress and Status	3
2.3 Future Directions	6
(2) Technical Reports	8
2.1 Microcolumn Test and Evaluation	8
2.2 Electron Optical Studies	41
2.3 Field Emission Source Development	80
2.4 Microlens and Column Fabrication	127
(3) Acknowledgments	150
(4) References	151

(1) Summary

This is the final technical report for the program entitled "Microcolumn Arrays for Nanolithography". This program is to explore a novel method, based on arrays of miniaturized electron beam columns operating in parallel (for lithography in the 100 nm and below linewidth regime). Throughput on the order of 10 to >50 wafers per hour for 100 nm lithography on 200 mm wafers is believed to be achievable depending on the number of microcolumns employed. It requires no mask and can be extended to the sub-25 nm linewidth regime. It offers the potential of a low cost, high throughput manufacturing process for the new generation of ultradense, ultrafast devices.

The objective of the current program is to develop the base technologies for the electron beam microcolumn and the related lithographic processes to allow its feasibility for high throughput multi-beam lithography to be evaluated. This is a joint IBM Research/Cornell University project with IBM focusing on microcolumn development, pattern generation and simple array multi-beam operation, and Cornell on low voltage lithographic processes, aspects of advanced field emission studies, and novel column fabrication techniques. This report covers only the activities at IBM Research.

1.1 The Basic Concept

In a significant departure from the conventional electron beam technologies, the microcolumns are based on a novel STM aligned field emission source in conjunction with microfabricated lenses to achieve a very significant reduction in physical size (column length and diameter). This miniaturization also results in reduced electron optical aberrations and electron-electron interactions so that the performance can surpass conventional columns. For lithography, an array of these microcolumns, each having a field emission tip as the source with individual STM controls, will be used in combination with micro-lenses to form focused beams of electrons. These beams can be individually deflected and blanked to perform the task of a scanned probe. An array of these microbeams can be used to generate patterns in parallel to achieve high throughput. It is envisaged that one or more such microcolumns will be used per chip with pattern writing and overlay performed on a chip by chip basis. Pattern can be written in either raster- or the vector-scan mode with the beam scanned over only a narrow stripe (<100 μm width) with a laser-controlled stage moving continuously in the orthogonal direction to build up the complete chip pattern using "stitching". Figure 0.1 shows the basic concept of this arrayed microcolumn approach. The array can also be used for metrology, inspection, testing, and other applications where the use of multi-beams for parallel processing is desired. While the microcolumns are not restricted to

low-voltage operation, low voltage has obvious advantages in terms of miniaturization, and in improving reliability and cost. Low voltage in the 1-2 kV range can also be attractive for lithography because proximity effect corrections may not be required. In addition, any one microcolumn writes only a small part of a large wafer, so the stage needs only to move a distance comparable to the chip size, and this can result in a compact overall mechanical assembly with important cost benefits.

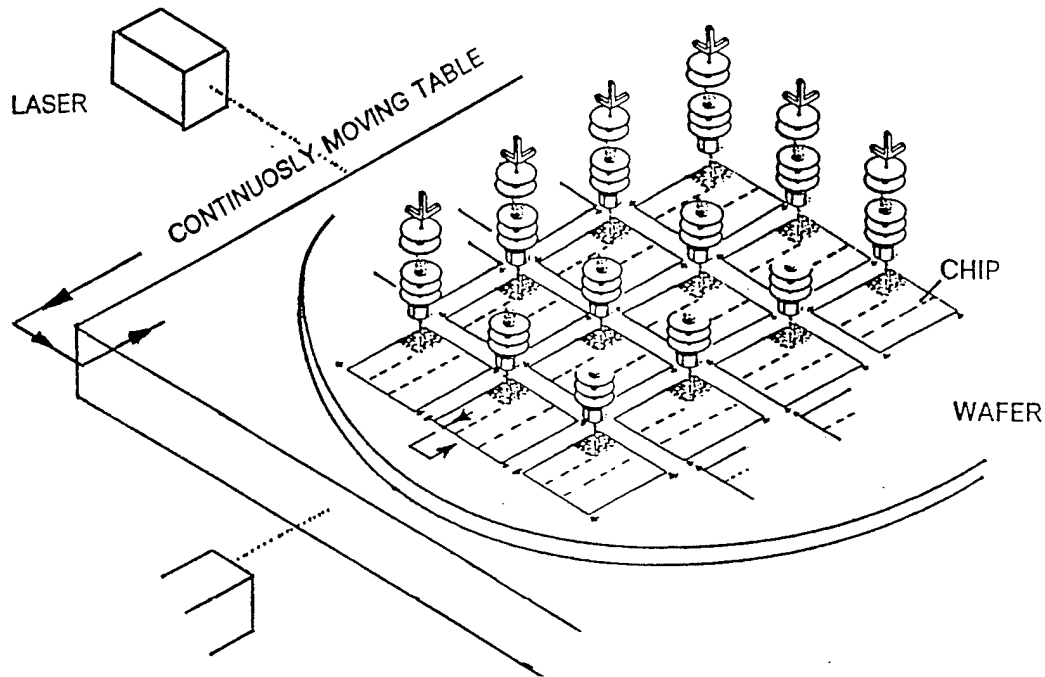


Fig. 0.1. The basic concept of arrayed microcolumns for high throughput lithography.

1.2 Progress and Status

We are able to report considerable progress in advancing the base technologies for the microcolumns, and in constructing and demonstrating individual 1 keV microcolumns with performance suitable for lithography of features with dimensions 100 nm and smaller. Preliminary, tenth micron lithography has been demonstrated with the microcolumn, and a simple array of microcolumns at 20 mm center to center spacing has been fabricated and is in-test. A brief summary of the progress is outline here.

1. A 1 kV electron beam microcolumn with a 20×20 mm square footprint for application in arrayed lithography has been successfully developed. The actual beam forming optics measured from the electron emitter to the last electrode in the beam focusing Einzel lens is only 3.5 mm in length. The electron source is a miniaturized, high brightness ($120 \mu\text{A}/\text{sr}$), low heating power ($<1.5 \text{ W}$) Zr/O/W Schottky field emitter that provides a stable beam current with $<1\%$ /hour current fluctuations. A miniaturized STM is used to align the emitter to the column. A custom designed, ultralow profile (0.8 mm high) annular microchannel plate (MCP) detector is fitted into the working distance, which can be varied between 1 and 5 mm, between the Einzel lens and the sample. The MCP provides a high gain, up to 1×10^4 , detector for secondary and backscattered electron detection from solid samples. The beam is scanned over the sample using a prelens double octupole deflector for large field size, $\geq 100 \mu\text{m}$, at low deflection aberrations. It is believed that the microcolumn described here is the world's smallest fully functional SEM.

At a working distance of 1 mm, a probe size of 10 nm with a beam current on the order of 1 nA at 1 kV has been obtained. The probe size is in good agreement with the electron optical design expectation and rivals the best of the conventional columns at this energy. The beam current meets the design expectation, and is at least one order of magnitude higher than a conventional column at the same probe size and beam energy. This significant improvement in beam current for a 10 nm probe is due in part to the increased brightness anticipated with the selectively scaled source used in the microcolumn, and in part due to the reduced electron-electron interaction in such a short column. Electron optical study shows that the probe size can be further reduced: down to 6 nm with improved Einzel lens at 1 kV and down to 2-3 nm by increasing the beam energy to 10 keV.

2. In support of this microcolumn development, advancements in a number of key technologies have been achieved in parallel. These include:
 - a. Electron optical design studies:
 - Extensive software and optimization techniques have been developed and acquired to design and analyze optical components (guns, lenses, deflection systems etc.) New techniques have been used to evaluate the effects of electron-electron scattering in microcolumns.
 - New einzel lens design with prelens double deflector has been designed and implemented for improved probe diameter and deflection field.
 - Advanced inlens deflector design has also been evaluated and proposed for further deflection improvement and vertical beam landing.

b. Field emission sources:

- An ultra-high brightness selectively scaled electron source has been designed and implemented.
- Miniature Zr/O/W Schottky field emitters with exceptional stability (<1% fluctuation per hour) at angular current density in excess of $100\mu\text{A}/\text{sr}$ have been successfully developed and are in routine use. These emitters exhibit long life, and one is still running after >8 months of continuous operation.
- Cold field emitters have been extensively evaluated. An oxygen assisted tip preparation process, which results in a more reproducible tip geometry, has been developed for single crystal tungsten emitters to improved performance. However, tungsten emitters, as a whole, do not provide adequate emission stability for lithography applications due to movement of W atoms under high electric fields. More recently, diamond tips have been evaluated showing encouraging initial results. Stable emission at angular current densities up to $\approx 10\mu\text{A}/\text{sr}$ has been achieved. More research is needed to further improve stability and to control on-axis emission.

c. Microlens fabrication:

- A precision fabrication process for the electrodes of microlenses based on silicon membranes, 1 to $2.5\mu\text{m}$ thick, has been developed. An electron beam system equipped with polar coordinate pattern generator, a proprietary resist system and reactive ion etching are used to produce extremely round lens bores as small as $1\mu\text{m}$ in diameter with edge roughness on the order of 5 nm.
- A novel anodic bonding technique allowing multi-layers of silicon lens components and Pyrex spacers to be assembled has been developed. Under the control of a custom built optical microscope alignment system, lenses and the complete column can be fabricated with axial alignment precision on the order of $1\mu\text{m}$.
- A process for forming tall structures ($\geq 200\mu\text{m}$) using an ultra-thick photoresist followed by RIE or plating has been developed. A potential application of this process is in the fabrication of the deflector and beam blankers from thick silicon substrates.

3. The microcolumn module was interfaced to a computer controlled pattern generator for electron beam lithography operation. Simple patterns showing <100 nm lines have been achieved in PMMA resist at 1 kV.

4. A simple 2×1 array of the microcolumn modules has been constructed and assembled. A new test system designed specifically for arrayed column testing has been developed. The system features a differentially pumped work chamber equipped with a laser interferometer controlled x-y stage and capable of accommodating a 200 mm wafer. The array has been installed in the test system and is ready for test.
5. A technology transfer of the microcolumn program from IBM to Etec Systems Inc., a U.S. semiconductor equipment manufacturer, has been agreed upon. This agreement calls for transfer of people, equipment and intellectual property rights to commence in November, 1996.

1.3 Future Directions

With the significant progress made in the basic technologies for the microcolumn at IBM and in high resolution low voltage resists and related processes at Cornell University, the focus of the next phase of the program will be on the microcolumn array fabrication and operation. The three key areas are:

1. Arrayed lithography: There is a need to explore and establish the optimum writing strategy for the multi-beams. A careful comparison of raster versus vector mode of writing has to be made. Interactions between columns during high speed pattern writing, especially at high column packing density, is a major concern and need to be addressed. Methods to achieve accurate overlay with multi-beams is also an issue that needs to be studied. There is also a need to explore the best path for the introduction of microcolumns to the lithography application. While high throughput direct write on wafer may still be the ultimate goal, multi-beam mask making may be an attractive and technically less demanding first step.
2. Advanced microcolumn engineering: This will aim at further reduction in physical dimensions (to less than 10 mm square) and improved performance in terms of resolution, beam current, deflection speed and field size. Wiring and interconnection of microcolumns will become increasingly more difficult with reduced dimensions and need to be addressed. An integrated column approach using wafer-scale fabrication and interconnections should be explored. This would also allow columns with a high packing density to be achieved. Improved beam-forming systems based on shaped beam optics to allow multiple pixels to be printed in a single shot, and inlens deflection to achieve a larger field size should also be explored. Research on improved field emission sources, detectors and improved lens and column fabrication techniques will also be pursued.

3. Advanced resist and related processes: The availability of reliable high resolution high speed resists and processes with performance compatible with device fabrication and industry standards will be necessary for the effective utilization of the microcolumn capabilities. The limited electron penetration range at the operating energies of the current microcolumn presents a considerable challenge in the fabrication area and an optimization study of the beam energy may be necessary. Novel resists materials including surface imaging resists from commercial and research sources will be evaluated to establish their resolution, defect density and sensitivity. Nano-scale resolution pattern-transfer processes will also need to be explored.

(2) Technical Reports

2.1 Microcolumn Test and Evaluation

2.1.1 Introduction

Electron beam microcolumns are being studied because their greatly reduced size and weight over conventional electron beam columns is expected to lead to new applications in surface analysis, inspection and metrology, electrical testing, and electron beam lithography. The small size of the microcolumn opens the possibility for arrayed operation on a scale commensurate with present semiconductor chip size. Arrayed microcolumns are expected to significantly improve the throughput of future electron beam lithography and metrology.^{1,1} In addition, the combination of field emission sources and microlenses has been predicted to result in better low voltage performance with respect to brightness and lens aberrations than conventional systems.^{1,2,1,3}

Highly miniaturized electron beam columns based on a field emission source and microfabricated electron optical components have been developed. The small size of the microcolumns has become possible through the use of silicon micromachined electrodes, which are precision optically aligned and anodically bonded using Pyrex insulating spacers, to build the lenses and other components of an all electrostatic electron optical column.^{1,4,1,5} Fully operational 1 keV microcolumns measuring 3.5 mm in column length have been successfully demonstrated.^{1,6} Electron beam microcolumn applications can be distinguished roughly by their requirements on resolution and beam current. The two primary areas of application are: high resolution (≤ 10 nm), low beam current (≤ 100 pA) scanning electron microscopy (SEM); and medium resolution (10 to 50 nm), medium beam current (≥ 1 nA) high speed electron beam lithography or metrology. Future extension into the area of low resolution (≥ 50 nm), but higher beam currents (≥ 10 nA) for specialized applications may become possible. The SEM application requirements can be met by microcolumns with cold field emission sources. Improved cold field emitters with angular emission density on the order of $10 \mu\text{A}/\text{sr}$ have been developed for this purpose.^{1,7} For applications requiring higher currents, microcolumns need to be equipped with a Schottky or thermal field emission source.^{1,8-1,10} Such sources can provide angular emission density in excess of $100 \mu\text{A}/\text{sr}$ with good stability when tested with a microlens.^{1,11}

A 1 keV microcolumn operating with a miniaturized Zr/O/W Schottky emitter has been successfully evaluated. Testing has shown a beam diameter of 10 nm at a beam current of about 1 nA and a working distance of 1 mm. This report discusses modifi-

cations of the new microcolumn versus earlier microcolumns and details some of the operating conditions, in particular for the Schottky emitter and the einzel lens, that were critical in obtaining this improved performance.

2.1.2 Modifications of 1 keV Microcolumn

The microcolumn as schematically shown in Fig. 1.1 has previously been successfully operated using cold field emitters as electron sources.^{1,6} The present microcolumn is operated with a Schottky emitter, because this type of emitter has the potential for better beam current stability at higher angular emission current densities and relaxed vacuum requirements. An earlier evaluation of Schottky emitters for microcolumn applications showed that the thin silicon membranes used for the extractor electrode can well withstand the associated temperature rise resulting from thermal radiation from the tip, heated to about 1800 K at a distance of 100 μm from the membrane, as well as from the power dissipated by the absorption of a large fraction of the up to 100 μA of emission current.^{1,11} The source lens was modified to accommodate the 4 mm diameter suppressor cap^{1,12} and to allow room for scanning the tip at 100 μm distance from the extractor membrane. The silicon chip carrying the extractor membrane was replaced by a large membrane, which results in a totally planar extractor surface with no risk of obstruction to tip movements. The tip holder was modified to provide the additional electrical contact to the suppressor cap and to provide some amount of thermal isolation between the hot tip assembly and the scanning tunneling microscope (STM) scanner on which the tip is mounted.

The anodic bonding used in the lens fabrication to bond the silicon membrane chips to the Pyrex insulating spacers minimizes the possibility of outgassing and contamination of the tip and column components.^{1,13} This is a greater concern with the Schottky emitter since the higher temperature of the source lens would lead to increased outgassing rates from adhesive bonding materials such as epoxies.

The einzel lens was redesigned and electrical insulation of the center electrode was improved to operate the lens at the roughly three times higher electric field strength required in the accelerating mode. The higher focusing voltage has caused electrical breakdown in previous attempts. To operate the einzel lens safely at these voltages, several modifications and improvements in lens design and fabrication have been implemented. For example, the thickness of the Pyrex insulating spacers has been suitably increased and the bonding used for electrical connection has been improved. With these changes, focussing voltages up to 3 kV can now be safely applied.

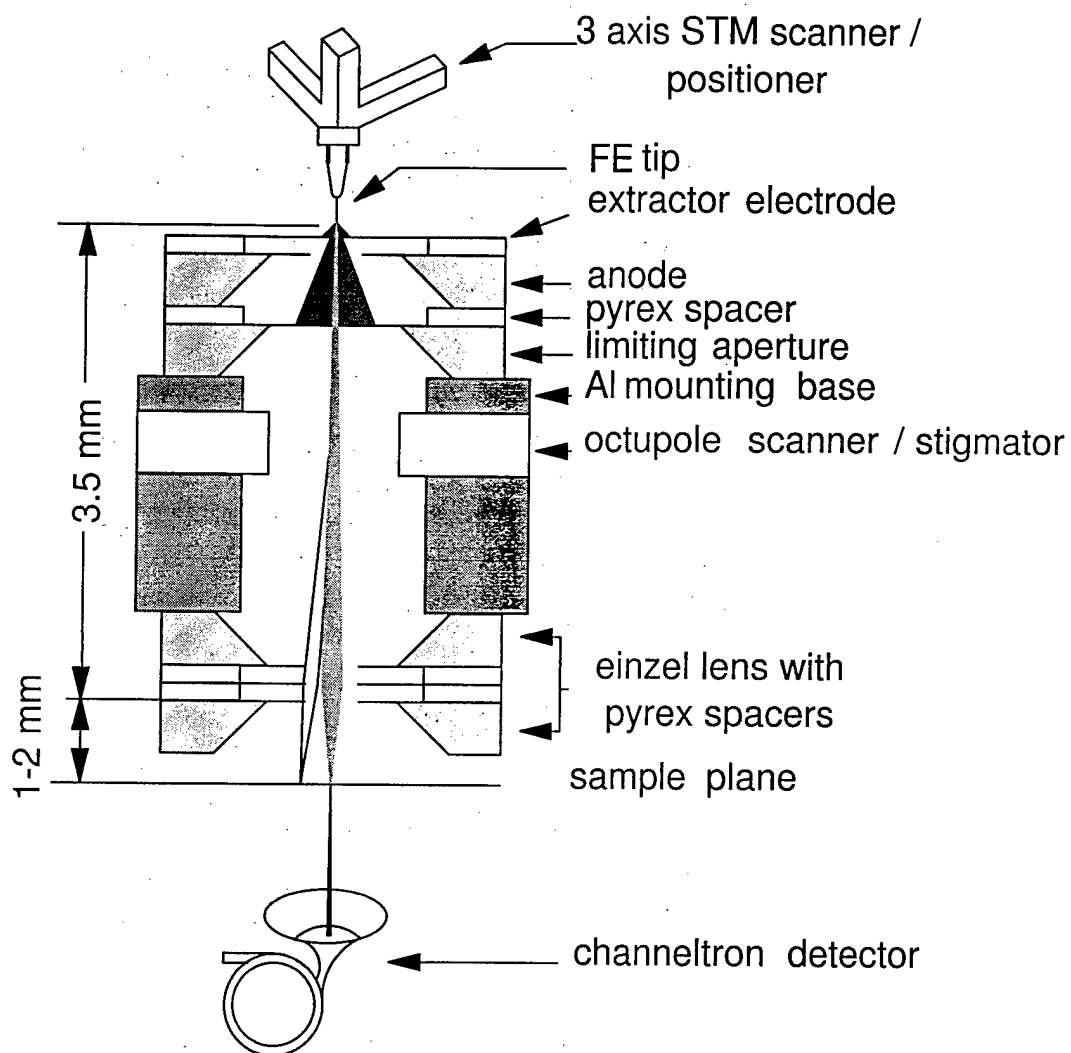


Fig. 1.1. Cross section of 1keV microcolumn.

2.1.3 Improved Resolution in Accelerating Mode

The resolution of the column with the einzel lens in the accelerating mode is tested in the transmission mode using an aluminum grid sample shown in a low magnification view at the top of Fig. 1.2. The image was taken at 1 mm working distance and 1 keV beam energy and a beam current of about 1 nA. The sample contains holes of $1 \times 1 \mu\text{m}$ size placed accurately on $3 \mu\text{m}$ centers using electron beam lithography. Small features on this sample can only be found in few places along the edges of the holes. One such feature with 10 nm size is shown at the bottom of Fig. 1.2. The accurate placement of the grid-holes and the good contrast of the 100 nm thick aluminum make the sample well suited for beam diameter measurements by scanning the electron beam across the edge of a hole. Figure 1.3 shows the result of this two-step measurement technique, a calibration scan and a measurement scan. In the calibration scan the beam deflection is calibrated using the known average $3 \mu\text{m}$ spacing between corresponding edges of neighboring holes. In the measurement scan the FWHM beam diameter is then determined by the 10% and 90% points of the edge signal. In the measurement shown in the lower half of Fig. 1.3 the beam diameter is 11.2 nm. A slight misorientation between the scan direction and the direction normal to the aluminum edge does not affect the measurement accuracy, as long as the calibration and the measurement scans are parallel to each other. It is noted, however, that some overestimate of the beam diameter is possible due to the finite width of the edge transition from fully opaque to fully transparent.

Another interesting type of transmission sample is a gold coated "holey" carbon sample.^{1,14} The upper half of Fig. 1.4 shows a low magnification view of the sample at 1 keV electron energy and 2 mm working distance. The holes in the gold coated carbon membrane appear as bright spots in the transmission micrograph. The image in the lower half of Fig. 1.4 is a view of the same sample at a higher magnification showing features as small as 20 nm, again with the einzel lens operating in accelerating mode. This is a significant improvement over the measured beam diameter of 30 nm at the same 2 mm working distance with the einzel lens operating in the decelerating mode.^{1,6}

The measured resolution improvement from operating the einzel lens in the accelerating mode compares very well with the results of the electron optical studies. In Fig. 1.5 the calculated spot size is plotted versus the working distance for 1 keV electron energy and an energy spread of 0.5 eV. The dashed line represents the spot size in the retarding mode, while the solid line represents the spot size in the accelerating mode of the lens. The squares and circles at 1 mm and 2 mm working distance rep-

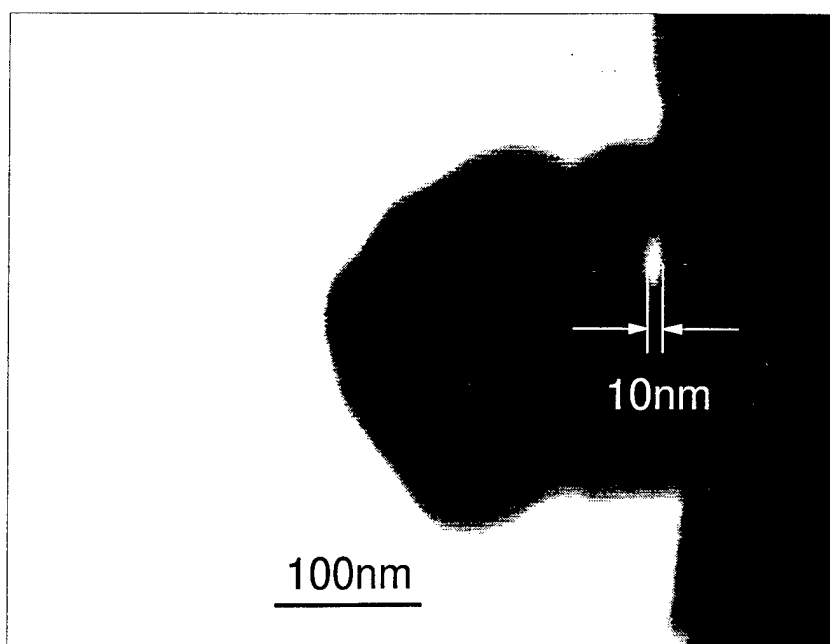
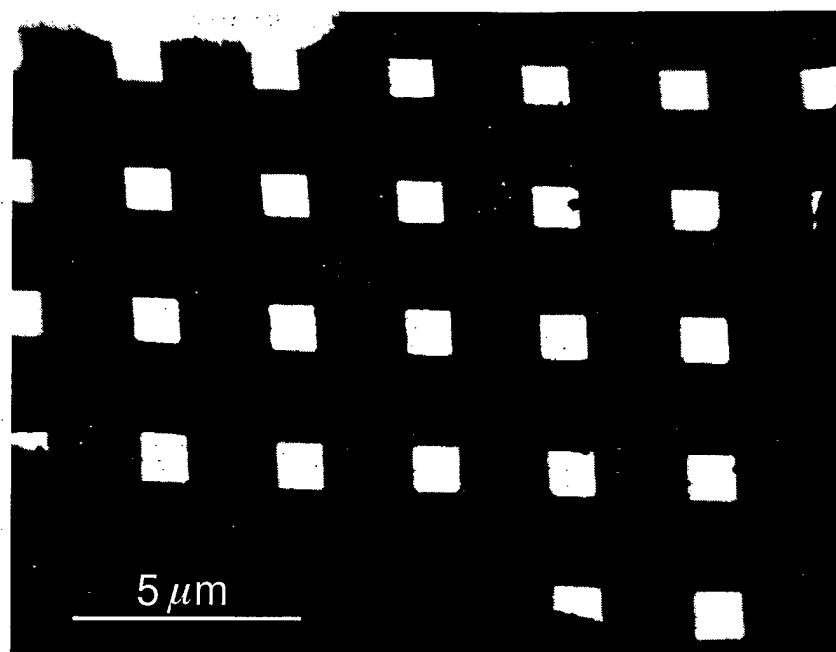


Fig. 1.2. Aluminum-grid sample images recorded at 1 keV beam energy, 1mm working distance, and 1 nA beam current with the einzel lens operating in the accelerating mode. Low magnification view (top) and higher magnification view (bottom).

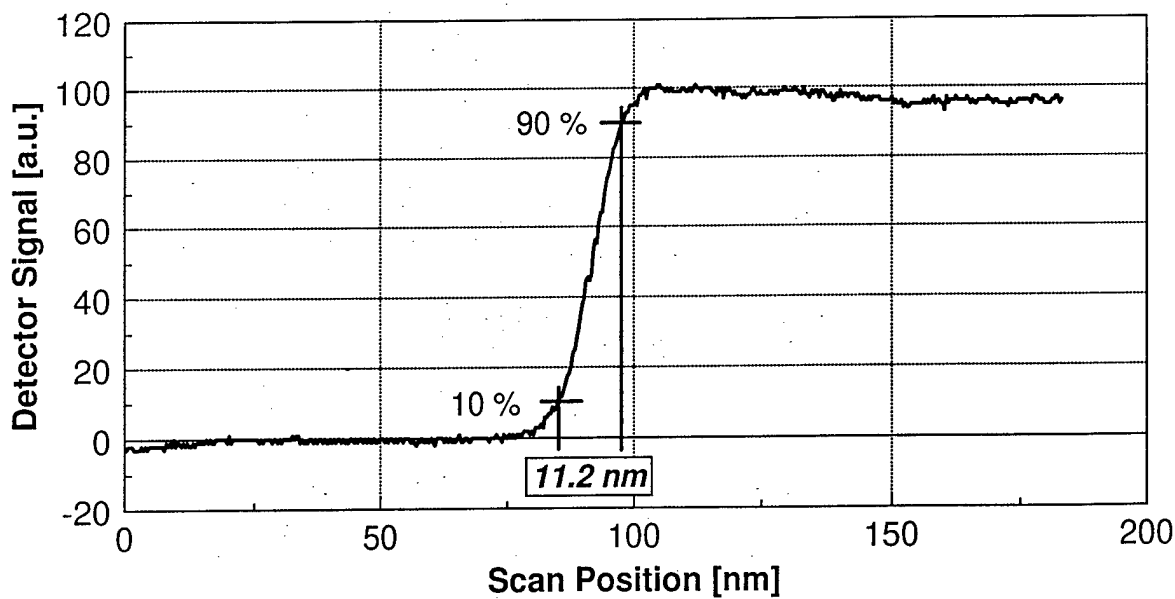
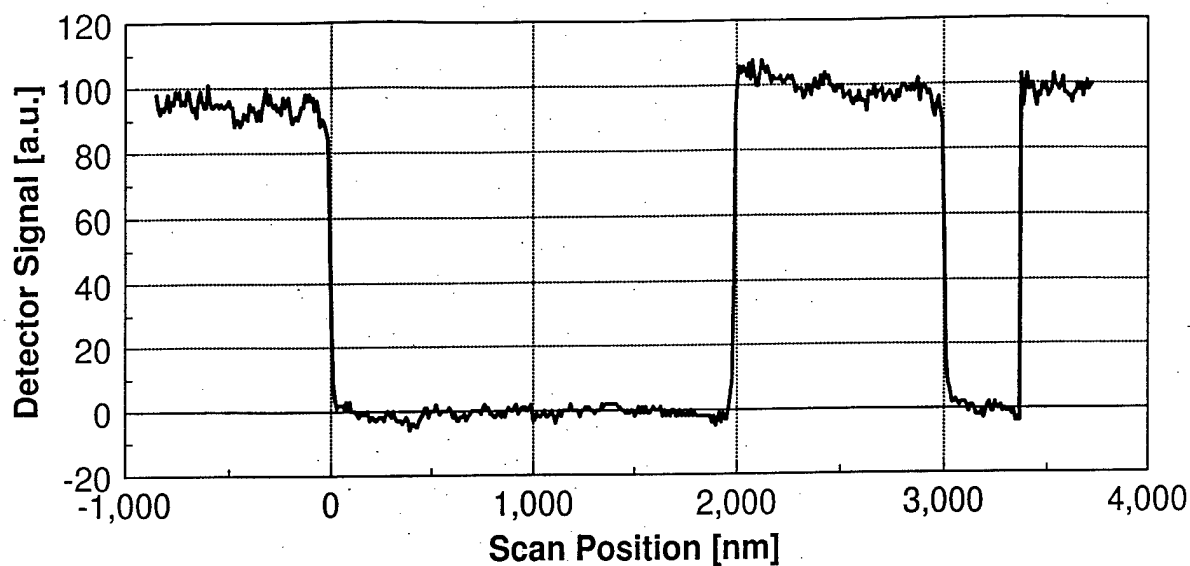


Fig. 1.3. Signal traces of calibration (top) and measurement (bottom) scan across an aluminum-grid sample edge measuring the FWHM beam diameter of 11.2 nm.

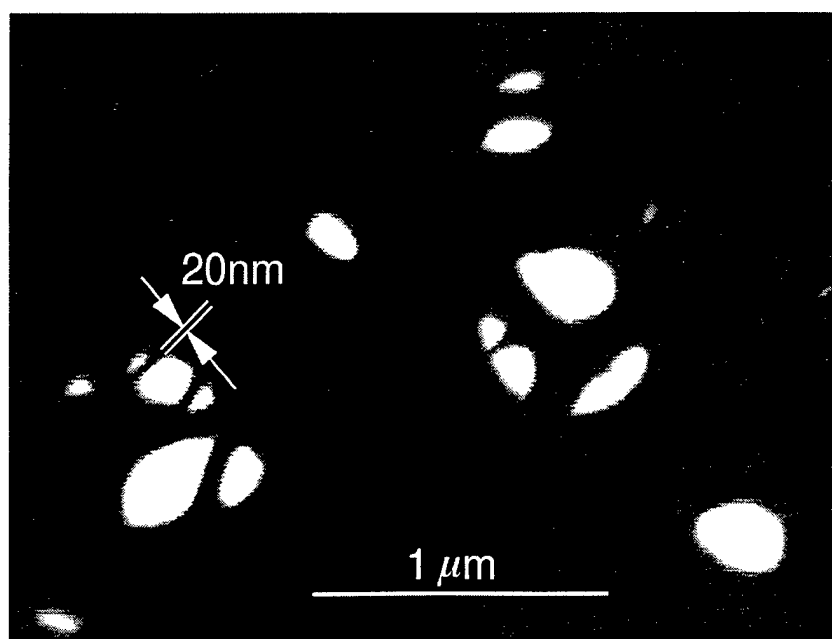
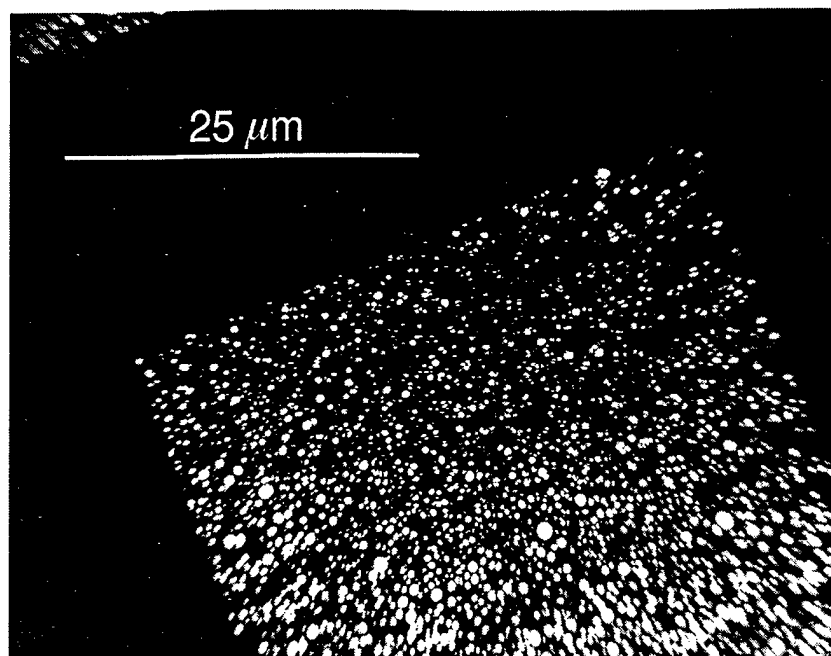


Fig. 1.4. "Holey" carbon sample images recorded at 1 keV beam energy and 2mm working distance with the einzel lens operating in the accelerating mode. Low magnification view (top) and higher magnification view (bottom).

resent the measured beam diameters in the accelerating and retarding mode of the lens, respectively. The agreement with the calculated spot size, in particular at 1mm working distance, is very good. In addition, Table I. shows a comparison of the electron optical modeling results. The table contains results for the two different einzel lens designs, here called “new” and “old”^{1.6} system, respectively, and for the two different operating modes of the einzel lens. Since the “old system”^{1.6} was operating with a cold tungsten field emitter an energy spread of about 0.4 eV is assumed, while the “new system” uses a Schottky emitter with an energy spread of about 0.5 eV. Starting with the rightmost column and proceeding to the left, Table I. shows the significant improvement in reduced aberrations and total beam diameter gained by reducing the working distance, redesigning the einzel lens for the “new system”, and finally switching to the accelerating mode of the einzel lens operation.

2.1.4 Schottky Emitter Operation

The present microcolumn has been operated with a Mini Schottky emitter.^{1.12} The overall dimensions of the emitter have been reduced to fit into a 4 mm diameter by 13.7 mm envelope and thereby meet the requirements of reduced size and weight for mounting the emitter in the STM scanner of the microcolumn. The heating power for a tip temperature of 1800 K is only 1.5 to 1.8 W. Typical tip radius is in the range of 0.3 to 0.4 μm leading to extraction voltages in the range of 1000 to 1800 V for emission currents of 10 to 100 μA and beam currents up to 1 nA. The angular emission current density is 150 $\mu\text{A}/\text{sr}$ at 1 nA beam current. The beam current is very stable showing less than 1% fluctuation over several hours.

Occasionally specimen damage has been observed when imaging samples of the type shown in Fig. 1.2 at beam currents of 1 nA. The shape of some small features along the edges of the holes changed irreversibly during imaging times of several minutes. We consider beam heating to be the most likely reason for the specimen damage as it has not been observed at lower beam currents.

As reported earlier with cold field emission tips, mechanically scanning the tip over a specially patterned extractor membrane and imaging the transmitted current is a very useful technique for tip alignment and emission characterization.^{1.6} This technique has also been successfully used with the Schottky emitters. The pattern etched through the extractor membrane consists of the 5 μm diameter central hole in the extractor, which is the entrance aperture into the column, and a large, approximately 250×250 μm size, arrow pattern surrounding the central hole.

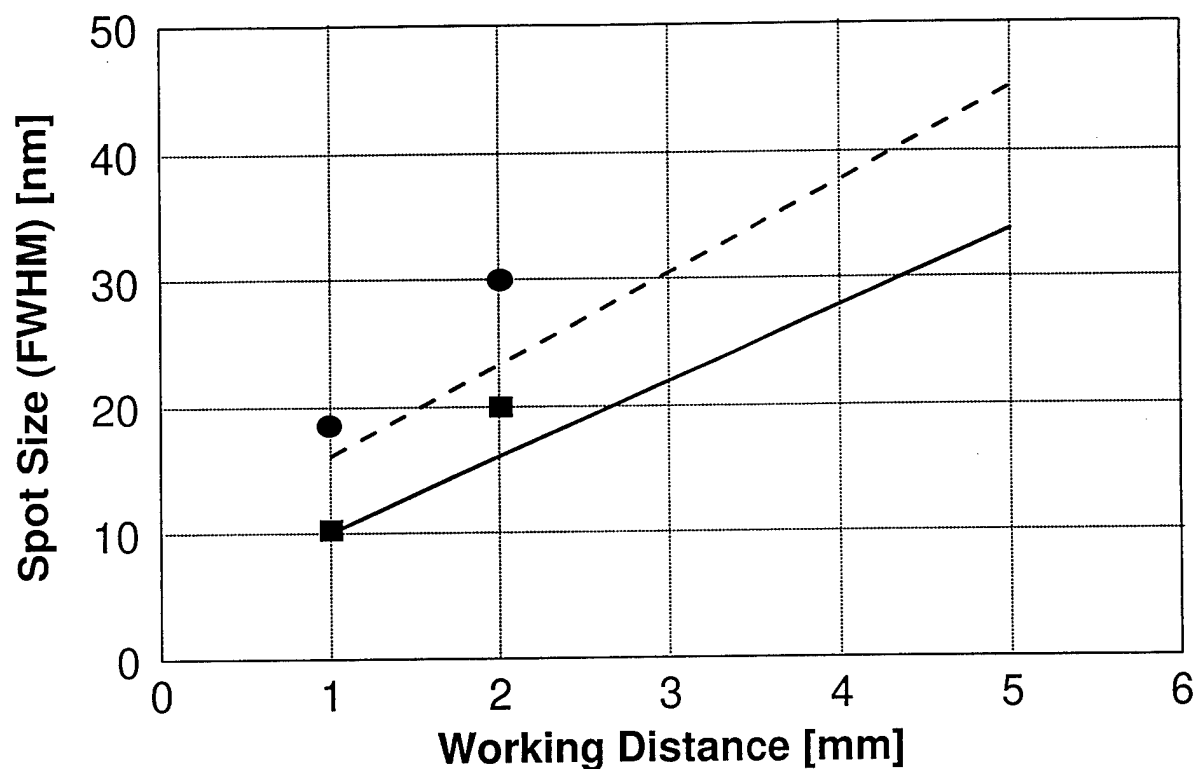


Fig. 1.5. Comparison between calculated and measured beam diameter (FWHM) at 1 kev electron energy, assuming 0.5 eV energy spread, versus working distance for the accelerating mode (solid line) and retarding mode (dashed line) of the einzel lens. Results of the measurements are plotted as squares and circles for the accelerating and retarding mode, respectively.

As schematically shown in Fig. 1.6, the field emission tip is mechanically scanned over the extractor membrane using the STM scanner. In the present microcolumn the anode is at ground potential while the FE tip potential is at a fixed -1 kV (U_b) for a fixed -1 keV beam energy. The extractor potential is then varied to obtain the required angular emission current density for a desired beam current. In the case of sharpened cold field emitters the extraction voltage (U_{ext}) is typically in the range of 300 to 700 V.^{1,6} This causes some of the electric field surrounding the extractor electrode to penetrate through the hole in the anode and terminate on the limiting aperture as illustrated in the left hand part of Fig. 1.6. However, the higher extraction voltages, in the range of 1000 to 1800 V, typically required for operating the Schottky emitter result in an electric field of opposite polarity, illustrated on the right hand side of Fig. 1.6, between the extractor and the limiting aperture. This has a direct effect on the polarity of the current (I_{image}) measured between the limiting aperture and the column ground as the secondary electron yield from the limiting aperture depends on the polarity of the field between the extractor and the limiting aperture. When the electric field lines originate on the limiting aperture ($U_{ext} < U_b$) the secondary electrons are returned to the limiting aperture, causing electrons to flow from the limiting aperture to column ground, or an electric current to flow into the limiting aperture ($I_{image} > 0$). On the other hand, when the electric field lines terminate on the limiting aperture ($U_{ext} > U_b$) the secondary electrons are attracted to the extractor, causing electrons to flow from column ground into the limiting aperture, or an electric current to flow out of the limiting aperture ($I_{image} < 0$). This causes a reversal in image contrast as shown in Fig. 1.6(a) and (b). In Fig. 1.6(a) the extraction voltage is smaller than the 1 kV beam voltage, while in Fig. 1.6(b) the extraction voltage is higher than 1 kV. Therefore, when the tip is positioned over the arrow pattern in the extractor and more electrons reach the limiting aperture, the image may become brighter or darker depending on the extractor voltage setting relative to the beam voltage. The reversal in image contrast is observed within less than ± 5 V extractor voltage change near the point where the extraction voltage equals the beam voltage.

The images produced by this technique are a convolution of the electron emission distribution from the tip and the pattern etched through the extractor membrane. In the case of a single, narrow angled emission from a cold field emitter tip, the result is simply a scanned image of the extractor pattern with a resolution that depends strongly on the tip to extractor distance and the emission angle from the tip. Images of this kind have been used to position the tip over the small central hole in the extractor. However, due to the finite amount of thermal emission, in addition to the Schottky emission, from a Schottky emitter the scanned images are more complex.

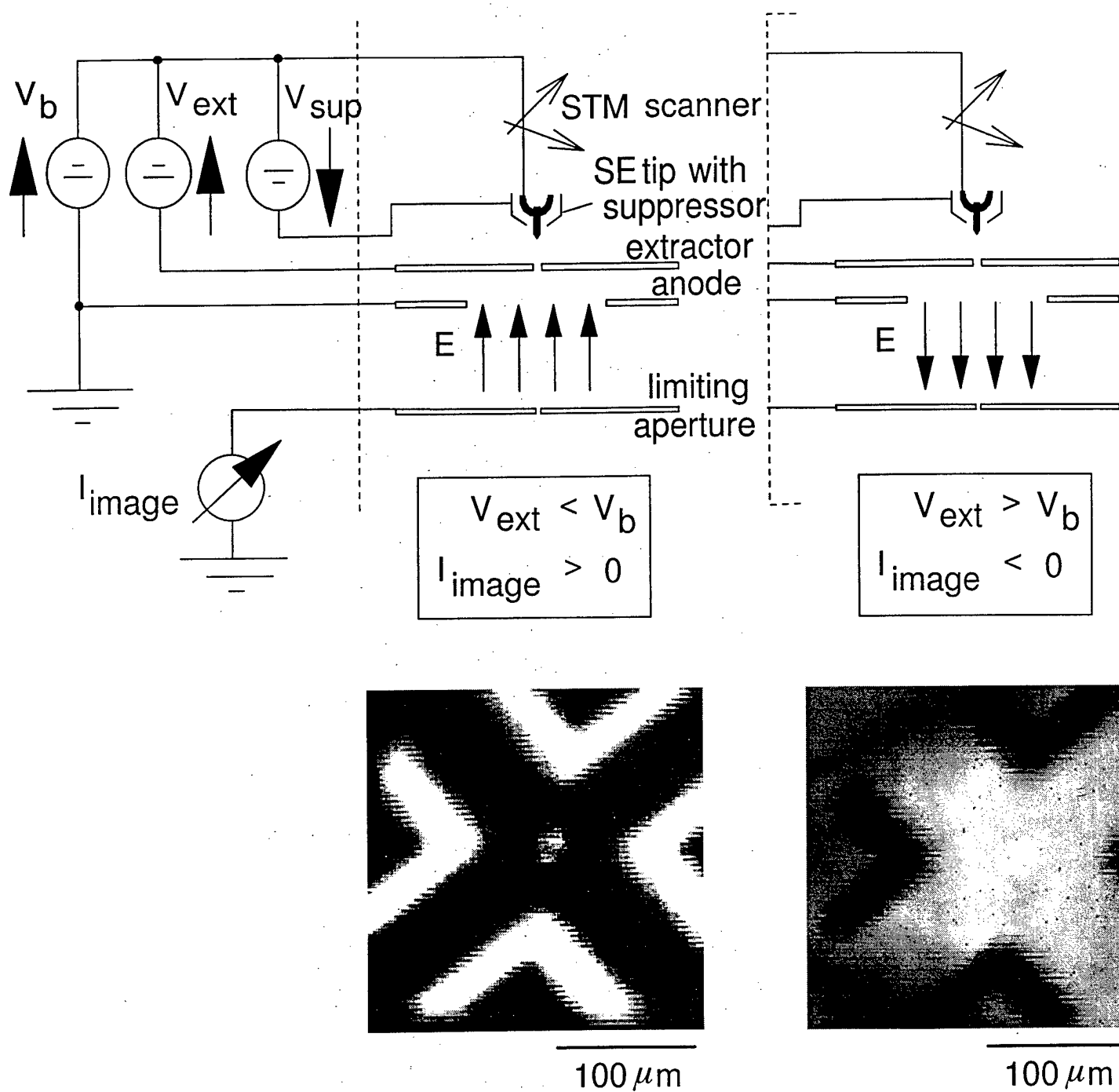


Fig. 1.6. Scanning images of the extractor pattern obtained by mechanically scanning the FE tip while collecting the electron current transmitted onto the limiting aperture. The image contrast depends on the electric field in the region between the extractor and the limiting aperture.

The image shown at the top of Fig. 1.7 shows a “light grey” central arrow pattern surrounded by a number of darker features. The position of these dark features in the image depend on the suppressor voltage (U_{sup}). Increasing the suppressor cap voltage moves the dark features closer to the center of the image. This points to the thermal emission from tip as being the source of these image features. The four-fold symmetry of the dark features matches the four-fold symmetry in the thermal emission distribution from the tip.^{1,12}

The light grey arrow pattern in the center is relatively unaffected by suppressor voltage changes but the image contrast of the arrow pattern depends strongly on the extraction voltage. The image contrast increases with increasing extraction voltage and thereby increasing Schottky emission from the tip, as shown in the lower part of Fig. 1.7. Used in this way, the mechanical scanning of the tip to image the extractor membrane becomes a valuable tool in optimizing the tip operating conditions.

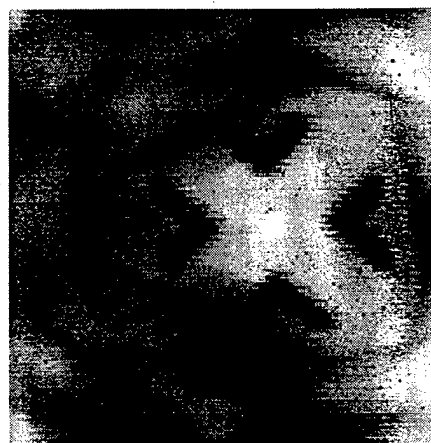
The purpose of the large arrow pattern in the extractor is to help find the small central hole. Great care must be taken to prevent electrons scattered at the edges of the arrow pattern to travel down the column and reach the sample plane. These stray electrons will have the effect of blurring the image, as shown at the top of Fig. 1.8. An appropriately designed source lens, where the inner diameter of the arrow pattern is carefully matched to the diameter of the anode aperture, minimizes the amount of stray electrons and thereby the image distortions throughout the deflection field as seen in Fig. 1.8. Both images in Fig. 1.8 are taken at 1 mm working distance and otherwise identical operating condition for tip and column. A significantly cleaner image over a larger field is achieved with the removal of the stray electrons.

2.1.5 FE tip alignment

For successful operation of the microcolumn, the FE tip needs to be accurately positioned with respect to the micron-size hole in the extractor membrane. Previously a coarse alignment step was done by viewing the tip position relative to an alignment pattern through a telescope as indicated by the picture at the top of Fig. 1.9. The tip is centered over the hole in the extractor membrane which is at the center of the four alignment arrow pattern. The distance of the tip from the extractor is about 100 μm . An apparent second tip is visible as the mirror image of the real tip in the membrane. For scale information it is noted that the diameter of the W wire used to make the tip is 125 μm , and the overall size of the alignment arrow pattern is about 200 \times 200 μm . The arrow pattern is formed by arrays of 2 \times 2 μm holes in the silicon membrane. The coarse alignment was then followed by imaging the micron-size hole in the extractor



100 μm



100 μm

Fig. 1.7. Images obtained by mechanically scanning the Schottky tip to image the extractor membrane and the emission pattern. Top image shows weak Schottky and strong thermal emission. Bottom image is taken at higher extractor voltage and slightly lower tip temperature resulting in strong Schottky emission.

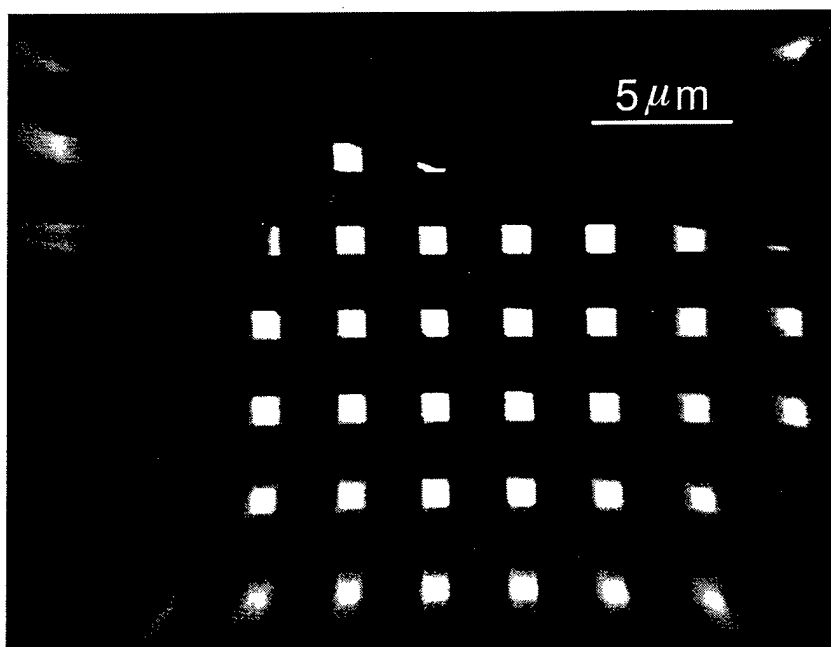
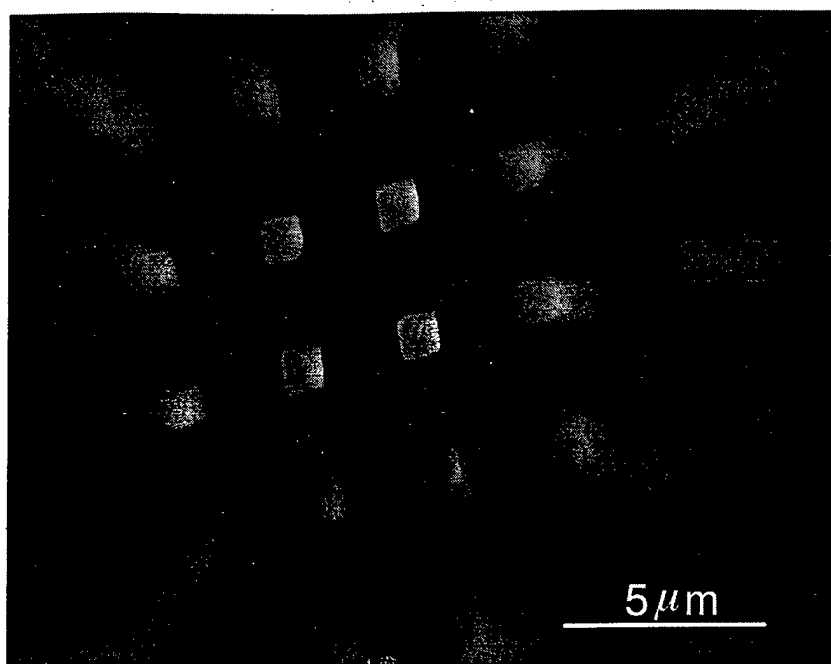


Fig. 1.8. Stray electrons causing image blurring (top) and sample imaged under the same conditions, but after source lens redesign to minimize the possibility of stray electrons reaching the sample plane.

membrane in STM mode using a $10 \times 10 \text{ }\mu\text{m}$ scan field. This alignment process is critically dependent upon the submicron to micron size tip to extractor membrane separation and not easily automated. Operating the tip in field emission mode at 50 to 100 μm distance from the extractor while monitoring the limiting aperture current is a more reliable and more easily automated approach.

By using the beam current intercepted by the limiting aperture, as shown in the lower part of Fig. 1.9, while scanning the tip, an image of the extractor membrane can be derived electronically. An increase in the limiting aperture current is observed whenever the tip is positioned over a hole in the extractor membrane. The resolution of this imaging process is shown in Fig. 1.10 and depends on the emission angle from the tip and the distance of the tip from the extractor membrane. The scan area for these images is $250 \times 250 \text{ }\mu\text{m}$ and the emission current is 1 μA . At 200 μm distance, details in the image are barely visible. Decreasing the distance to about 50 μm results in a well defined image of the 5 μm hole in the extractor. Zooming in on this center hole can then be used as an automatic tip alignment technique. By comparing the current on the limiting aperture to the emission current under the assumption of constant angular emission current density, an emission half-angle of 5° is typically calculated for the oxygen processed tips.

2.1.6 FE tip characterization

Since the above described imaging technique is very sensitive to the emission conditions, it can be used to periodically monitor the emission characteristics of the FE tip during operation of the microcolumn. As such, the technique can be used to visualize the effect of the tip flash as shown by the top row of images in Fig. 1.11. The images are taken immediately before and after a tip flash. The images at the bottom of Figure 1.11 give examples of diagnostic capabilities of the extractor imaging technique. The image at the bottom left shows multiple extractor pattern images caused by multiple discrete emission sites on the FE tip. The image at the bottom right shows the effect of excessive emission current noise with a bandwidth limited to 100 Hz.

2.1.7 A $20 \times 20 \text{ mm}$ footprint 1 keV Microcolumn Module

This report reports the successful operation of a fully functional $20 \times 20 \text{ mm}$ footprint microcolumn module and discusses, in particular, the field size improvements achieved through the use of a pre-lens double deflection system, the performance of an ultra-thin MCP based secondary/backscattered electron (SE/BSE) detector, and first results of using this microcolumn module for electron beam lithography on semiconductor substrates.

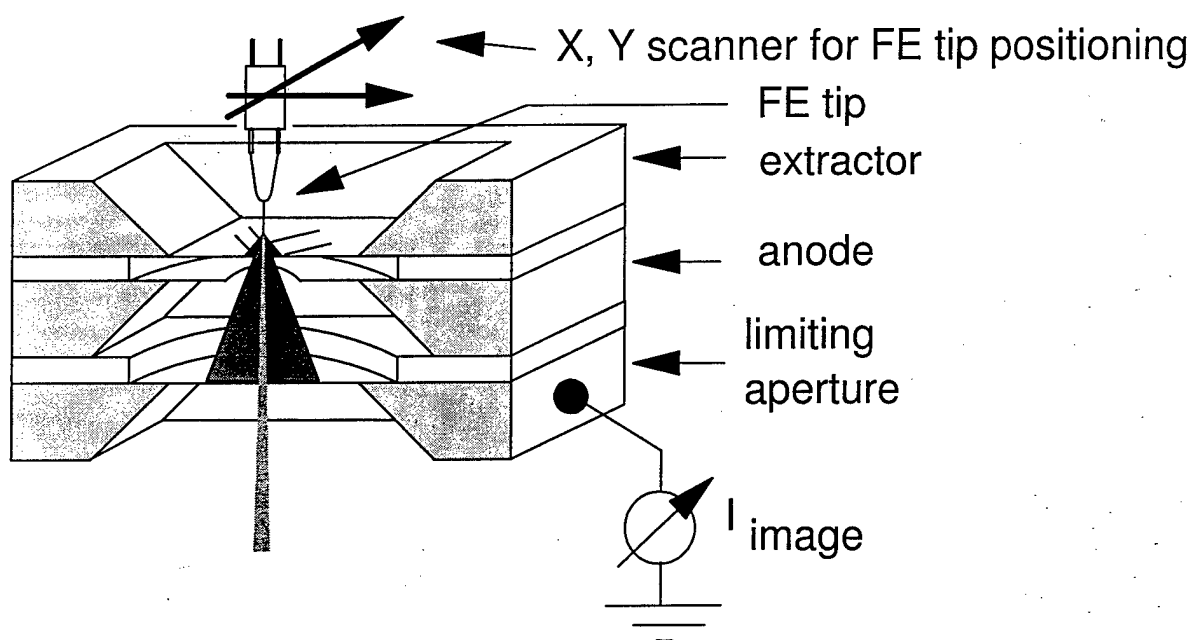
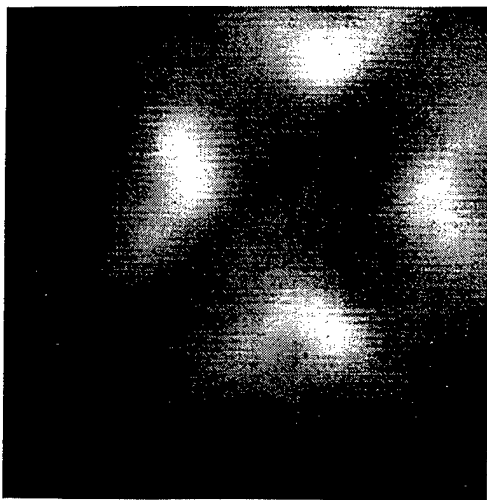
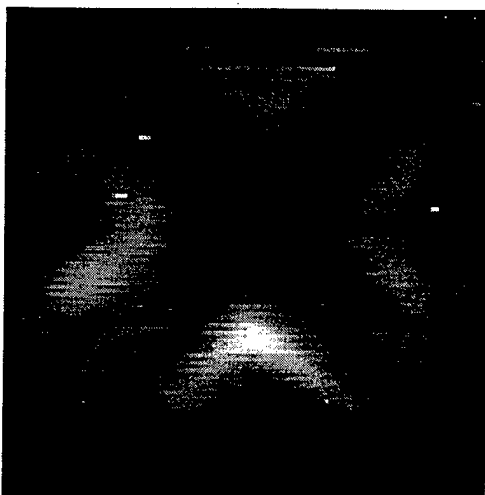


Fig. 1.9. Tip alignment methods: top shows optical tip alignment with respect to arrow pattern centered around the 5 μm hole in the extractor membrane; bottom shows electronic tip alignment configuration which images the extractor membrane pattern by measuring the limiting aperture current.

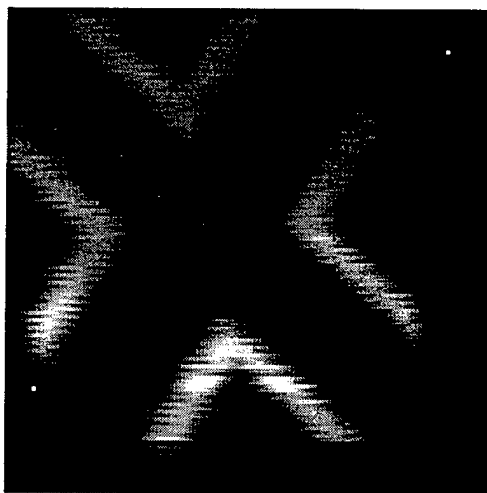


scan area: $250 \times 250 \mu\text{m}$
emission current: $1 \mu\text{A}$
tip to extractor distance:

$200 \mu\text{m}$

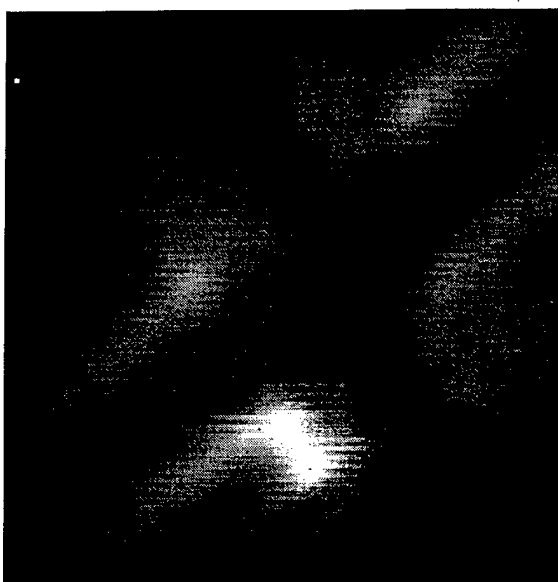


$100 \mu\text{m}$

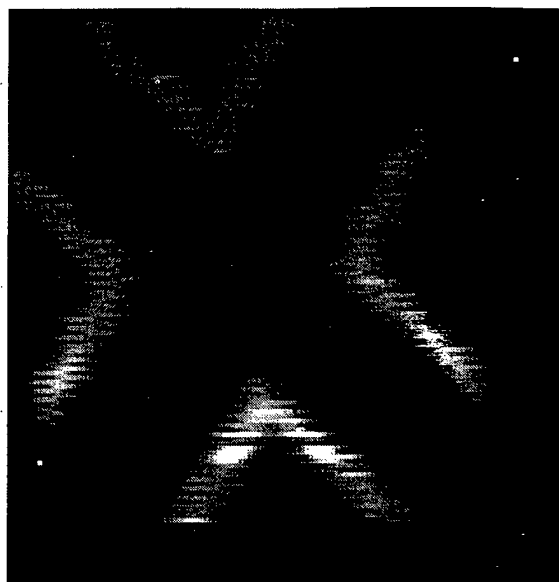


$50 \mu\text{m}$

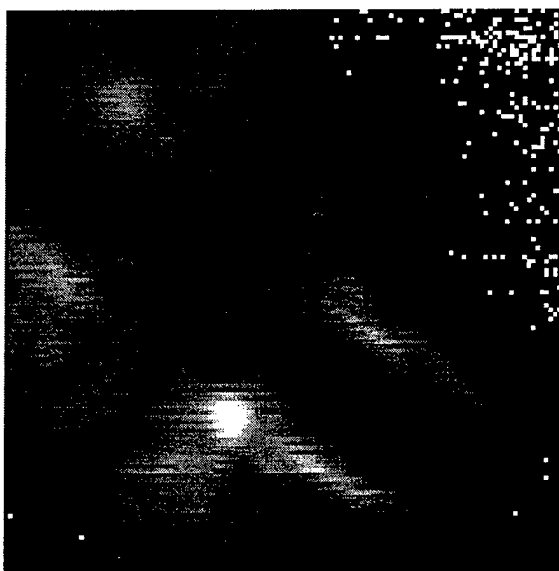
Fig. 1.10. Extractor membrane imaging for tip alignment. The resolution in the images is a function of the tip to extractor membrane distance and the emission half-angle from the FE tip.



before tip flash



after tip flash



tip with multiple emission lobes



noise ($f < 100$ Hz)

Fig. 1.11. Tip emission characterization by extractor membrane imaging. The effect of the tip flash can be visualized and emission characteristics, such as multiple emission sites and emission current noise, monitored.

The microcolumn module consists of a miniature Zr/O/W Schottky field emitter^{1.15} mounted on a three-axis scanning tunneling microscope (STM) positioner,^{1.16} the beam forming optics, a double octupole deflector, and an MCP detector. A schematic of the column cross-section is shown in Fig. 1.12 along with a picture of a microcolumn module. The total column length is about 3.5 mm from the emitter tip to the last electrode of the einzel lens. The working distance is typically in range of 1 to 5 mm, with short working distances intended for high resolution microscopy, down to 10 nm beam diameter,^{1.17} and longer working distances for applications requiring larger field size, up to 150 μm at 5 mm working distance.

The STM positioner is used to align the Schottky emitter with the column. The range of movement is about 1×1 mm. A vacuum pressure in the low 10^{-9} Torr range is required for the stable operation of the Schottky emitter, and under these UHV conditions many types of drive bearings have the tendency to freeze up after a few hours or days of operation. This is caused by the lack of lubricants and therefore increasing friction between the moving parts, in this case the shear piezos and the slider. We found that a combination of ruby rods sliding in alumina V-grooves is a material combination that does not exhibit this problem. We have also built an electronic driver circuitry which generates parabolic output voltages for constant acceleration followed by a short fly-back time to achieve the most efficient "stick/slip" operation. The Schottky emitter mounts into the STM with a cylindrical Macor sleeve for thermal insulation between the hot suppressor cap and the temperature sensitive shear piezos in the STM drives.

The Schottky emitter is operating at a temperature of approximately 1800 K and an angular current density of up to 120 $\mu\text{A}/\text{sr}$ at a distance of about 50 to 100 μm from a 5 μm diameter bore extractor electrode which is made from a 2 μm thick silicon membrane. To date, reliable operation of both the emitter tip and the extractor membrane over periods in excess of five months has been observed.

The extractor together with the anode form a selectively scaled source lens, followed by the beam limiting aperture. This stack of three silicon electrodes is bonded together using Pyrex insulating spacers and mounted on an aluminum base plate, shown in the lower part of the microcolumn picture in Fig. 1.12. Integrated into this aluminum base is a double octupole deflection system with the wire pairs from the corresponding deflector plates sticking out the side of the base. Hidden from the view in the picture in Fig. 1.12 is the symmetric einzel lens, which is mounted on the underside of the aluminum base plate. Immediately following the einzel lens is the detector assembly.

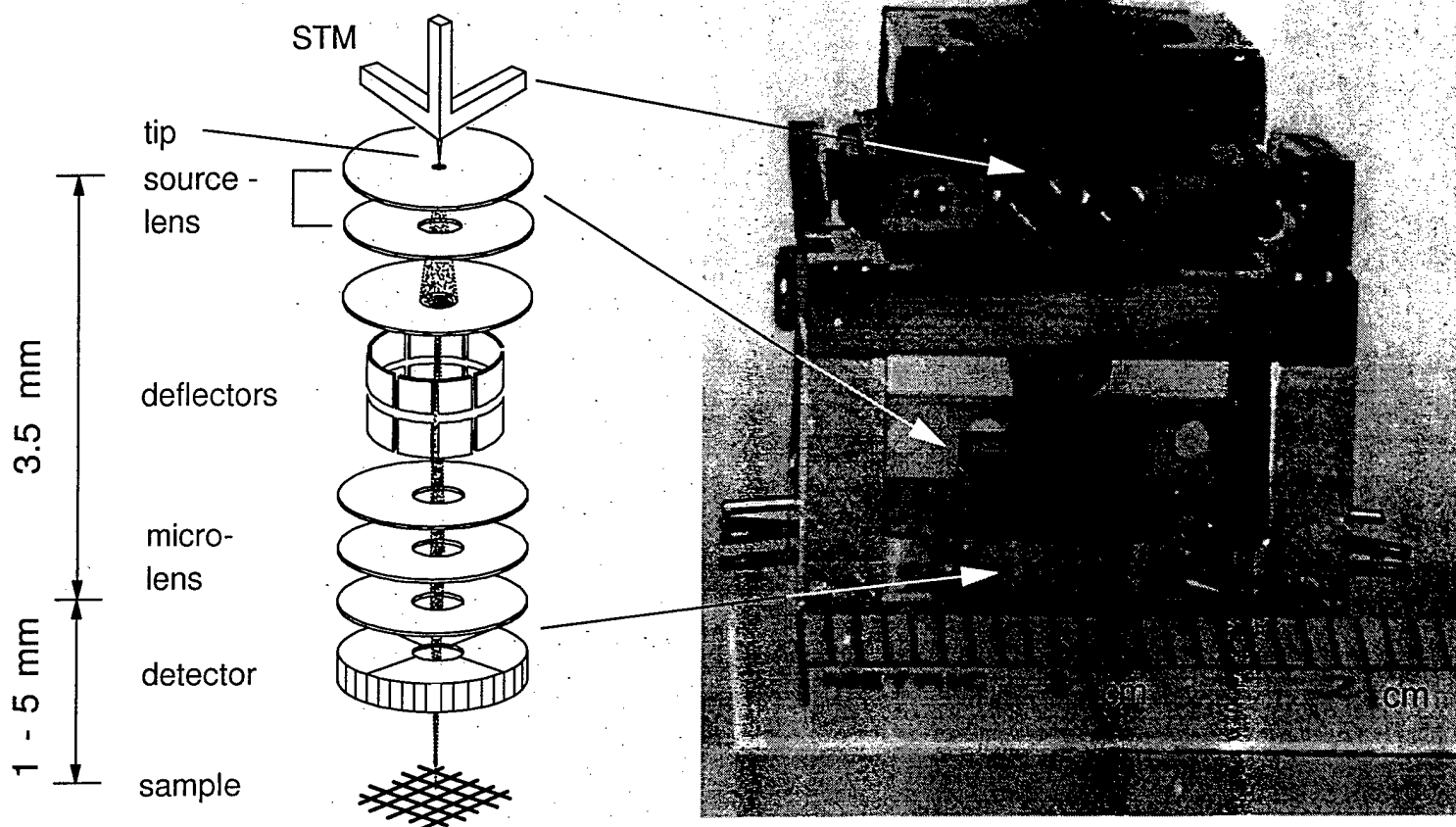


Fig. 1.12. Sideview of 1 kV microcolumn module and diagram of the electron optical components.

2.1.8 MCP detector Implementation for SE and BSE Imaging

Because of the relative low energy of 1 keV electrons, the short, 1 to 5 mm, working distance, and the low distortions required for lithography application, the implementation of a SE or BSE detector is rather challenging. Conventional PIN- or Schottky diode type solid-state detectors cannot be used, because electrons entering the detector would lose several keV of energy before reaching the active detector region.^{1,18} Also, detectors such as Everhart-Thornley scintillator/photo-multiplier combinations or channeltron electron multipliers, which use a strong axially asymmetric electric field to attract secondary electrons are prohibited, because the detector field would introduce astigmatism in the beam spot and cause deflection field distortions.

Single or double stage MCP detectors are high gain, low noise, continuous dynode type electron multipliers.^{1,19} The high gain, 10^4 to 10^8 , is obtained at an operating voltage of 1000 to 3000 V for single or double stage MCP detectors, respectively. The high intrinsic gain of the detector allows the use of relatively low gain, high bandwidth electronic amplifiers for signal processing. Except for the challenging mounting and electrical isolation requirements for this type of detector within the constraints of the small working distance in the microcolumn, MCP detectors offer the best performance for SE and BSE detection in the microcolumn. Other detector types, in particular metal-semiconductor-metal (MSM) detectors, have the advantage of being easier to integrate with einzel lens fabrication. In the microcolumn they can be used for BSE detection only with a gain in the range of 200 to 1000.^{1,20,1,21}

A schematic of the MCP detector implementation in the microcolumn is shown in Fig. 1.13 along with a picture of the components. Given the dimensions (4 mm inner diameter, 14 mm outer diameter) of the commercially available MCP,^{1,22} for best geometric collection efficiency for BSE detection the detector has to be mounted as high as possible above the sample. Therefore the einzel lens fabrication was changed to use 2 μm thin silicon membranes not only for the center electrode, but also for the last electrode of the lens. The detector is mounted directly to the bottom of the einzel lens. The detector consists of two pieces: the MCP, and the anode/collector electrodes which are machined out of Macor with patterned electrode made by metal vacuum deposition and electroplating. Thereby the whole detector assembly, operating at 1000 V between the input and output side of the MCP, is only 0.8 mm high. A maximum gain of 3×10^4 has been measured.

Scanning electron microscope (SEM) images in SE mode have been obtained with the 1 kV microcolumn using this detector. The image shown in Fig. 1.14 was obtained

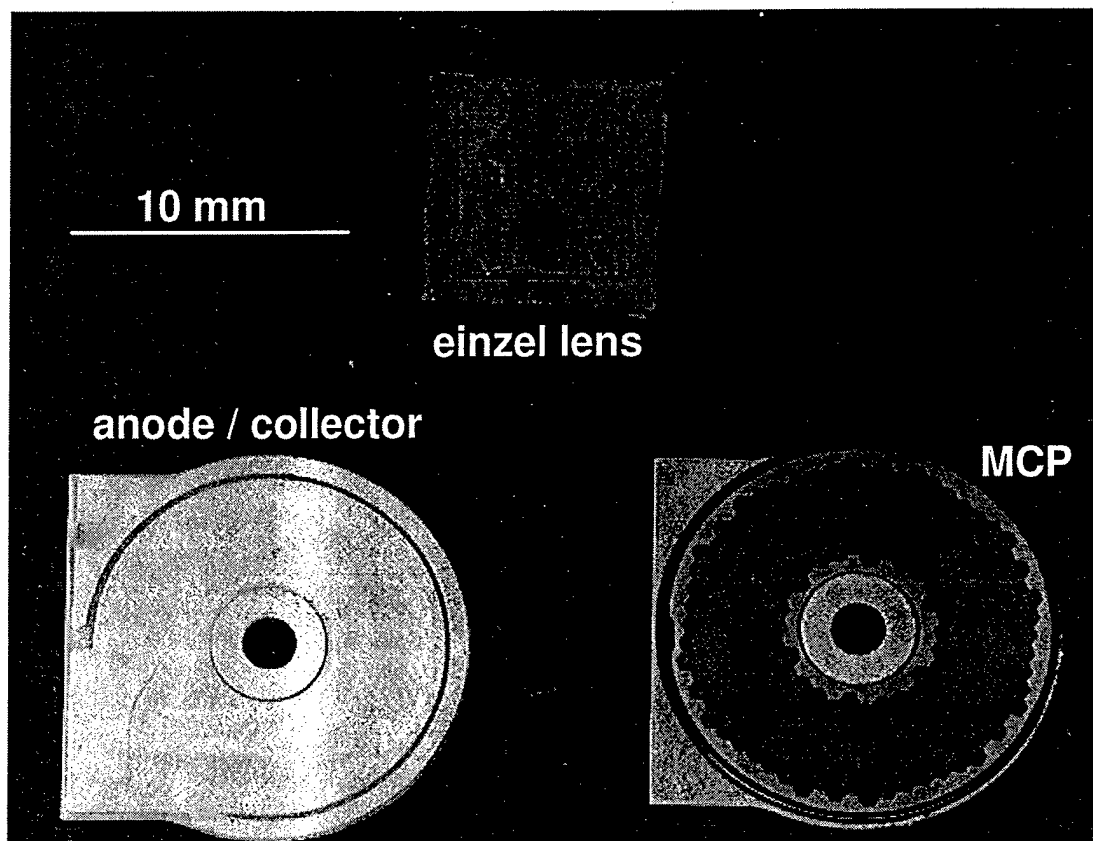
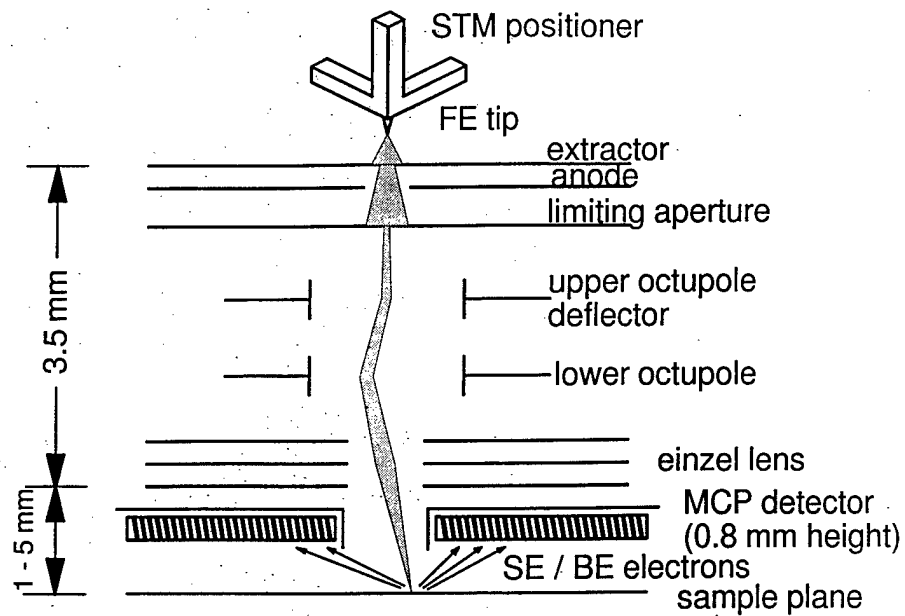


Fig. 1.13. Schematic of the MCP detector implementation in the microcolumn. Also shown are the detector components together with an einzel lens.

using a beam current of about 50 pA at a working distance of 4.5 mm. The inset shows a higher magnification view of the grainy gold deposit on this carbon membrane sample. For SE detection the input electrode of the MCP is typically biased about +100 V. To suppress SE detection in the BSE imaging mode, the input electrode is biased slightly negative, about -10 V. This comparison is demonstrated in Fig. 1.15, where a SE and a BSE image of the same sample area are shown. In the BSE mode of operation enhanced material contrast is evident in those areas of the sample where small broken pieces of the membrane with the carbon side facing up are lying on top of the gold coated membrane. At the higher electronic gain applied in the case of the BSE image some periodic interference becomes visible.

2.1.9 Microcolumn Field Size Improvements

With a single stage pre-lens deflector, deflection distortions and aberrations are minimized when the off-axis deflection of the beam on its path through the einzel lens is minimized. Even better results are achieved by using a pre-lens double deflector and optimizing the deflection ratio between the upper and the lower deflector. The double deflection system also has the advantage of being able to apply beam tilt and shift alignment corrections to the beam on its path from the micro-source to the einzel lens. Thereby, the column alignment tolerances become less critical. The analytical results for the 1 kV microcolumn of the probe diameter dependence on the deflection field diameter are shown in Fig. 1.16 for a working distance of 4 mm. The “usable” deflection field diameter is here defined as the field size diameter within which the probe diameter increases by less than 20% between the center of the field and the edge of the field. The four graphs show that with a single stage deflector the field size increases from about 6 μm to 23 μm when the deflector position is moved from 1.8 mm to 0.8 mm distance from the einzel lens. Operating two deflectors in the form of a double deflection system increases the field size to about 104 and 142 μm with the einzel lens operating in the accelerating and the retarding mode, respectively. To achieve this performance the deflection ratio has to be optimized for minimum spot size distortion.

This field size improvement is shown qualitatively in Fig. 1.17 for three of the above mentioned four cases. For demonstration purposes, the results shown here are for the einzel lens operating in the retarding mode. A silicon grid with $1 \times 1 \mu\text{m}$ holes on 3 μm centers is imaged here in SE mode at the two positions for the single stage pre-lens pre-lens deflector and with the double deflector. The respective improvements in field size are evident from the diminishing flare at the edge of holes close to the edge of the imaging field. The double deflection system was operated close to the calculated

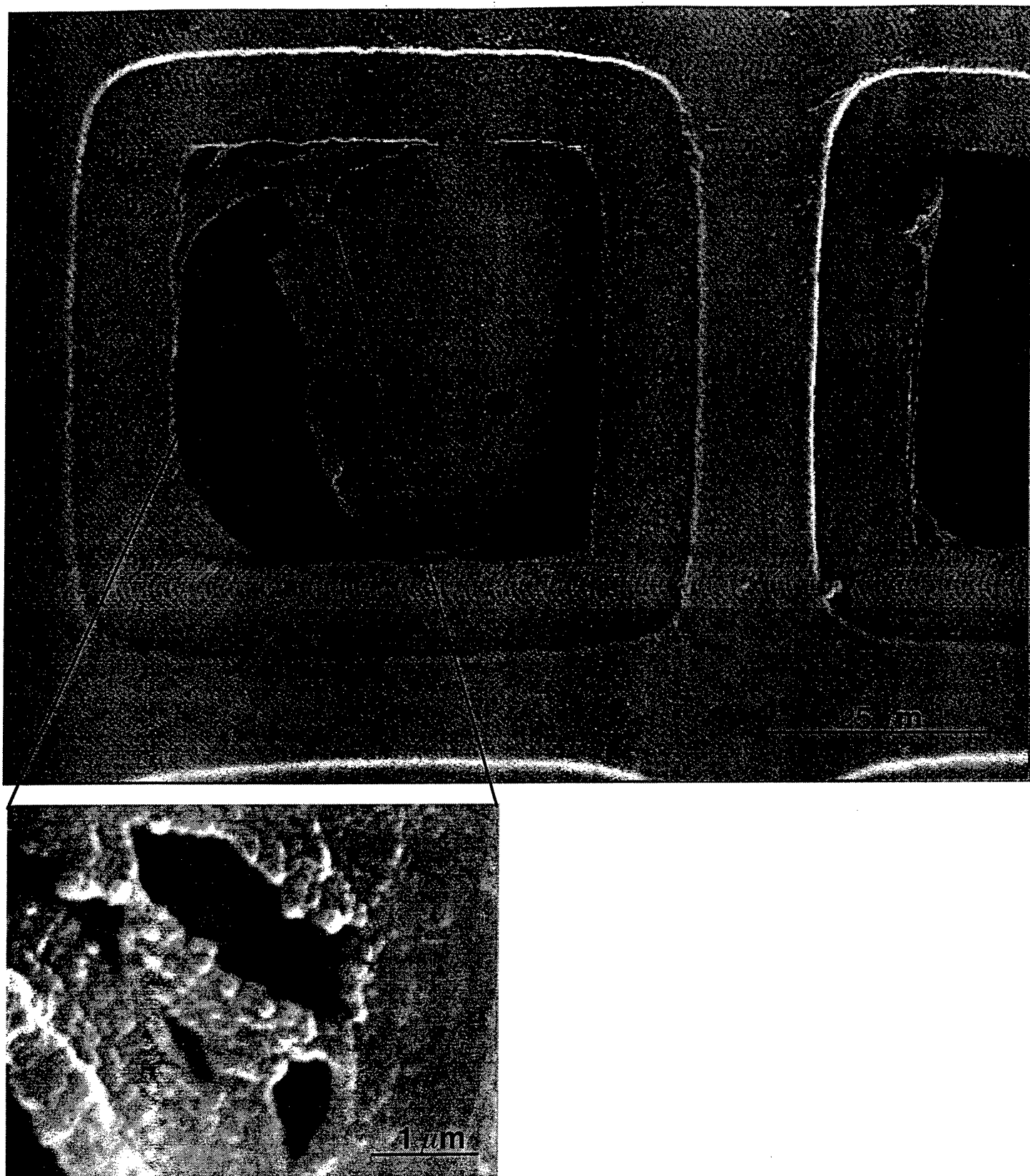


Fig. 1.14. SEM images obtained in the microcolumn at 1 keV beam energy using the MCP detector.

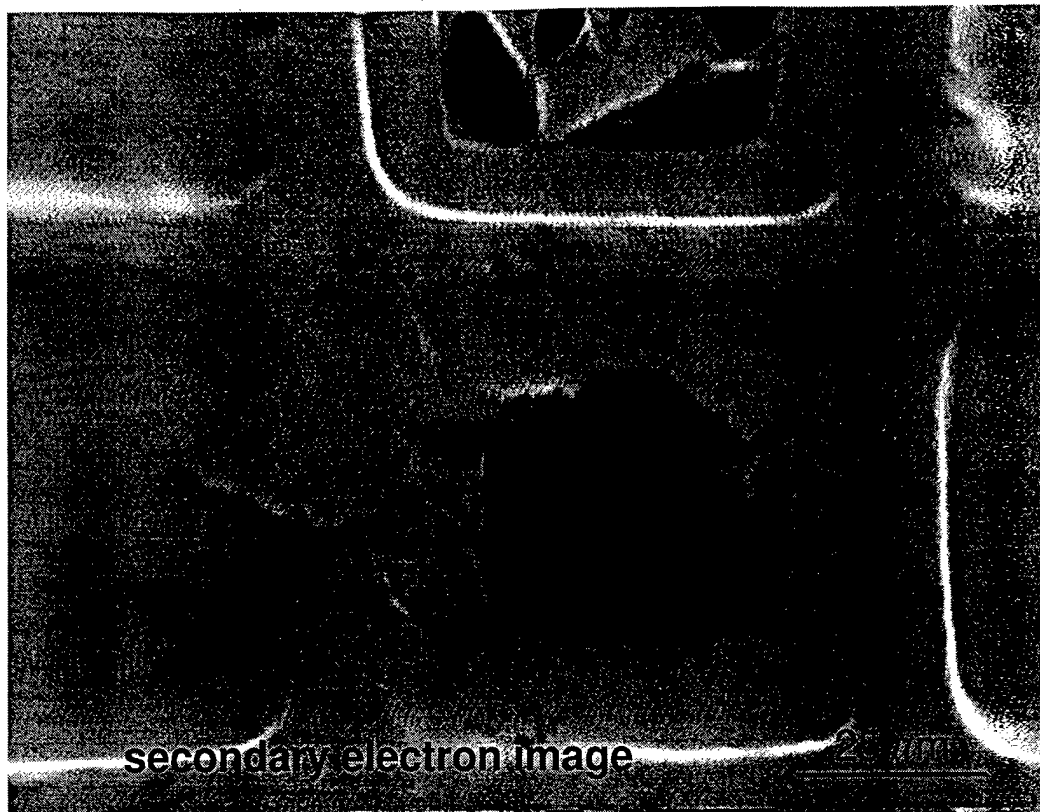


Fig. 1.15. Comparison of the secondary and backscattered electron imaging mode of the MCP detector in the microcolumn.

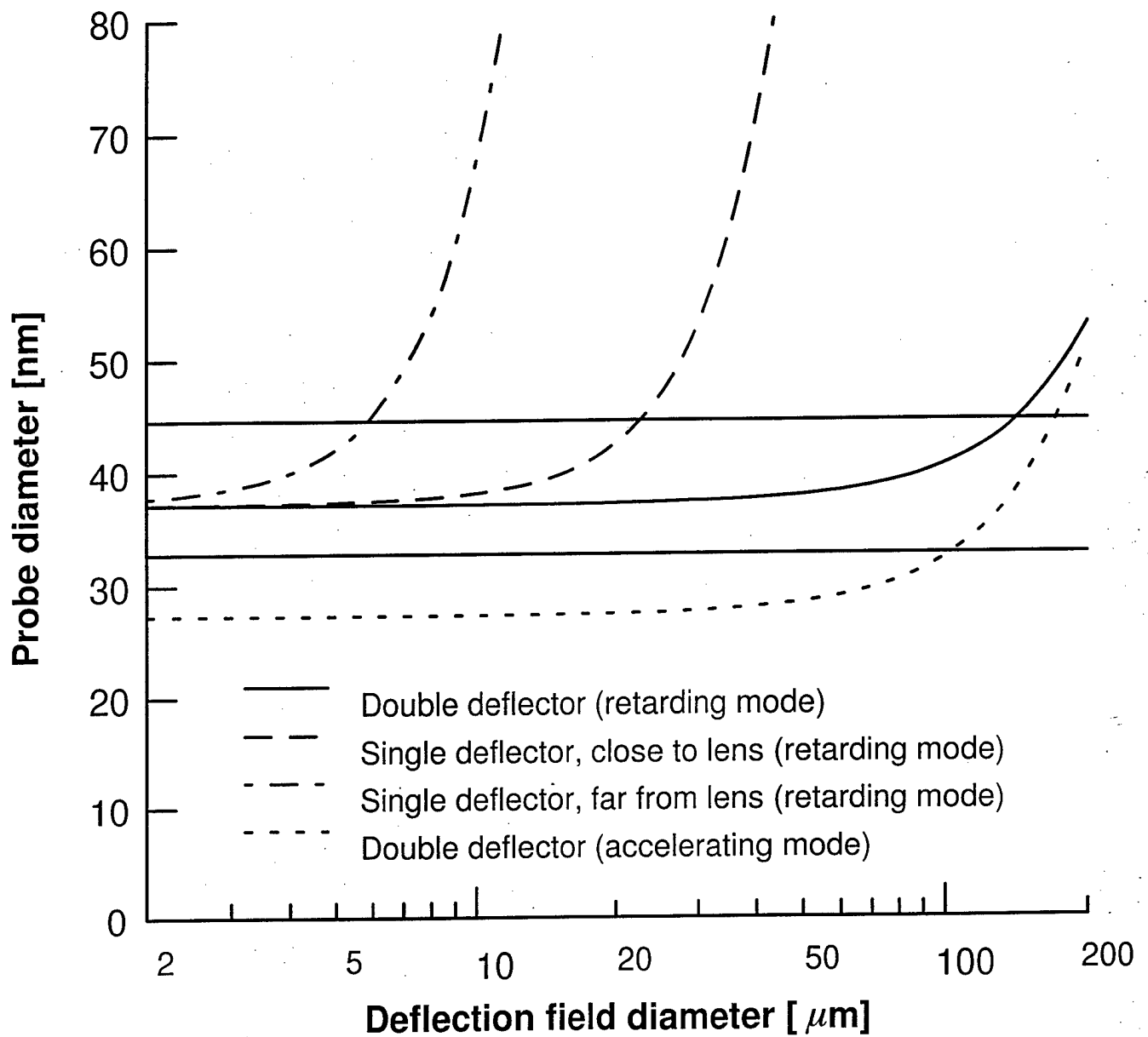


Fig. 1.16. Calculated probe diameter at the edge of a deflection field of a given size for three deflector options and two operating modes of the einzel lens. The working distance is assumed to be 4 mm.

optimum deflection ratio and astigmatism corrections were added to the octupole deflection signals.

2.1.10 Lithography Operation

The microcolumn has been interfaced to a computer controlled digital pattern generator for electron beam lithography operation, and some early results have been obtained with this configuration. The digital pattern generator consists of two computer controlled arbitrary waveform generators capable of a sample rate of up to 50 Mhz for moving the beam in nanometer size steps across the resist coated substrate. The beam is scanned across a rectangular shape primitive of programmable size at a programmable beam stepping rate. The scan mode is a baustrophodonical or meander scan to minimize settling effects in the deflection electronics. Complex patterns are composed of a number of rectangular shape primitives. The beam stepping rate is adjusted so that the optimum exposure dose for any given resist and development process is applied at a given beam current and beam diameter. The beam is measured precisely through the use of a faraday cup integrated onto the substrate carrier right next to the resist coated wafer. The beam step size is selected to match the beam diameter for a uniform exposure.

Samples have been prepared by spinning a 35 to 40 nm thick layer of PMMA (2% Elvacite in xylene, molecular weight 495k) on top of an evaporated layer of 20 nm tungsten on a silicon substrate. The resist is exposed at 1 kV with a line dose of 0.16 nC/cm. The resist pattern is shown in Fig. 1.18 after development in 1:2 MIBK:IPA solution at 21°C for 30 s followed by a rinse in IPA for 30 s. The sample was then etched in a CF₄ plasma at 100 W RF power and 15 mTorr pressure for 60 s, which is just enough time to etch through the 20 nm tungsten layer. Figure 1.18 shows the less than 100 nm wide lines etched into the tungsten layer. Much of the edge roughness in the lines is due to tungsten layer thickness variations and is therefore absent in the image of the developed resist lines. A more systematic evaluation of the 1 kV microcolumn lithography including the patterning of higher resolution features, more advanced pattern generator, an evaluation of the proximity effects, and process optimization for various pattern transfers is planned for the future.

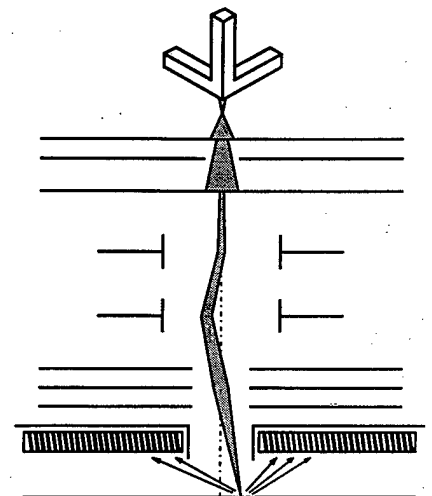
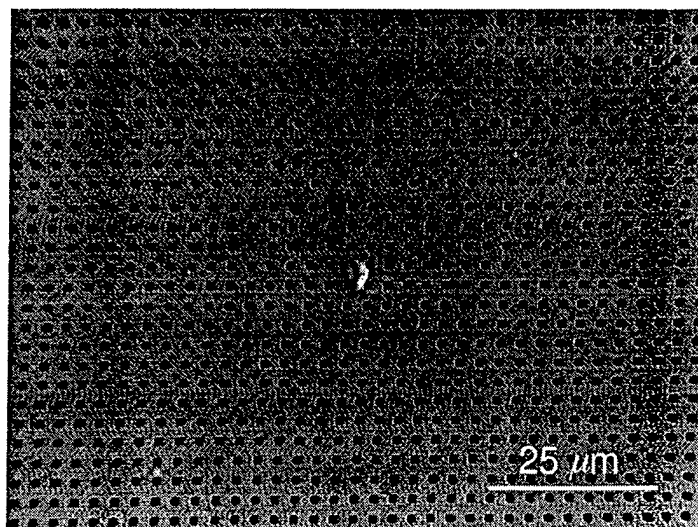
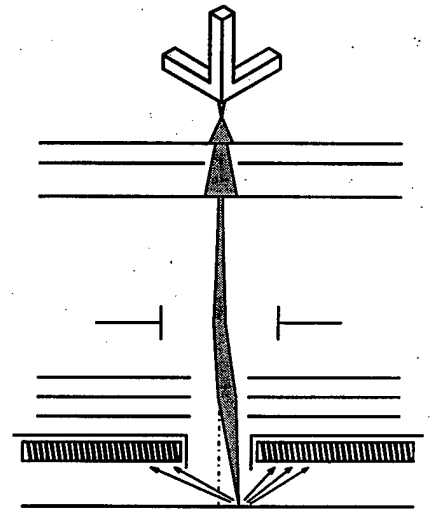
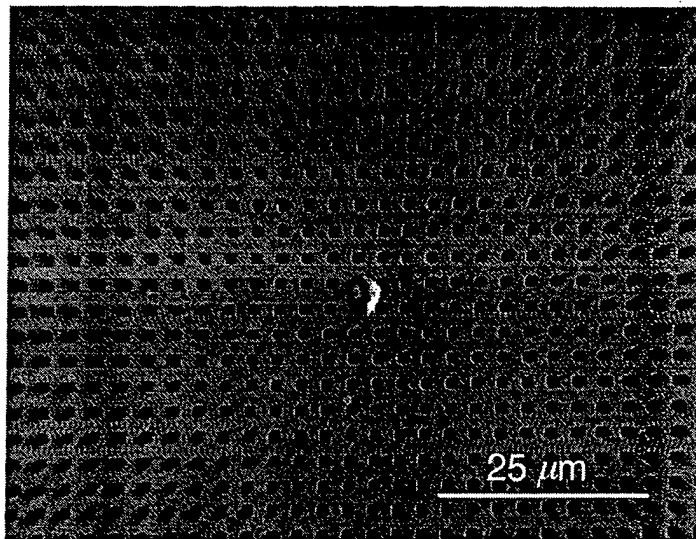
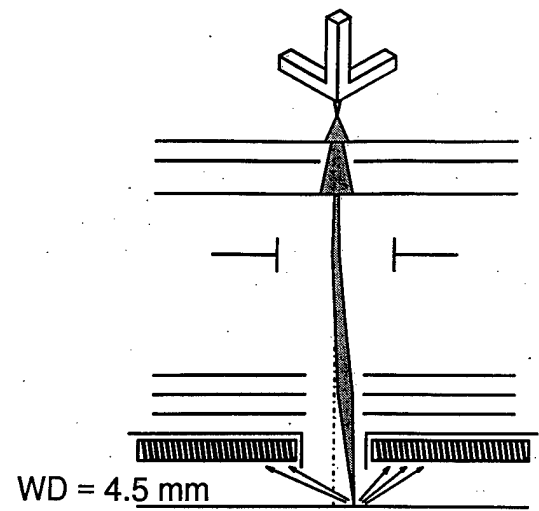
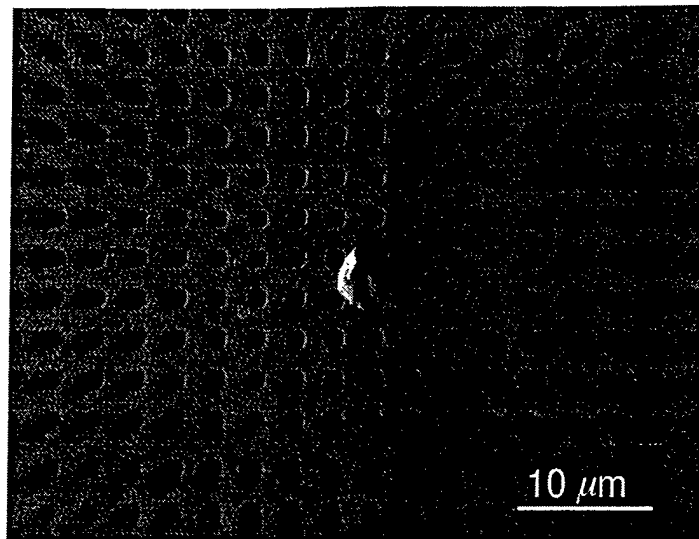
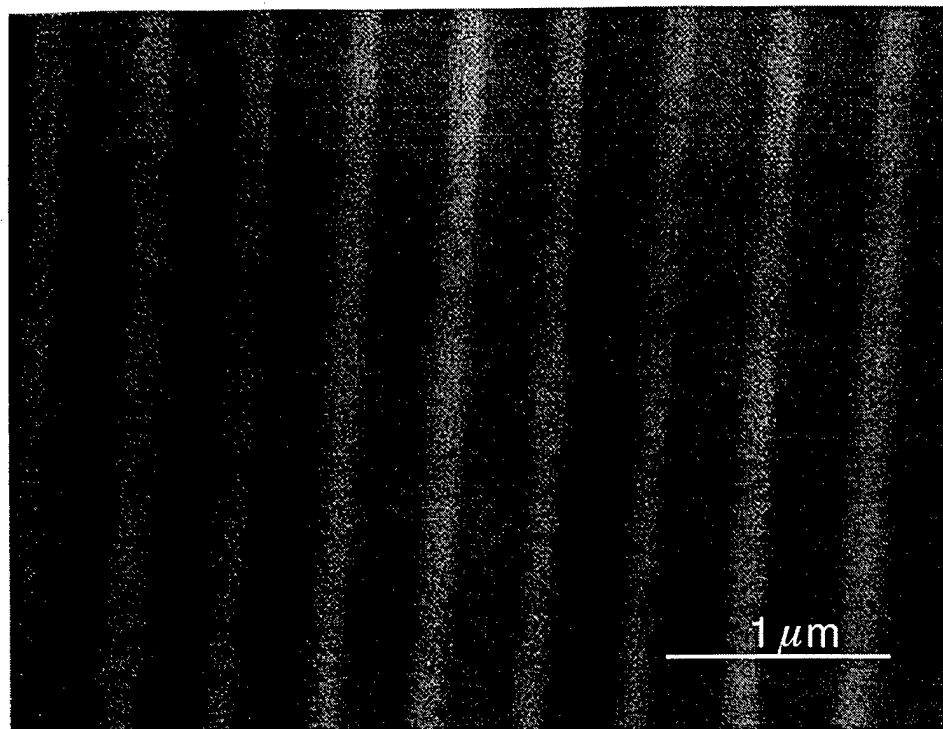
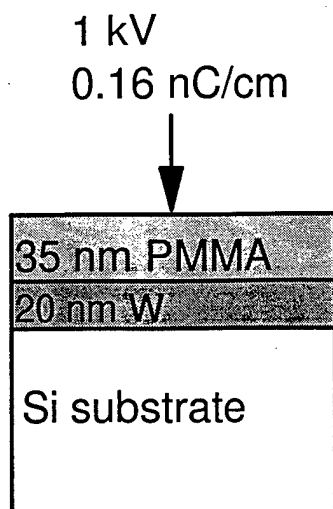
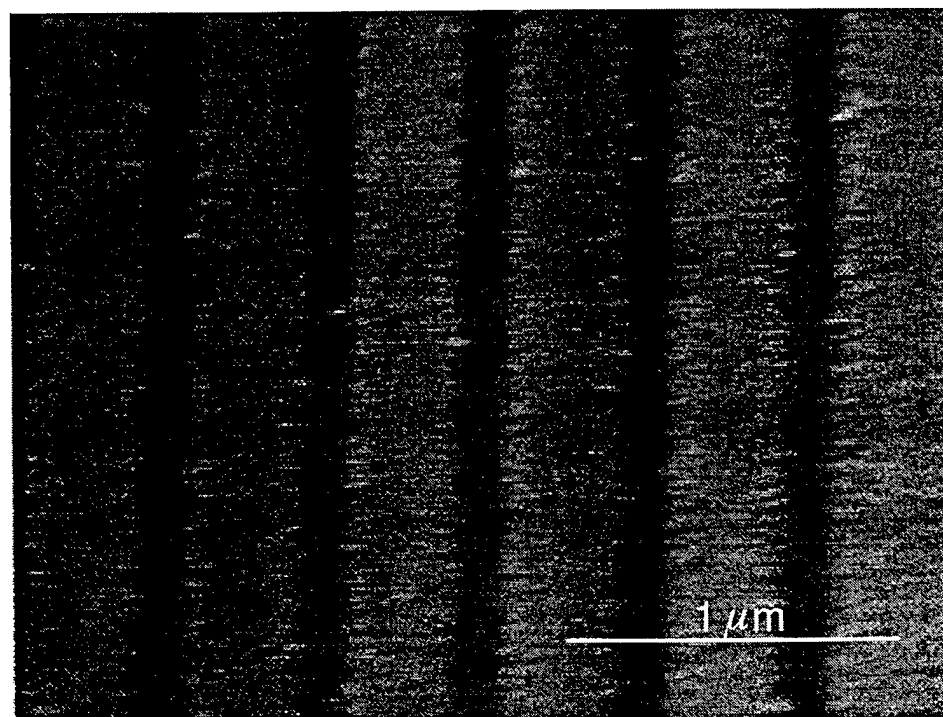
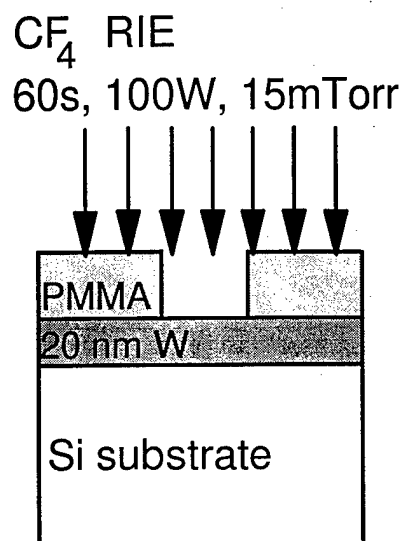


Fig. 1.17. SEM images showing the field size improvements from moving a single stage deflector closer to the lens, and from using a pre-lens double deflector.



PMMA resist after exposure and development



100 nm lines etched into tungsten layer

Fig. 1.18. Example of 1 kV lithography with the microcolumn resulting in less than 100 nm lines transferred by reactive ion etching into a tungsten layer using a PMMA resist pattern as the etch mask.

2.1.11 Arrayed Microcolumns Testing

A simple 2×1 array of the microcolumn modules has been constructed and assembled. The array has been installed in a test system ready for the following tests and experiments:

1. A demonstration of the basic operation of multi-beam lithography.
2. An evaluation of the interaction between columns, during high speed pattern writing and with different column wiring and interconnection schemes.
3. A study of the overall issues with multi-beams.

Fig. 1.19 shows photos of the completed 2×1 array assembled on an intermediate carrier plate before and after its installation into the arrayed column test system. The columns are of identical design to the 2×2 cm footprint microcolumn described earlier. The columns are spaced at 2 cm centers. Special attention has been given to screen the cables carrying the deflection signals to minimize their interactions. A separate annular MCP detector is provided for each column to allow fully independent SEM operation which is needed for focusing and registration operations.

A new test system designed specifically for arrayed columns testing has been developed. A view of the completed system showing the mechanical, UHV pumping, and part of the control electronics is shown in Fig. 1.20 (top). The system features a specially designed work chamber designed to handle a 200 mm wafer. The chamber has two sub-chambers to facilitate differential pumping. The lower sub-chamber, which houses the wafer and a laser controlled stage, has a special rectangular airlock port in addition to a number of ports for laser beams and feedthroughs. The upper sub-chamber, which houses the microcolumn array, also has a rectangular port for differential pumping and numerous additional ports for feedthroughs. An intermediate plate which carries the microcolumn array can be introduced from the top of the chamber to separate the upper and lower sub-chambers. Fig. 1.20 (bottom) shows the work chamber which measures 330 mm × 330 mm × 290 mm high. This relatively small chamber together with an *X-Y* stage of 25 mm travel and appropriately arranged arrays of microcolumns can be used for lithography covering a full 200 mm wafer.

2.1.11 Summary

We have demonstrated a fully functional 1 kV microcolumn module with a 20×20 mm footprint and a height of about 25 mm. This microcolumn module has all the required features for arrayed electron beam lithography evaluation on semiconductor wafers. Testing has shown a beam diameter of 10 nm at a beam current of about 1 nA

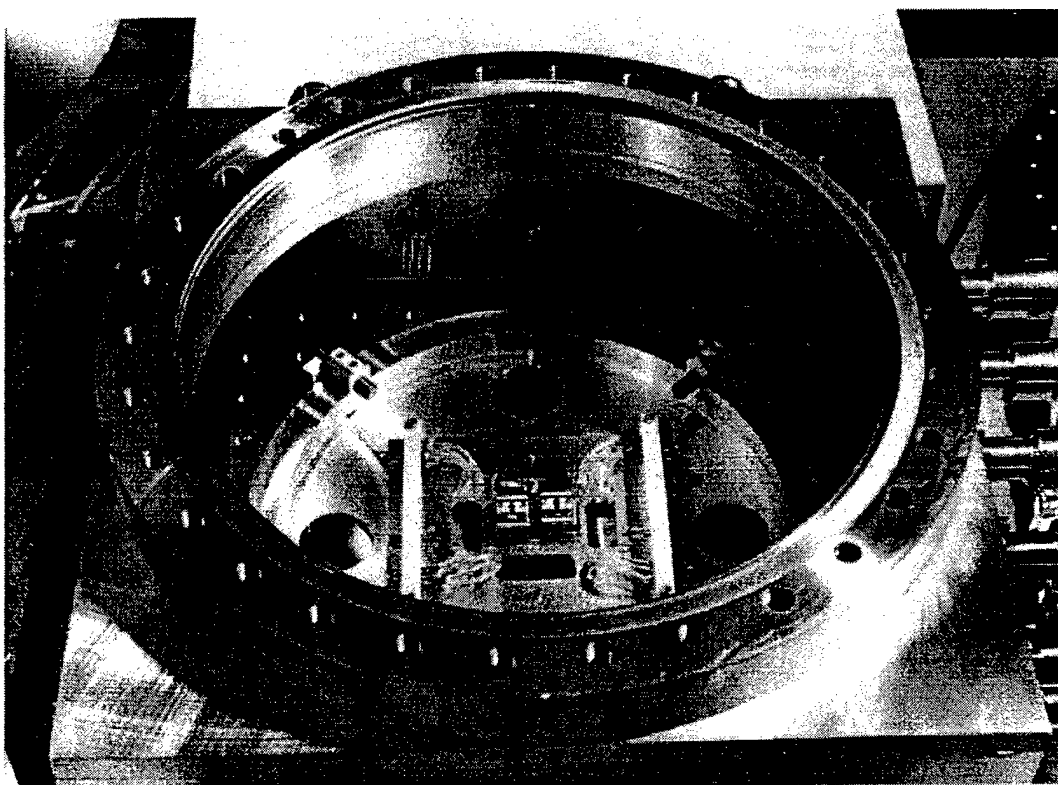
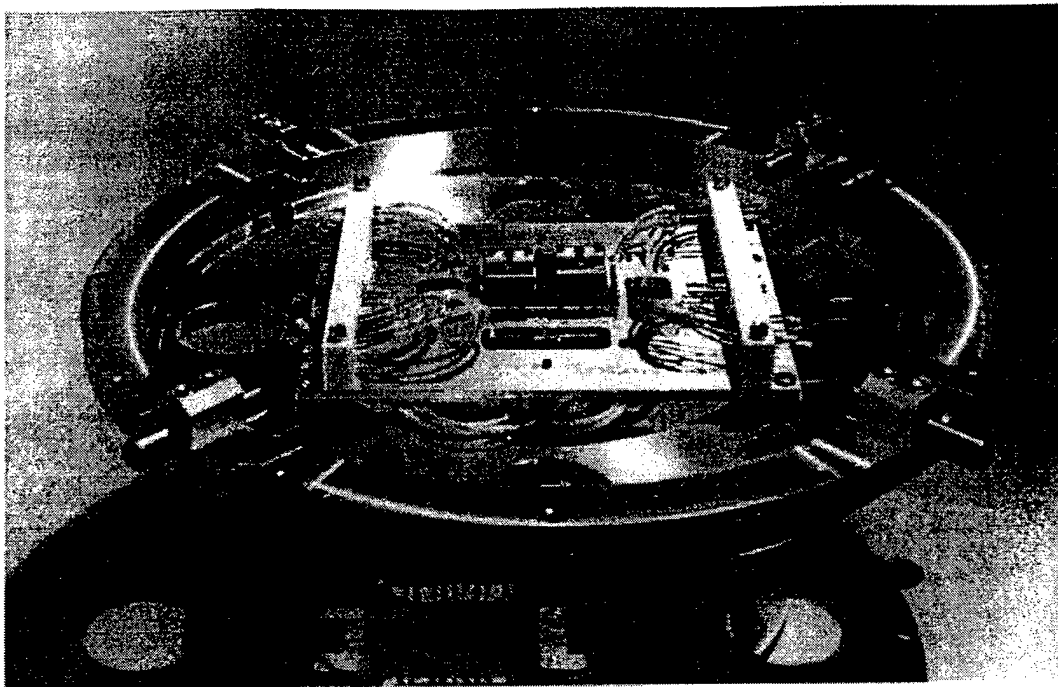


Fig. 1.19. A simple 2×1 array of microcolumns installed on an intermediate carrier before (top) and after (bottom) its introduction to the test system.

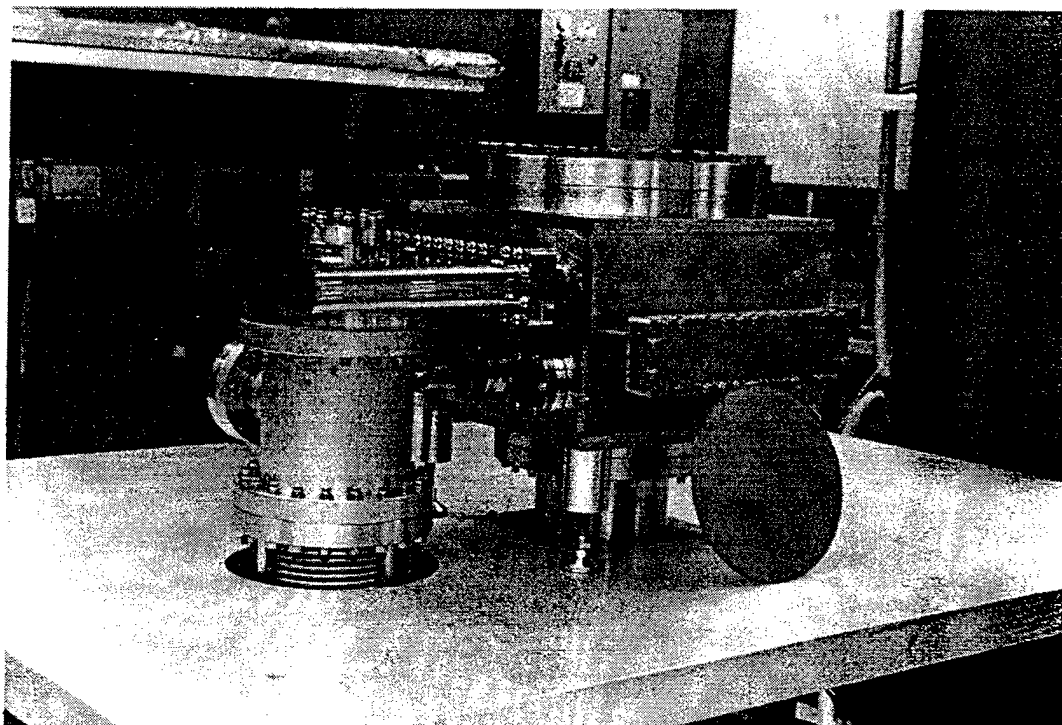
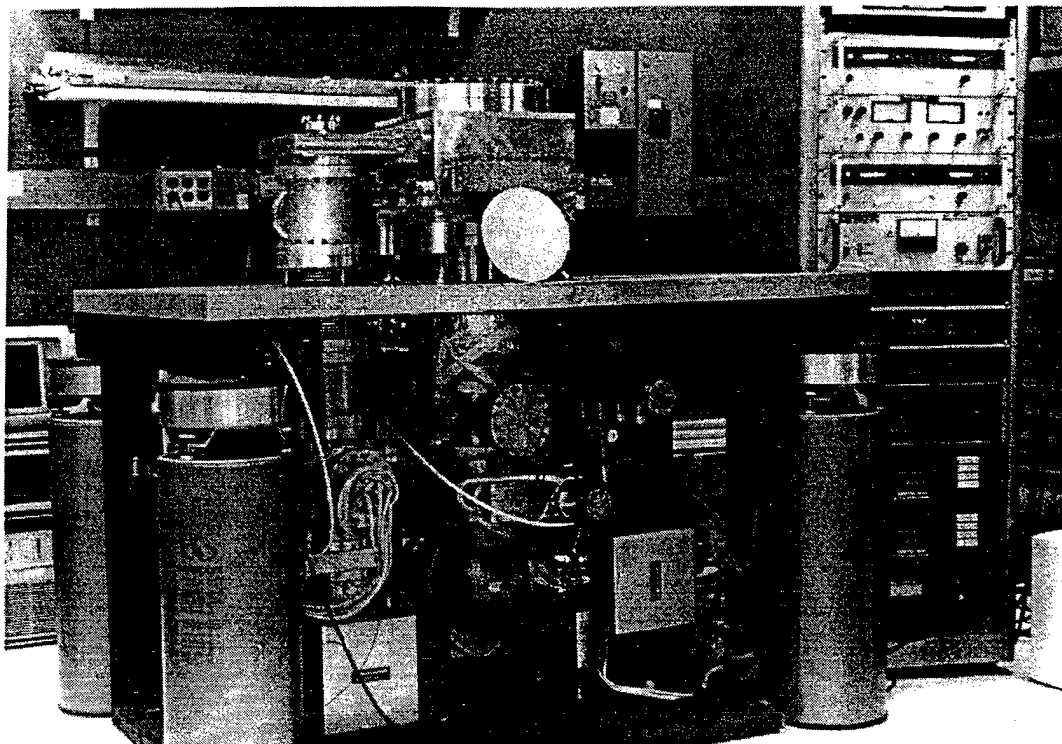


Fig. 1.20. A view of the new arrayed columns test system (top) and the differentially pumped work chamber designed to handle a 200 mm wafer.

and a working distance of 1 mm. This beam current is at least an order of magnitude larger than the beam currents obtained in previous microcolumns with cold field emitters, while maintaining very good emission current stability.

The microcolumn has also been shown to operate as a fully functional low voltage SEM for inspection of solid samples in various imaging modes, including SE, BSE, and also specimen current (SC) imaging. SE and BSE imaging has become possible through the addition of a high gain, ultra-low profile MCP detector. Initial low voltage electron beam lithography with the microcolumn has resulted in lines less than 100 nm wide transferred into tungsten layers on silicon substrates. Further work towards higher resolution patterns is in progress. The deflection field size has been improved by incorporating a pre-lens double deflection system, and field size $\geq 100 \mu\text{m}$ at 4.5 mm working distance has been demonstrated.

The measured beam diameter is an excellent confirmation of the resolution expectations for the present microcolumn based on electron optical modeling.

The microcolumn modules has been interfaced to a computer controlled pattern generator and preliminary $0.1 \mu\text{m}$ lithography demonstrated. A simple 2×1 array of microcolumns has been constructed and installed in a new test system ready for various arrayed lithography experiments.

2.2 Electron Optical Studies

2.2.1 Introduction

The electron-beam microcolumn is based on the *selective scaling principle*.^{2,1} The on-axis performance of any electron lens can be characterized by its coefficients of spherical and chromatic aberration, and these are reduced if the lens dimensions as well as its working distances are scaled to smaller dimensions. If electrostatic lenses are used (as they must be in the gun accelerator), the field strengths cannot exceed certain values determined by experiment, and these dictate lower working voltages as the spacings between lens elements are reduced. To accomplish this, the beam energy E_0 must also be reduced. Chromatic aberration δ_c is related to the chromatic aberration coefficient C_c by $\delta_c = C_c \alpha \Delta E/E_0$, where α is the beam convergence semiangle and ΔE is the energy spread of the electrons in the beam, so the advantage of the smaller C_c is offset by the smaller value of E_0 . However, considerable advantage remains in the current microcolumns^{2,2} with component dimensions much less than 1 mm, and working distances not much greater than 1 mm.

The sizes of all the electron-optical components (accelerator, deflector, and the final focusing lens) are constrained to be smaller than about 1 mm. In order to maintain high brightness with low energy spread, the electron source is typically a room-temperature field emitter, or a Schottky emitter operating at 1800 K. When operating at high current, the energy spread can be as large as 0.5 eV full width at half maximum (FWHM), so the relative energy spread at 1 keV beam energy is 5×10^{-4} . The size of the final focused probe will be dominated by diffraction and by chromatic aberrations. The lenses and the deflection system must have very small chromatic aberration coefficients. A diagram of the deflection system and focusing lens is shown in Fig. 2.1.

The extremely short focal length and physical size make a magnetic lens impractical. Starting from any basic electron optics text,^{2,3} it can be shown that the peak field in a magnetic lens scales approximately with $E_0^{1/2}/(w_m \times f)^{1/2}$ where E_0 is the beam energy, w_m the width of the axial magnetic field distribution (determined by the bore diameters and spacing of the pole pieces), and f is the focal length. In a microcolumn, it is usual to reduce E_0 , w_m , and f to much smaller values than used in conventional columns. If, for example, all three are reduced by a factor of 25, high magnetic fields (5 times larger) would be required, and the space required for the magnetic pole pieces would not be available. In an electrostatic einzel lens, the field scales approximately with $E_0/(w_e \times f)^{1/2}$ where w_e represents the dimension of the axial electrostatic field distrib-

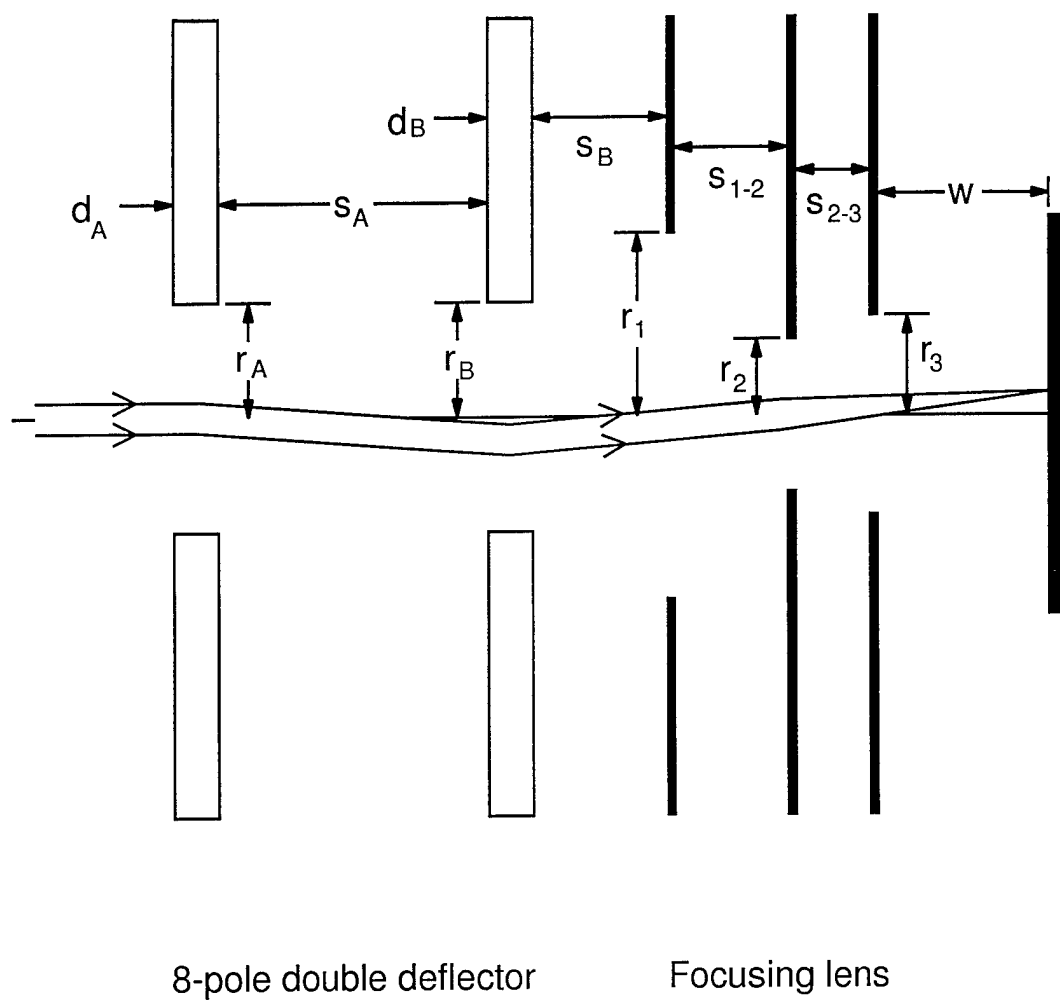


Fig. 2.1. The optical diagram of the einzel focusing lens and the double deflection system showing the parameters which can be varied by the optimization procedure. A typical deflected trajectory is shown.

ution. Again, E_0 , w_e , and f may all be reduced 25 times, in which case the peak electric field strengths will not change.

The lenses must also be compatible with the fabrication processes available at these small sizes. The lens electrodes are currently fabricated from silicon membranes about 1 μm thick, with bore diameters between 1 and 500 μm , and the proposed lenses are consistent with this. Another important factor is the alignment tolerances, since fabrication errors may be a more significant fraction of the lens bore than for conventional lenses. The aberrations produced by misalignment must be predicted for the different lens types, and designs selected which can tolerate the electrode misalignments which are inherent in their assembly.

For simplicity of construction, the deflector is also electrostatic. It must be designed in concert with the focusing lens to achieve the largest possible deflection field at these low beam energies. Multipole deflectors are used to save space and so that the functions of beam alignment and astigmatism correction can also be combined with deflection scanning.

The ultimate probe size and current in an electron-beam column are determined in part by the electron-electron interaction effects within the electron beam. These effects will change if we scale the geometry of a column to a different size, or if we change the energy of the electron beam. The effects of interactions have been investigated for column lengths as small as 4 mm, and the results compared to those for lengths up to 0.4 m with beam energies from 1 to 100 keV. The probe currents available in a 25 nm-diam probe are compared.

A number of proprietary and other electron-optical analysis packages were used to evaluate the optical properties of the microcolumn, but modified versions of commercially available programs^{2,4} were used for most of this work. The finite element was used for the electron gun, the finite difference method for the lenses, first order perturbation theory for determination of tolerances, and the three-dimensional boundary charge element method for the deflectors. An optimization strategy was devised to obtain the best lens and deflector configuration.

2.2.2 Lens and Deflector Design

2.2.2.1 Introduction

The most important criterion for the design of the optical system was the size of the focused probe at any given value of the *working distance* w , defined as the distance between the last electrode of the focusing lens and the substrate plane. Probe diameters smaller than the final desired probe diameter are required because there is additional broadening caused by electron-electron scattering within the beam as the current is increased. The design must also take into account the allowable tolerances in the accuracy of the lens components and in the assembly of these components. The contributions to the probe diameter due to errors which are inherent in the fabrication processes were estimated.

Once a lens design was completed, the deflection system was optimized to gain the largest possible size of the scanned field. Because this field size is very small compared to tradition designs in full-size optical designs, some innovative deflection techniques were explored.

In all cases, the assumption was made that the energy spread in the beam was approximately 0.5 eV (FWHM). This value will vary as the gun emission current is made smaller or larger, but is a reasonable starting point for a field emission or a Schottky emission gun.

2.2.2.2 Optimization

An optimization strategy was devised to obtain the best lens and deflector configuration. A frequently used optimization method is to characterize the axial potential or field distribution as a function of a number of parameters, and to change the distribution to optimize the performance.^{2.5,2.6} The resultant potential can then be extended off-axis, and electrodes designed which will produce the desired distribution. The optimization can be fast, but the lens may either be impossible to manufacture, or suffer from requiring impractical voltages or field strengths. In order to ensure that the resulting design could be fabricated, a different approach was taken.^{2.7} The geometry of the lenses and deflectors were characterized by a number of parameters (see Fig. 2.1), and when these parameters were changed by the optimization routine their values were constrained to lie between specified limits. To ensure that the operation of the lenses would also be practical, the excitation voltages and the interelectrode electric field strengths were constrained so that they could not exceed certain values (usually 2500 V and

2×10^7 V/m, respectively). For each set of values of the geometric parameters, the potential distribution was computed, and the optical properties calculated. Because of the computation required to obtain the potential distribution, particularly for a three-dimensional case such as a deflector, this method required much more computer time. The optimization was carried out using the sequential quadratic programming algorithm subject to nonlinear constraints.^{2.8,2.9}

An interface was devised so that the optimization routine could use any of many other programs to evaluate the optics and return the aberration coefficients. Additional programs were written to generate the data required to specify the lens and deflector geometry as well as the finite element mesh for these programs. The results output from the commercial programs were not smooth functions of the input parameters. They had to be modified so that a small fractional change in the input (less than 1 part in 10^6 , say) would produce a corresponding small change in the output.

The optimization was used to find the minimum probe diameter or the maximum scanned area. The maximum scanned area was defined as the area at the edges of which the probe diameter would be 20% larger than the axial diameter. This is a restrictive criterion, suitable for lithographic applications, which leads to small scanned field sizes. Much larger fields may be usable in other applications such as scanning electron microscopy.

The diameter of the deflected probe was obtained by adding in quadrature the diffraction, spherical aberration, axial chromatic aberration, coma, curvature of field, third order astigmatism, and chromatic change in magnification. The image of the virtual source was not included, since this will depend on the optics of the complete system, and the emission current used. Since chromatic change in magnification was as large as any other deflection aberration, dynamic correction of curvature of field and third order astigmatism were less effective and not used in the results presented below; nor was the lens strength changed to balance defocus against curvature of field.

The optimization was carried out on an IBM RS/6000 model 540 workstation using the AIX™ operating system. Most of the optimizations could be completed in less than 1 h, but more time was required for more than five variables, or when repeated three-dimensional deflector field determination was required.

2.2.2.3 Focusing Lenses

The current fabrication techniques require that the lens electrodes be fabricated from silicon membranes, approximately 1 μm thick. Because of limitations in the alignment and bonding fixtures, the maximum bore diameter must not be greater than 0.5 mm, and the insulating spacers between the electrodes must be between 0.1 and 0.5 mm thick. The maximum voltage which can be safely applied to the center electrode is 2500 V, and, to avoid breakdown at these small dimensions, the electric field between the electrodes must be less than 2×10^7 V/m. These conditions are referred to in the remainder of this report as the microcolumn constraints. At any required working distance w (defined as the distance between the last electrode and the focal plane), the lens can be operated with the central electrode either positive (accelerating mode) or negative (retarding mode).

Subject to the above constraints, the lens was optimized for a number of working distances between 1 and 5 mm, and the resulting probe diameters are shown in Fig. 2.2. Symmetric and unsymmetric lenses were analyzed. A symmetric lens is one which has a plane of symmetry in the center, so the bore radii of the two grounded electrodes and their distances from the center electrode must both be equal ($r_1 = r_2$ and $s_{1-2} = s_{2-3}$ in Fig. 2.1). Three parameters were varied: the inner bore radius, the outer bore radius, and the electrode separation. In an unsymmetric einzel lens, all three bore radii and the two separations may be different. There were five variable parameters. Note that there is considerable advantage to be gained by using the accelerating mode. Some of the underlying aberration coefficients and other parameters for lenses using accelerating mode are given in Table I. Probe diameters as small as 8 nm at $w = 1$ mm or 21 nm at $w = 5$ mm can be achieved.

For larger values of the working distance, the lens dimensions are limited by the maximum allowable values dictated by the fabrication procedures, so the unsymmetric and symmetric lenses become the same. At smaller values, the central bore diameter must be reduced so that the excitation voltage will not exceed 2500 V. These requirements were removed to see how much improved a lens in the accelerating mode could be. Figure 2.3 shows the resultant probe diameters, which are about 20% smaller. Another technique for improving the probe diameter is to use an electron beam at higher energy, and to use a retarding lens so that the beam lands on the target plane at 1 keV. The probe diameter possible at $w = 1$ mm when the beam energy begins at 7 keV is also shown in Fig. 2.3. The further improvement was found to be small (7%). There are other reasons for using a higher beam energy in the column, such as the reduced effects of electron-electron scattering.

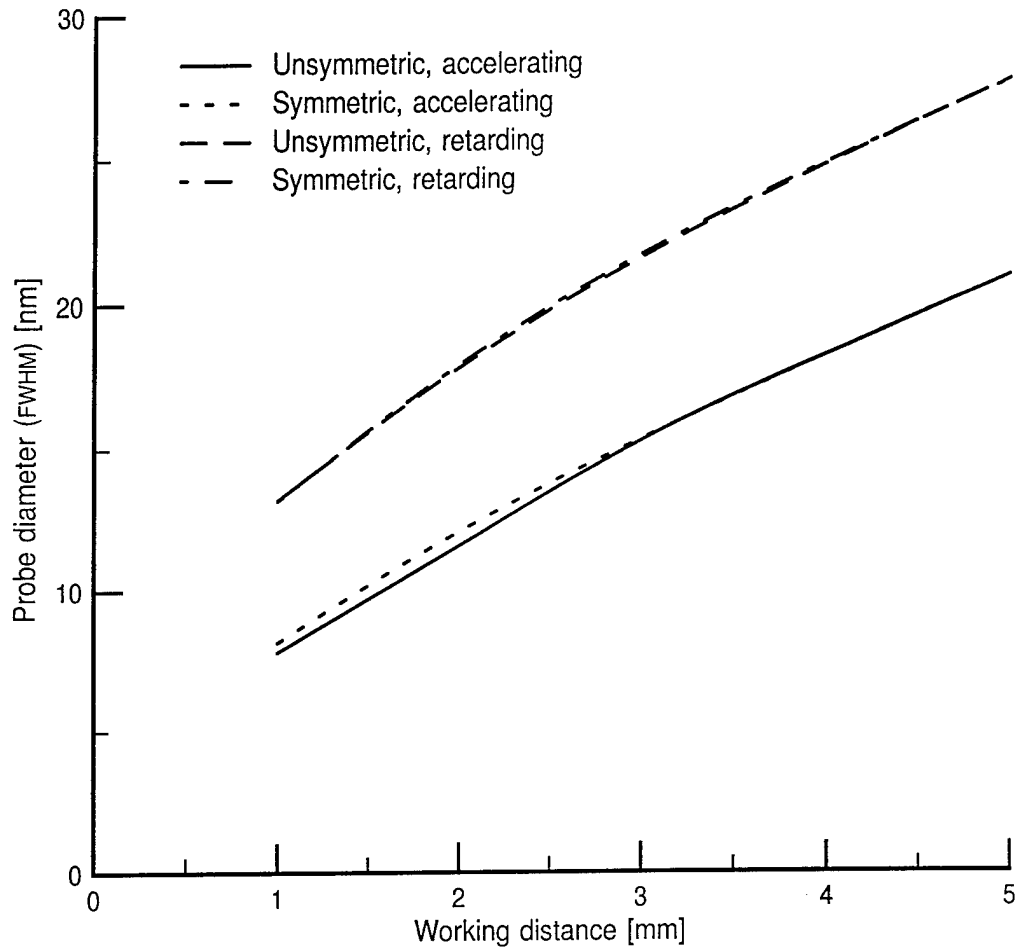


Fig. 2.2. The probe diameters formed by symmetric and unsymmetric optimized einzel lenses with thin electrodes. The beam energy is 1 keV, and the energy spread 0.5 eV (FWHM). The excitation voltages and lens dimensions are all subject to microcolumn constraints. In all cases, the electric fields are limited to be less than 2×10^7 V/m. The probe diameters formed by symmetric and unsymmetric retarding lenses are almost identical.

Table I. The properties of optimized einzel lenses using the accelerating mode. w is the working distance, C_s is the coefficient of spherical aberration, C_c is the coefficient of axial chromatic aberration, α_{opt} is the optimized beam convergence semiangle at the image plane, and d_{opt} is the optimized probe diameter (FWHM). The coma produced by a misalignment s is equal to $\epsilon s \alpha^2$ where ϵ is given in the table. δ is the coma (FWHM) produced by a 1 μm misalignment using the optimum convergence semiangle α_{opt} .

	w (mm)	C_s (mm)	C_c (mm)	α_{opt} (mrad)	d_{opt} (nm)	ϵ	δ (nm)
Constrained	1.00	27.12	1.150	7.404	8.16	78.02	4.277
symmetric	5.00	955.23	8.147	2.950	20.96	185.20	1.612
Constrained	1.00	19.21	1.121	7.879	7.82	59.95	3.721
unsymmetric	5.00	955.23	8.147	2.950	20.96	185.20	1.612
Relaxed	1.00	3.14	0.830	10.369	6.33	3.37	0.362
constraints	5.00	77.18	4.711	4.401	15.02	22.32	0.432

The most significant misalignment error found was a displacement of the central electrode of the einzel lens with respect to the other two. The alignment tolerances are shown in Fig. 2.4 as the coma produced by a 1 μm misalignment of this electrode when the beam convergence semiangle α is 1 mrad. The coma is proportional to α^2 , so at typical values of $\alpha = 5$ mrad it will be 25 times larger than the numbers plotted. As before, the accelerating mode has considerable advantage over the retarding mode, and some of the results for accelerating mode are shown in Table I. Since it is desirable that the contribution from misalignment is substantially less than the probe diameter, the allowable misalignment is less than 1 μm in some cases. The misalignment aberration is proportional α^2 , so it can be reduced by working at a smaller value of α .

In the results discussed above, the lens was optimized for each different working distance. In practice, a fixed design may have to be used for a range of distances. The probe diameters using an existing fixed design (a symmetric design with bore radii all

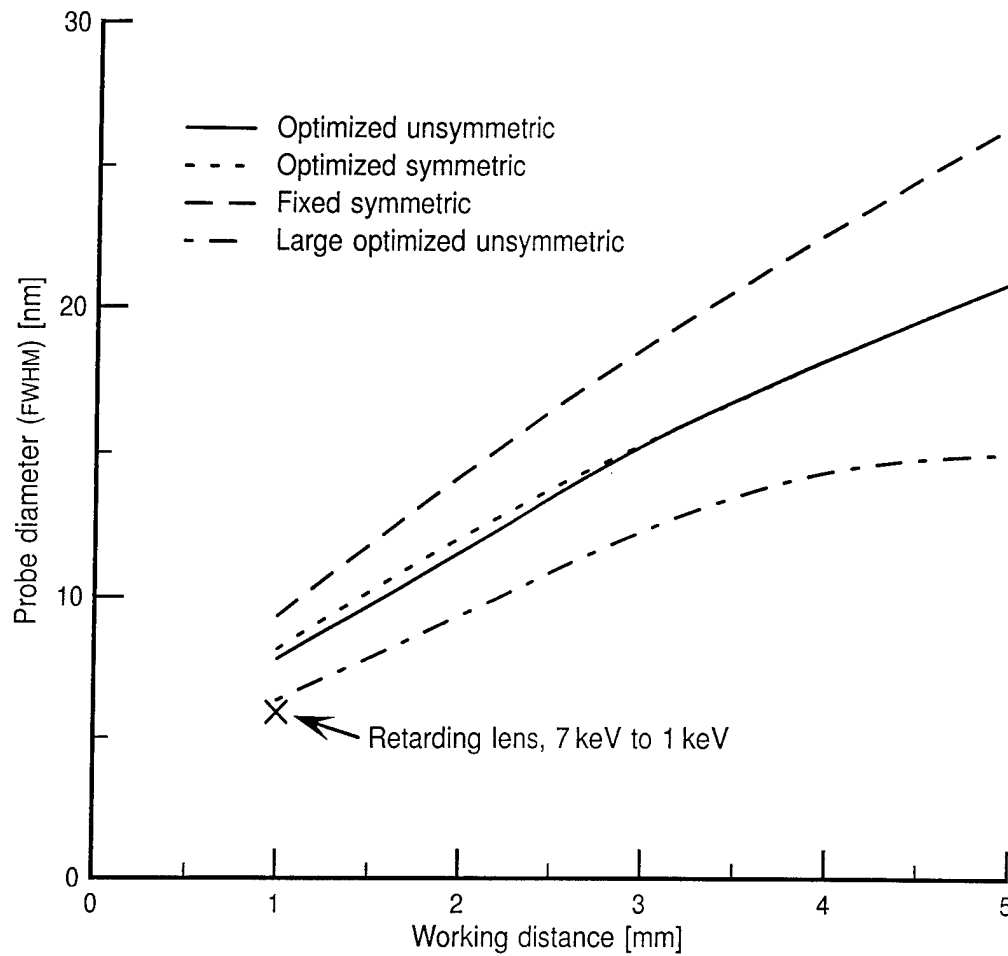


Fig. 2.3. The probe diameters from symmetric and unsymmetric einzel lenses with thin electrodes operated in the accelerating mode. The beam energy is 1 keV, and the energy spread 0.5 eV (FWHM). Except in the case of the large, optimized unsymmetric lens, the excitation voltages and lens dimensions are subject to microcolumn constraints. In all cases, the electric fields are limited to be less than 2×10^7 V/m.

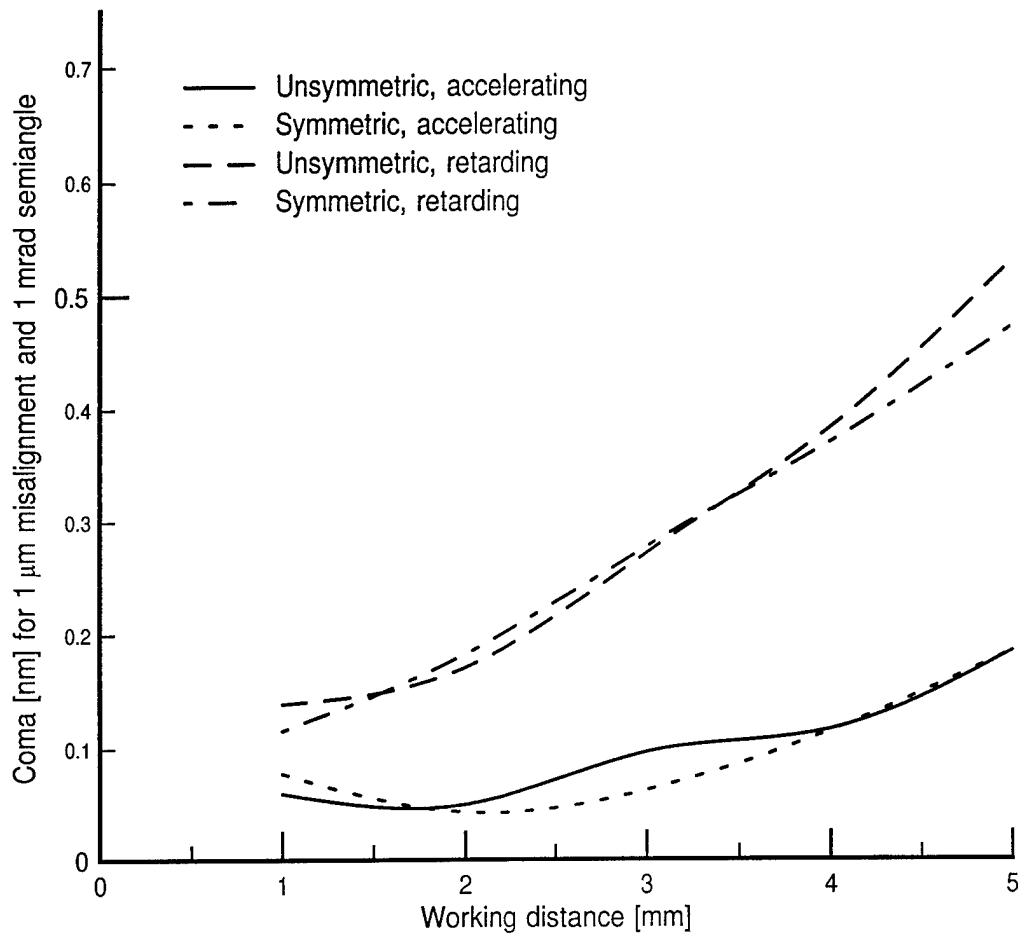


Fig. 2.4. The misalignment error from optimized symmetric and unsymmetric einzel lenses with thin electrodes. The beam energy is 1 keV, and the energy spread 0.5 eV (FWHM). The excitation voltages and lens dimensions are all subject to microcolumn constraints. The coma produced by misalignment of the central electrode relative to the outside two is shown.

0.10 mm and spacings 0.25 mm) is shown in Fig. 2.3. There is obviously some loss of performance, particularly at large values of w .

During the generation of the data to generate the results presented here, some general guidelines became apparent. To optimize the einzel lens, it is necessary to reduce chromatic and spherical aberrations by using the accelerating mode, reduce chromatic aberration by reducing the focal length (reduce the image-side electrode spacing and increase the object-side bore radius and electrode spacing), and reduce spherical aberration by increasing bore radii and electrode spacings as much as possible. The fabrication tolerances can be improved by using the accelerating mode and increasing the bore radii and electrode spacings.

2.2.2.3.1 Extension to Higher Beam Energy

The current design of the microcolumn employs an electron accelerator and an electrostatic focusing lens with electrode separations which are in the range of 0.1 to 0.25 mm. Electric fields are limited to about 10 kV/mm, so the beam energy cannot exceed 1 to 2 keV. There are some applications (such as lithography using existing resist processing) where a much higher beam energy is necessary. This can be achieved by a number of methods, and one of the theoretically simplest is to scale the entire column by a factor of (new beam energy/1 keV). If all the dimensions and working distances are scaled in this way, the lens excitation voltages will also scale with the beam energy, and the electric fields will be unchanged. If a beam energy in the range 10 to 20 keV is required, the column must be scaled 10 to 20 times. The disadvantage of this approach is that many new fabrication and assembly techniques will be required to construct such a new, larger column. Electrode bore diameters will be about 1 mm, and insulator thicknesses about 2.5 mm.

As the lenses are scaled up in size, their coefficients of spherical and chromatic aberration scale similarly. At low beam energies, the diameter d of the focused probe depends primarily on chromatic aberration and electron diffraction. The energy spread ΔV in the beam will remain approximately constant, so $\Delta V/V_0$ will decrease. Thus chromatic aberration $C_c \propto \Delta V/V_0$ (where α is the beam convergence semiangle) will not change greatly. The wavelength of the electrons $h/\sqrt{-2emV_0}$ (h is Planck's constant, e and m are the electronic charge and mass) decreases with increasing energy, so diffraction will decrease as the energy is increased. Overall, we can expect the focused probe diameter to decrease.

The properties of a scaled column are shown in Fig. 2.5. The focusing lens is shown operating in either accelerating or decelerating modes. The excitation voltages required in decelerating mode are lower, but the performance is not as good. The scaling is carried out in two ways. In one, the working distance w is scaled together with the size of the entire column, so that $w = 1$ mm at 1 keV and 10 mm at 10 keV. For the accelerating lens, the probe diameter decreases from 9.8 nm to 6.4 nm. In the other, w is maintained at a constant 10 mm at all scaling factors. In this case, the probe diameter is 60 nm at 1 keV and, again, 6.4 nm at 10 keV.

Higher beam energies can thus be achieved with improved probe size by scaling the entire column to maintain the same electric field strengths. At 10 keV, the column length will be 35 mm instead of the current 3.5 mm at 1 keV. The size is still much smaller than conventional 10 keV columns. Further studies will be required to find the behavior of the deflection field size and the electron-electron scattering effects.

2.2.2.4 Deflection Systems

2.2.2.4.1 Pre-Lens Double Deflector

Using einzel lens configurations which had been previously optimized for minimum probe diameter, the prelens double deflection system was then optimized to obtain the maximum scanned field size. The criterion used was that the probe diameter at the edge of the field was greater than that in the center by a factor of 1.2. The deflector bore diameters (r_A and r_B in Fig. 2.1), deflector positions (s_A and s_B), and the ratio of the deflector drive voltages were all used as variable parameters. It was found that increasing the deflector bore diameters, moving the first deflector away from the lens, and moving the second towards the lens all improved the scanned field size, but not by a great amount. It was important to use the correct excitation ratio.

The improvement had to be balanced against practical disadvantages. Increasing the bore diameter increased the required drive voltage. While there is no fixed limit on the drive voltage available, high voltages make high speed deflection more difficult and increase the power dissipated by any transmission line termination resistors. Moving the first deflector away from the lens increased the column length, thus increasing the electron-electron scattering. Moving the second deflector towards the lens is possible to some degree, and suggests the approach of integrating the deflector with the lens itself (see below). With reasonable values of the deflector positions (1.8 and 0.8 mm before the first lens electrode) and bore radii (0.25 mm), the available field radii are shown in Fig. 2.6. The larger possible field at larger values of w and for the retarding mode are

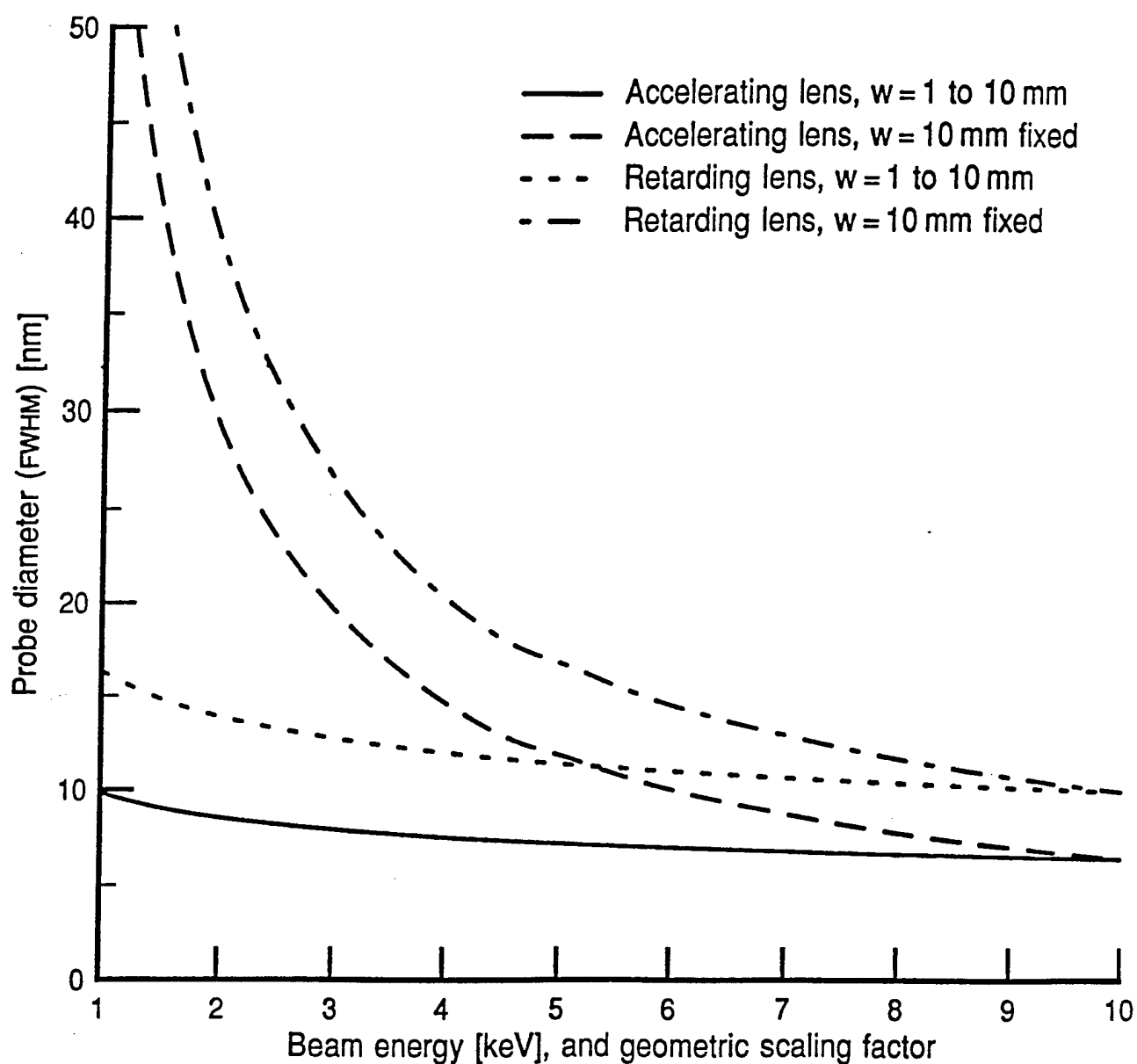


Fig. 2.5. The probe diameter available as a function of the beam energy. The dimensions of the column are scaled in proportion to the beam energy, so the electric field strengths remain approximately constant. The final convergence semiangle is optimized, and the beam energy spread is 0.5 eV (FWHM). When the working distance w is scaled, $w = 1$ mm at 1 keV up to 10 mm at 10 keV.

almost entirely due to the larger value of the axial probe diameter, which allows a larger contribution from deflector aberrations to increase this by a factor of 1.2. Correcting the curvature of field and third order astigmatism with dynamic correction methods leads to an increased field, but, for reasons given above, the increase is always less than a factor of 2.

At present, the primary lithographic application is to write patterns with 100 nm minimum features, and this can be accomplished using a 25 nm-diameter probe. The larger probe size can be most simply achieved for a given working distance by changing the beam convergence semiangle so that it is no longer optimal. The size is primarily influenced by geometric and chromatic lens aberrations (which increase as the convergence angle is increased), and by diffraction (which decreases). A larger probe can be obtained by either increasing or decreasing the convergence angle, but since decreasing it will also reduce deflection aberrations, this is the method analyzed here.

Figures 2.3 and 2.6 show the performance of an optimized unsymmetric accelerating lens and the deflection field which can be obtained. The deflection system is a pre-lens double-deflector, operated at the optimum ratio. As the working distance w is changed from 1 to 5 mm, the probe diameter varies from 7.8 to 21.0 nm, and the field diameter from 14.1 to 62.6 μm . Using the same lens and deflector, the final convergence semiangle is decreased until the probe diameter becomes 25 nm (FWHM). The deflection field diameter possible for a 20% increase in the probe diameter is shown in Fig. 2.7. There is a substantial improvement, particularly at smaller working distances, when the optimized probe diameter is much smaller than 25 nm. Between 1 and 5 mm working distance, the field is now between 51.3 and 83.7 μm diameter.

2.2.2.4.2 Advanced in-Lens Deflection Systems

There are many applications for focused electron beam systems, such as scanning electron microscopes and lithography directly on silicon wafers, where the angle at which the beam lands on the substrate is not important. In these cases, to minimize deflection aberrations, the deflection system is often designed so that the beam always passes through the focusing lens very close to the axis, and then lands at an angle on the substrate plane. There are some other applications, such as lithography on photomasks, which require that the electron beam is always normal to the substrate plane at all points within the deflection field so that height errors do not cause beam position errors. This is referred to as telecentric deflection. Both styles of deflection are important, and both are considered below.

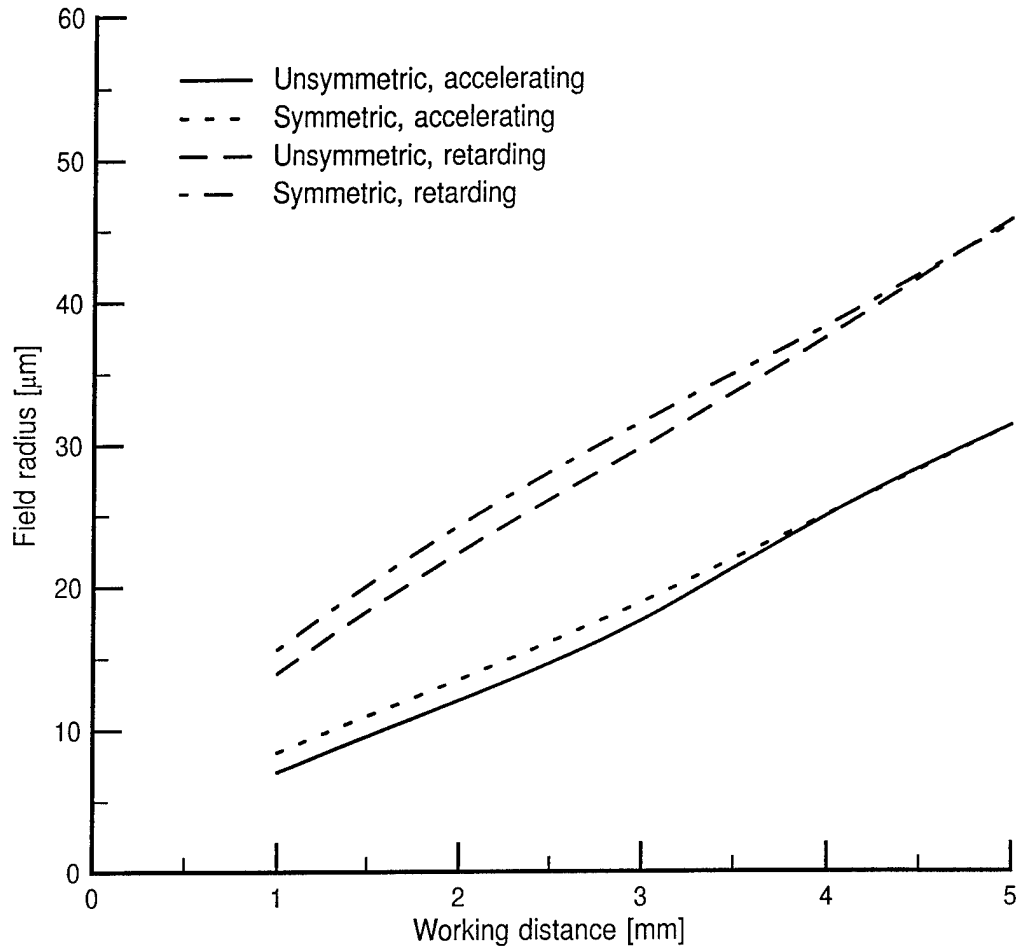


Fig. 2.6. The radius of the deflection field available from optimized symmetric and unsymmetric einzel lenses. The beam energy is 1 keV, and the energy spread 0.5 eV (FWHM). The excitation voltages and lens dimensions are all subject to microcolumn constraints. The field radius for a 20% increase in probe diameter using prelens double deflection is shown.

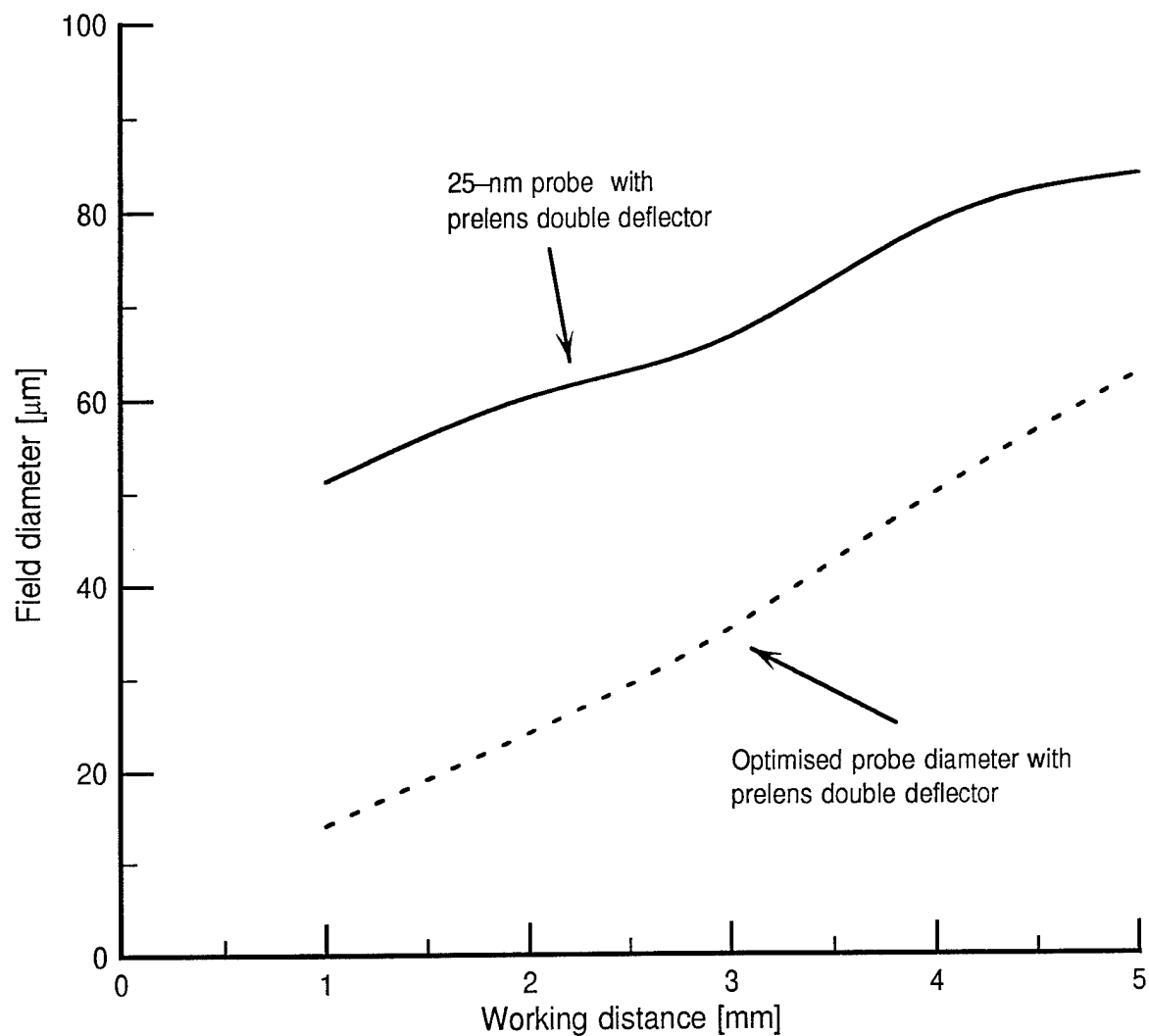


Fig. 2.7. The deflection fields available from an optimized einzel lens operating with a 25 nm probe diameter obtained by reducing the beam convergence semi-angle α . The performance with an optimized value of α is shown for comparison. The beam energy is 1 keV, and the energy spread 0.5 eV (FWHM).

Telecentric deflection can be achieved by predeflecting the beam as above so that it passes through the center of the lens at an angle, and then using a postlens deflector to make the beam parallel to the axis again. This technique is rarely used because of the distance necessary between the lens and the substrate to accommodate the added postlens deflector. This large working distance degrades the resolution of the focusing lens. An alternative scheme is to predeflect the beam at the back focal plane so that it passes off-axis through the lens and is then made parallel to the axis by the focusing field of the lens. No postlens deflector is required and a short working distance can be used. The disadvantage is that when the beam passes through the lens in this way it suffers substantial additional aberrations which severely limit the field size available. Prelens deflection has been used in a Microcolumn and the performance is described below.

Kern^{2.10} has examined a number of possibilities for avoiding these difficulties for full size systems with magnetic electron lenses and pointed out that one of the most favorable is provided by the magnetic Moving Objective Lens (MOL). This concept was first described by Ohiwa et al^{2.11} and is described in detail by Hawkes and Kasper.^{2.12} The magnetic field in a lens is modified by the addition of deflectors and other components so that the lens appears to be the same as the original lens shifted to a new axis parallel to the old. The additional field components usually added are sufficient to make the resemblance accurate to fourth order in off-axis distance. An electron beam entering the lens along this new axis will not be deflected and will not suffer any deflection aberrations up to third order. The third order deflection aberrations remaining will be those of the prelens double deflector required to deflect the beam so that it enters the objective lens along the shifted axis. Of course the original spherical and chromatic focusing aberrations will still be present.

2.2.2.4.3 The Electrostatic Moving Objective Lens

As shown above, magnetic lenses cannot be used in the Microcolumn. A similar moving objective lens analysis has thus been carried out for electrostatic lenses^{2.13} with the result that a MOL can be implemented by adding electrostatic deflecting fields to the lens field and correcting the remaining curvature of field and third order astigmatism. If necessary the third order deflection distortion can also be corrected.

To estimate probe sizes, the appropriate aberrations are combined in quadrature. The third order deflection aberrations which must be considered are coma, curvature of field, third order astigmatism, and third order distortion. The axial probe size is approximately defined by combining spherical aberration, chromatic aberration, diffraction of the electrons, and the image of the electron gun's source size. At high currents, electron-

electron scattering must also be taken into account (see below). The deflection field size is limited by the additional contributions from coma, field curvature, third order astigmatism, and chromatic deflection error.

Let the deflection in the substrate plane be (x_0, y_0) , and let $r_0^2 = x_0^2 + y_0^2$. It is possible to correct field curvature by adding a correction voltage (proportional to r_0^2) to the lens focusing voltage. The third order astigmatism has the same form as normal first order astigmatism, but with a magnitude proportional to r_0^2 . It can be corrected by adding a signal to one of the 8-poles to generate a potential distribution equal to $(x^2 - y^2)P(z) + 2xyQ(z)$ where $P(z)$ is proportional to $(x_0^2 - y_0^2)$ and $Q(z)$ is proportional to $x_0 y_0$. These corrections can both be more conveniently applied by the addition of correcting elements outside the lens. The coma, however, cannot be corrected. It must be eliminated by adding inlens electrostatic deflecting fields $F_x(z) = -0.5\phi''(z)x_0$ and $F_y(z) = -0.5\phi''(z)y_0$, where $\phi(z)$ is the potential along the axis due to the lens alone.

It has previously been suggested^{2,14} that an inlens electrostatic deflecting field can be produced by segmenting the lens electrodes into eight equal parts and adding suitable voltages to each of these parts. A deflecting field will be produced, and if the gaps between the segments are small, the disturbance of the original lens field will not be significant. (Since the gaps are equivalent to a 16-pole element, any additional unwanted aberrations will be of 7th and higher order.) For the central electrode, the deflection drive voltages must be added to the lens excitation voltage. By defining the electrodes using electron-beam lithography and deep etching techniques,^{2,15} sufficient precision can be achieved.

The form of the required field, $-0.5\phi''(z)$, is shown in Fig. 2.8. All three lens electrodes must be used as deflectors in order to produce the field with regions of different signs as shown. In order to obtain a good match between the electrostatic deflecting fields produced in this way and the desired function, additional shields must be positioned outside the lens (Fig. 2.8). As an example, we use a typical lens with three 10 μm -thick electrodes with 200 μm bore diameters spaced 250 μm apart. The shields are 1 μm thick with 200 μm bore diameters spaced 100 μm from the outside lens electrodes. The required and the resultant deflecting fields are shown in Fig. 2.8.

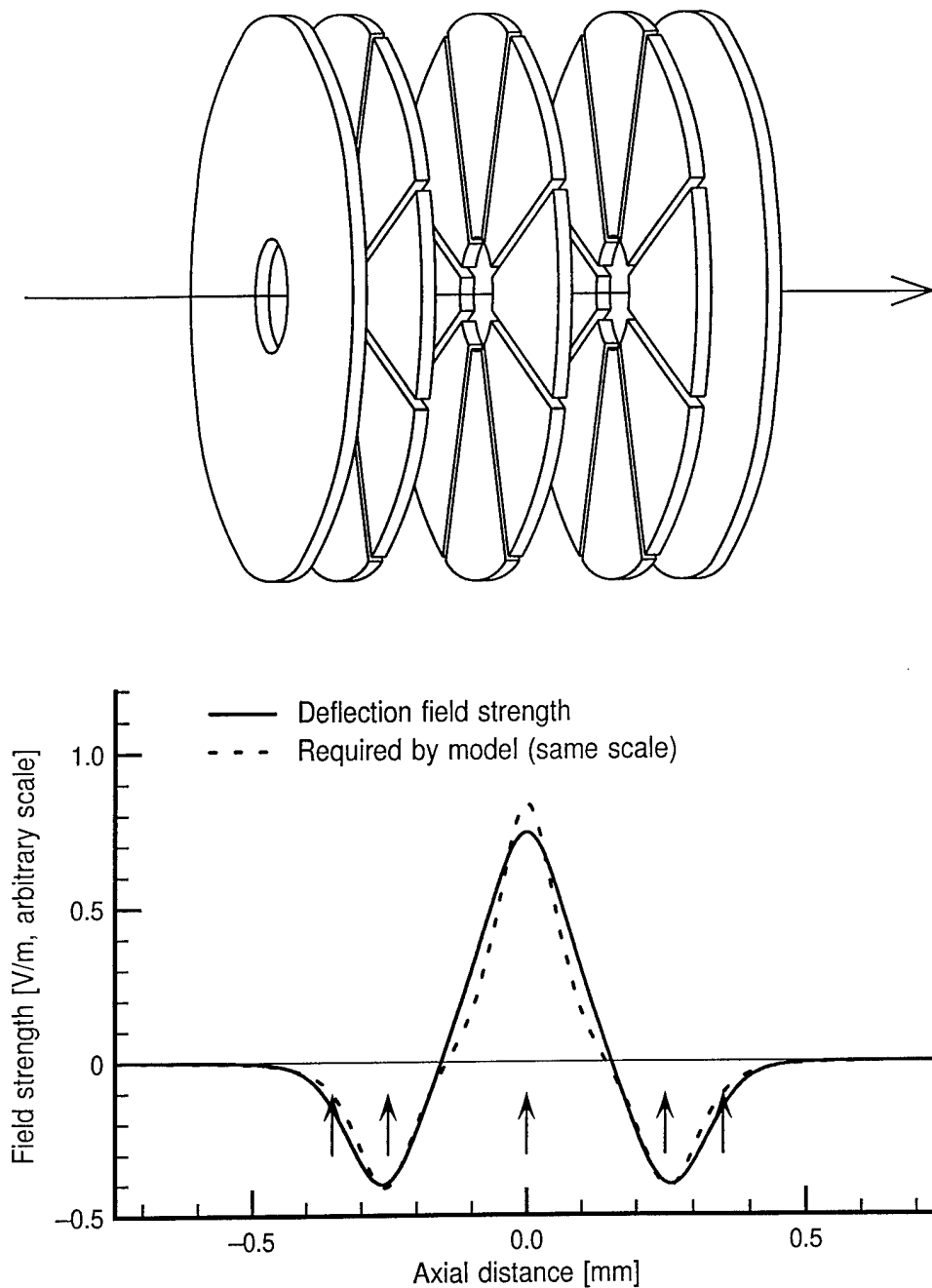


Fig. 2.8. Top: The focusing lens with shields and segmented electrodes. Bottom: The Moving Objective Lens concept requires an inlens electrostatic deflecting field proportional to $\phi''(z)$ where $\phi(z)$ is the axial potential of the focusing lens. The dashed curve shows this function, and the solid curve shows the deflecting field produced by segmenting the three lens electrodes and applying suitable voltages. The positions of the electrodes and shields are indicated by arrows.

2.2.4.4 Analysis methods

The potential distribution within the lens was computed using finite difference analysis, and the deflecting fields due to each electrode were computed using the boundary element charge density method. The deflection properties of the system using two pre-lens and the three inlens deflectors were then analyzed. All of these computations were accomplished using modified versions of commercially available software packages.^{2,4} Because the elimination of aberrations relies on the cancellation of lens focusing fields and deflecting fields, particular care had to be taken to ensure the accuracy of the numerical procedures. The optimization strategy described above (section 2.2.2.2) was then used to vary parameters to obtain the maximum field size in any given situation.

Some distortion and a significant increase in probe diameter at the edges of the scanned field is allowable in SEM applications. Telecentric scanning is most often used in lithography applications, where the distortion must be extremely small (or at least consistent, so that it can be corrected), and the probe diameter can increase by only a very small amount without having a measurable effect on the quality of the patterns written. The criterion used here is a 20% increase in the diameter of the probe at the edge of the deflection field. For small probe diameters, this criterion is very restrictive. The third order distortion is also important, but it is not taken into account because it can be corrected by appropriate design of the deflector drivers.

The beam energy is always set to 1 keV. The focusing einzel lens is always used in the accelerating mode, where the central electrode is positive with respect to the outer two. Although higher voltages are required than in the decelerating mode, the lens properties are substantially better. The beam convergence semiangle is always set to give the smallest probe taking into account spherical aberration, chromatic aberration with a 0.5 eV energy spread, and diffraction.

2.2.2.4.5 Moving Objective Lens

The pre-lens double deflector was set up to provide a beam parallel to the z axis entering the lens. Approximations to the strengths of the three inlens deflectors were set so that the beam passed through the lens with very little deflection. In addition, the curvature of field and third order astigmatism must be corrected. The curvature of field can be corrected by adding a correction signal to the focusing lens, or by adding another weak lens before or after the focusing lens. The third order astigmatism can be corrected by adding a signal to an 8-pole deflector which must be present in any case to correct any first order astigmatism. If necessary, the third order distortion can be corrected by

modifying the voltages used to drive the deflectors. All of these additions or modifications are simple functions of the deflection signals, and are known as “dynamic correction”.

The optimization procedure was then used to vary the strengths of the three inlens deflectors to find the maximum deflection field size using dynamic correction of third order astigmatism and curvature of field. The beam was constrained to be telecentric with a deflection equal to that defined by the prelens deflectors. The first order chromatic and third order geometric deflection aberrations were reduced to negligible values, so the resultant field size based on only these aberrations was extremely large (more than 1 mm). In practice the field size is limited by aberrations of fifth and higher orders (which have not been calculated), since the bore diameter of the lens is only 0.2 mm. It is unlikely that a field diameter of more than about 50 μm is possible without increasing the bore diameter.

2.2.2.4.6 Other Telecentric Deflection

The MOL is a complex system. It is advantageous for the microcolumn to be extremely compact, and it is difficult to find space for the additional components required for dynamic correction. It is thus instructive to consider the field sizes without this correction, and these are shown in Fig. 2.9 for the deflector configurations shown in Fig. 2.10. The simple prelens deflection configuration provides a maximum field diameter of from 6.8 μm at 1 mm working distance to 7.2 μm at 5 mm. The field size available by using the MOL deflection without dynamic correction is 9.6 μm at 1 mm to 14.1 μm at 5 mm. To get the best possible performance without dynamic correction, the two prelens and three inlens deflectors (as shown in Fig. 2.10, bottom) can all be used with their excitations optimized to maximize the deflection field size. In this way we can achieve a field diameter of 29.1 μm to 30.8 μm with the trajectories shown in Fig. 2.10(c). All of the deflection field sizes which can be achieved using these configurations are relatively small, because without a postlens deflector the beam must always pass through at least part of the focusing lens with an off-axis distance equal to the final deflection distance.

2.2.2.4.7 Non-Telecentric Deflection

In a non-telecentric system, the beam can remain much closer to the axis while passing through the lens, and a larger deflection field size is generally possible. The results are given in Fig. 2.11 for the configurations in Fig. 2.12 and the same lens and deflector geometries as before.

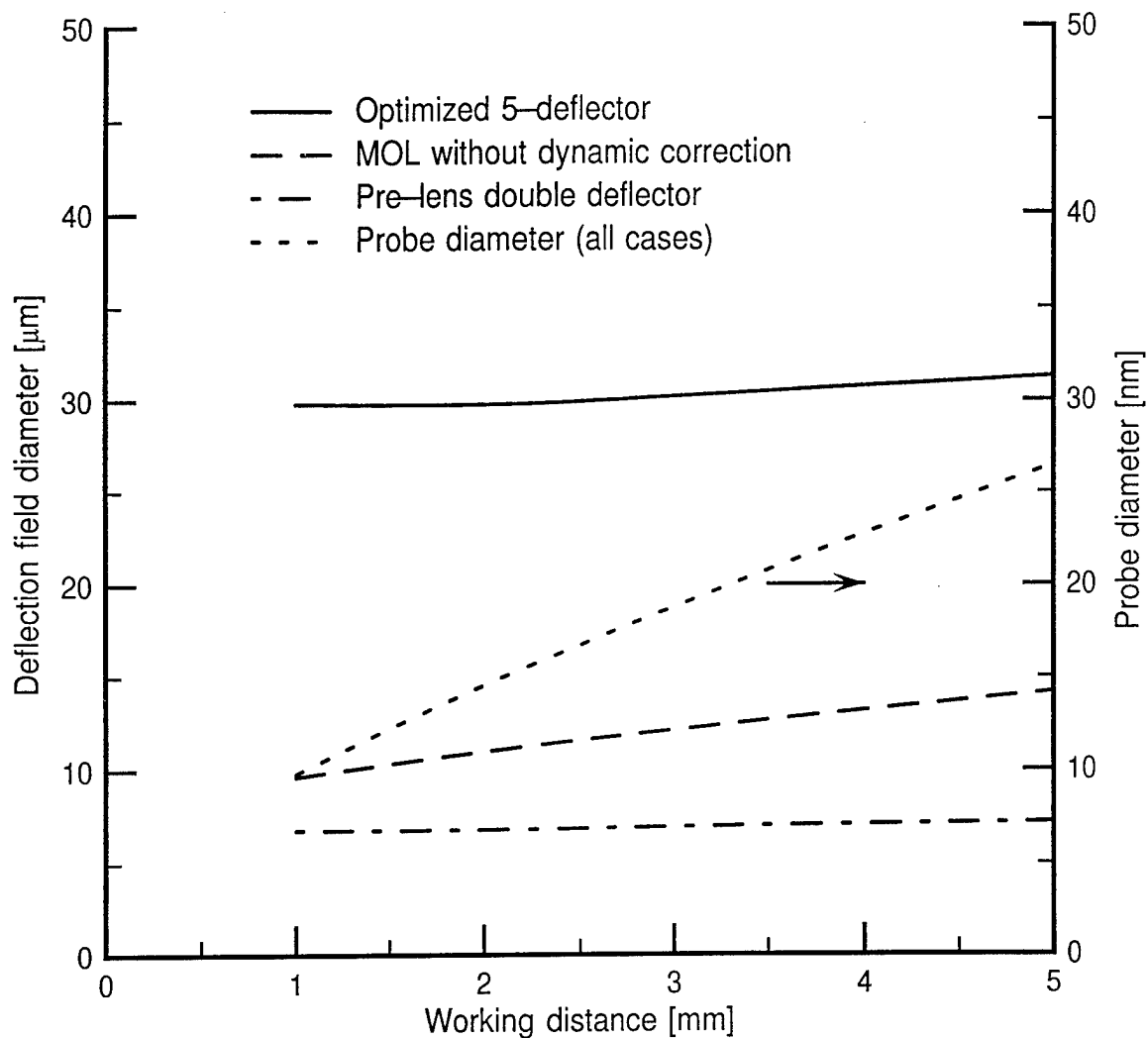


Fig. 2.9. The probe diameter (full width at half maximum, FWHM) and telecentric deflection field diameter available with a symmetric einzel lens with electrodes 200 μm in diameter and 10 μm thick. Dynamic correction of astigmatism and field curvature is not used. The beam energy is 1 keV, and the energy spread 0.5 eV (FWHM). The field diameter for different deflector configurations is shown for a 20% increase in probe diameter at the edges.

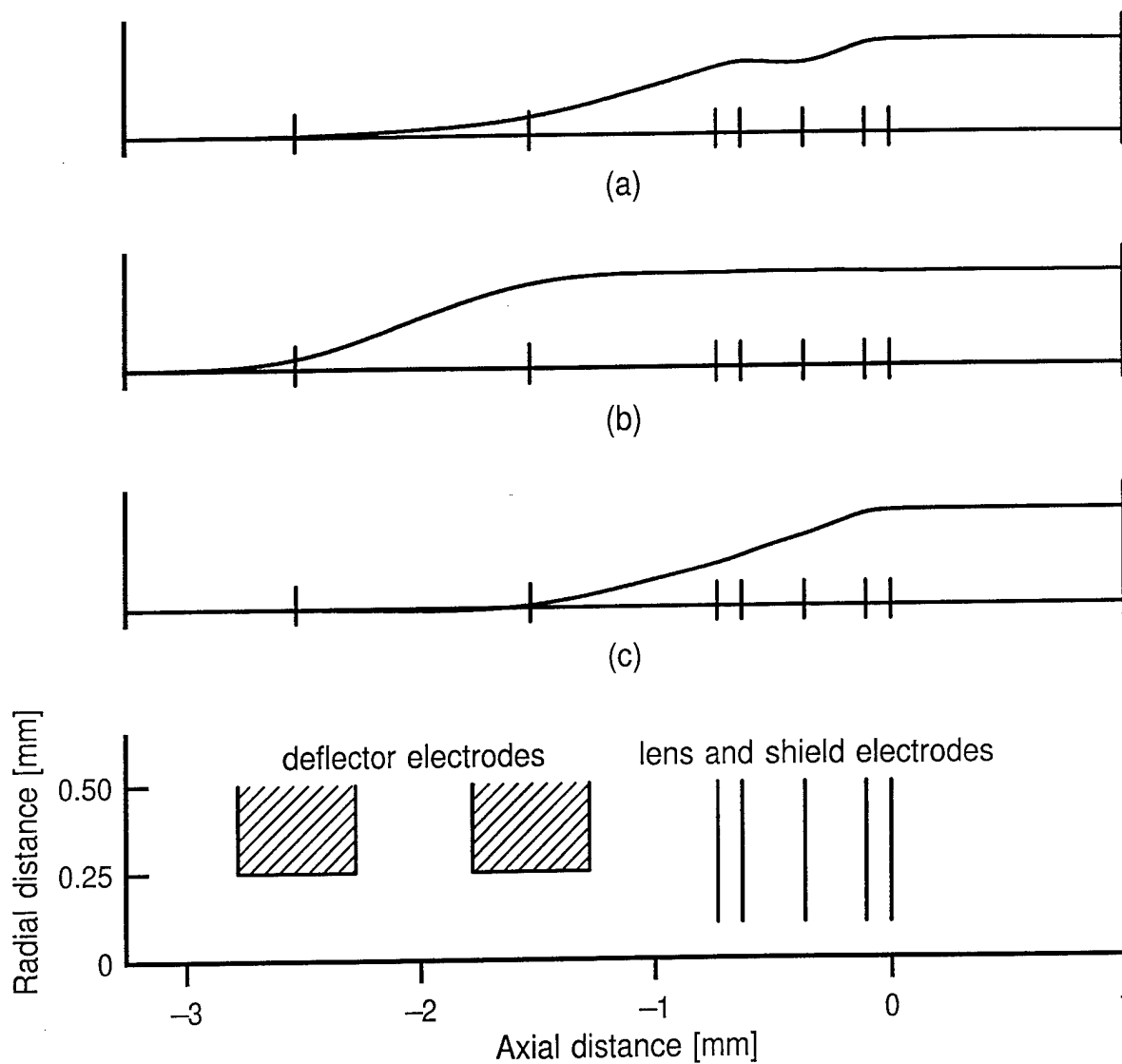


Fig. 2.10. Sample deflected trajectories with vertical landing and a 1 mm working distance. In (a), a prelens double deflector is used. (b) is a Moving Objective Lens, and in (c), all five prelens and inlens deflectors are used for maximum field diameter without dynamic correction. The horizontal and vertical scales are not the same.

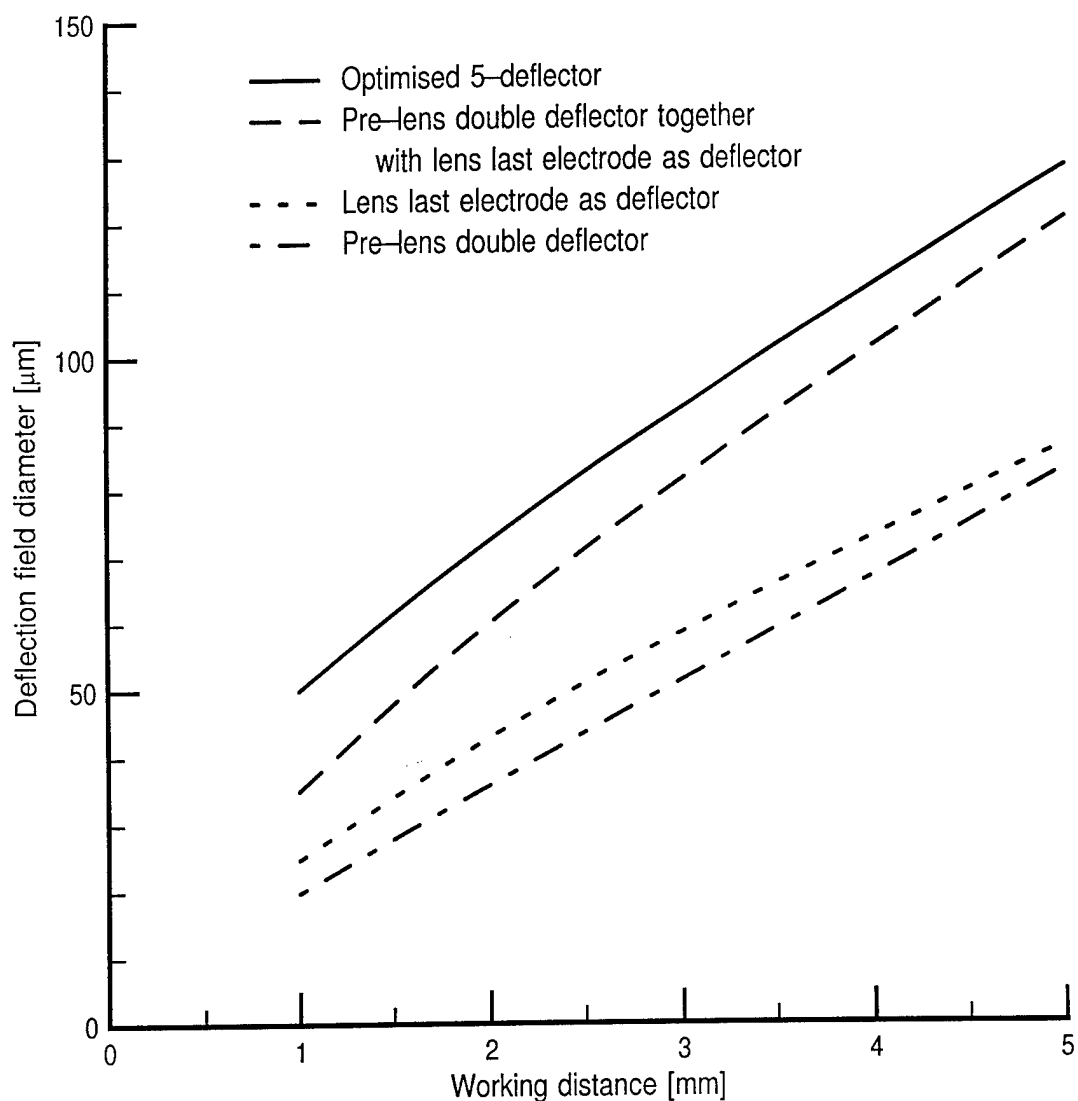


Fig. 2.11. The non-telecentric deflection field diameter available with a symmetric einzel lens with electrodes 200 μm in diameter and 10 μm thick. Dynamic correction of astigmatism and field curvature is not used. The beam energy is 1 keV, and the energy spread 0.5 eV (FWHM). The field diameter for different deflector configurations is shown for a 20% increase in probe diameter at the edges. The axial probe diameter is the same as shown in Fig. 2.9.

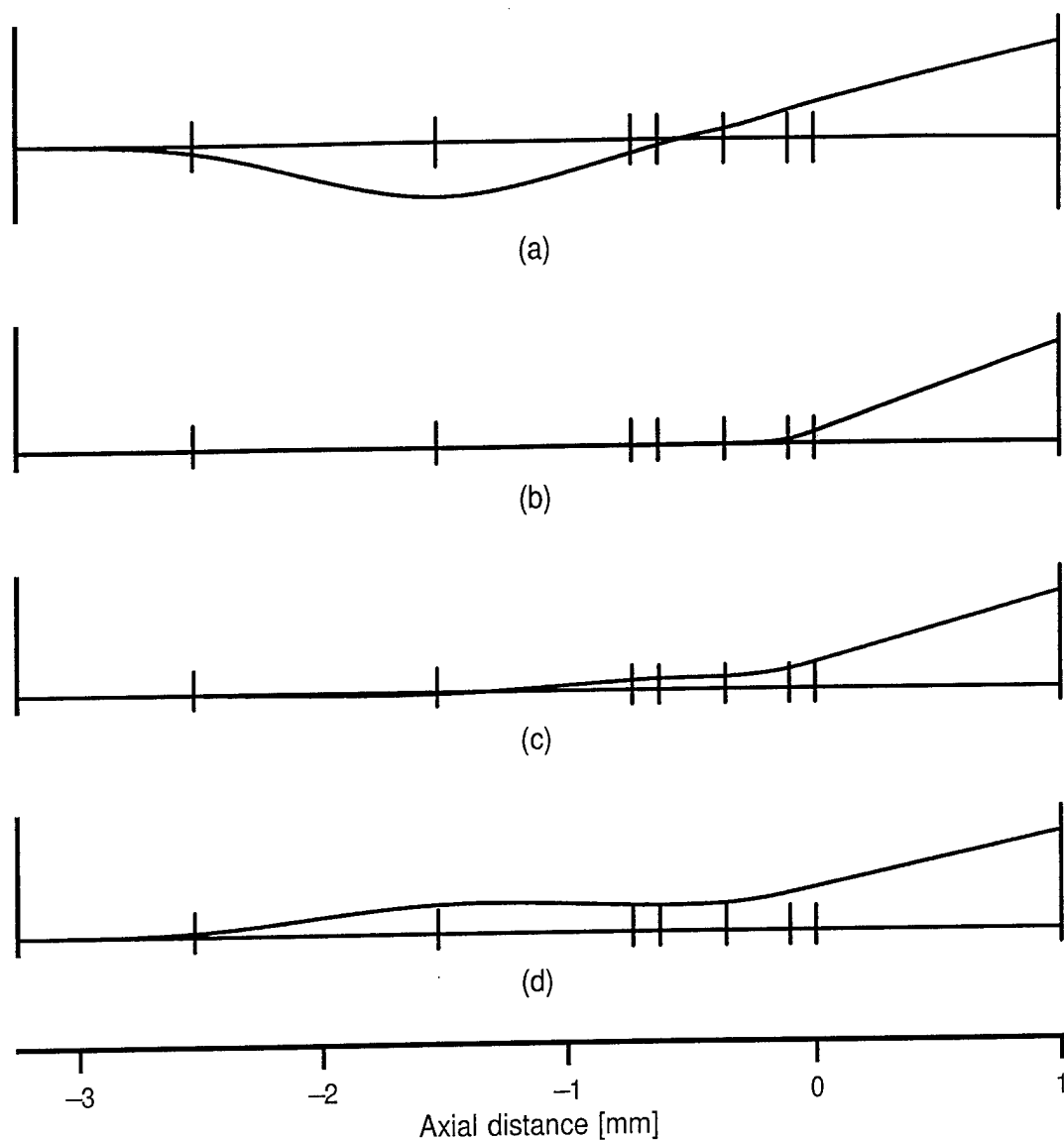


Fig. 2.12. Sample deflected non-telecentric trajectories with a 1 mm working distance. In (a), a prelens double deflector is used; in (b) the last lens electrode is used as the deflector; in (c), the prelens double deflector is used together with the last lens electrode; and in (d), all five prelens and inlens deflectors are used for maximum field diameter without dynamic correction. The configuration is the same as shown in Fig. 2.10.

It is interesting to note that the field size available for the combination of the prelens double deflector and the last lens electrode deflector is substantially better than either the prelens deflectors or the last lens electrode deflector alone. This is a valuable result, since there are practical difficulties in adding the deflecting voltages to the lens center electrode, which is normally at a potential of several thousand volts. Obviously, these schemes with larger deflection field sizes than the telecentric cases should be used where possible.

Dynamic correction can be applied to these configurations just as for the telecentric case. The third order geometric and first order chromatic deflection aberration coefficients can be reduced to negligible values, so the field size is again defined by higher order terms. However, since the deflection in the substrate plane in the optimized case is now typically three times the off-axis distance of the beam inside the focusing lens, a significantly larger deflection field diameter than in the telecentric MOL case is achieved.

2.2.2.5 Lens and Deflector Design Summary

Optimization techniques can be effective in designing improved lenses and deflection systems which are practical to fabricate and to operate. With the addition of a number of added programs, we have used a standard optimization routine with a variety of optical analysis programs.

We have designed einzel lenses with improved performance, capable of producing an 8 nm probe diameter at 1 mm working distance or 21 nm at 5 mm, both with a 1 keV beam energy. The accelerating mode gives better performance and improved tolerance of electrode misalignment. Further improvement can be realized if the constraints on electrode dimensions and excitation voltage can be relaxed. These results are also applicable to ion-beam columns where the beam energy is 10 keV and the energy spread 5 eV.

Microcolumn deflection systems can also be optimized, but the design of a double deflector is a compromise between performance, drive voltages, and column length. Without dynamic corrections, a scanned field 16 μm in diameter can be achieved at 1 mm working distance and a 20% increase in probe diameter.

The deflection performance can be greatly improved for both telecentric and non-telecentric deflection by using deflectors inside the lens itself, with or without a prelens double deflector. For telecentric deflection, the Moving Objective Lens (MOL) concept

can be extended from magnetic to electrostatic lenses. The lens electrodes can be segmented to produce electrostatic deflecting fields as well as focusing fields, and shields can be added before and after the lens to shape the deflecting fields so that they are a good match to the MOL theory.

If dynamic correction of field curvature and third order astigmatism is used, the deflection field sizes available on the substrate plane are much larger, limited only by the small bore diameter of the microcolumn lenses and by higher order aberrations (which were not analyzed). Even without dynamic correction of curvature of field and third order astigmatism, the use of inlens deflectors leads to substantial improvement. For non-telecentric deflection, the use of the third lens electrode as a deflector is an improvement over prelens double deflection, and the combination of the two is even better.

2.2.3 Electron-electron Scattering

2.2.3.1 Introduction

The ultimate probe size and current in an electron-beam column are determined in part by the electron-electron interaction effects within the electron beam. These effects will change if we scale the geometry of a column to a different size, or if we change the energy of the electron beam. Because of the interest in extremely small microcolumns,^{2,1} the effects of interactions are investigated for column lengths as small as 4 mm, and the results compared to those for lengths up to 0.4 m with beam energies from 1 to 100 keV. The probe currents available in a 25 nm-diameter probe are compared.

In practice, exact scaling of the geometry would be unlikely, since simplifications are usually required at very small dimensions where the number of optical components would be kept to a minimum, and typically there might be no beam crossover within the column. To investigate the scaling effects in a systematic way, a very simple microcolumn column design is used for all sizes. For optimum probe size and current, a field emission gun must be used.^{2,1} The design of the gun is determined by practical considerations, and may not scale with the rest of the column. The effects of changes in the gun geometry and cathode type are investigated separately.

As the electron beam energy is changed, the scattering cross section within the target changes. As a result, for a given interaction at the surface, the incident current density must be scaled directly with the beam energy.^{2,16,2,17} This relationship is incorporated when evaluating the relative merits of different configurations.

2.2.3.2 Scattering Effects

An overview of interactions between electrons in an electron beam is given by Jansen.^{2,18} They can be divided into bulk space charge and stochastic interactions. In the case of space charge, electrons are deflected by the total charge of all the other electrons in the beam; the deflection depends on the total charge, not the size of the individual electronic charge. If the charge distribution is uniform, the net effect is primarily to shift the positions of the beam crossovers (including the final focus), and this can be compensated for by small changes in the strengths of the individual lenses. This does not place a limit on the ultimate performance of the column, and so is not treated here.

Stochastic interactions (electron-electron scattering) manifest themselves in two ways — changes in the transverse momentum (a deflection, the *trajectory displacement effect*), and changes in the axial momentum (an energy change, known as the *Boersch effect*^{2,19}). The deflections give rise to shifts in the positions where the electrons cross the final image plane, and thus the size of the focused probe increases. The energy broadening also leads to an increased probe size because of the chromatic aberration of any lenses through which the beam must subsequently pass.

The stochastic interactions have been treated by many authors, and a summary has been provided by Hawkes and Kasper.^{2,20} Here the analytic approximations developed by Jansen^{2,18} are employed. These approximations do not apply to some situations (such as close to the field emission cathode where the electrons have very low energy and very high accelerations), and the more reliable Monte Carlo simulations^{2,21-2,23} developed by Groves, Hammond and Kuo^{2,22} have been used.

The system which has been analyzed is shown in Fig. 2.13. It consists of a field emission electron gun, accelerator, beam limiting aperture, and a focusing lens. As mentioned above, we treat the gun separately, since different analysis techniques must be used, and since it is straightforward to combine the results.

2.2.3.2.1 Field-Emission Electron Gun

The choice of cathode radius, material, and operating temperature for the electron gun are usually dictated by practical considerations, and the properties of some commonly used configurations have been predicted. Tungsten cathodes are characterized by a work function of 4.4 eV, and oxygen-processed zirconium-tungsten (usually operated at 1800 K) by a work function of 2.8 eV.^{2,24} Conventional theoretical models, in-

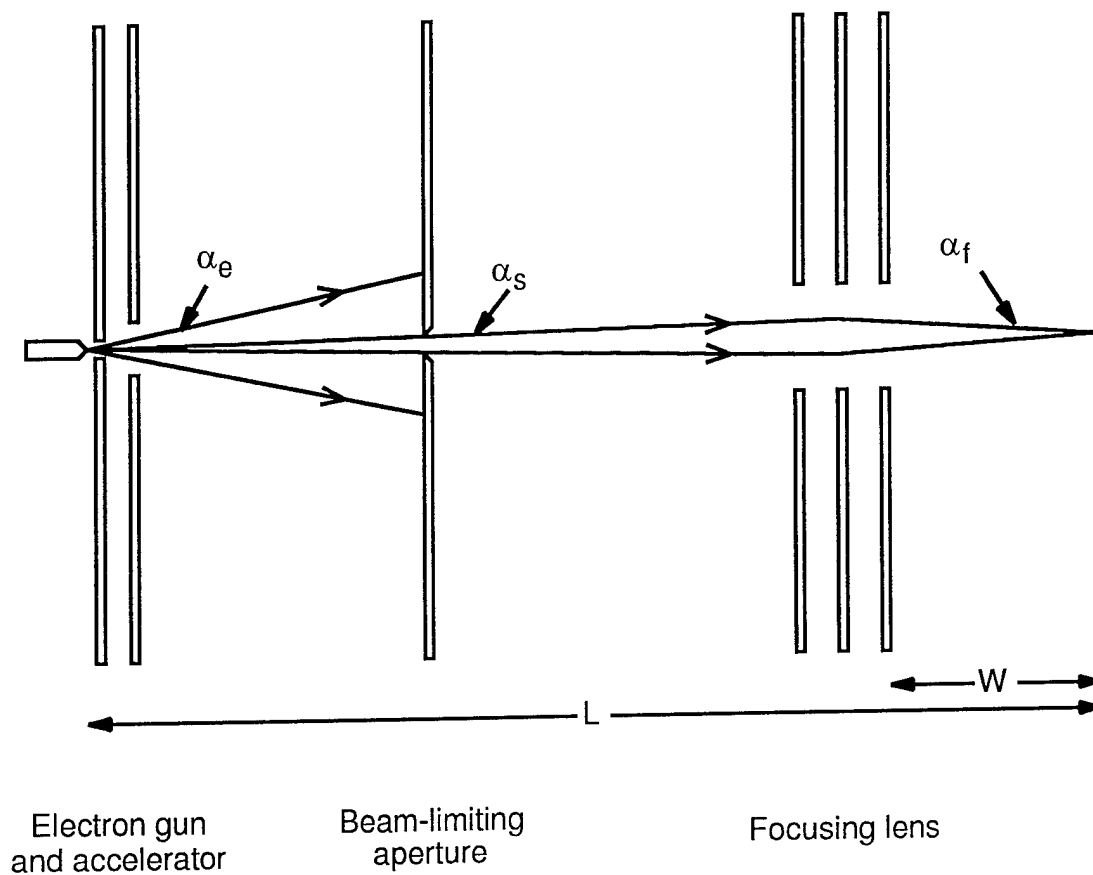


Fig. 2.13. The complete electron-beam column which consists of the electron gun, accelerator, beam limiting aperture, and the focusing lens. The overall optical length from cathode to focused probe is L , and the working distance is W . The electron gun emits electrons in a beam with semiangle α_e , and the beam-limiting aperture selects a reduced semiangle α_s . The final convergence semiangle is α_f .

cluding the Fowler-Nordheim and Richardson-Dushman equations, with the approximations detailed by Hawkes and Kasper,^{2.25} have been used to predict the emission current, energy spread, and mean transverse energy from cathodes of both types. The tungsten cathodes at 300 K are treated as field electron emitters, while the zirconium-tungsten cathodes at 1800 K are extended Schottky emitters. The results from this analysis are used as the starting point for a Monte Carlo simulation of the acceleration to the potential of the extractor electrode. The standard deviation, σ , of the energy distribution is converted to a full width at half maximum (FWHM). Because of the shape of this distribution, the conversion is approximate and was represented by $\text{FWHM} = 1.5\sigma$ instead of 2.35σ which would be appropriate for a Gaussian distribution.

The electron gun is assumed to consist of a pointed cathode with a spherical tip, an extractor electrode, and an accelerator electrode. For the scattering calculations, it is modeled as a spherical cathode with a concentric spherical anode. The potential difference between the two is determined by the requirement that the electrons will be emitted with the required angular current density. The electrons in the Monte Carlo model are emitted from the cathode at random times with random direction and energy. These random distributions are such that they satisfy the mean current density, axial energy spread, and mean transverse energy which were determined above. Most of the electron-electron scattering then takes place close to the cathode where the density of electrons is very high, and the velocity is still relatively low. The simulations are started at the cathode, and terminated at a sufficiently large radius so that there would be no significant further energy broadening. The results are shown in Figs. 2.14 and 2.15. They show that for a given required angular emission current density and given cathode radius, room-temperature field emission gives a lower energy spread than Schottky emission. In fact, the energy widths at low emission densities ($\leq 1.0 \times 10^{-5} \text{ A sr}^{-1}$) are essentially the same as the widths of the cathode emission for all the curves shown. At higher densities, the additional contribution from the Boersch effect becomes dominant. These results are consistent with earlier results,^{2.26} although the method for determination of the energy full width at half maximum may not be identical.

The scattering also deflects some of the electrons, and the increase in the virtual source size is equal to the product of the deflection angle and the distance from the scattering location to the virtual source plane. Since the virtual source plane is close to the center of the cathode, and since almost all the scattering takes place within a few micrometers of the cathode, the increase in virtual source size due to the trajectory displacement effect is negligible when compared to the effect elsewhere in the column. There is also an increase in the virtual source size because electrons are emitted from any point on the cathode at different angles with non-zero energy, and these electrons

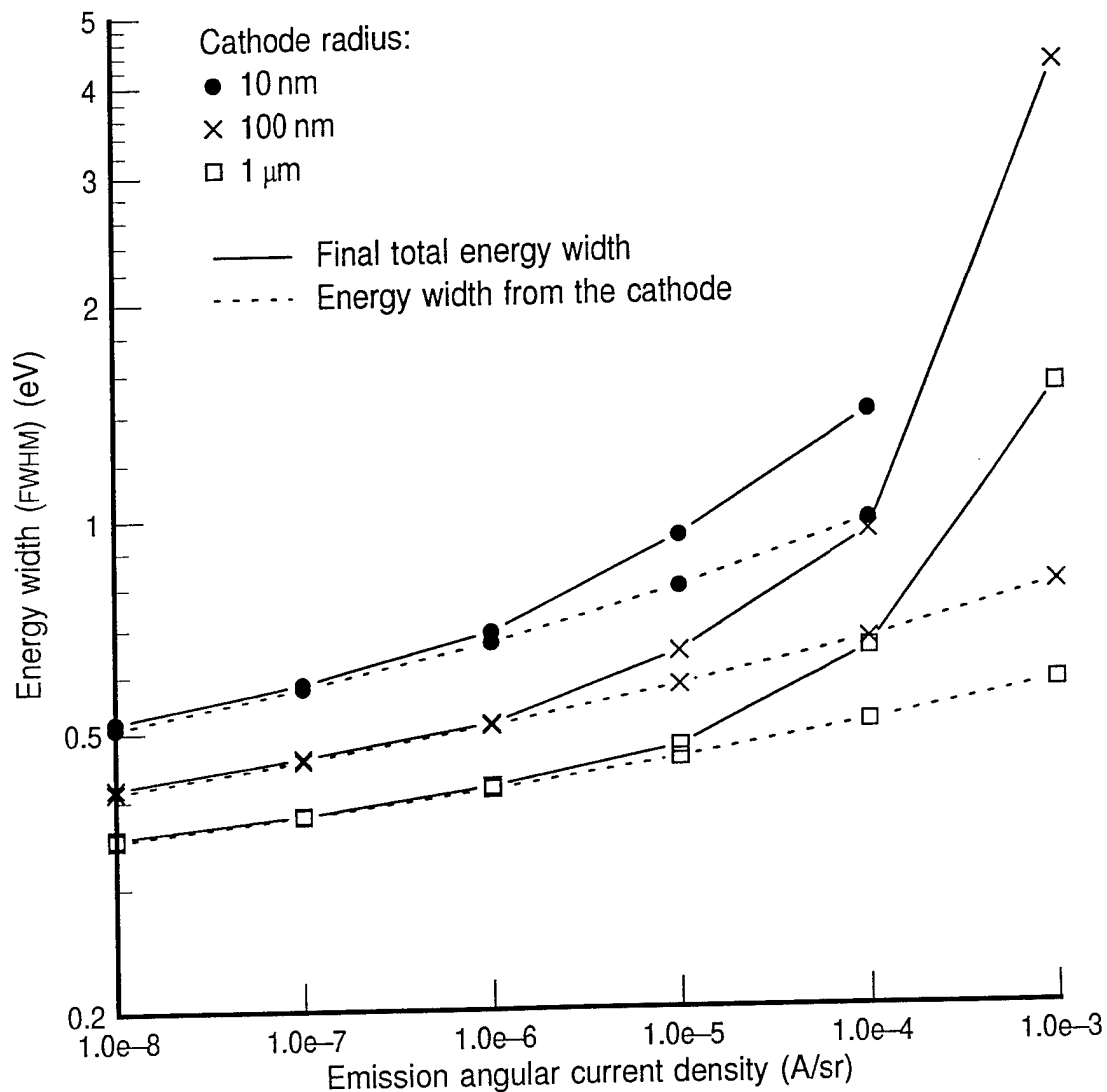


Fig. 2.14. Predictions (based on Monte Carlo simulations) of the Boersch effect in a field emission electron gun. The cathode is tungsten, with a work function of 4.4 eV, operated at 300 K.

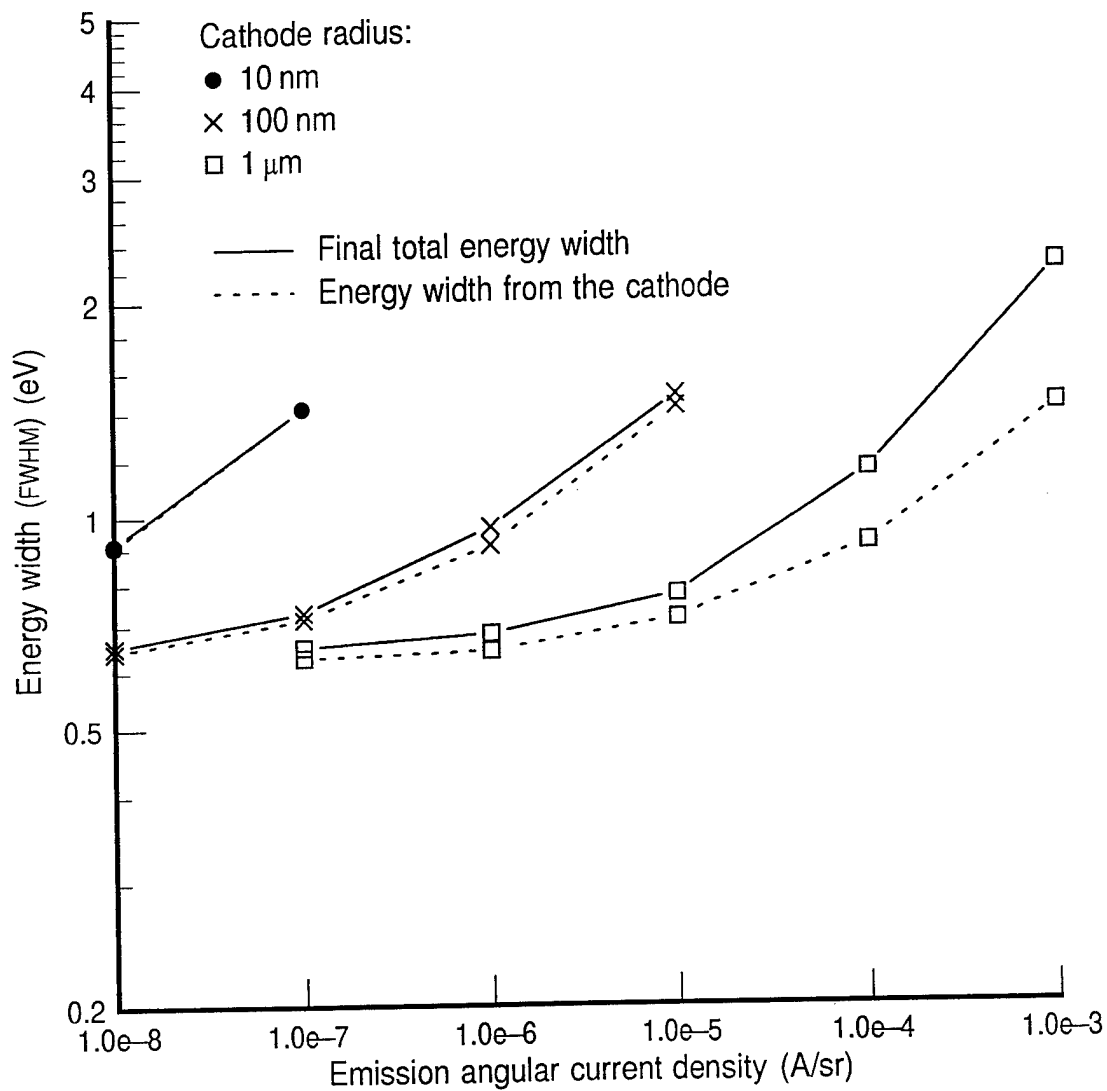


Fig. 2.15. Predictions (based on Monte Carlo simulations) of the Boersch effect in a field emission electron gun. The cathode is oxygen-processed zirconium-tungsten, with a work function of 2.8 eV, operated at 1800 K (Schottky emission).

do not all appear to be originating from the same axial point. The transverse energy of electron emission is known, so this contribution to the source size has been calculated,^{2,27} and is combined (after demagnification by the electron-beam column) with other effects to determine the final probe diameter. Other aberrations caused by the lack of spherical symmetry in the source region have been neglected.

The electrons must be accelerated to the required final energy of the electron beam. It is assumed that the accelerator is designed so that the angular current per unit solid angle emitted from the cathode is increased by the ratio of the final energy to the extraction energy. Since the virtual source size in a field emission gun is usually negligible compared to other lens aberrations, this results in optimum performance.

2.2.3.2.2 Electron-Beam Column

The remainder of the electron-beam column is analyzed using the formulation of Jansen.^{2,18} The approximate electron trajectories are first determined using conventional analysis techniques.^{2,28} The column is divided into thin sections (bounded by planes of constant z), and the scattering effects in each section evaluated. All the sections are then combined to give the total effects. The increase in energy spread is evaluated only up to the plane of the focusing lens, since any increase after passage through this lens will have no effect on the probe size. The lateral scattering and energy broadening in the column as a function of probe current are shown in Fig. 2.16 for a fixed 5 mrad beam convergence semiangle. For the smaller column sizes, the contribution to the trajectory displacement effect is found to be proportional to $(IL/E^2)^{2/3}$ where I is the probe current, L the total column length, and E the electron-beam energy. For easy comparison, the lateral scattering and energy broadening have been plotted against I/E while L/E has been kept constant, and these quantities can each be represented by one curve for all $L \leq 40$ mm.

The final probe size can now be calculated. For any given probe current and convergence semiangle, the required emission angular current density is found, and the energy spread from the cathode is added to an estimate of the gun Boersch effect (Figs. 2.14 and 2.15). The total energy spread and coefficient of chromatic aberration for the focusing lens then give the total chromatic aberration. The addition of chromatic and spherical aberrations, the image of the virtual source, the trajectory displacement effect, and diffraction is complex because of the very different nature of these terms. Spherical aberration and diffraction are wave-optical effects, while the other terms are not. As a convenient approximation, the probe size is taken as the sum in quadrature. While this may lead to some error in the size of the final probe, it should be sufficient

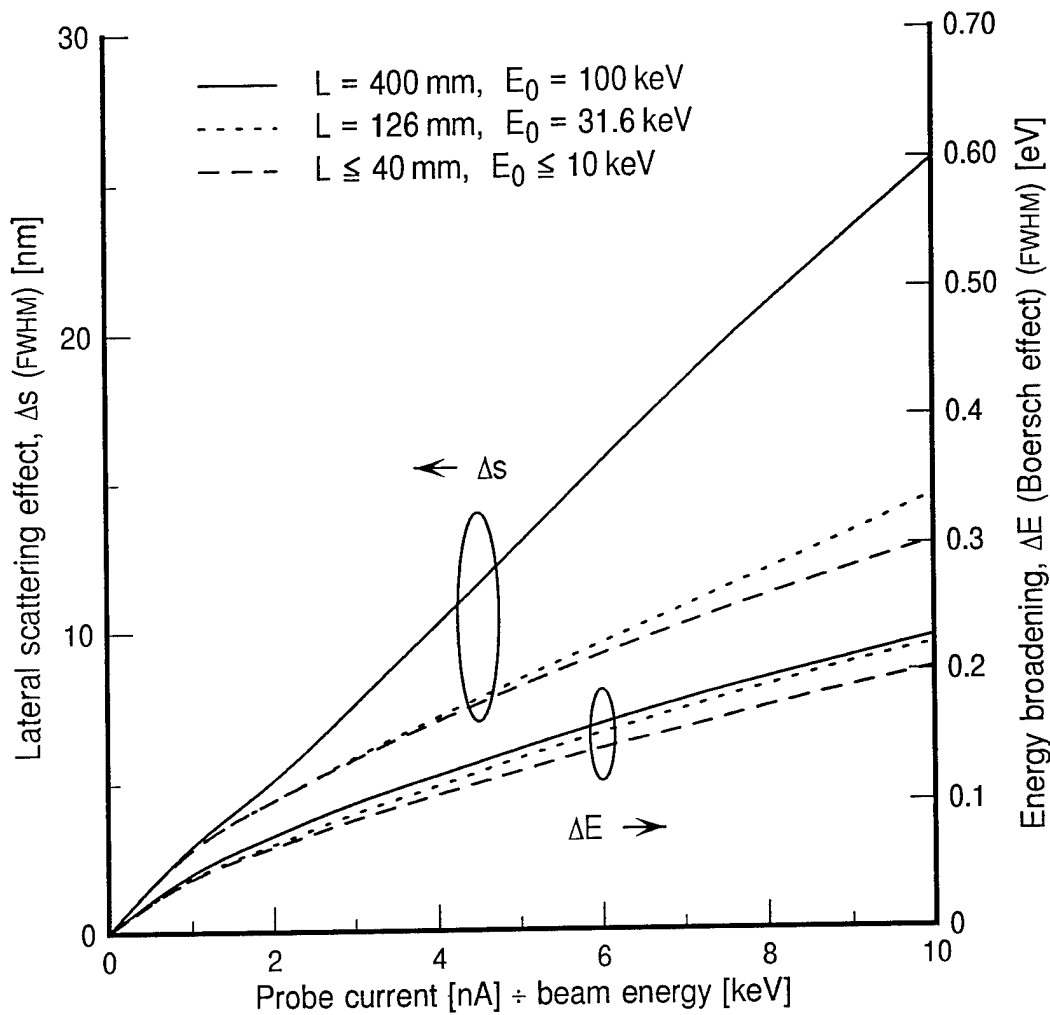


Fig. 2.16. The lateral scattering and Boersch effects caused by electron-electron scattering for different column sizes and beam energies. The values shown are theoretically predicted contributions after the beam has been accelerated to full energy, and do not include emission from the electron gun. At smaller column lengths (with the same scaling), the results are very similar to those for 40 mm. The probe currents range from 0 to 1 μ A at $L = 400$ mm, from 0 to 316 nA at $L = 126$ mm, and from 0 to 100 nA at $L = 40$ mm. The total emission semiangle α_e is very large.

to demonstrate the variations as the geometric size and beam energy are changed. Unless specified otherwise, the convergence semiangle has been optimized for minimum probe size taking into account all the preceding factors.

2.2.3.3 Scaling with Geometric Size and Beam Energy

The effects of scaling this column can now be shown. In all the following results, the cathode has been chosen to be 100 nm-radius tungsten operated at 300 K. The comparison is different for different methods of scaling the column. If the beam energy is kept constant, and only the scale of the column is changed, the small size is clearly advantageous because of the reduced scattering effects. As an example, we compare the maximum current available in a 25 nm-diameter probe. The current available in fixed 1 keV systems of different sizes is shown in Fig. 2.17. In this case, the focusing lens aberration coefficients were kept constant (spherical aberration coefficient, C_s , and chromatic aberration coefficient, C_c , both equal to 2 mm). If the chromatic aberration coefficient is scaled with column size, it becomes impossible at larger sizes to achieve a 25 nm probe at any current. (Of course, there are other strategies such as using a higher energy throughout most of the column and decelerating the beam in the last lens.)

One can also scale the energy of the column with the size. For example, if the energy is proportional to the column length, one can scale from a 1 keV 4 mm column up to 100 keV, 400 mm column. As mentioned before, for equal interaction in the target a larger current is required at higher energies because of the reduced scattering cross section in the target. Two cases are shown in Fig. 2.17. In one, the lens aberration coefficients are scaled with the column size, and in the other, they are kept constant (reflecting the greater freedom at larger dimensions to design optimal lenses). The current I is shown as I/E , and the energy E is scaled linearly with the column length L . In all cases, the beam convergence semiangle has been set to optimize the available current.

At low energies, the probe size is limited by the beam energy spread (chromatic aberration) and diffraction. At high energies, with the values of C_c and C_s used here, the limit is set by the spherical aberration and trajectory displacement effect. It is thus critical to minimize these lens aberrations, and the comparison of different columns will depend on the assumptions made for these quantities. Microcolumns are usually advantageous because of the very low aberration coefficients of the very small lenses which can be used. High energy conventional columns are only superior if they can be designed with lenses with the same properties, and this is particularly difficult because of the higher beam energy. In microcolumns at low energies, the spherical aberration

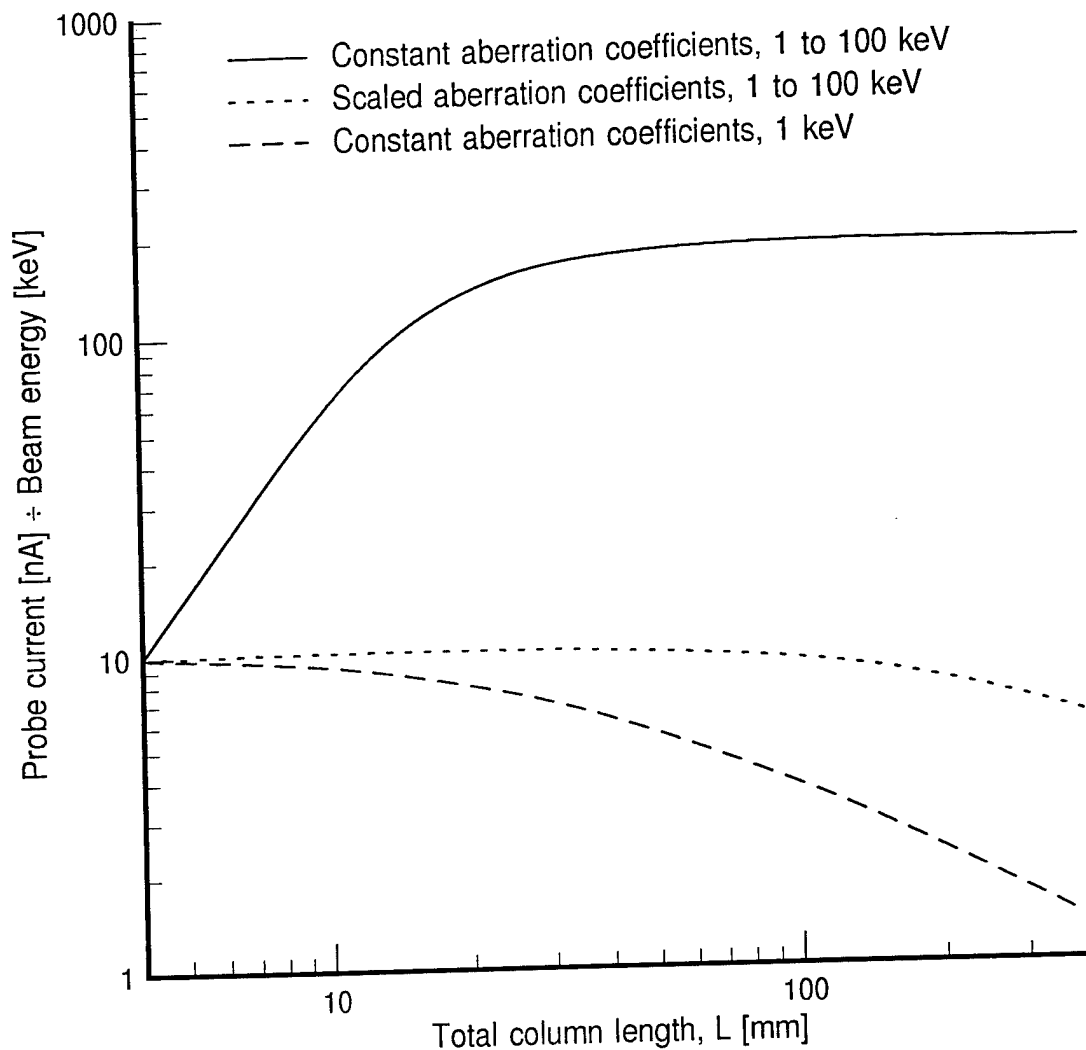


Fig. 2.17. Total current available in a 25 nm probe. The focusing lens spherical and chromatic aberration coefficients (C_s and C_c) are representative of a magnetic microlens. They are either held constant at all beam energies ($C_s = C_c = 2 \text{ mm}$ at 1 keV), or scaled linearly with column size (from 2 mm at $L = 4 \text{ mm}$ to 200 mm at $L = 400 \text{ mm}$). The beam energy is either held constant at 1 keV, or scaled linearly so that it is equal to 1 keV for each 4 mm of column length (i.e., 1 to 100 keV).

is not significant, so electrostatic lenses with much larger spherical aberration coefficients can be employed. When comparing different columns at constant, low beam energies, the smaller columns are always advantageous.

For optimum performance, the gun energy spread must be minimized. This can be achieved by using the largest practical cathode radius, and by designing the optics so that the emission angular current density is as small as possible. The simple models used here do not take this into account.

2.2.3.4 Reduction of Trajectory Displacement Effect

Further insight can be gained by examining the contributions to the scattering from different parts of the column. Consider a 4 mm-long column operating at 1 keV with a 10 nA probe current. After the beam has passed through the limiting aperture, the total current is 10 nA. At 1 keV energy, the average axial separation between electrons is 0.3 mm. In the column design used for these comparisons, this part of the column has a length of 2.7 mm, so an average of only nine electrons can contribute to any scattering effects, and the contribution to trajectory displacement and energy broadening is very small. The major contribution comes from interactions which take place before the beam passes through the aperture. The electrons in the inner part of the beam are scattered by interacting with the much larger number in the outer part (which is subsequently intercepted by the aperture). In all the preceding results, the emission semiangle α_e has been very large.

The scattering can be reduced by removing these electrons in the outer part of the beam. Either place the aperture as close as possible to the cathode (for example, at the extraction electrode), or reduce the diameter of the extraction electrode so that a much smaller number can pass. The scattering effects with these changes are shown in Figs 2.18 and 2.19.

2.2.3.5 Electron-Electron Scattering Summary

In any system, electron-electron scattering limits the current available in a probe of given size. The scattering is much reduced in a small electron-beam column, but the gain may be partially offset by increased chromatic aberration if the small column must operate at lower beam energy. The comparison depends on the way the focusing lens chromatic and spherical aberration coefficients are scaled. Limiting the current in the column by appropriate design of the beam-limiting aperture and spray apertures can greatly reduce the trajectory displacement effects.

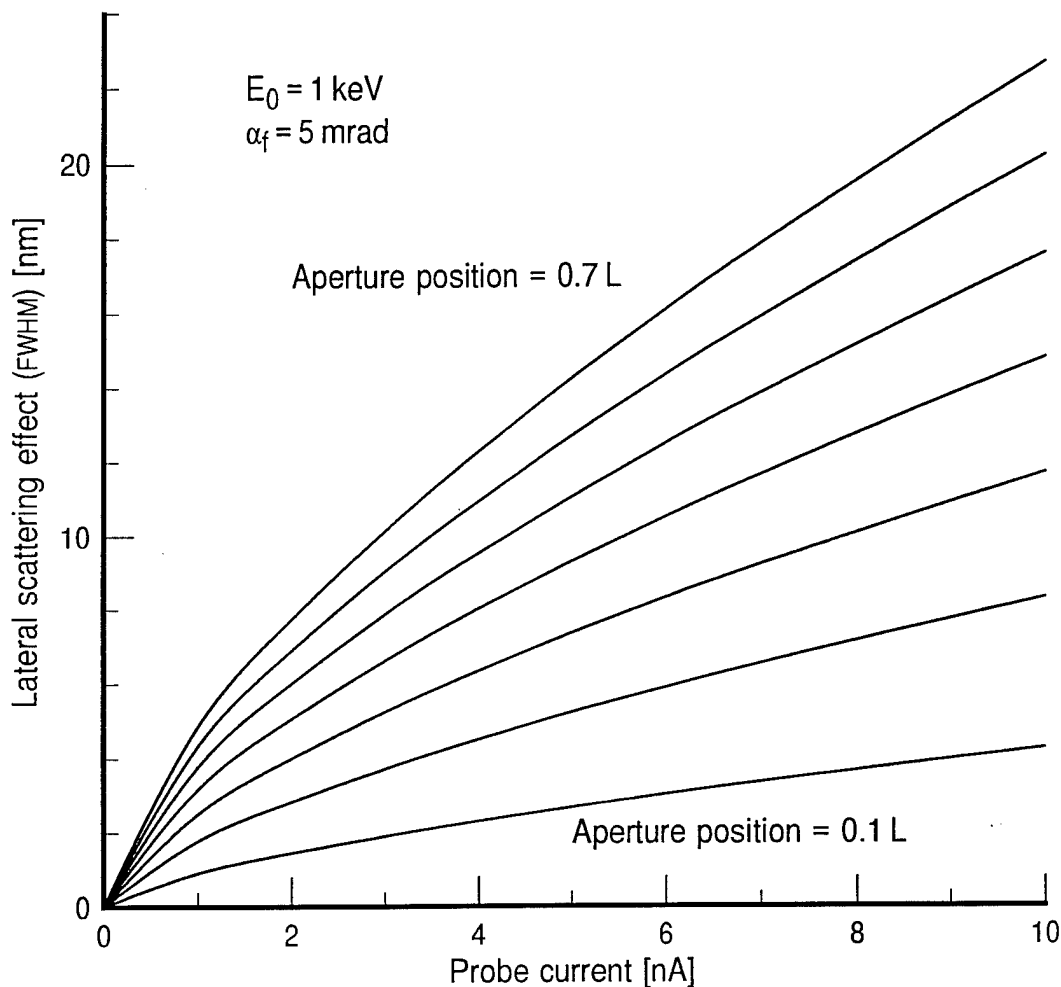


Fig. 2.18. The lateral scattering effect caused by electron-electron scattering for a 1 keV beam. The values shown are theoretically predicted contributions after the beam has been accelerated to 1 keV, and do not include emission from the electron gun. The beam limiting aperture is placed at different positions in the column, between $0.1L$ and $0.7L$ from the cathode in steps of $0.1L$. The final convergence semiangle is 5 mrad, and α_{subve}/α_s is very large.

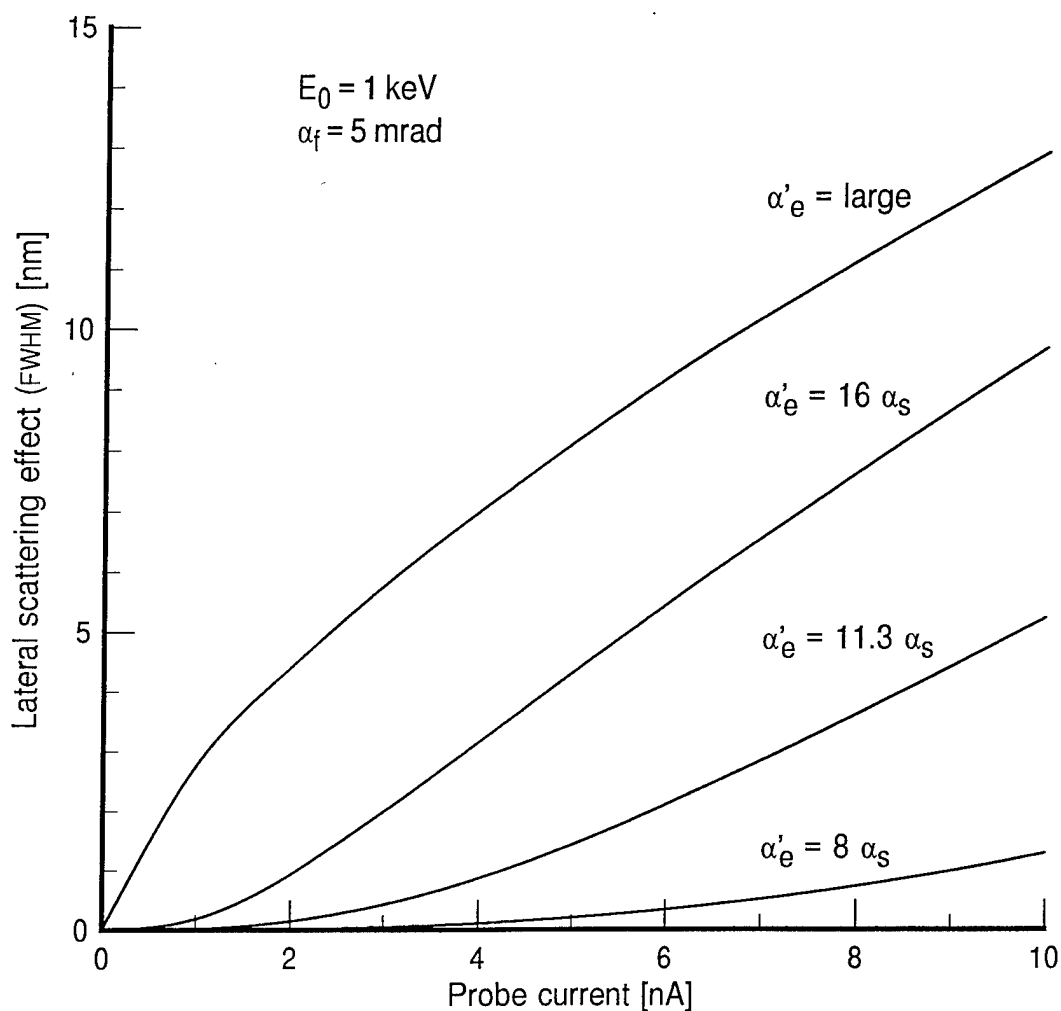


Fig. 2.19. The lateral scattering effect caused by electron-electron scattering for a 1 keV beam. The values shown are theoretically predicted contributions after the beam has been accelerated to 1 keV, and do not include the electron gun. The gun has an aperture which allows electrons to be emitted in a cone with semiangle α_e , while a cone with semiangle α_s is selected for the final probe current. The final convergence semiangle is 5 mrad, and the beam-limiting aperture is a distance $0.34L$ from the cathode.

2.3 Field Emission Source Development

2.3.1 Introduction

An important issue for the operation of a microcolumn is the field emission source. The field emitter has to operate very close (1-100 μ m) to the extraction electrode which is fabricated of thin silicon membrane with bore diameter a few micrometers in size. The desirable properties for microcolumn emitter tips are stable emission, low energy spread, low extraction voltage, small emission angle, and long lifetime.

For operational simplicity, cold (300K) field emitters are the cathodes of choice. Techniques for processing and annealing of such field emission tips for microcolumn operation have been developed.^{3.1-3.3} In particular, an oxygen induced tip sharpening process has been developed which provides a reproducible tip radius for the desired low voltage microcolumn operation. A more detailed discussion can be found below. Emission stability, measured in terms of noise fluctuations, of these oxygen processed tips is typically a few percent over a 30 minute period, and is adequate for operation of a microcolumn as an SEM.^{3.4} In general, emission stability of such a cold field emission source depends on many factors including emission currents, tip radius and apex geometry, tip materials, tip preparation and annealing procedures, vacuum levels, etc.. A more detailed discussion on this issue with specific reference to microcolumn operation is given by Yu et al.^{3.3}

Schottky emission tips have been proven to provide an electron beam of high brightness with good emission stability for conventional electron microscopy and e-beam lithography.^{3.5-3.9} Nevertheless, the use of these tips for microcolumn systems is very challenging due to the heat transferred to the membrane lens at the small tip to lens spacing. The microfabricated lens is made of a silicon membrane, typically 1 to 1.5 μ m in thickness, 1mm \times 1mm in size prepared in the center of a silicon chip. When used as an extractor, the membrane has a center hole of 1 to 5 μ m diameter. Tip to extractor spacing ranges from 50 to 100 μ m depending on the operating conditions.

2.3.2 Field Emission at 300 K and Schottky Emission

This report evaluates Zr/O/W Schottky emitters as an alternative to cold field emission sources for microcolumn applications. For this study, we set up a test system which consists of a Schottky emitter, an extractor, a Faraday cup with a limiting aperture and a micro-channel plate with a phosphor screen. The tip can be accurately aligned to the extractor with x,y and z motions. Emission patterns, I-V characteristics, and emission

stability of Schottky sources measured with the test system in a UHV environment will be presented.

Schottky emission tips have been widely used as an electron source for microscopy and electron beam lithography with high brightness, good emission stability, and long lifetime.^{3,5} As shown in Fig. 3.1, the field emission of the cold emission tip occurs by electron tunneling through the potential barrier near the Fermi level (E_F). In the Schottky emission case, the work function is lower and electron transmission occurs primarily over the top of the potential barrier with a smaller electric field, F_{se} . The current density expressions for the cold field emission (J_{fe}) and Schottky emission (J_{se}) are given by

$$J_{fe} = a(F^2/\phi) \exp(10.4/\phi^{1/2}) \exp(-b\phi^{3/2}/F) \text{ (A/cm}^2\text{)}$$

$$J_{se} = 120T^2 \exp(-(\phi - 3.8F^{1/2})/kT) \text{ (A/cm}^2\text{)}$$

where $a = 1.54 \times 10^{-6}$, $b = 0.644$, $k = 8.617 \times 10^{-5} \text{ eV/}^\circ\text{K}$, T is the tip temperature in $^\circ\text{K}$, F is the electric field strength in V/\AA , and ϕ is the emitter work function in eV. From these equations, the Schottky emission is highly sensitive to the tip temperature, while both depend strongly on the electric field and the emitter work function.

Table I shows the comparison between cold field emission and Schottky emission sources. The cold field emission cathodes typically used are single crystal $\langle 111 \rangle$ and $\langle 310 \rangle$ tungsten. Most cold field emission cathodes have radius of about 100 nm after annealing. The Schottky emission cathode most commonly used is a ZrO coated $\langle 100 \rangle$ oriented tungsten emitter. The ZrO reduces the work function of W(100) from 4.5 eV to 2.7 eV. A disadvantage of a Schottky emitter is that the tip is operating at 1800K, and requires a few watts of heating power. It also has a larger energy spread when compared to a cold field emitter at a given angular emission current density.^{3,10,3,11} However, Schottky emitters have a much more stable emission current than the cold field emission due to the lower electric fields and the larger and more stable emitting areas. Typically it has less than 1% of noise fluctuation over several hours. The Schottky emitter can also be operated at poorer vacuum condition than the cold field emission source. The operating pressure range is 10^{-8} to 10^{-9} Torr.

Figures 3.2(a) and 3.2(b) show operations of a Zr/O/W tip in both a conventional and a microcolumn system. A Schottky emitter needs a suppressor cap to reduce the number of thermionic emitted electrons from the filament and the shank of the tip. In a typical conventional system shown in Fig. 3.2(a),^{3,12} the emitter has a gap of about 500 μm to an extractor. The extractor has an aperture of about 400 μm in diameter. The microcolumn system has a similar emitter and suppressor cap as the conventional sys-

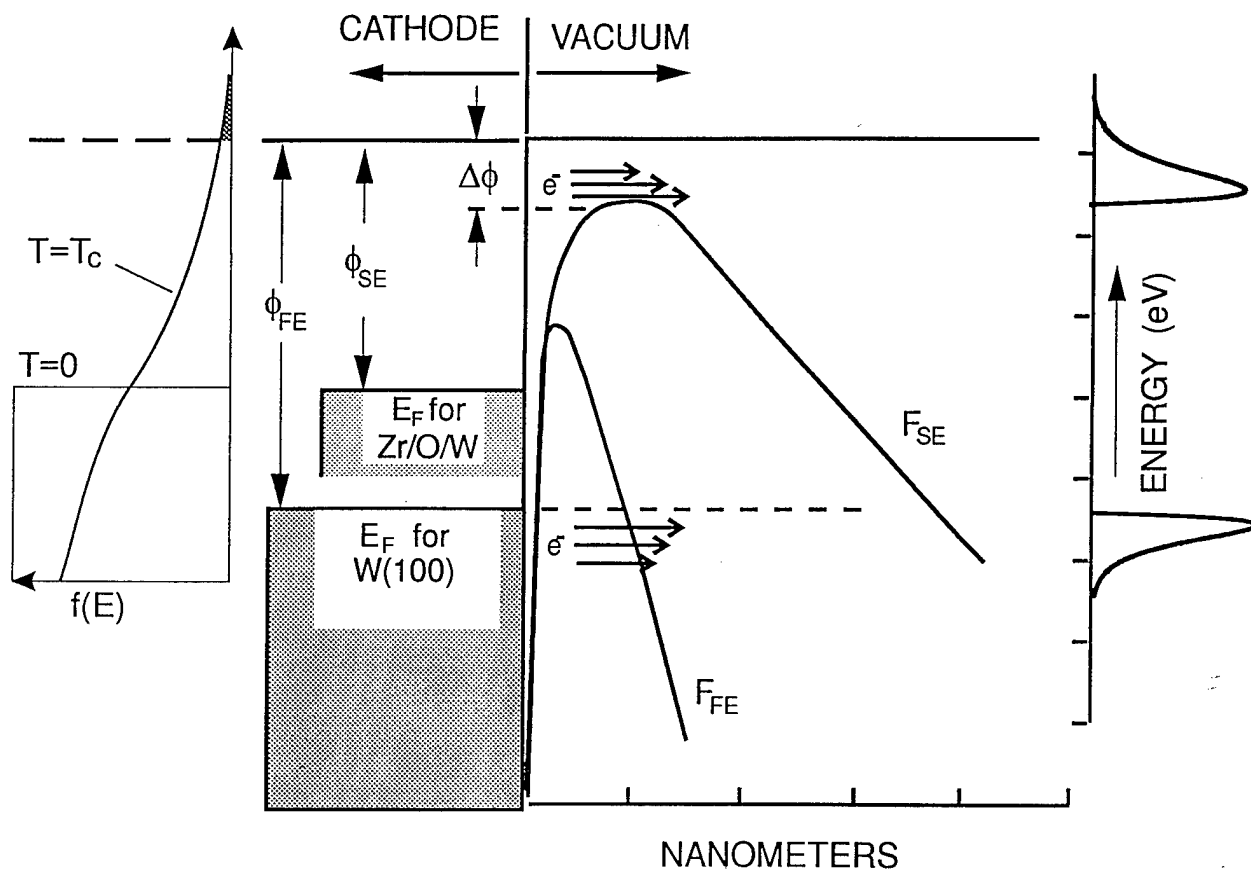


Fig. 3.1. Potential energy diagram for cold field emission (F_{FE}) and Schottky emission (F_{SE}). $\Delta\phi$ is the field reduction of the work function for Schottky emission. A Fermi distribution $f(E)$ for a relatively high temperature is plotted on the left, and energy distributions of emitted electrons are plotted on the right.

Table I. Comparison of cold field emission tip and Schottky emission tip.

Property	Cold F.E. Source	Schottky E. Source
Cathode	W single Crystal <111>,<310>	Zr/O/W
Radius	$\leq 100\text{nm}$	$\sim 1\mu\text{m}$
Temperature	300K	1800K
Work Function	4.4 eV	2.7eV
Virtual Source Size	$\sim 5\text{nm}$	$\sim 15\text{nm}$
Emission Current	$\sim 10\mu\text{A}$	$\sim 100\mu\text{A}$
Angular Emission	$< 100\mu\text{A/sr}$	$> 100\mu\text{A/sr}$
Energy Spread	0.3-0.8eV	0.6-1.2eV
Heating Power	none	$\sim 2\text{W}$
Stability (noise)	a few%	$< 1\%$
Vacuum Pressure	10^{-10} - 10^{-11} Torr	10^{-8} - 10^{-9} Torr

tem. The extractor for the microcolumn system, however, is made from a silicon membrane which has a thickness of 1-1.5 μ m. The aperture of this extractor is only a few micrometers in diameter. The distance between the emitter and extractor is about 50 to 100 μ m as shown in Fig. 3.2(b). Thus, the use of Schottky emission tips for microcolumn systems is very challenging due to the need to operate the tip in such close proximity to the microlens and thus exposing the microlens material (a thin silicon membrane) to high temperature. Because the structure must be compact and operate at lower extraction voltage, the tip radius must be small to obtain high emission current. For the evaluation of Schottky emission tips with a microlens, the Zr/O/W emission tip has a radius from 0.25 to 0.5 μ m. The extractor voltage (V_{ext}) was less than 1kV to obtain emission currents (I_e) from 10 to 100 μ A.

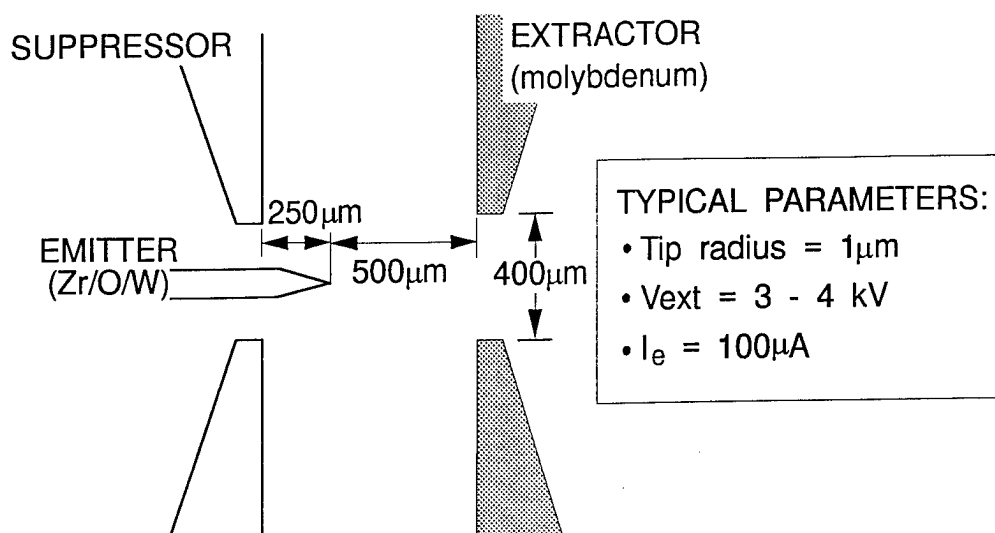
2.3.3 Oxygen Processed Field Emission Tips

2.3.3.1 Oxygen Induced Tip Sharpening Process

Tungsten field emission tips need to be annealed at high temperature to heal the crystallographic defects and damage introduced by the etching process during tip preparation, damage from ion sputtering during use, and to remove surface contaminants. It has been shown^{3,13,3,14} that the resultant geometry of a tip after the annealing process is defined by the competitive actions of the two principal mechanisms: surface diffusion and evaporation. Surface diffusion due to the capillary forces tends to increase the radius of curvature and thus causes the tip to become blunt as the thermal annealing proceeds. On the other hand, evaporation reduces the radius of curvature and thus sharpens the tip. Evaporation becomes significant only at temperatures above 0.7 T_m , the melting temperature, which is about 3810 K for tungsten. Hence tip sharpening will be effective only at temperatures above 2500 K, and tip blunting by surface diffusion dominates at lower temperatures. The use of a relatively low annealing temperature coupled with an applied field, low temperature field assisted annealing (LTFA),^{3,1} has allowed sharp tips suitable for microcolumn applications to be formed. This process, however, does not provide sufficient accuracy in the control of the radius nor does it permit a blunt tip to be resharpened.

The oxygen induced tip sharpening process now being developed for the microcolumn application utilizes a careful balance between self-diffusion and evaporation of tungsten to allow a properly annealed tip with well controlled radius to be achieved. When a tungsten tip is exposed to oxygen, it forms tungsten oxides such as WO, WO₂, WO₃ W₂O₆. The tungsten oxides sublime readily at a lower temperature than the pure tungsten. The sublimation temperatures of the tungsten oxides are typically between

(a) CONVENTIONAL SYSTEM



(b) MICROCOLUMN SYSTEM

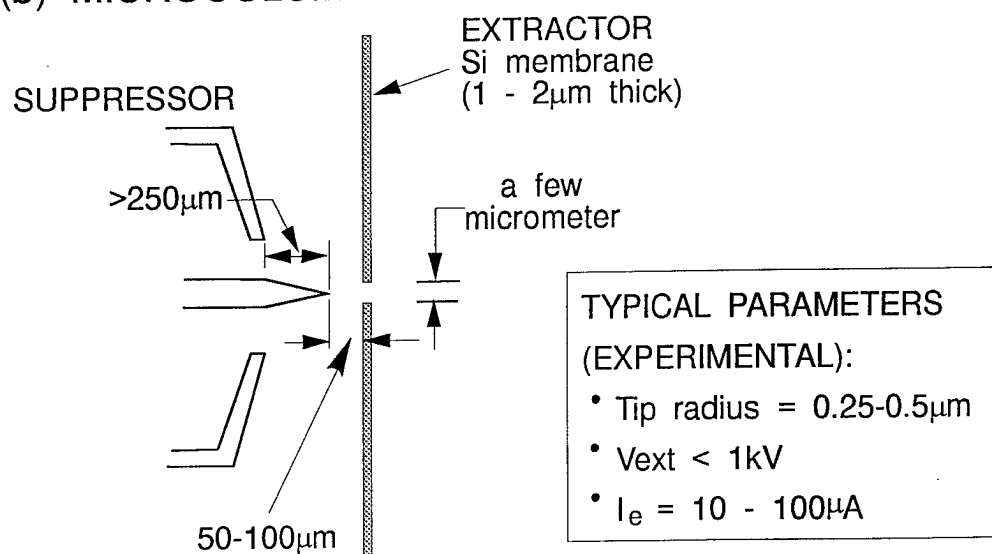


Fig. 3.2. Schematic diagrams of operation of Zr/O/W tip in a (a) conventional system and a (b) microcolumn system.

1200K and 2000K.^{3,15} Therefore, with the oxygen assistance, the balance between diffusion and evaporation at the tungsten surface can be readily controlled at lower temperatures.

The oxygen induced tip sharpening process reported here involves the following steps. First, a single-crystal W<111> wire is electro-chemically etched to form a tip with a typical radius of less than 500Å. Next the tip is heated in ultra-high vacuum (UHV) to about 900K for a few minutes to desorb physisorbed contaminants. This is then followed by an annealing step which heats up the tip to about 1600K for a few seconds to further clean and to heal the defects and damage. At the end of this step, the tip has a clean surface but a radius larger than the desired value. The tip is then sharpened in oxygen with a partial pressure of 4×10^{-5} Torr at a temperature of ≈ 1650 K. The oxygen processing time varies from a few seconds to a few minutes, which depends on the annealed tip radius and the desired final tip radius. After the oxygen treatment, the tip is flashed at a relatively low temperature of about 1200 K to avoid blunting, for a few seconds in UHV to remove the residual tungsten oxides. After this process, a very clean and sharp tip is formed with a number of properties desirable for the microcolumn application. Figure 3.3 shows examples of the oxygen induced tip sharpening process. Two newly etched tips with different initial radii of 200Å and 800Å respectively have been annealed and reformed to obtain the same radius of 400Å using this oxygen process.

As mentioned earlier, the process is intended primarily for use with newly etched tips to achieve a properly annealed ultra-sharp tip with well controlled geometry. It can also be used for *in situ* repair and resharpener of a damaged or blunt tip. A damaged tip, Fig. 3.4(a), has been resharpener using this process to achieve dramatic modification of tip geometries. In this case, the damaged W <111> tip which has an initial radius in the order of 5000Å has been processed in oxygen for a few hours to achieve a final radius of 300Å, Fig. 3.4(b).

Figure 3.4(c) shows the tip shape evolution during the oxygen process. It is a superposition of four SEM images. Each SEM image was consecutively taken one hour apart during the oxygen treatment. From this result, a tungsten removal rate of approximately 13Å/min at a temperature of 1650K and an oxygen pressure of 4×10^{-5} Torr was measured. This removal rate depends on processing temperature and oxygen pressure. At higher temperatures, a faster rate can be achieved at the same oxygen pressure, as shown in Fig. 3.4(d).

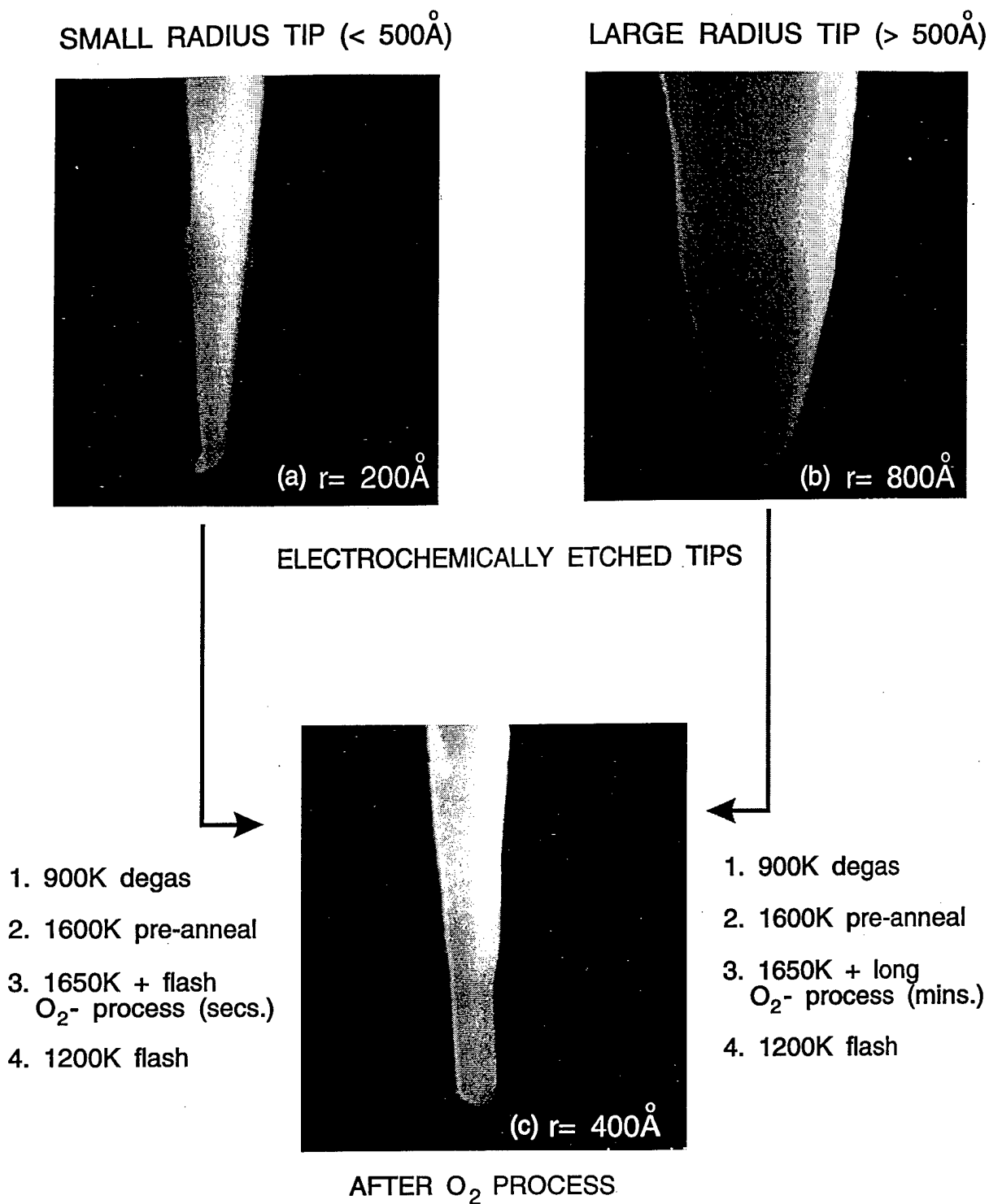


Fig. 3.3. Examples of the oxygen induced tip sharpening process. Two electrochemically etched tips have radii of (a) 200\AA and (b) 800\AA . (c). After the oxygen process, the same tip shown in (a) has been processed to an increased radius of 400\AA . The 800\AA radius tip can be sharpened to the same radius of 400\AA after about 30 minutes oxygen process.

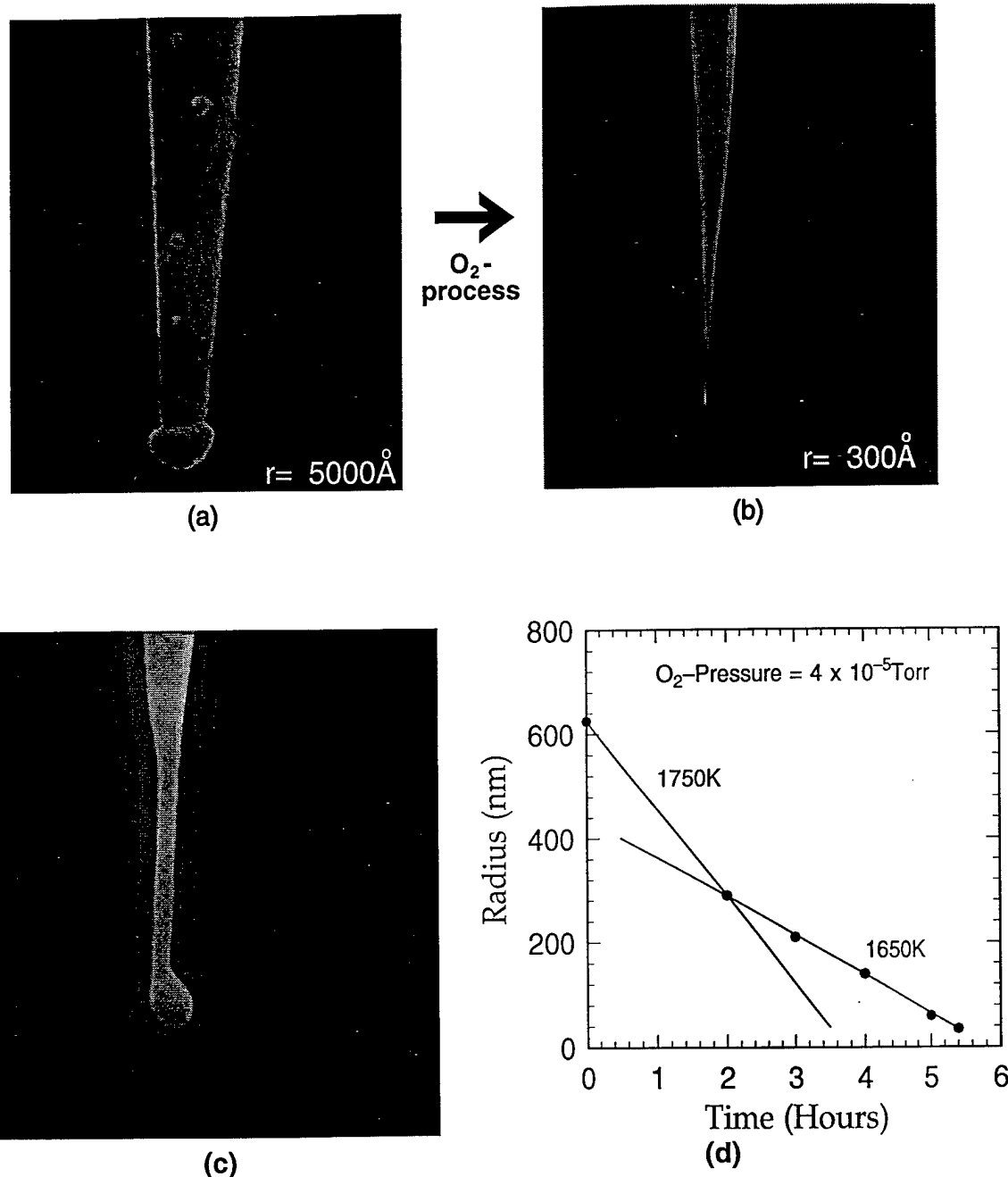


Fig. 3.4. Scanning electron micrographs showing an extreme case of the sharpening process. (a) A damaged tip with radius of $\approx 5000 \text{ \AA}$ (b) The same tip after the oxygen process, achieving radius of $\approx 300 \text{ \AA}$ (c) A superposition of four SEM images shows tip shape evolution by the oxygen induced sharpening process. The shank radii change from 2900 \AA , 2100 \AA , 1400 \AA , to 600 \AA . (d) Tungsten removal rate of approx. 13 \AA/min was measured at a processing temperature of 1650 K and an oxygen pressure of $4 \times 10^{-5} \text{ Torr}$. Increasing temperature to 1750 K , the removal rate is approx. 25 \AA/min .

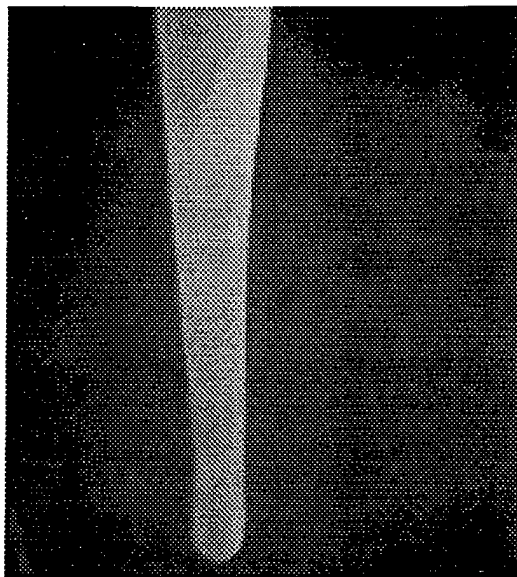
2.3.3.2 Experimental Evaluation

Experiments have been conducted to evaluate the geometric structure and field emission properties of oxygen processed tips. Figure 3.5 shows the results of such a study. In this case, a tip with an initial radius of 1600Å was processed under careful control of the operating parameters until it reaches $\approx 700\text{Å}$ radius. Geometry and radius of the tip were monitored by moving the tip from the oxygen processing chamber to an SEM at regular intervals. In addition, I-V characteristics were measured as the oxygen sharpening process proceeds. Figure 3.5(a) to 3.5(c) show examples of the SEM images of this tip at three stages of the process, $t = 0$ min., 30 min., and 100 min. The tip radii, defined as half-width of the end shank, measured from the SEM images were 1600Å, 1400Å, and 700Å respectively. Using I-V measurements taken at these three stages, the corresponding Fowler-Nordheim plots can be generated and they are shown in Fig. 3.5(d). The “effective” tip radius, r_{eff} , can be derived from the Fowler-Nordheim equation,^{3,16}

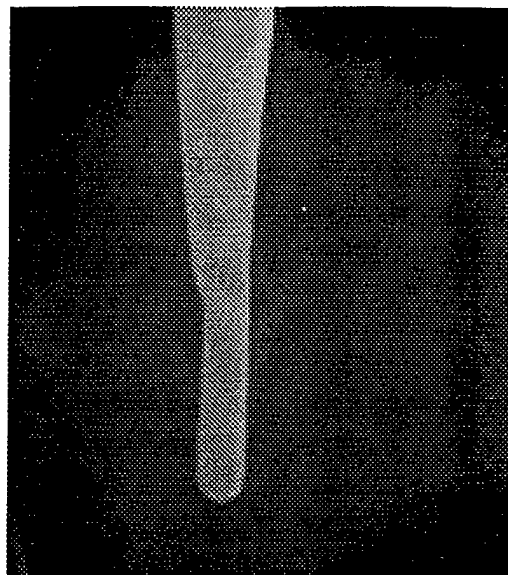
$$I/V^2 = a \exp(-b\phi^{3/2}/V),$$

where $a = 6.2 \times 10^{-6} A(\mu/\phi)^{1/2}(\mu+\phi)^{-1} (\alpha k r_{eff})^{-2}$, $b = 6.8 \times 10^{-7} \alpha k r_{eff}$, I is the total current, V the voltage, ϕ the workfunction of the tip, A the total emitting area, α the Nordheim image-correction term (≈ 1), μ Fermi level, and k the form factor which depends on tip-anode geometry and emitter shape (≈ 5 for a large separation between the tip and anode). A plot of $\ln(I/V^2)$ versus $1/V$ is therefore linear as shown in Fig. 3.5(d) with a slope give by $-b\phi^{3/2}$. A value of r_{eff} can then be found from the slope if ϕ is known and uniform. The effective tip radii measured for the same three stages from the F-N plot gave values of 2090Å, 1790Å and 900Å using a ϕ value of 4.5 eV. These values are fairly close to and proportional to the radii measured in the SEM. The F-N radii are consistently about 20% larger than the SEM measurements. Thus, it appears that the I-V data can be used as a means to monitor the tip radius during the process. The other interesting feature to note is the end shape of the oxygen processed tips. It can be seen from Fig. 3.5(b) and 3.5(c) that the oxygen process invariably produces a tip ended with a distinctive short stub or shank which has an approximately zero degree cone angle and a length of approximately $1.5\mu\text{m}$. The reason for this distinctive stub is not yet fully understood and is believed to be related to faceting which is yet another notable feature of this oxygen process.

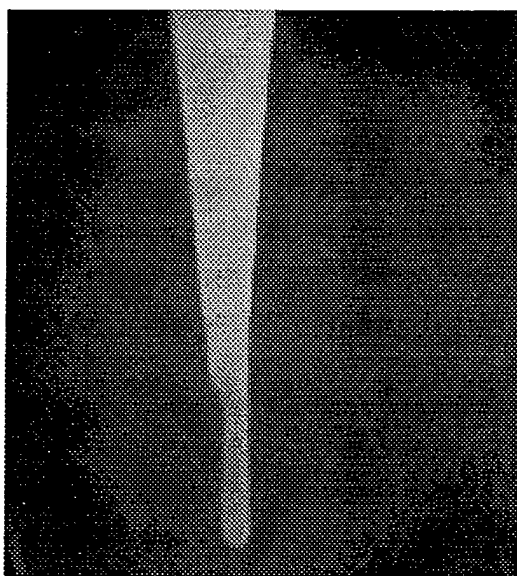
Faceting of the tip caused by the oxygen process is shown in Fig. 3.6. Figure 3.6(a) and 3.6(b) show SEM images at low magnification of a tip before and after the oxygen process. Transformation of the tip from a smoothly curved surface to that of a surface



(a) $t_1 = 0$ mins. $r = 160\text{nm}$



(b) $t_2 = 30$ mins. $r = 140\text{nm}$



(c) $t_3 = 100$ mins. $r = 70\text{nm}$

Fowler-Nordheim Plots (for in situ radius measurement)

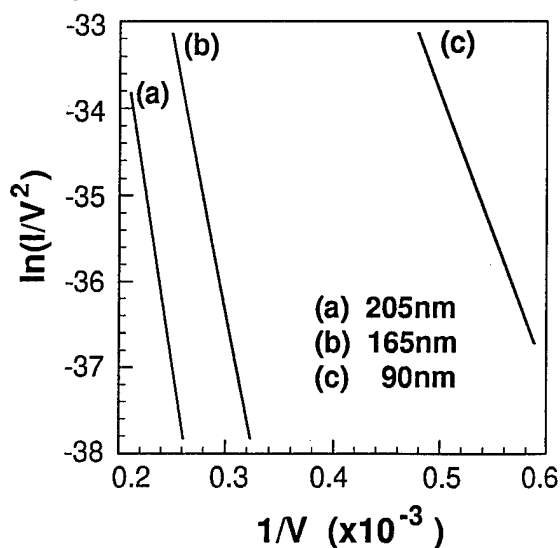
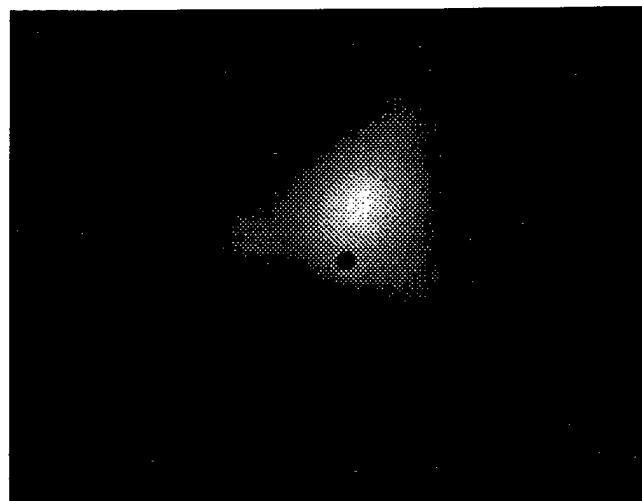


Fig. 3.5. The oxygen processed tip geometry and Fowler-Nordheim plots. SEM images were consecutively taken at different stages of the oxygen process with radii of (a) 1600\AA (b) 1400\AA (c) 700\AA . The 0° cone angle shank with a length of about $1.5\mu\text{m}$ is formed during the oxygen process. (d). From Fowler-Nordheim plots, the “effective radii” of (a) 2090\AA (b) 1790\AA (c) 900\AA are calculated. These values can be use as a monitor during the oxygen process. The values of ϕ , k , and α used in this calculation are 4.5eV , 5 , 1 respectively.

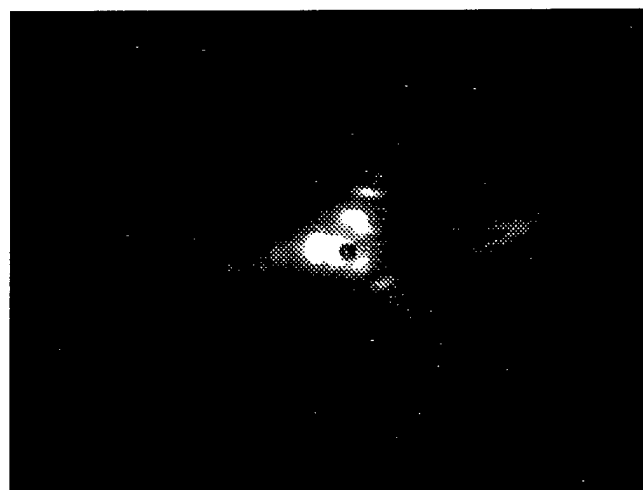
with sharp corners after the oxygen process can be clearly seen. An SEM top view, Fig. 3.6(c), shows the final shape of such a faceted W(111) tip as three faceting planes which continue to the tip apex. An x-ray diffraction study shows that the faceting planes intersect in the directions $(\bar{1}01)$, $(01\bar{1})$ and $(\bar{1}10)$ as shown in Fig. 3.6(d).

The oxygen processed tips have been evaluated in a field electron emission microscope which can be readily converted to a field ion microscope. Figures 3.7(a) and 3.7(b) show images of FEEM and FIM of an oxygen processed tip. The images always show 3-fold symmetric patterns which are consistent with the faceting effect discussed earlier. The major contribution to the emission pattern comes from the (111) plane at the tip apex. The emission half-angle was measured to be about 5 degrees. This was measured from the emission spot size in the FEEM image on the microchannel plate screen and the distance between the screen and the tip. The small half cone angle is desirable for SAFE microcolumn operation as it increases the angular emission density.

The emission stability of an oxygen processed tip has been measured with the microcolumn system and a typical set of results is shown in Fig. 3.8. The tip is generally processed at a large distance, about 2mm, away from the first electrode to avoid damaging the first lens by the high temperature. The first data, Fig. 3.8(a), was taken at this tip position immediately after the oxygen process. It shows that there is typically an initial decay period over which the initial emission current, 10nA in this case, slowly decays to half its value, 5nA, in approximately 30 minutes. After this period, the emission reaches a stable state. This behavior is very similar to that of conventional field emission tips.^{3,17} After the initial decay, emission current is restored to its original value, 10nA, by increasing the extraction voltage and emission stability is then measured at different tip to lens separation. At a large separation, such as 750 μ m, Fig. 3.8(b), stable emission with less than 1% of rms fluctuation over a 25 minutes period was observed. As the separation decreases, the emission remains generally stable, but some noise in the form of steps and spikes begins to appear intermittently. Fig. 3.8(c) and 3.8(d) show these results at tip positions of 100 μ m and 5 μ m respectively. The frequency of appearance of this noise increases with decreasing tip distance. At these two close tip positions, the effect of increasing the emission current from 10nA to 100nA was also studied and the results are shown by the upper lines in Fig. 3.8(c) and 3.8(d). As can be seen, the noise, mainly in spike form, increases with increasing emission current. This type of intermittent spike noise, generally referred to as popcorn noise,^{3,18} is usually associated with the vacuum conditions. It is believed that the increase in noise might be caused by an increase in outgassing from the first electrode as the electron bombardment from the tip becomes more intense as the tip gets closer. Methods to more

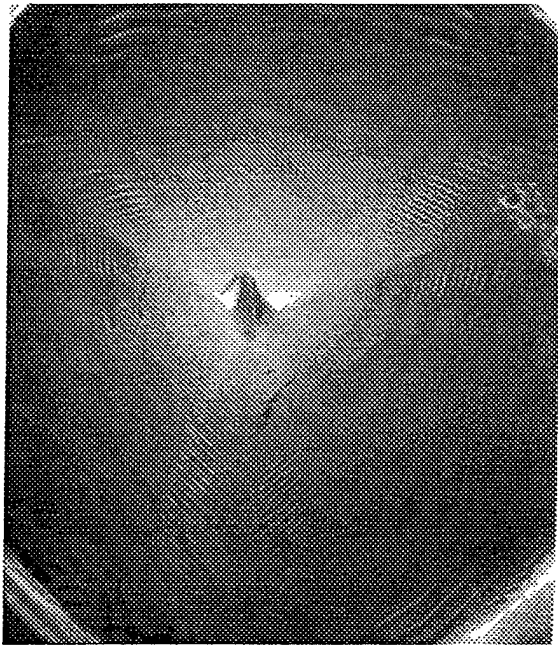


(a)

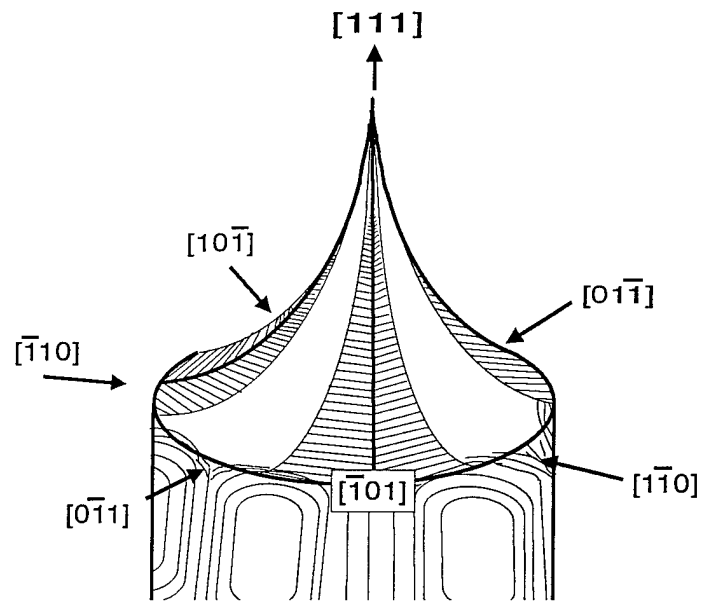


(b)

Fig. 3.6. (a) FEEM image of an oxygen processed W(111) tip (2.2kV, 130K). (b) FIM image of the same tip (13.2kV, 1×10^{-4} Torr He, 130K). Both images showing 3-fold symmetry patterns. The emission half angle of $\approx 5^\circ$ was measured from FEEM data. The dark spots at the center of each image are a probe hole of the channel plate.



(a)



(b)

Fig. 3.7. (a) Top view of faceted W (111) tip after oxygen process. (b) The faceting planes intersect in the direction of $(0\bar{1}1)$ and its equivalent.

effectively prebake the lens to reduce outgassing are currently being developed as well as improvements to the STM feedback bandwidth to better suppress this noise.

The data on emission stability presented here represent only preliminary studies. Considerably more work is needed to further understand this very complex and important issue. However, the results obtained so far have been encouraging and, on the whole, emission stability of oxygen processed tips is at least as good as the best tips we have seen so far in our microcolumn experiments.

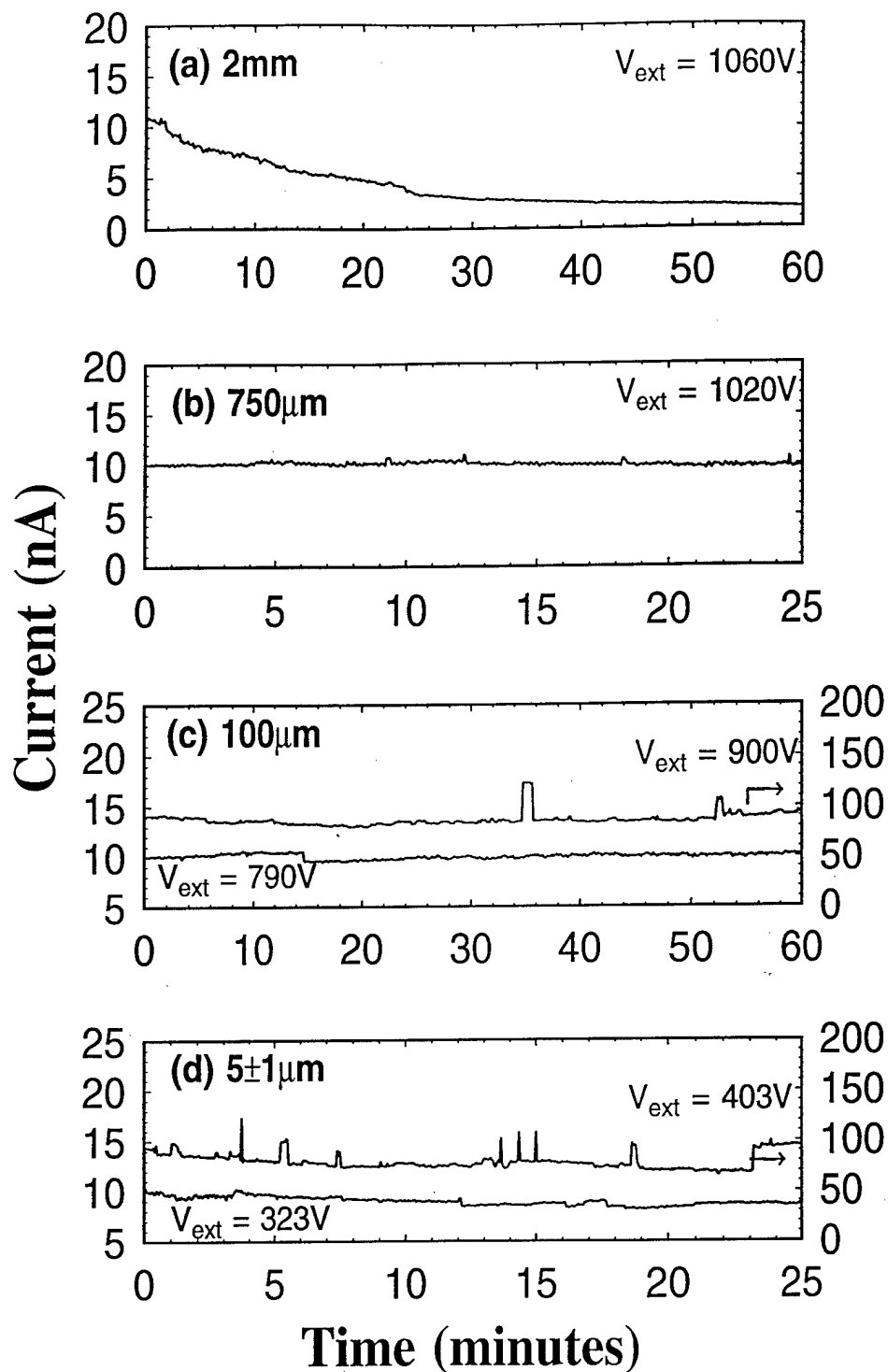


Fig. 3.8. Emission stability of oxygen processed tip with microcolumn system. The emission stabilities were measured at (a) 2mm, (b) 750 μm , (c) 100 μm , and (d) 5 \pm 1 μm positions. After initial decay, stable emission current was observed. At the positions of 100 μm and 5 \pm 1 μm , two emission currents, 10nA and 100nA, were measured. The upper lines is for 100nA emission current and belong to the right vertical axis. Note the decrease of extraction voltage, V_{ext} , with decreasing with tip distances.

2.3.4 Cold Field Emitters

2.3.4.1 Hafnium Carbide

Electron emitters based on cold field emission are very attractive for use in our microcolumn. One potential candidate is the ultra sharp tungsten emitter, which has high brightness, narrow energy spread, and low extraction voltage. However, our research has shown that stable electron emission from these emitters is limited by the electric field induced migration of atoms at the apex. In view of the difficulties with the tungsten based cold field emitters, we have studied field emission from single crystal carbides in collaboration with Professor William Mackie of Linfield Research Institute in Linfield College, Oregon,

Refractory-metal carbides are metallic conductors. They are mechanically hard and have very high melting temperatures.^{3,19} The thermal and mechanical stability apparently translates into lower atomic mobility, and hence better emission stability. The properties of carbide cold-field-emitters have been reviewed by Plomp^{3,20} and Adachi.^{3,21} Recently, we have shown that^{3,22} tungsten carbide covered tungsten emitters and HfC<100> emitters can provide stable emission angular current density up to 10 $\mu\text{A}/\text{sr}$. This is practically ten times better than the more conventional ultrasharp tungsten tips.^{3,22} We have also measured the total energy distributions (TED) of electrons field emitted from hafnium carbide and tungsten carbide tips. They have single-peaked TEDs similar to those of tungsten emitters and the full width at half-maximum (FWHM) was about 0.33 eV. We observed that a common mode of emission instability at high emission currents is step increase in the emission current density in an angularly confined region. This is similar to the effect of high emission current treatment of TiC<110> tips used by Adachi,^{3,21} and similar treatments of NbC<110> tips by Ishizawa et al.^{3,23} to obtain good angular-confinement and stability of the emission. They have not, however, reported any measurement of TEDs. We observed interestingly multiple-peaked TEDs at these emission sites on tungsten carbide, hafnium carbide, and zirconium carbide emitters. To our knowledge, this is the first observation of such an emission instability induced phenomenon.

All our emitter testing and tip preparation were performed in UHV systems with base pressure 1×10^{-10} Torr or better.^{3,3} Our VG FIM-100 system has a UHV preparation chamber where we did our tip treatments and coating. The tips were transferred in-situ into the field ion microscopy (FIM) chamber for FIM and field emission microscopy (FEM) analysis. In the FIM chamber, we also measured the Fowler-Nordheim characteristics, emission current densities, and emission stability. In a separate UHV chamber,

we have a VSW HR-50 hemispherical energy analyzer with about 55 meV resolution for TED measurements.^{3,22} We found it useful to use the Fermi level of the emitter as our energy reference point. This is easily determined since the mid-points of the high energy edges of the energy distributions from tungsten and our carbide tips are close approximations to the Fermi levels.^{3,16}

Both of our ZrC<100> and HfC<100> tips were prepared from oriented single crystal rods. The hafnium carbide emitters were fabricated by Mackie. Currently the hafnium carbide crystal is ground to the correct shape and brazed into a rhenium cup which is spot welded on to a rhenium filament. Relatively high power is needed to heat the tip to the annealing temperature because of the size, approximately 200 μm , of the cup and wire used. Cups and wires of a smaller size will be used in the future and a special jig will be provided to improve tip alignment during assembly. Tips with radii of curvature 50 nm or less were prepared by electrochemical etching, 2000 K annealing, field evaporation, and acetylene treatment to give a carbon rich surface. This last procedure is critical for improving the emission stability. The acetylene treatment was typically a 100-400 L (Langmuir) of acetylene exposure in the 10^{-6} Torr range at 1100-1150 K. The dosage is not too critical. Our tungsten carbide tips were prepared by carburizing ultra-sharp tungsten <100> and <111> emitters.^{3,22} The tungsten tips were prepared by the sequence of electrochemical etching, thermal annealing, and oxygen treatment. The tips were then carburized with 4×10^{-6} Torr acetylene at 1100K for 30s.

All three kinds of carbide emitters have shown that they can deliver stable emission up to 10 $\mu\text{A/sr}$ for over one hour. As mentioned above, instability often occurred as a step increase in the current density.^{3,22} The top left inset in Fig. 3.9 shows an FEM image of such a site with instability induced enhanced emission on a HfC<100> tip. Current increases were associated with an enhancement of the emission in an angularly confined region of 2 - 3° semi-cone angle. The top right inset is the FIM image showing a bright round atomic image. It suggests a single atom at the apex. Unfortunately, we were not able to control the field evaporation well enough to systematically analyze the whole structure of the apex.

Electrons from many of these enhanced emission sites showed unexpected multiple-peaked energy distributions. Energy distributions of electrons emitted from our carbide tips before current instabilities all have single peaks as expected from a metallic emitter. Figure 3.9 curve (a) shows the TED of electrons from a tungsten carbide coated W<111> tip. The TEDs from ZrC<100> and HfC<100> tips are similar. Their FWHMs are about 0.23 eV, 0.22 eV, and 0.32 eV for tungsten carbide, ZrC<100> and HfC<100> respectively. In comparison, the instability-induced sites emitted with multiple-peaked

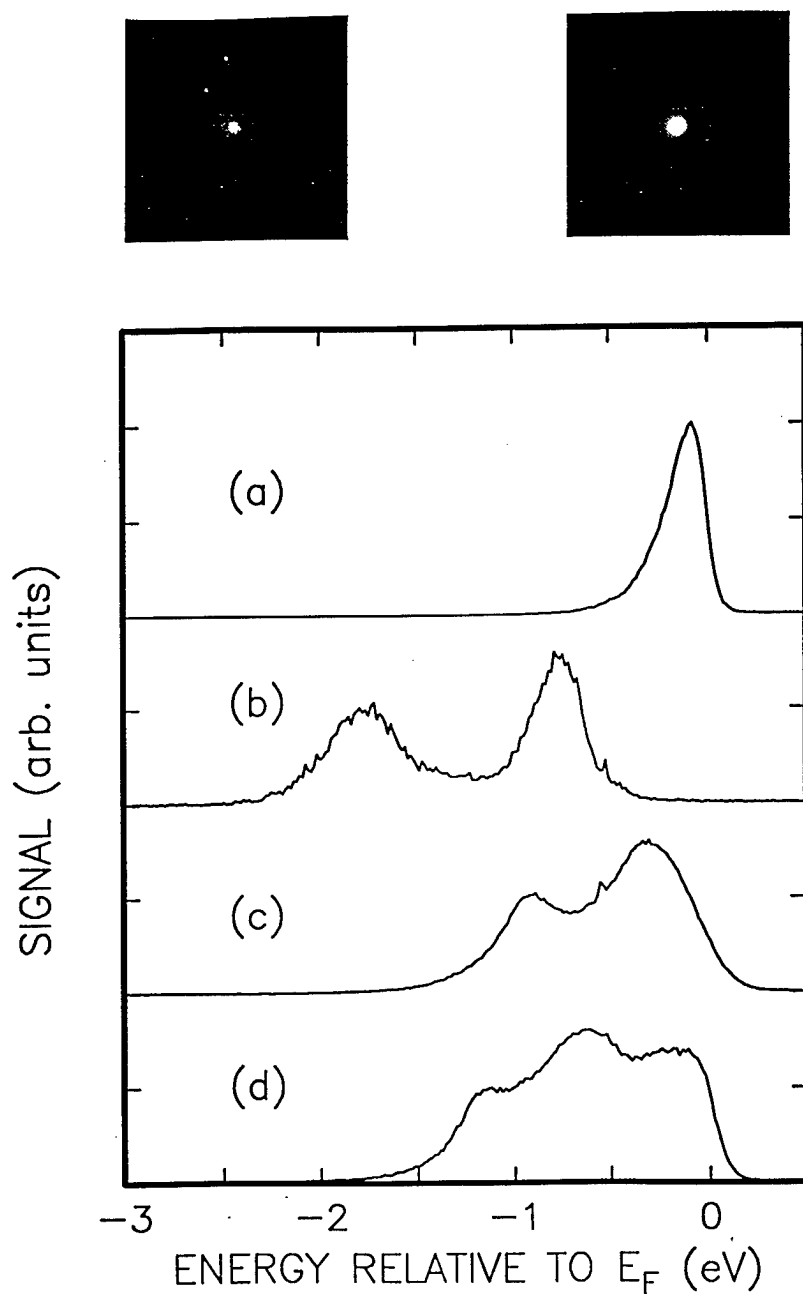


Fig. 3.9 Total energy distribution of field emitted electrons from (a) tungsten-carbide-coated W<111> tips before instability, (b) same tip after instability, (c) HfC<100> after instability, (d) ZrC<100> after instability. The top left inset shows an FEM image of the instability-enhanced emission site on a HfC<100> tip. The top right inset shows the corresponding FIM image. The magnification of the FEM image is 0.38 times that of the FIM image.

energy distributions that spanned up to 2 eV. Curves 1b, 1c, and 1d depict the multiple-peaked TEDs obtained from instability-induced sites on tungsten carbide, HfC<100>, and ZrC<100> tips. The positions of the peaks and their relative magnitudes varied from experiment to experiment.

The relative magnitudes of the energy peaks change gradually with the extraction field. Figure 3.10 depicts a set of TEDs from a ZrC<100> tip taken at different extraction voltages. Curve 2a shows a TED of electrons emitted from a ZrC<100> tip before instability. It has a FWHM of about 0.22 eV. Curves 2b to 2e show the TEDs from an instability-induced site with extraction voltages varying from 1150 V to 1300 V in 50 V steps. The higher extraction fields enhance the ratio of the low (-1.2 eV) energy peak to the high (-0.65 eV) energy peak. There is also a very small shift of the peak positions to the low-energy side with increasing extraction field at a rate approximately -0.5 mV/V. These observations are qualitatively consistent with the Fowler-Nordheim theory where the width of the tunnel barrier decreases with increasing extraction field.^{3.16}

Our experimental evidence strongly suggests that the instability-induced enhanced emission sites were built-up sites, and not caused by positive ion bombardment or gas adsorption. We did the following test. In the conventional thermal-field buildup process, a large electric field is applied to the tip.^{3.24} The electric field F generates a driving force $\nabla(F^2/8\pi)$ to move the tip atoms toward the local field maximum^{3.25} and produces a nano-protrusion. The tip is heated to promote atomic mobility. Since the driving force only depends on the magnitude of the electric field and not on its direction, a tip biases negatively as in field emission or biased positively should have the same effect. We tested this idea by applying a positive 14 kV bias on the tip at 1100 K. The buildup procedure produced enhanced emission sites. Again, multiple-peaked TEDs were observed from these sites. Our present interpretation is that the multiple-peaked TEDs are the result of the presence of discrete energy levels in the tip atom similar to those reported by Binh et al. for built-up W<111> tips.^{3.26} This is discussed further in another publication.^{3.27}

Our attempt to use the HfC<100> emitter in the microcolumn was, however, a disappointment. A HfC<100> emitter was processed in our UHV chamber to produce stable and well-confined emission. The emitter was then transferred through air to a microcolumn. The emitter showed large current instabilities in the form of current jumps between stable periods. The stable periods usually spanned a few minutes. The emission current was no longer confined along the <100> axis. These instabilities were most likely related to contamination adsorbed during the air exposure.

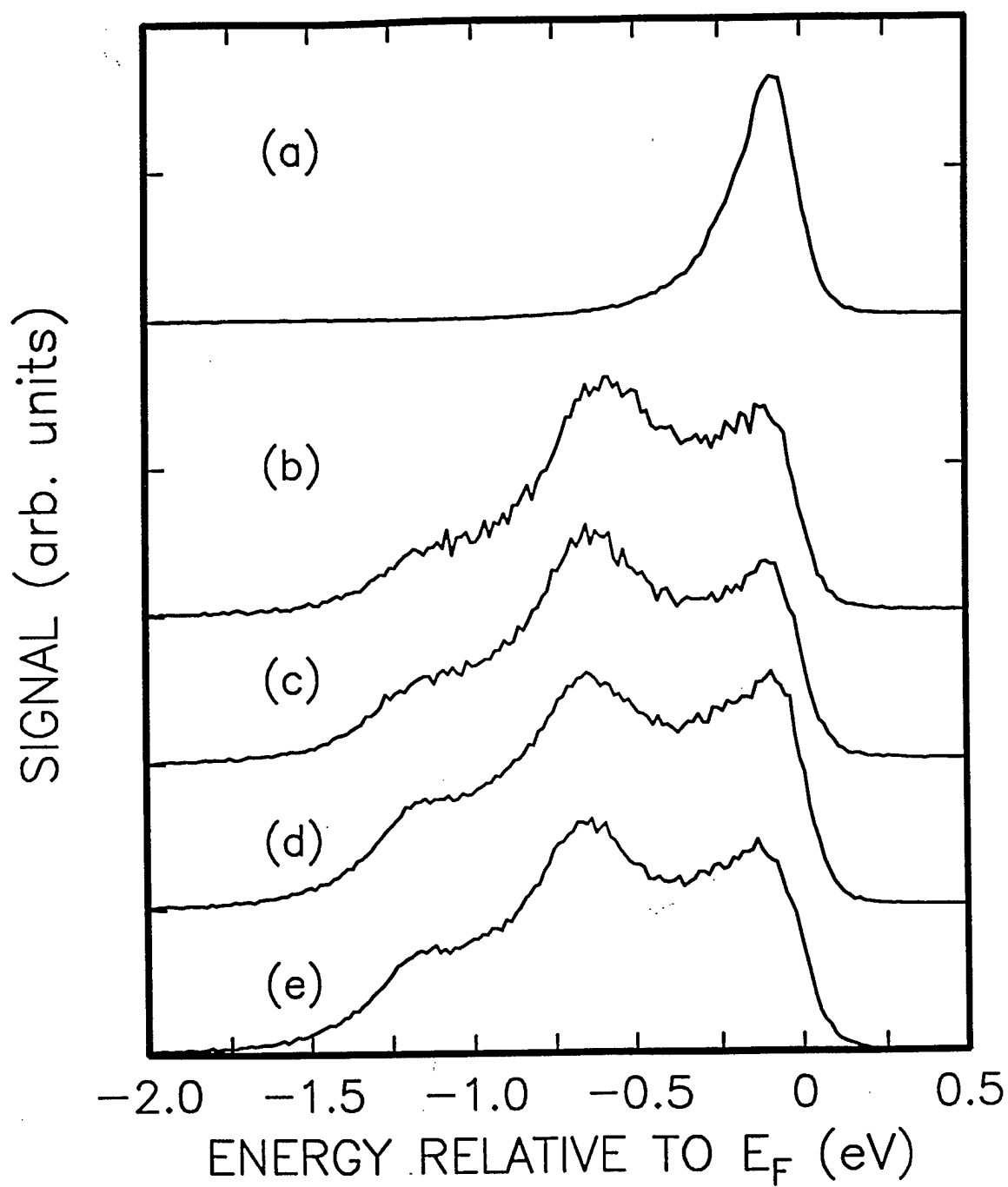


Fig. 3.10 Total energy distribution of field emitted electrons from ZrC<100> emitters (a) before instability, (b-e) after instability with extraction voltages of 1150, 1200, 1250, and 1300 V respectively.

We have shown that acetylene treatment at elevated temperatures can dramatically alter the cold field emission characteristics of thermally (2000K) annealed hafnium carbide $\langle 100 \rangle$ field emitter tips. There are two important improvements:

1. The thermally annealed HfC $\langle 100 \rangle$ tips have strong four-fold off-axis electron emission. The emission along the $\langle 100 \rangle$ direction is very weak and is therefore not useful as an electron source for our electron beam microcolumn. Acetylene treatment alters the emission pattern with the strongest emission along the $\langle 100 \rangle$ axis. Beam confinement to within about 3° semi-cone angle along the $\langle 100 \rangle$ axis have been obtained.
2. Electron emission from the annealed HfC $\langle 100 \rangle$ tip invariably decays gradually with time. Acetylene treatment improves the emission stability. Stable emission with angular current densities up to $12 \mu\text{A}/\text{sr}$ have been observed up to an hour.

Our experiment has provided us a much better understanding of the working of the hafnium carbide field emitter. The acetylene pyrolyzes on the HfC tip surface to deposit carbon. It generates a "carbon-rich" surface at the tip apex to give the desirable field emission properties.

Field emission angular distribution is controlled to a large extent by the work function of the different planes around the tip apex. The 2000 K annealed HfC $\langle 100 \rangle$ surface has a higher work function ($\sim 3.6 \text{ eV}$) than those of the higher index planes (110) and (210) ($\sim 3.3 \text{ eV}$). Since higher work function increases the energy barrier for electron tunneling, field emission along the $\langle 100 \rangle$ direction is weak as observed. The acetylene carburization process, we believe, reverses the ordering of the work functions such that the (100) plane is surrounded by planes of higher work functions. Electron emission is then dominated by that from the (100) facet at the apex. For a given radius of curvature, angular confinement is improved when the area of the (100) facet is small.

The gradual decay in emission current with time is normally caused by the electric field assisted adsorption of residual gas molecules on the tip. The normal HfC(100) plane has a Hf/C ratio of unity. Hafnium is much more reactive than carbon. The carburized HfC $\langle 100 \rangle$ tip with its higher carbon content should have a lesser tendency to adsorb residual gases. This is consistent with the more stable emission current from the carburized HfC tip as observed.

Prolonged testing of the carburized HfC $\langle 100 \rangle$ tips showed that stable emission was always interrupted by a single step jump in emission current. It could be caused by ion bombardment (from the ionization of residual gases by the emitted electrons) or by the

atomic motion at the tip. Flash annealing for about one second at 1100 K would restore the tip in most cases.

The improved HfC field emitter is still not competitive in stability with the Schottky emitter (see below). We are continuing to search for ways to improve the field emission stability by trying new tip materials and tip processing procedures.

2.3.4.2 Diamond-like Emitters

Cold-field emitters are high-brightness electron sources. Our interest is to develop them for use in electron beam microcolumns.^{3.28} A narrow electron energy spread is highly desirable to minimize the effect of chromatic aberrations especially at low beam energies. Recent developments have indicated that metal carbide and diamond cold field emitters are potentially stable electron sources. In this report, we report that the electron energy distribution properties of these emitters can differ significantly from those of conventional tungsten cold field emitters.

Diamond cold-field-emitters have attracted a lot of attention lately especially for field emission display applications.^{3.29} Diamond, similarly to the carbides, also has very good mechanical and thermal stability. Hence good emission stability has also been expected. However, there was only one reported measurement of TEDs from diamond known to us. Xu et al.^{3.30} measured the TEDs of electrons field emitted from chemical vapor deposited (CVD) diamond films on flat molybdenum substrates. They reported FWHMs of about 1 eV with large (2-3 eV) shift of the onsets of the TEDs from the Fermi level. They suggested that the emitted electrons were "hot", and the electrons suffered significant energy loss. These properties are significantly different from the TEDs from tungsten field emitters. It is hence of interest for us to make TED measurements on diamond emitters with sharp tip geometry.

We prepared our diamond emitters by coating the ultrasharp tungsten field emitters with diamond. We used the well-known hot-filament chemical vapor deposition technique.^{3.31} We first carburize the tungsten tips by the acetylene treatment described above to form a thin tungsten carbide layer on the tungsten surface. This procedure reduces the incubation time and makes the control of the diamond deposition more reproducible.^{3.32} We used the FIM-100 preparation chamber as a UHV-CVD reactor. A 1-15% methane-hydrogen mixture at 10 Torr was let into our chamber. A tantalum filament at 2300 K was used to dissociate the gas molecules. The carburized tungsten tip heated to 1400 K was brought to about 5 mm from the tantalum filament for diamond deposition for 30 minutes. These emitters were prepared by coating sharpened tungsten

tips with half to few thousand Angstroms of diamond films. No intentional dopant was added to the gas mixture to promote electrical conductivity. Many groups reported that carbon inclusion is important to sustain stable emission from diamond.^{3.33,3.34} We found that diamond tips could be insulating and showed no field emission when the concentration of methane was low (<1%) in our gas mixture. When the methane concentration was high (> 15%), graphitic carbon and carbon black were often deposited instead. Our tips were all flashed to 1200 K in UHV to desorb any hydrogen remaining on the surface.^{3.35} We found that there were too little deposited materials at the end of the tungsten tips to perform Raman analysis^{3.36} in our laboratory to characterize the deposited coatings. Therefore, we shall conservatively call our films diamond-like carbon coatings.^{3.36}

Figure 3.11(a) shows the typical scanning electron microscope (SEM) image of a diamond-like carbon coated tungsten tip. The diamond-like layer was polycrystalline with very rough morphology. It suggests that there can be many high field spots at the sharp asperities. An FIM image of such a tip is shown in Fig. 3.11(b). It shows that many of the atomic images have oblong shapes. This indicates spatially asymmetric electric fields at the apexes.^{3.37} There was no clear evidence of long range order. Figure 3.12 shows the Fowler-Nordheim plot of a W <111> tip after the diamond processing step. The emission current followed closely the Fowler-Nordheim relation for field emission and is consistent with many other reports.^{3.33,3.38} It suggests that the phenomenon originates from electron tunneling. The effective tip radius estimated from the Fowler-Nordheim plot gave about 110 Å if we assume a work function of 4.5 eV. The significance of this estimate should not be over emphasized since the mechanism of field emission from diamond is still being debated.

We were able to obtain a few diamond emitters that can deliver stable total emission current exceeding 1 µA and angular emission current exceeding 10 µA/sr for over 24 hours. Fig. 3.13 shows a six-hour segment of the stability run of a tip at about 5 µA/sr showing the good stability with less than 0.5% rms fluctuation. Emission stability was usually interrupted by sudden increase or decrease in the emission current, very much similar to the carbide emitters.

Figure 3.14 shows the energy distributions of the field-emitted electrons from a tip coated with about 1000 Å of diamond-like carbon coating. Curves 5a to 5c were obtained at extraction voltages of 700, 750, and 800 V respectively. Our data differ from those reported by Xu et al.^{3.30} in several important aspects. The FWHM is about 0.4 eV. It is broader than that of tungsten (0.23 eV) and tungsten carbide (0.22 eV) but is much narrower than those reported by Xu et al. (1 eV). Another difference from the result of

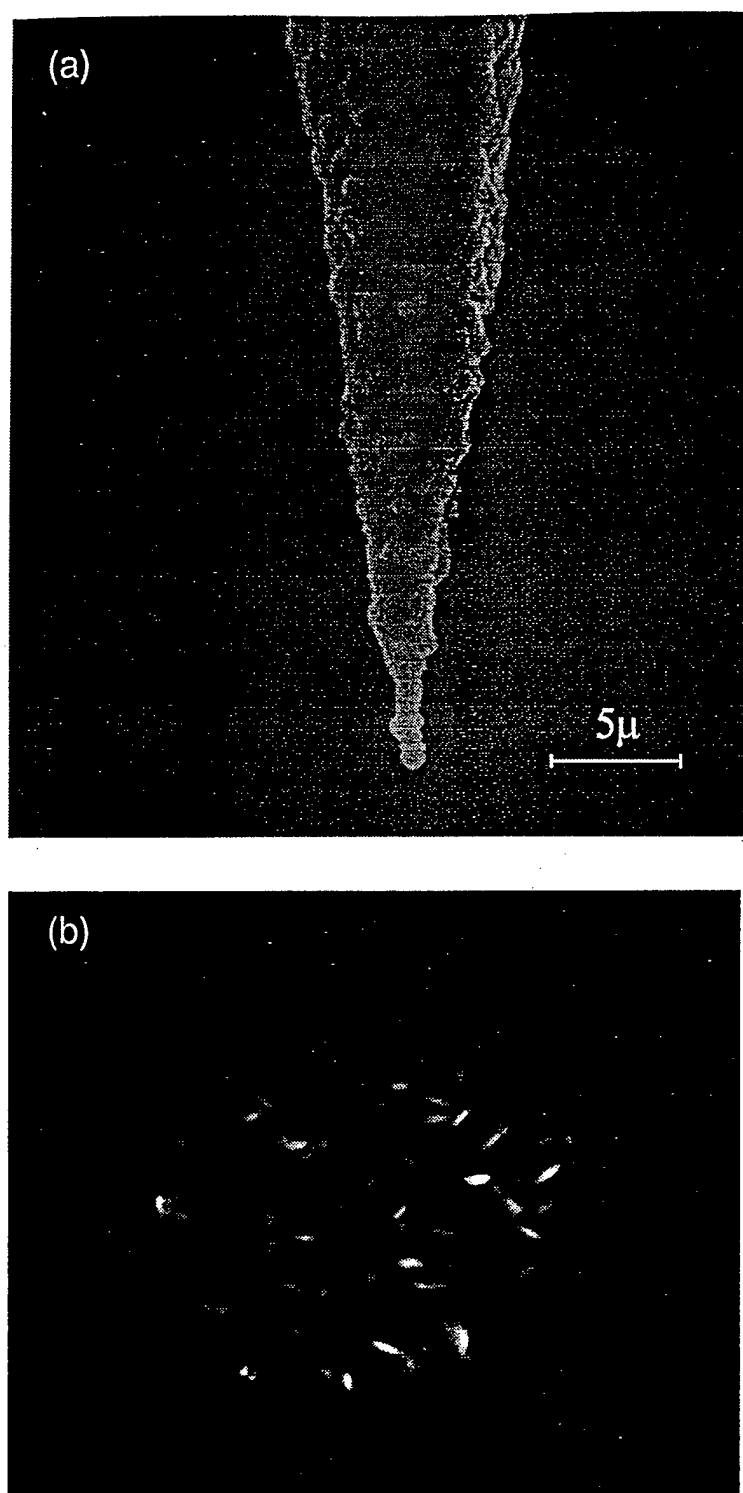


Fig. 3.11 (a) an SEM image of a diamond-like carbon coated tip. (b) an FIM image of such a tip was taken with neon gas at 4584 V.

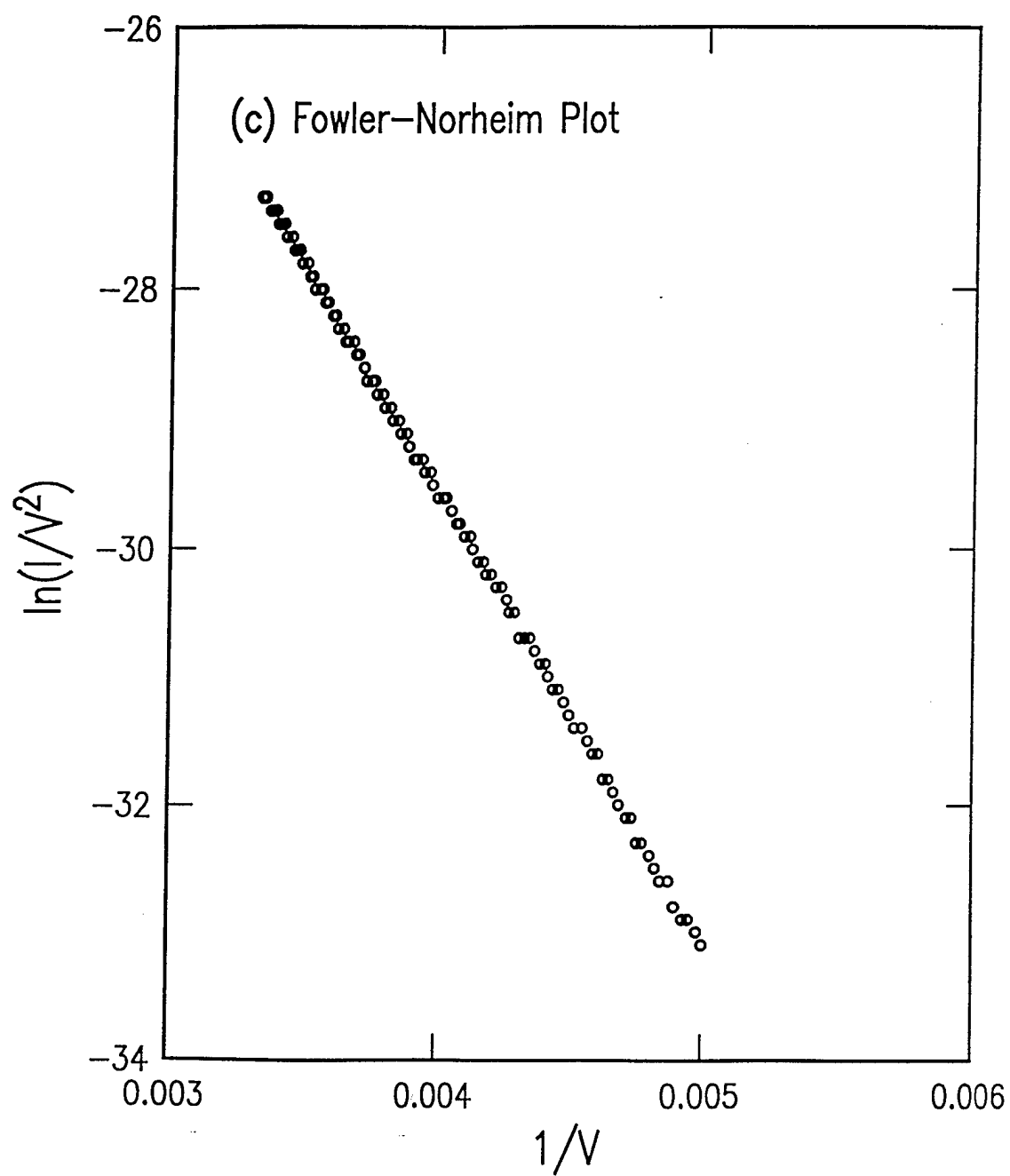


Fig. 3.12 Fowler-Nordheim plots of a W <111> tip with diamond-like carbon coating.

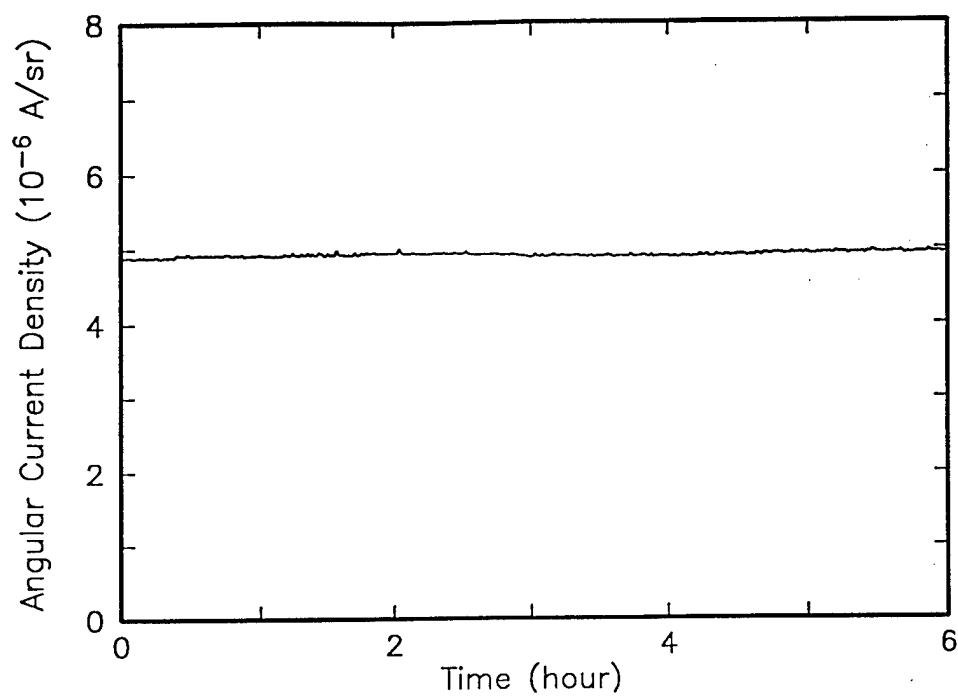


Fig. 3.13 Emission current as a function of time of a diamond-like carbon coated tungsten tip.

Xu et al. is that the onsets of the TEDs in our data do not show much shift from the Fermi level. Instead, the peaks of the TEDs shift significantly to the low energy end with increasing extraction voltages. The total shift in the peak as the extraction voltage changed from 700 to 800 V is approximately 0.25 V. The rate is -2.5 mV/V. The TEDs did not show any multiple-peaks after current instabilities. This is a major difference from the carbide tips. The physical significance of this difference is still under investigation.

Xu et al.^{3,30} speculated that there is an energy loss mechanism in the diamond. We note that the emission current increased from 2.3 nA to 8.6 nA when the extraction voltage was increased from 700 to 800 V. If the peak shift of 0.25 V is due to a resistive loss, the diamond film would have an equivalent resistance of about 40 M Ω for the 1000 Å film. This may be an estimate of the resistance of the conducting path within the diamond. While the mechanisms for all these features are still unknown, such changes in the TED with emission current can be important. An example is the use of diamond emitters in operations sensitive to the electron energy, such as in a low energy electron beam column.

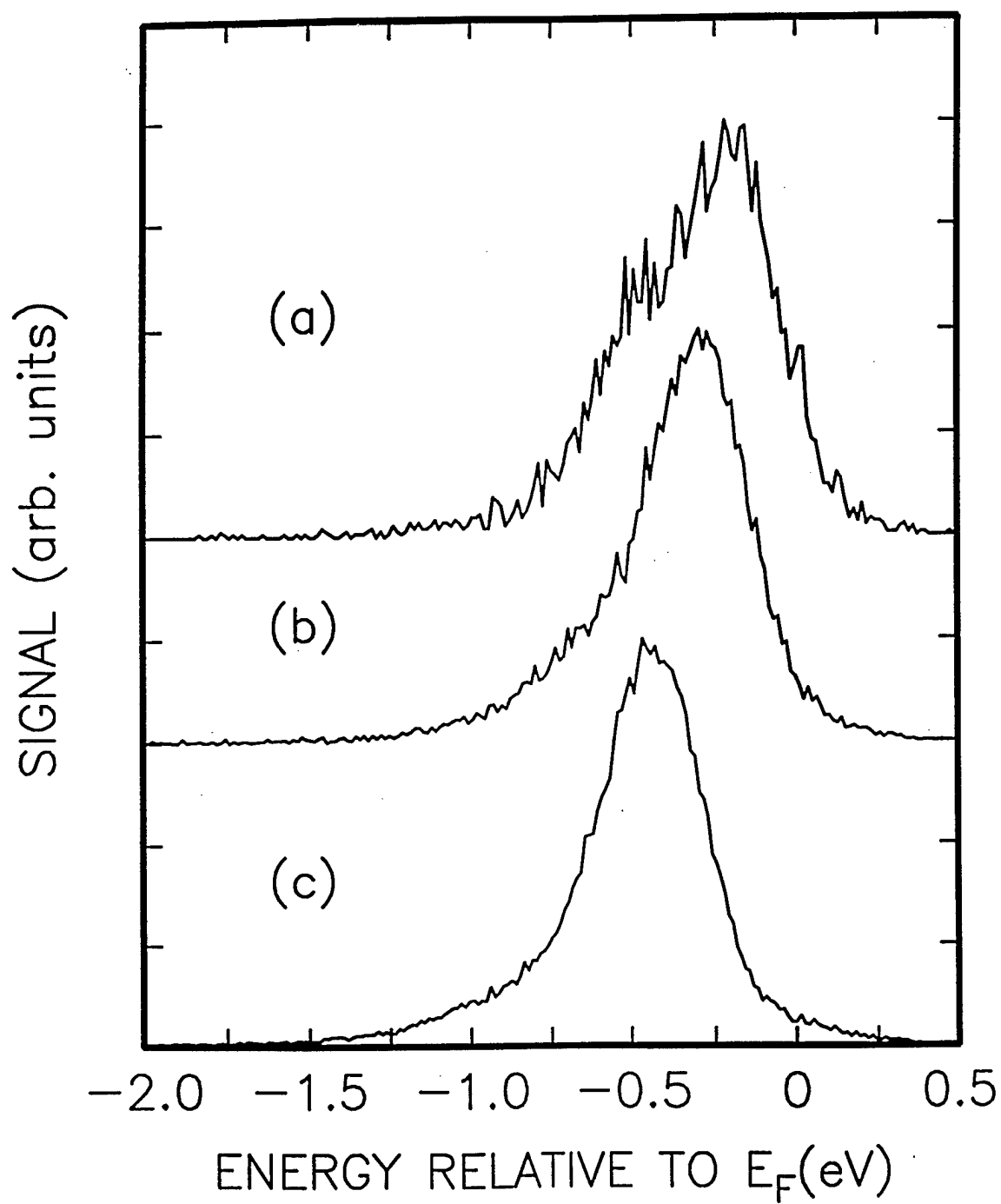


Fig. 3.14 Total energy distributions of field emitted electrons from diamond-like carbon coated tungsten tips. Curves (a) to (c) were obtained at extraction voltages of 700, 750, and 800 V respectively.

2.3.5 Schottky Electron Sources

2.3.5.1 A Miniature Schottky Electron Source

The miniature Schottky electron source consists of a Zr/O/W<100> tip mounted on a miniature filament enclosed in a suppressor cap. The entire assembly, as shown in Fig. 3.15, measures 4 mm in diameter by 13.7 mm in length. When used in the microcolumn, the emitter assembly is mounted in a miniature STM^{3,39} which provides an approximately 1 mm motion in x, y and z axes with sub-nm positioning capability to allow the tip to be aligned to a microlens. The complete source including the extractor electrode and the STM measures approximately 20 mm × 20 mm × 14 mm.

An important issue for such an electron source is the heat distribution. To reduce the heating power, the tip was mounted on a thinner 75µm tungsten diameter filament. It requires approximately 1.5 - 1.8 W of heating power to reach the operating temperature of 1800K as compared to 2.5 - 3.5 W for a conventional Schottky source mounted on a 125µm tungsten filament. Special attention has been given to reduce the heat flow from the emitter to the suppressor, the mini-STM, and the microlens. The temperatures of the source area were carefully measured with precision fine wire thermocouples during the tip operation. The temperature of the suppressor cap reached approximately 300 °C at a tip temperature of 1800 K (measured with an optical pyrometer). The emitter assembly including the suppressor cap was surrounded by a low thermal conductive material holder, such as a MacorTM tube, to reduce the heat flow from the source to the STM scanner. The temperature of the tube was about 200 °C at the operating temperature. The heating effect of such a source on the membrane extractor due to radiation and electron bombardment has been carefully examined. After prolonged tests at up to 100 µA of emission current, the microlens membrane remained intact.

2.3.5.2 Evaluation of a Miniature Electron Source

The miniature electron source has been tested in two modes. In the first mode, see Fig. 3.16(a), the test was performed with a silicon grid which consists of 1 µm × 1 µm holes on 3 µm centers in a thin silicon membrane of 1mm × 1mm size in the center of a silicon chip. This grid acts as an extractor electrode just as the actual extractor in the microcolumn would, while at the same time providing a highly transparent membrane to view the entire emission pattern. The tip is operated in close proximity, typically on the order of 100 µm, to such a grid. The entire emission pattern can then be viewed on a micro-channel-plate. Figure 3.16(b) and 3.16(c) are example of this mode of operation. The axial Schottky emission can be clearly distinguished from the four-

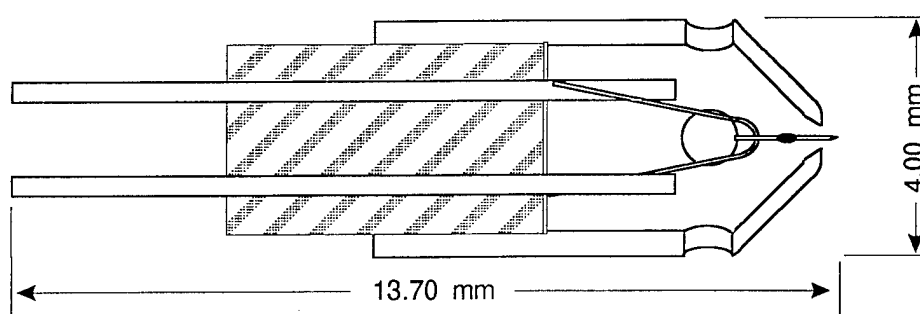
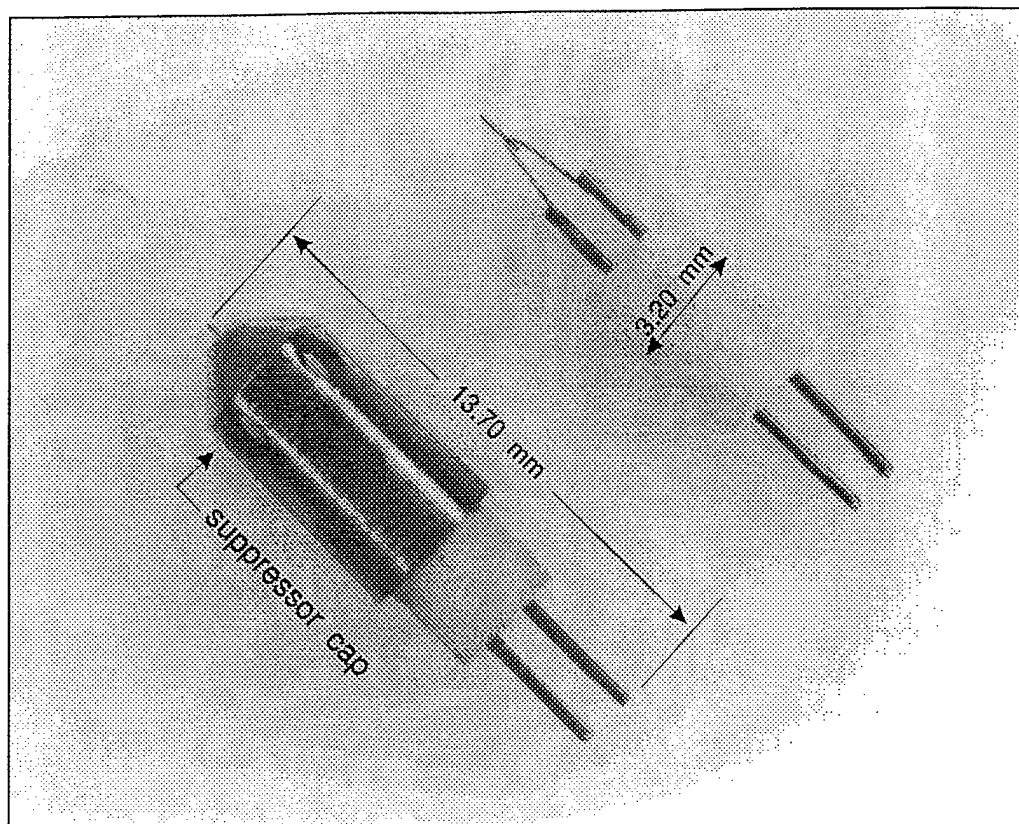


Fig. 3.15. A miniature Schottky electron source. The image at the top shows the emitter without the suppressor cap and the image at the bottom shows the emitter with the suppressor cap. The source is 4 mm diameter and 13.7 mm long. Note that a conventional Schottky source typically has a diameter of 17 mm and a length of 20 mm.

fold thermionic emission. The Schottky emission projects well defined images of the grid holes on the channel-plate showing that the emission must come from a point source. The fourfold thermionic emission pattern is consistent with the symmetry of the $W<100>$ orientation of the Schottky tip. The image, on the other hand, is very diffused and does not project sharply defined grid lines. This can be interpreted as emissions from relatively large planes on the shank of the tip rod as anticipated. Schottky emission patterns at different gap sizes between the emitter and the silicon grid are shown in Fig. 3.16(b) and 3.16(c). Reducing the gap size from 200 μm to 100 μm as shown here does not significantly affect the total emission angle which remains at about 6° semi-angle for both gap sizes.

In the second mode, the test was performed with an extraction electrode in the form of a planar silicon membrane with a small hole in the center. This represents the normal operating mode and is used to provide information on I/V characteristics, emission stability and angular current density. The effect of the suppressor has been studied to evaluate its effectiveness in suppressing the undesired thermionic electrons as shown in Fig. 3.17(a). It can be seen that varying the suppressor voltage from 0 to -100 V, a very large change in emission current occurred. However, when the suppressor voltage was increased from -100 V to -400 V, a relatively small decrease in total emission current was observed which indicates that the thermionic emission has been effectively suppressed. This range of suppressor voltage can therefore be considered as an effective operating range for the source.

A Faraday cup was placed behind the extractor hole to measure the probe current. From the distance of the extractor and the tip, the solid angle subtended by the Faraday cup can be determined thus allowing the angular current density to be derived. Figure 3.17(b) shows the total emission current and angular current density at different suppressor voltages for an 0.8 μm radius tip operating at a 200 μm gap. The data shows that changing the suppressor voltage from -200 to -300 V can cause a noticeable reduction in the total emission current, but has little effect on the angular emission density. An angular current density of approximately 100 $\mu\text{A}/\text{sr}$ has been achieved with a total emission current of 130 μA at 1800 K in this case.

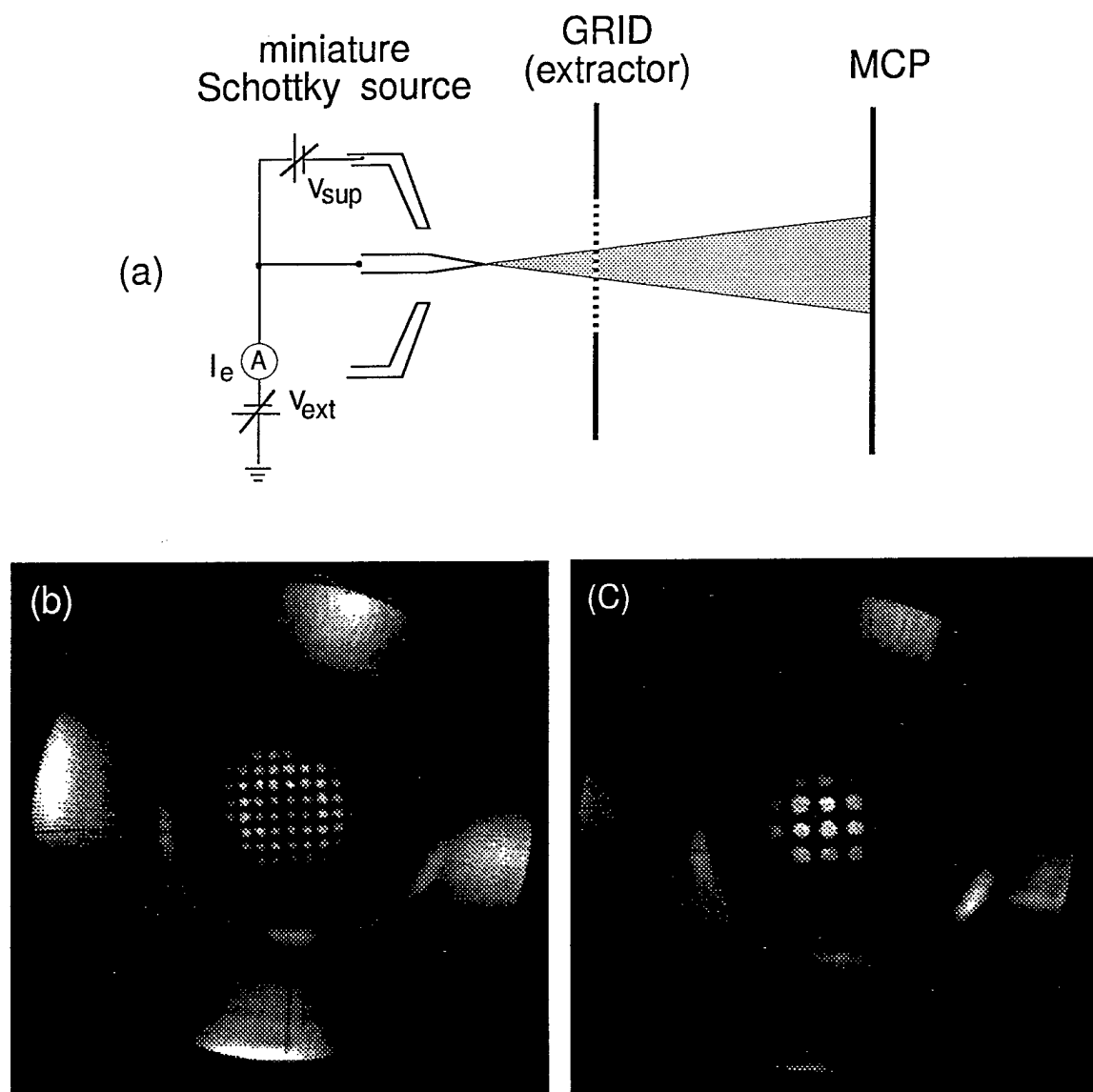


Fig. 3.16. (a) Schematic diagram of the test modes for the miniature Schottky electron source. Emission patterns of the source with a grid as extractor show both the Schottky (center bright part) and thermionic emission using (b) a 200 μm and (c) a 100 μm gap between the tip and the silicon grid at the same suppressor voltage of -300V. The grid consists of 1 $\mu\text{m} \times 1 \mu\text{m}$ holes on 3 μm centers in a thin silicon membrane of 1mm \times 1mm size in the center of a silicon chip.

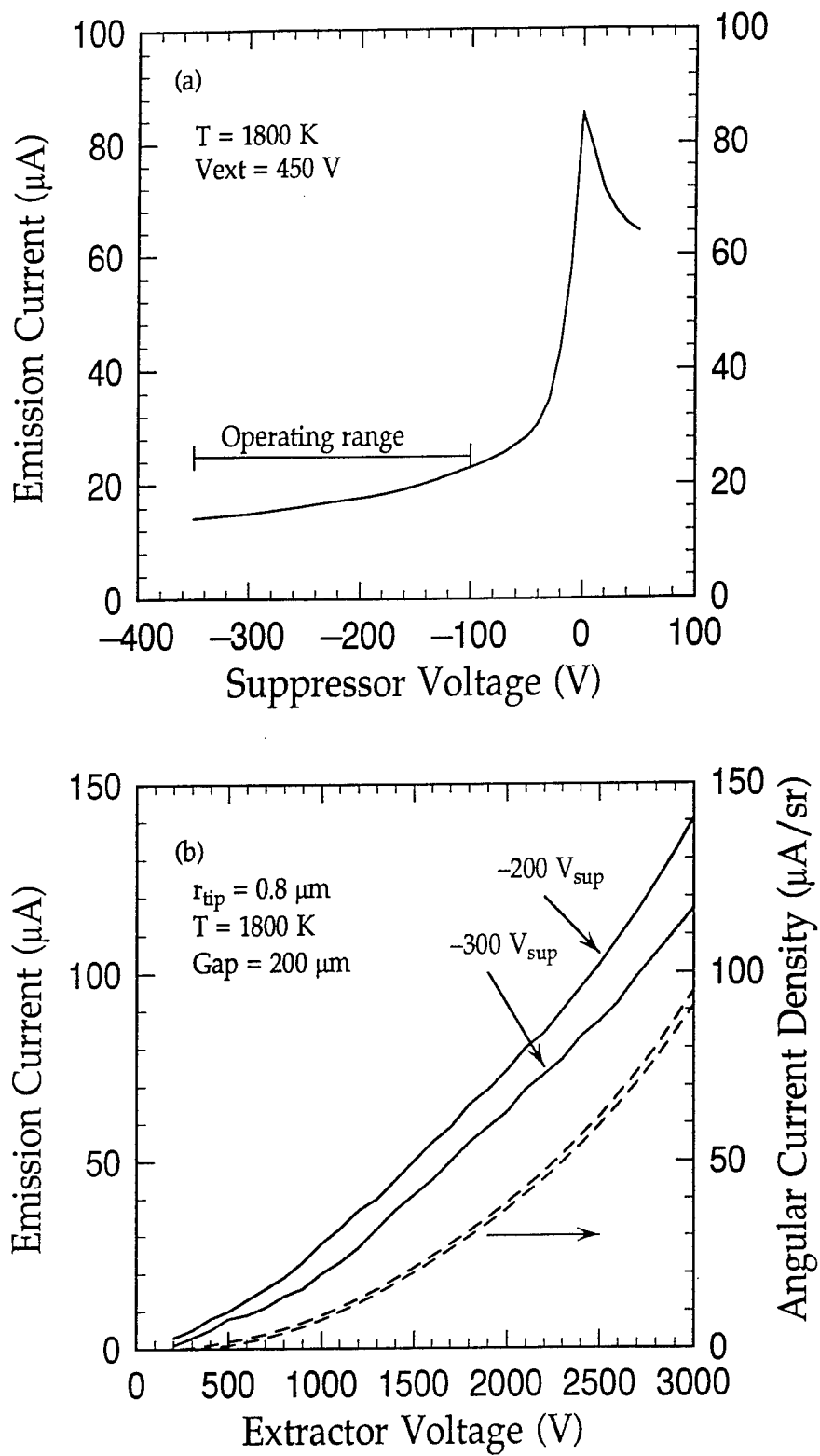


Fig. 3.17. (a) Suppressor voltage effect on the total emission current from the emitter. (b) Emission (solid lines) and angular current density (dashed line) of $0.8 \text{ }\mu\text{m}$ radius Schottky emitter ($T = 1800 \text{ K}$) at a $200 \text{ }\mu\text{m}$ gap between tip and extractor with different suppressor voltages.

2.3.5.3 Energy distributions of Zr/O/W Schottky electron emission

2.3.5.3.1 Introduction

The energy distribution of electron emission from an electron source is an important issue for low energy electron beam systems,^{3,28} because the energy spread affects the final beam size through chromatic aberrations. Two types of electron emitter are of interest: cold field emitters operating at a temperature of 300 K, and Zr/O/W Schottky emitters^{3,40} operating typically at 1800K. While the energy distribution measurements for cold field emitters have been reported,^{3,41-3,45} the corresponding measurements for Schottky emitters have not been as well studied.^{3,11,3,46-3,48} The Schottky emission cathode most commonly used is a ZrO coated <100> oriented tungsten emitter. The ZrO reduces the work function of W(100) from 4.5 eV to 2.8 eV.^{3,41,3,46} The Schottky emitter needs to be operated at a high temperature, such as 1400 K - 1800 K, to obtain Schottky emission.^{3,40} It has a larger energy spread when compared to a cold field emitter at a given angular emission current density.^{3,4,3,48} However, Schottky emitters have a much more stable emission current than the cold field emitters due to the lower electric fields and the larger and more stable emitting areas.^{3,46,3,49,3,50}

In this report we present detailed experimental measurements of the energy distributions of the emitted electrons from Schottky emitters as functions of tip temperature and angular emission current density. The measurement results have been compared with the theoretical predictions. We also discuss the relation between the height of the surface energy barrier and the measured energy distribution.

2.3.5.3.2 Theory

Figure 3.1 depicts a diagram of the energy levels for field emission and Schottky emission. Unaided, the electrons in cold field emitters cannot overcome the work function barrier ϕ_{FE} . Instead, a strong field F_{FE} is applied and emission occurs by electron tunneling through the barrier with total energy equal to or slightly less than the Fermi energy E_{FE} . Note that the barrier height is reduced by the action of the field.

If the cathode temperature is increased, the Fermi distribution is broadened at the Fermi level. Some electrons will have energies above the Fermi level, and these will more readily tunnel through the barrier, and a lower external field will be required. At sufficiently high temperatures, some electrons will have enough energy to pass above the lowered barrier. This is known as Schottky emission. The temperature at which Schottky emission occurs can be much reduced by using a cathode such as oxygen

processed Zirconium tungsten which has a work function lower than that of pure tungsten.

The current density, j_{SE} , for Schottky emission with a work function barrier, ϕ_{FE} , is approximately.^{3.51}

$$j_{SE} = A_R (k_B T_c)^2 \exp \left[- \frac{\phi - \Delta\phi}{k_B T_c} \right] \quad (3.1)$$

where $\Delta\phi = (e^3 F / 4\pi\epsilon_0)^{1/2}$, A_R is the Richardson constant, k_B is the Boltzmann constant, T_c is the tip temperature, F is the electric field at the tip surface, and ϵ_0 is the permittivity constant. The current density is very strongly dependent on the tip temperature and the field at the surface, and a small change in tip temperature can cause a large change in the current density. We note that

$$\Delta\phi = (e^3 F / 4\pi\epsilon_0)^{1/2} = 3.79 F^{1/2} \text{ eV} \quad (3.2)$$

with F expressed in $V/\text{\AA}$, represents the lowering of the barrier height brought by the applied field. As a result, the peak of the energy distribution shifts to the lower energy side with increasing applied field.^{3.52-3.54}

At the surface of an actual tip, $\Delta\phi$ equals $3.79(V/\beta r)^{1/2}$, where V is the applied voltage, r is the tip radius, and β is the form factor which depends on tip-anode geometry and emitter shape. It is difficult to determine the form factor for Schottky emitters,^{3.41} because the presence of the suppressor and the proximity of the extractor might have changed the value. However, by assuming β to be 5,^{3.18} one can estimate the effective tip radius at a temperature and the change of work function between two temperatures from a Schottky plot ($\ln(I)$ vs $V^{1/2}$), where I is the total emission current.^{3.54} The Schottky line is expressed by $\ln(I) = \phi/k_B T - 3.79 F^{1/2}/k_B T$ obtained from Eq. 3.1. Figure 3.18 shows Schottky emission from a 0.3 μm radius tip at 1800 K, 1700 K, and 1450 K. The experimental data were obtained with special care to allow the emission to reach the stability after each change of the extraction voltage and temperature. The measurements at each temperature are compared with the theoretical predictions in solid lines in Fig. 3.18, showing good agreement.

The normalized total energy distribution of thermally emitted electrons from a metal is approximately given by^{3.51}

$$j_0(E) = \frac{E}{(k_B T_c)^2} e^{-\frac{E}{k_B T_c}} \quad (3.3)$$

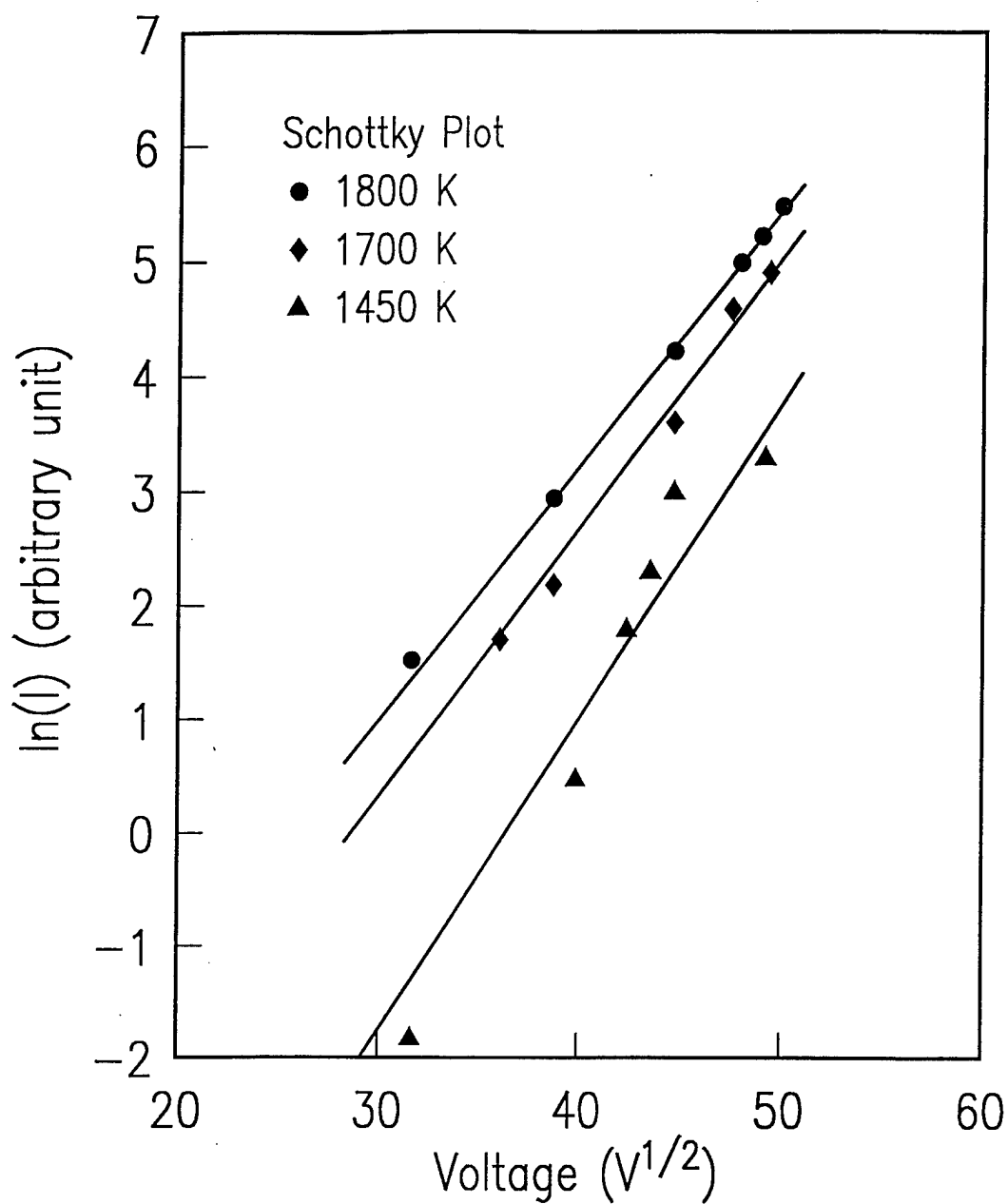


Fig. 3.18. Schottky plots ($\ln(I)$ vs $V^{1/2}$) of data measured at three tip temperatures. The solid lines represent Schottky lines from Eq. 3.1 at each temperature using a work function of 2.8 eV. We also measured the energy distribution at each data point. These are shown in Fig.3.19, 3.20, and 3.21.

where E is the energy measured from the top of the surface potential barrier. The formula shows the dependence of the energy distribution of the emitted electrons on the tip temperature. Only electrons with energy above the top of the potential barrier contribute to the emitted current. From this equation, the most probable energy, corresponding to the maximum of the distribution, is $E_p = k_B T_c$. It shows that the position of the peak of the energy distribution changes with the tip temperature.^{3,52} The full width at half maximum (FWHM) of the energy distributions is $\Delta E = 2.45 k_B T_c$. Thus, for a tip temperature of 1800 K, the FWHM will be 0.38 eV. It applies only at low emission current densities. Therefore, by measuring the energy distribution at very low emission current densities, we have a way to determine in-situ the operating temperature of the Schottky tip. This temperature could then be compared with that measured by an optical pyrometer. The agreement has been good as shown in Fig. 3.18. At higher emission densities, the energy distribution is also affected by electron tunneling and electron-electron interaction which increase with increasing angular emission current densities.^{3,10,3,48}

2.3.5.3.3 Experimental Setup

The focus of this study is the energy distribution of the emitted electrons from a Schottky emitter and the effects of tip temperature and angular current densities. The measurements of the energy width from a Schottky emitter have been conducted at a tip temperature ranging from 1450 K to 1800 K, and an angular current density from 0.1 $\mu\text{A/sr}$ to 240 $\mu\text{A/sr}$. We have measured energy distributions using a VSW HR-50 hemispherical electron energy analyzer with a resolution of about 55 meV. The Schottky electron source consists of a Zr/O/W<100> tip mounted on a filament, enclosed in a suppressor cap to reduce the number of thermionically emitted electrons from the filament and the shank of the tip. The tip is operated in close proximity, on the order of 100 μm , to an extraction electrode. Following the extractor is a phosphor screen which also acts as the ground plane of the analyzer. A small probe hole in the phosphor screen allows about 0.8 msr of electron emission from the Schottky emission source to pass through to the analyzer. The emitter was biased at -1 kV with respect to the ground of the analyzer. The extractor voltage is the voltage difference between the emitter and the extractor. With this arrangement, no change in the emitter voltage and analyzer setting was necessary when we studied the shift of the energy distributions with different extraction voltage and tip temperature.

2.3.5.3.4 Results and Discussion

A sequence of measurements of the energy distributions as a function of angular emission current density (J_α), which varies with the extraction voltage (V_{ext}), is shown in Fig. 3.19, 3.20 and 3.21 at three temperatures of 1800K, 1700K, and 1450K respectively. The distributions are normalized along the y-axis for clarity. At 1800 K, Figures 3.19(a) to 3.19(e) depict the energy distributions with increasing angular emission densities. The dashed line of each curve shows theoretical calculation of thermionic emission from Eq. 3.3. At the lowest angular current density of about 19 $\mu\text{A}/\text{sr}$ as shown in Fig. 3.19(a), a measured FWHM is about 0.54 eV. The energy peak of the theoretical curve is numerically matched with the maximum peak of the measured data. The shape of the energy distribution follows theoretical thermionic emission well on the higher energy side, but differs considerably from the thermionic shape on the low-energy side. As we reported previously,^{3,48} we suspect that the electron tunneling at the top of energy barrier mostly contributes to the energy broadening on the low-energy side. Figure 3.19(b) depicts an energy distribution with a FWHM of about 0.85 eV at an angular current density of 69 $\mu\text{A}/\text{sr}$. The shape shows modification of the energy distribution on both the high- and low-energy sides. We suspect that both the tunneling effect and electron-electron scattering are taking place. The electron tunneling mainly contributes to the total energy broadening on the low energy side, but a small effect of the electron-electron scattering seems to appear on the high energy side. In Fig. 3.19(c) to 3.19(e), the shapes of the energy distribution are clearly broadened on both the high- and low-energy sides at increasing angular current densities. Both electron tunneling and electron-electron scattering clearly contribute to the energy broadening at these high angular current densities. The effect of the electron-electron scattering seems to increase rapidly at $J_\alpha \geq 100 \mu\text{A}/\text{sr}$.

The position of the peak of the energy distribution changes gradually with the tip temperature and the electric field.^{3,53} From the Eq. 3.3, one can estimate the changes from the effect of the tip temperature. For example, with a change in tip temperature from 1800 K to 1450 K, the peak position shifts about 0.03 eV. In our experiment, the effect of the temperature for the change of the energy peak position is negligible due to the limited resolution of our analyzer.

We approximate the top of the effective energy barrier by the low point of the low-energy side in the theoretical curve shown in Fig. 3.19(a). With the value for the tip radius determined at 1800 K from Fig. 3.18, we calculate the shift of the effective energy barrier with the extraction voltages. These are presented as dashed curves to compare with the experimentally observed energy distribution at each angular current

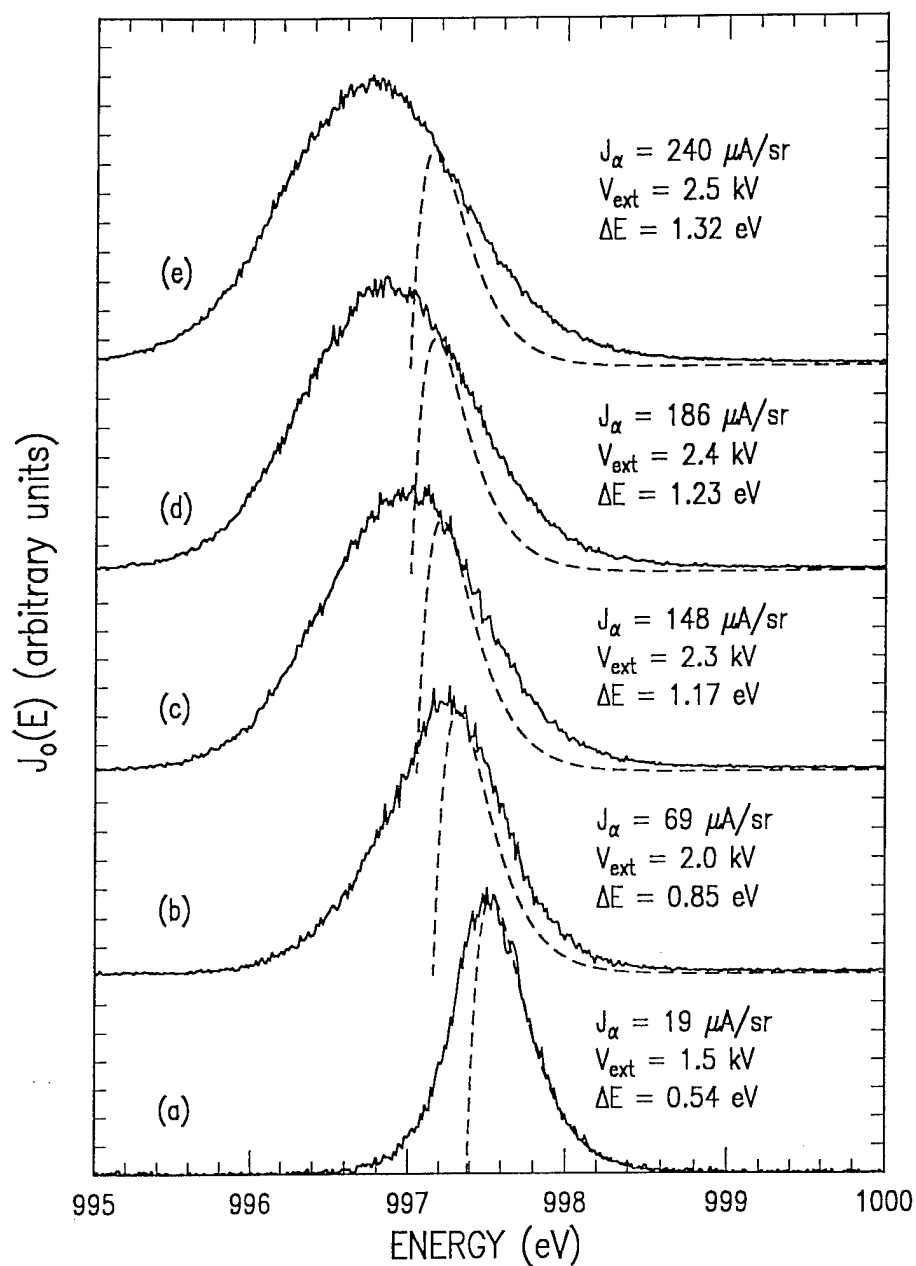


Fig. 3.19. Energy distributions of Schottky emission measured at a tip temperature of 1800K. The calculated energy distributions (dashed lines b-e) are shifted relative from line (a) using Eq. 3.2. The energy width (ΔE), angular emission current density (J_α), and applied extraction voltage (V_{ext}) are shown on the right side of each curve.

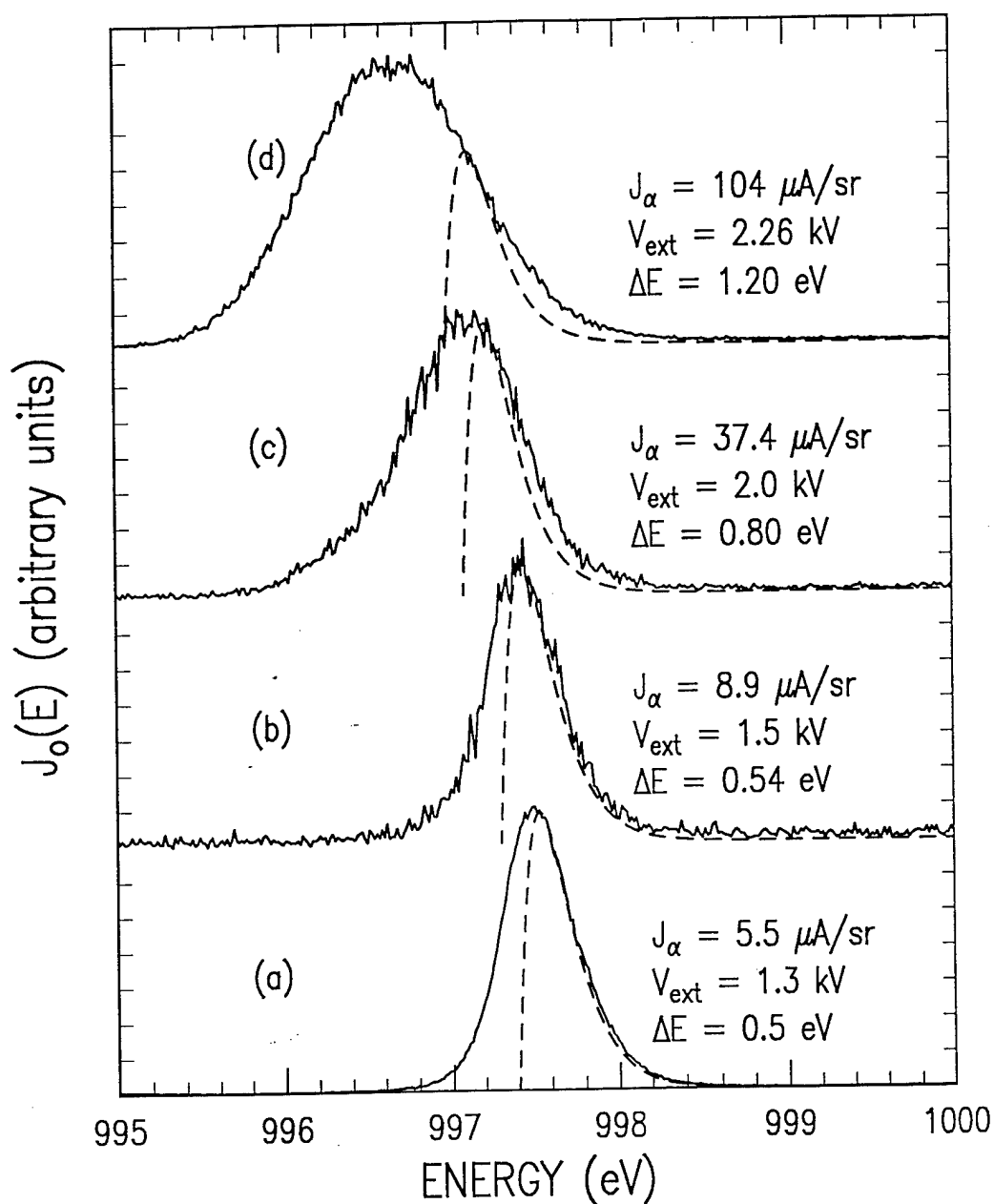


Fig. 3.20. Energy distributions of Schottky emission measured at a tip temperature of 1700K. The calculated energy distributions (dashed lines b-d) are shifted relative from line (a) using Eq. 3.2. The energy width (ΔE), angular current density (J_α), and applied extraction voltage (V_{ext}) are shown on the right side of each curve.

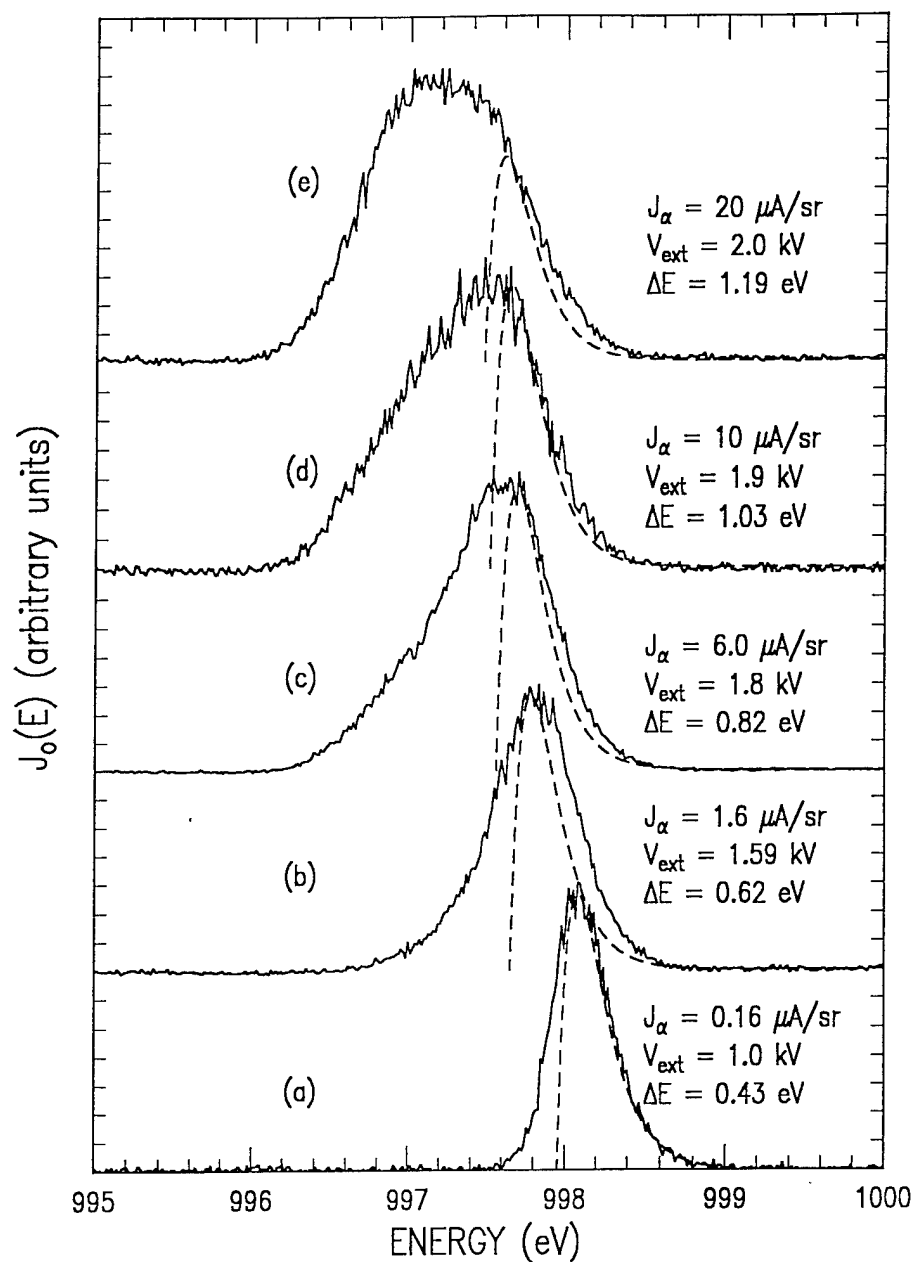


Fig. 3.21. Energy distributions of Schottky emission measured at a tip temperature of 1450K. The calculated energy distributions (dashed lines b-e) are shifted relative from line (a) using Eq. 3.2. The energy width (ΔE), angular current density (J_α), and applied extraction voltage (V_{ext}) are shown on the right side of each curve.

density. The calculated shift rates are in good agreement with the experimental data at low angular current densities, as shown in Fig. 3.19(a) and 3.19(b). However, we notice that the positions of the peaks of the energy distribution do not agree with those of the theoretical energy distribution at higher angular current densities. An explanation is that the increase of the electric field lowers the barrier and also decreases the width of the tunneling barrier.^{3.18,3.53} As a result, probably more electrons penetrate through the barrier than over the top of the barrier. Therefore, the energy peak of the distribution is broadened toward to the low energy side. This phenomenon occurs clearly at lower temperatures as shown in Fig. 3.20 and 3.21. Previous studied in experimental measurements^{3.11,3.52} and theoretical calculations^{3.53} have also shown similar results.

Figure 3.20 shows the energy distributions at a tip temperature of 1700 K with increasing angular current densities. We observe the similar changes of the energy distribution's shape as previously discussed for a tip temperature of 1800 K. However, the energy distributions at 1700 K seem to be more broadened than those at 1800 K at the same angular current density. This phenomenon is more apparent at lower temperatures as shown in Fig. 3.21.

Figure 3.21 shows the energy distributions measured at a tip temperature of 1450 K. Figure 3.21(a) shows a energy distribution at an angular current density of $0.16 \mu\text{A}/\text{sr}$ with a FWHM of 0.43 eV. The energy distribution follows the theoretically calculated energy spread of thermionic emission (dashed line) well on the higher energy side. Figures 3.21(b) and 3.21(c) at $1.6 \mu\text{A}/\text{sr}$ and $6 \mu\text{A}/\text{sr}$ respectively change rapidly on the low-energy side with increasing an angular current density, while these distributions still follow the theoretically calculated energy spread of thermionic emission. In Fig. 3.21(d) and 3.21(e) with an angular current density of $10 \mu\text{A}/\text{sr}$ and $20 \mu\text{A}/\text{sr}$ the shapes change at both low- and high-energy sides. It is due to the effects of the electron tunneling and electron-electron scattering. Obviously, the energy spread at 1450K is larger than that at 1700 K and 1800K at the same angular current density. For instance, it is clearly shown in Fig. 3.19(a), and 3.21(e) which have the same angular current density of about $20 \mu\text{A}/\text{sr}$, the energy spread at 1450K is 1.2 eV FWHM compared to 0.54 eV FWHM and 1800 K. It indicates that there is more contribution from electron tunneling at 1450K, because the emitter at the lower temperature requires a higher electric field to obtain the same angular emission current density than at the higher temperature.

We have also observed that the energy distributions at the same extraction voltage (1.5 kV) and different temperatures have a similar shape and width as shown in Fig. 3.19(a) and 3.20(b). It is probably because the electric field is not changed. The

widths of the energy distributions at both temperatures follow that of thermionic emission because the contribution from electron tunneling does not change. However, the distribution at 1450 K, shown in Fig. 3.21(e), is broader than those at higher temperatures (Fig. 3.19(b) and 3.20(e)), although they have the same extraction voltage of 2.0 kV. We suspect that there are changes of the work function and the effective tip radius at 1450 K. The Schottky plot shown in Fig. 3.18 also shows a similar symptom at lower temperatures.

Figure 3.22 shows a comparison of the measured energy width at three temperatures with that of Monte Carlo simulations. The simulations allow the inclusion of electron tunneling and electron-electron interactions into the electron emission process.^{3,10} The lines represent theoretical predictions of the energy width from a 0.3 μm radius Schottky emitter at three values of tip temperature and angular current densities from 0.1 $\mu\text{A}/\text{sr}$ to 100 $\mu\text{A}/\text{sr}$. Electric fields of 0.01 $\text{V}/\text{\AA}$ to 0.14 $\text{V}/\text{\AA}$ at 1800K were applied to obtain the theoretical data. In addition, the measurements of the energy width from a 0.3 μm radius Schottky emitter are also shown. The results are in very good qualitative agreement with theoretical calculations of the width. The energy widths of both theoretical and experimental results increases with increasing angular current density. It also shows that the energy width increases with decreasing tip temperature. Specifically, we compare the values for 1800 K operation in Table II. At a low angular emission current of 0.1 $\mu\text{A}/\text{sr}$, the theoretical calculation shows an energy width of 0.39 eV, which is very close to the value for thermionic emission from Eq. 3.3. It means that there are no effects to broaden the energy distribution. However, with increasing angular emission current density, the electron tunneling is increased. A small effect of electron-electron scattering also appears. At an angular current density of 100 $\mu\text{A}/\text{sr}$, the proportion of the electron-electron scattering is larger than at lower angular current densities. The results are in good agreement with the experimental data shown in Fig. 3.19.

2.3.6 Summary

1. A new technique for the preparation of field emitter tips for use in a STM aligned field emission microcolumn has been developed. The oxygen induced tip sharpening process was identified as an effective method for microcolumn tip preparation, and can be used to control tip radius very accurately. The tungsten removal rate of the process depends on temperature and oxygen pressure. This process forms a distinctively faceted tip with a 0° angle and 1.5 μm length shank. This technique can be applied to a newly etched tip as well as to a damaged or blunt tip.
2. Room temperature field emitters suffer from emission current instability. Hafnium carbide and diamond-like cathodes were investigated because their great mechanical

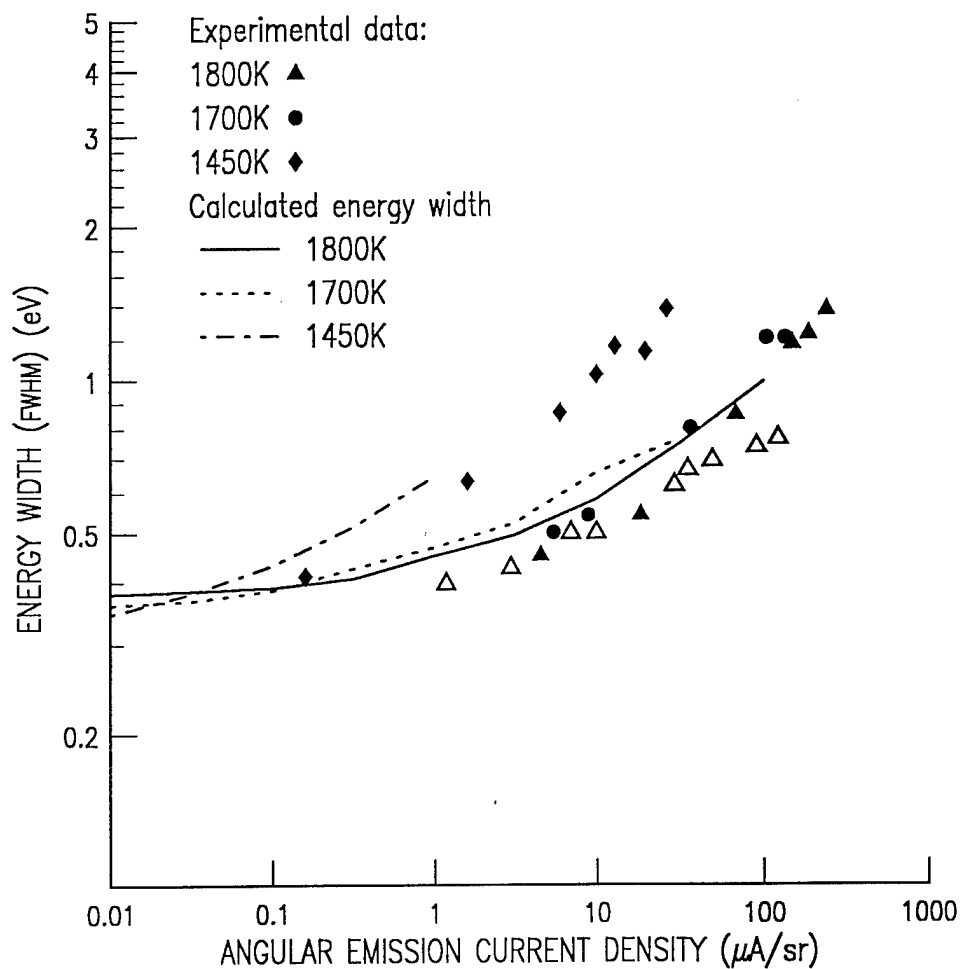


Fig. 3.22. Theoretical predictions and experimental measurements of the energy width for a $0.3 \mu\text{m}$ radius Schottky emitter at three values of the tip temperature (1450K, 1700K, 1800K) and angular current densities from $0.1 \mu\text{A}/\text{sr}$ to $240 \mu\text{A}/\text{sr}$. The results show that the energy width increases with increasing angular current density, and decreasing tip temperature. The open triangles are data points from reference.^{3,48}

Table II. Comparison of energy widths of the theoretical predictions and experimental measurements.

Cathode	J_α ($\mu A/sr$)	ΔE_1 (eV)	ΔE_2 (eV)	$\Delta E(\text{ exp})$ (eV)
Zr/O/W<100> 1800 K	0.1	0.39	0.39	
	1	0.43	0.45	0.40
	10	0.56	0.58	0.50
	70			0.85
	100	0.88	0.99	
	140			1.17

ΔE_1 : Energy width including the tunneling effect only.

ΔE_2 : Energy width including the tunneling effect and electron-electron interactions.

$\Delta E(\text{ exp})$: Energy width of the experimental measurement.

stabilities may prevent emission current fluctuations caused by atomic motion. Much improvement over single-crystal tungsten was observed, but they are still not as stable as Schottky emitters.

3. A miniature Schottky electron source has been developed and evaluated for application in a new generation of STM aligned field emission (SAFE) microcolumns. The optimum operation of a Schottky emitter has been obtained from the results of these measurements. The miniature Schottky emitters are now in routine use in the microcolumn showing consistently good stability and high angular emission intensity.^{3,10}
4. We have presented the detailed energy distribution measurements of emitted electrons from a Schottky emission source. The tip temperature and angular current

density of the emitter can both affect the energy broadening. The experimental measurements of the energy width are in very good agreement with theoretical predictions. A decrease of the tip temperature increases the energy width at the same current density due to the tunneling effect and electron-electron interactions. At 1800K, the energy widths at a low angular current density ($\leq 1.0 \mu\text{A}/\text{sr}$)^{3,7} are essentially the same as the widths for thermionic emission. The energy widths at intermediate current densities ($1.0 \mu\text{A}/\text{sr}$ to $\leq 100 \mu\text{A}/\text{sr}$) are broadened mostly by electron tunneling effects at the top of the energy barrier. At higher current densities ($\geq 100 \mu\text{A}/\text{sr}$), the energy widths are broadened by both electron tunneling effects and electron-electron interactions. There is more energy broadening at lower temperatures than at higher temperatures. This is because the emitter requires a higher electric field to reach the same angular current density, and a higher field causes more electron tunneling effects.

2.3.7 Acknowledgments

We acknowledge S.J. Wind, D. Rathkey, G. Schwind, and J. Orloff and S.M. Gates for useful discussions.

2.4 Microlens and Column Fabrication

2.4.1 High aspect ratio aligned multilayer microstructure fabrication

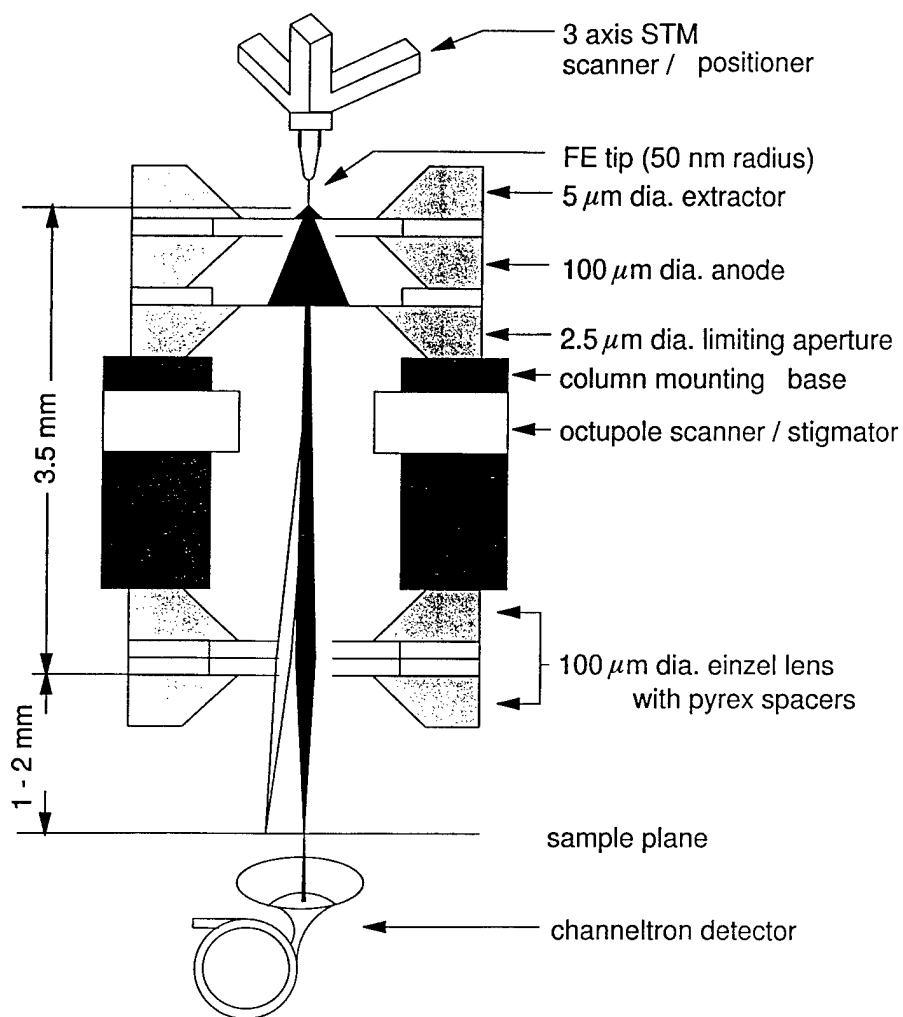
2.4.1.1 Introduction

Silicon micromechanical technology based on standard silicon microcircuit fabrication techniques has enabled sophisticated micromechanical structures to be made. The fabrication of truly high aspect ratio three-dimensional microstructures, such as electron microlenses for microcolumns requiring precisely aligned structures of millimeter heights, is currently beyond the scope of standard silicon technology. One approach for realizing such 3-D structures is by stacking together 2-D structures. The requirements for this are (1) the ability to accurately align the different 2-D layers, and (2) the ability to bond the layers together reliably with a high degree of parallelism. We have developed such a method for building very high aspect ratio multilayer microstructures based on anodic bonding of silicon and Pyrex^{4.1} glass. This technique can be used in a wide variety of applications such as packaging, micromechanical devices, 3-D VLSI and optoelectronic devices. An application of this technique for building fully functional microlenses is described here. In particular, we focus on the fabrication of the electron gun electrodes and the einzel microlenses as contained in a 1 kV electron-beam microcolumn as shown in Fig. 4.1.

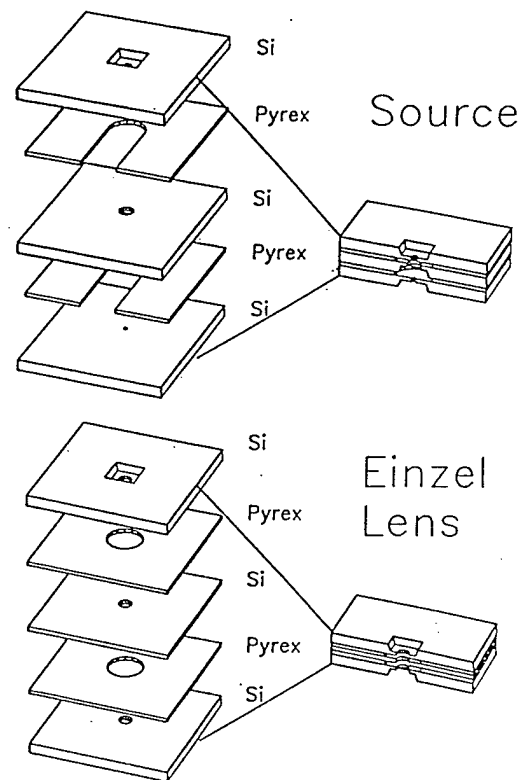
Our microlenses comprise micro-electron-optical components spaced apart by 100-250 μm thick insulating spacers. The micro-electron-optical components are either microelectrodes or apertures with 1-200 μm diameters. For optimal resolution, the roundness and the roughness of the micro-electron-optical components are required to be in the nanometer regime and alignment accuracy between components on the order of 1 μm . The assembled columns have to be compatible with ultra-high vacuum. These requirements are met by using (1) silicon fabrication technology to form micro-electron-optical components on silicon membranes, (2) Pyrex glass spacers which facilitate anodic bonding, and (c) optical microscopy to align the components.

2.4.1.2 Micro-Electron-Optical Components Fabrication

Micro-electron-optical components are 1-200 μm diameter apertures or microelectrodes. These are made from 1-1.5 μm thick silicon membranes by electron-beam lithography and reactive-ion etching (RIE). The fabrication steps are shown schematically in Fig. 4.2. The starting material is a 100 mm diameter and 500 μm thick double sided polished wafer containing arrays of 7×7 mm chips. At the center



(a)



(b)

Fig. 4.1 (a) cross-sectional view of an IBM 1 keV Microcolumn based on STM Aligned Field Emission (SAFE) (after Kratschmer et al⁴), and (b) perspective views of the source and einzel lens

of each chip is a 1×1 mm membrane formed by wet isotropic etching using either a highly boron doped^{4.2} or a reverse-biased p/n junction etch stop.^{4.3} The wafer is first cleaned in 8:1:1 $\text{H}_2\text{SO}_4:\text{H}_2\text{O}_2:\text{H}_2\text{O}$ and then primed with HMDS before being coated with a layer of 1 μm thick KRS resist. KRS^{4.4} is an electron-beam positive tone chemically amplified resist which provides the advantages of very high resolution and high aspect ratio patterning, and very high RIE resistance. The resist is baked in an oven at 110°C for 5 minutes before electron-beam exposure at 50 kV using a base dose of 30 $\mu\text{C}/\text{cm}^2$. Each chip is exposed with one of the following patterns; a single 1 or 2.5 μm circle (for limiting apertures) a single 100 or 200 μm circle (for anodes in source and for electrodes in einzel lenses) with alignment marks, or single 1-5 μm circle with alignment marks (for extractor electrodes in source). After exposure the wafer is developed in 0.15N TMAH (tetra-methyl ammonium hydroxide) for 85 s.

Next, the silicon wafer is reactive-ion etched in $\text{SF}_6/\text{CBrF}_3$ using the developed KRS layer as the mask. The RIE is performed at 20 mTorr with a gas flow rate of 3.5:18.5 sccm $\text{SF}_6/\text{CBrF}_3$. At a power of 150W, the average silicon and KRS etch rates are 0.1 and 0.01 $\mu\text{m}/\text{minute}$ respectively. The high etch selectivity obtainable with KRS allows holes to be etched through the silicon membranes from the masked surface. This was not possible previously when a multilayer mask of PMMA on silicon oxide was used.^{4.5} Due to lack of RIE selectivity, additional blanket etching on the back surface of the silicon membrane was necessary in order to etch the holes through. This restricted the final membrane thickness to less than 1 μm .

The vertical developed KRS profile [Fig. 4.3(a)] combined with very small lateral KRS erosion during the RIE step result in very vertical etched profiles. After the RIE step the wafer is broken into individual 7×7 mm chips. The remaining resist is stripped in hot NMP (n-methyl pyrrolidinone) followed by O_2 ashing. Prior to the assembly step below, the chips are cleaned in 8:1:1 $\text{H}_2\text{SO}_4:\text{H}_2\text{O}_2:\text{H}_2\text{O}$ and then etched in buffered HF. Figures 4.3(b) and 4.3(c) are SEM micrographs of an extractor microelectrode. The V-shaped marks are used for alignment and for positioning the field emission tip. The roughness on the sidewalls after etching is less than 10 nm [Fig. 4.3(c) and 4.3(d)].

2.4.1.3 Microlens Assembly

The microlens assembly involves stacking together the silicon micro-electron- optical components and Pyrex glass spacers [Fig. 4.1(b)]. Central to this is a precisely aligned multilayer anodic bonding process which we have developed.

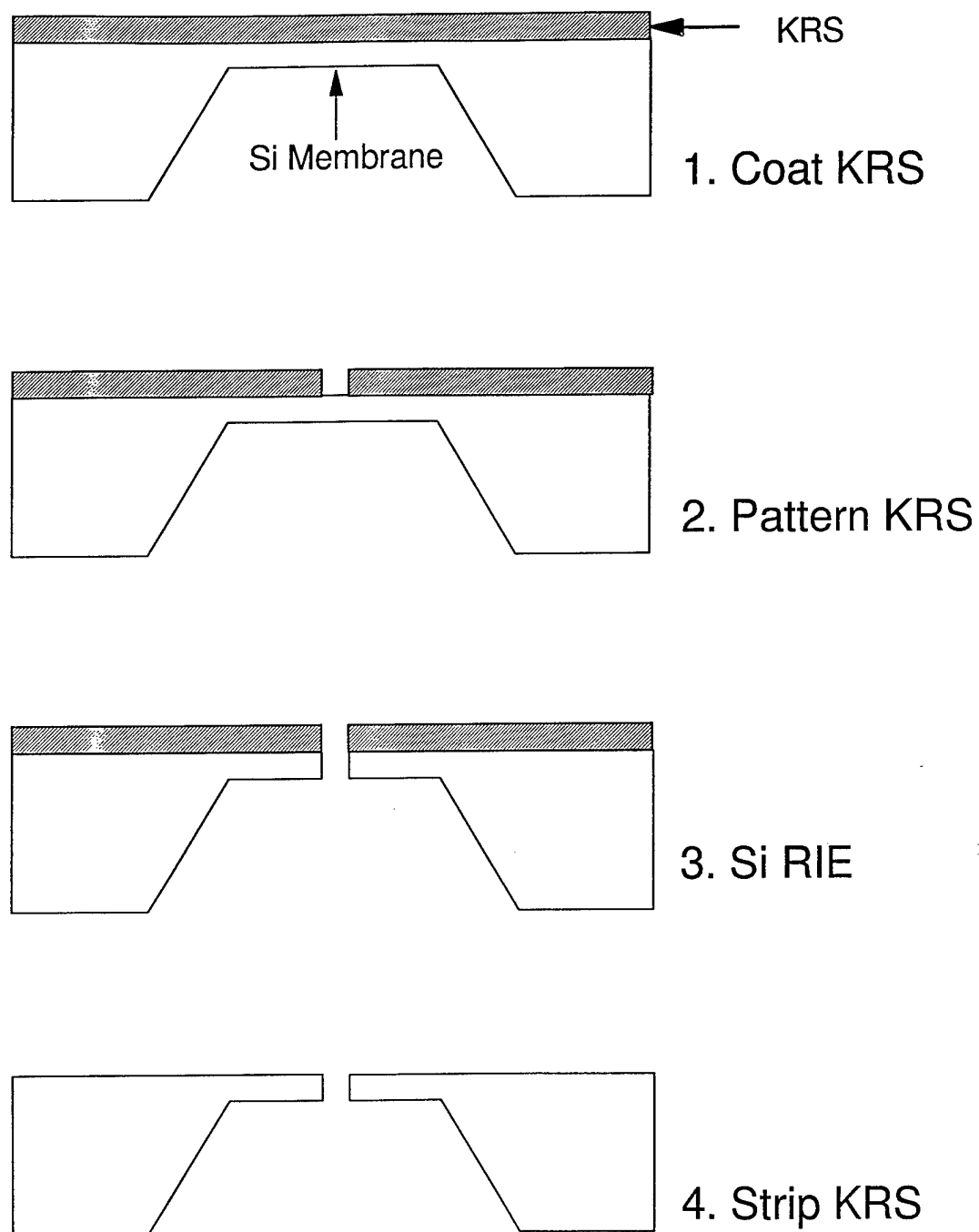
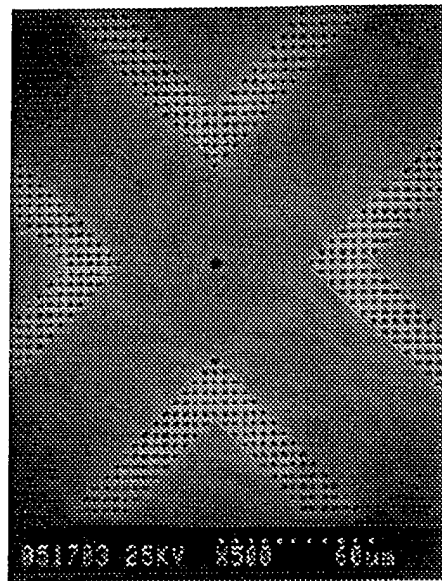


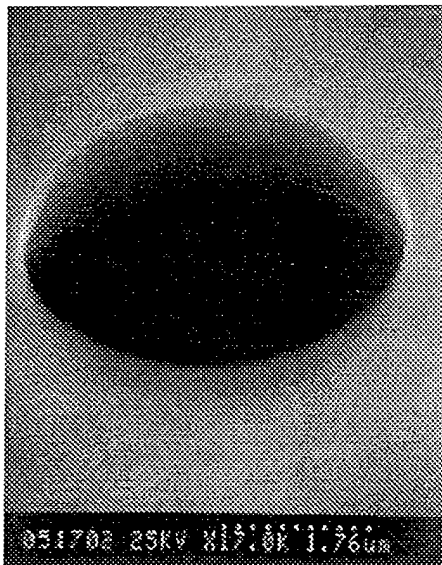
Fig. 4.2 Schematic illustration of the silicon micro-electron-optical component fabrication steps.



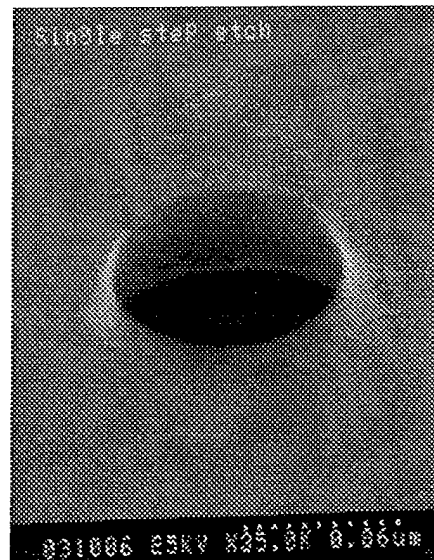
(a)



(b)



(c)



(d)

Fig. 4.3 SEM micrographs showing (a) KRS developed profile, (b) the extractor electrode consisting of a 5 μm hole and alignment marks, (c) tilted image of the 5 μm extractor showing very smooth sidewalls, and (d) a 1 μm limiting aperture.

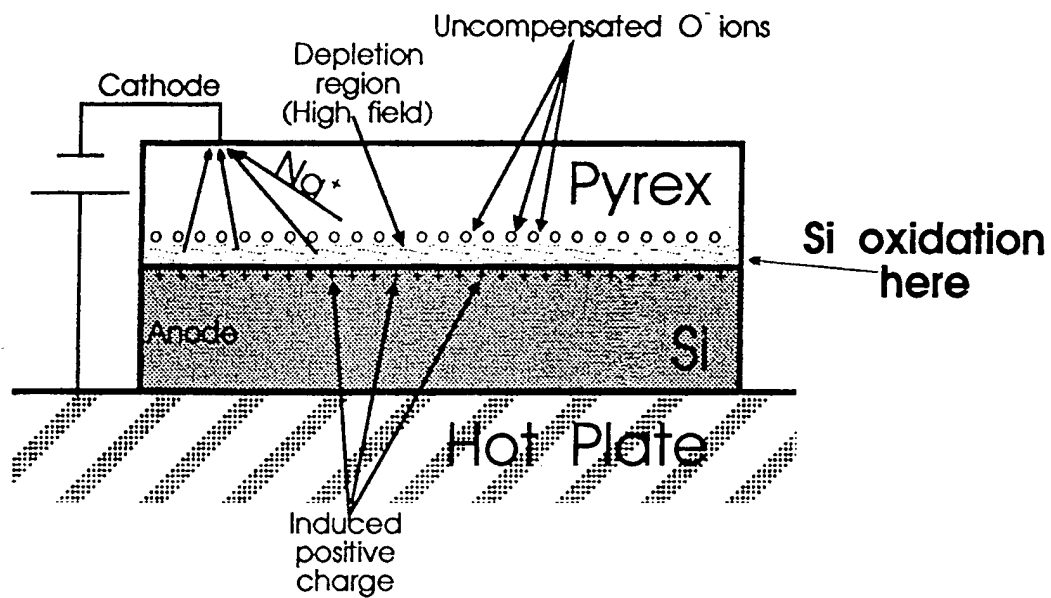
2.4.1.3.1 Multilayer Anodic Bonding

Anodic bonding is an electrochemical process for low temperature (300-600°C) sealing of glass to metal or semiconductor where the metal or the semiconductor to be joined is biased positively.^{4,6-4,8} Figure 4.4(a) illustrates the bonding process between silicon and Pyrex glass. Pyrex glass is a trade name for borosilicate glass containing traces of Na_2O . At elevated temperatures, sodium ions from the dissociation of Na_2O within the Pyrex glass are depleted in the presence of the electric field from the vicinity of the anode by drifting to the cathode where they are plated.^{4,8,4,9} This in turn enhances the electric field within the depletion region and the electrostatic attraction, and cause the transport of oxygen anions towards the anode, in this case, the silicon chip. There the oxygen anions react with the silicon anode to form chemical bond (i.e. oxidation of the silicon by the anions).^{4,9}

The above process has so far only been used for single bonding of thick silicon wafers and Pyrex glass. We have extended the process for bonding thin silicon membranes and for multiple layer bonding. The former is possible because the thermal expansion coefficients of silicon and Pyrex glass are similar and the process is done at low temperatures, both of which minimize stress in the membrane. The concept of multiple layer anodic bonding is illustrated in Fig. 4.4. Key to this process is the irreversibility of anodic bonding.^{4,9} After the first silicon to Pyrex glass bond [Fig. 4.4(a)], another silicon chip can be bonded to the free surface of the Pyrex glass by reversing the applied bias [Fig. 4.4(b)]. Bonding at the new interface takes place following the same mechanism, i.e. silicon oxidation. However, the reversed electric field cannot undo the bond at the opposite interface because it is a chemical rather than an electrostatic bond. The procedure can be repeated to build up the stack. To achieve satisfactory multilayer bonding, special attention has to be given to the control of temperature, the applied voltage, the bond time and in particular, the surface condition of the layers.

In the case where the Pyrex glass is on top of the stack, it is possible to view the bonding process by eye. When the bonding process is not visible during multilayer bonding, end-point is determined by monitoring the bond current and the bond time. This is because the rate of reaction is governed by current flow and the extent of the reaction is a function of charge transfer^{4,8} as anodic bonding is electrochemical in nature. The same current is maintained regardless of the number of layers in the stack. The applied voltage required to maintain the bond current is dependent on the number of layers in the stack, and the condition of the bond wire and the surfaces of the components. This is typically between 100 and 1000V.

(a)



(b)

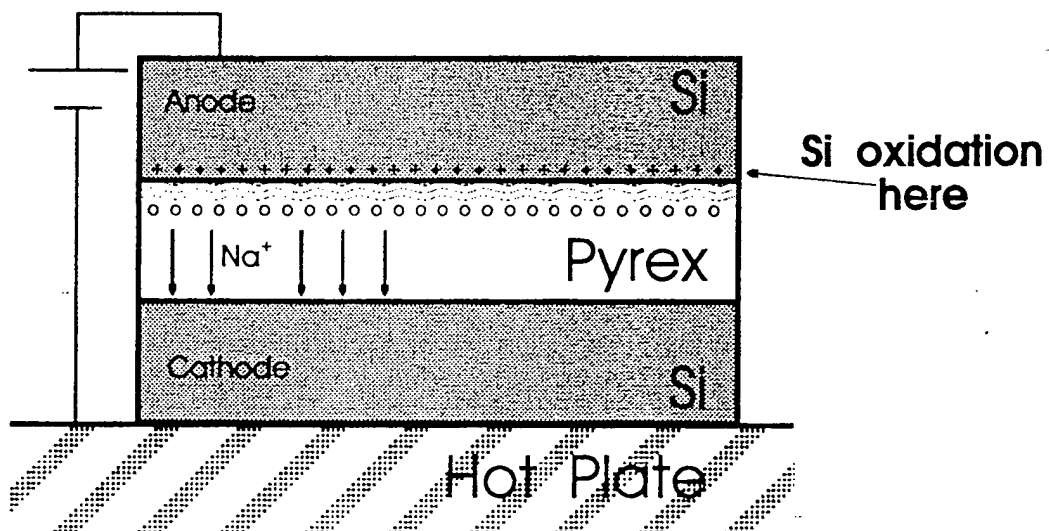


Fig. 4.4 Schematic illustration of multilayer anodic bonding process.

For microlens assembly, anodic bonding provides these advantages. Firstly, the Pyrex glass seals conformally to the silicon surface (even around particulates) thus ensuring flatness and parallelism. Secondly, the bond does not outgas and is thus UHV compatible for reliable microcolumn operation. Thirdly, the bond is instantaneous which greatly benefits the alignment process (discussed below) by eliminating relative drift between components during bonding.

2.4.1.3.2 Alignment

The microlens assembly is performed on a custom built stage as shown in Fig. 4.5. The system consists of a heated stage which is motor driven and can be moved in sub-micron steps. The first component is fixed onto this stage by vacuum while the second component is positioned on top so that the two components are held together only by gravity and a small point force exerted by a bonding wire. A component can be a Pyrex glass chip, a silicon micro-electron-optical component or a silicon/Pyrex glass sub-assembly. A pin chuck attached to a micromanipulator is used to move the top component relative to the bottom one by pushing it. The alignment process involves aligning the two components, one at a time, under an optical microscope to the cross-hair of the eye piece. For this purpose alignment marks are etched through the membrane of all the silicon micro-electron-optical components except the limiting aperture. In the latter case, the cross-hair is aligned to the aperture itself. This is carried out at room temperature when the components slide freely on each other. Once both components are aligned to the cross-hair, the stage temperature is raised for bonding. Attached to the objective lens of the alignment microscope is a cone shaped cover which allows high temperature viewing by cutting out image distortion due to air turbulence. We found that there is very little relative drift during the temperature ramp up so that re-alignment at high temperatures is not necessary. The critical alignment is between two micro-electron-optical components (i.e. silicon chips). The placement of Pyrex glass is not critical and is normally done by eye.

2.4.1.3.3 Electron Gun Assembly

The configuration of a source is shown in Fig. 4.1(b). All the Pyrex glass chips are U-shaped (formed by machining). The width of the slot is 2 mm and the Pyrex glass thickness is 150 μm . The U-shaped Pyrex glass chips allow better vacuum pumping of the source. This is essential due to the proximity of the field emission tip. The assembly of the source lens is shown schematically in Fig. 4.6(a). A silicon micro-electron-optical component with a 5 μm diameter hole and marks (the extractor electrode) is fixed onto the stage. A Pyrex glass chip is then bonded onto the extractor

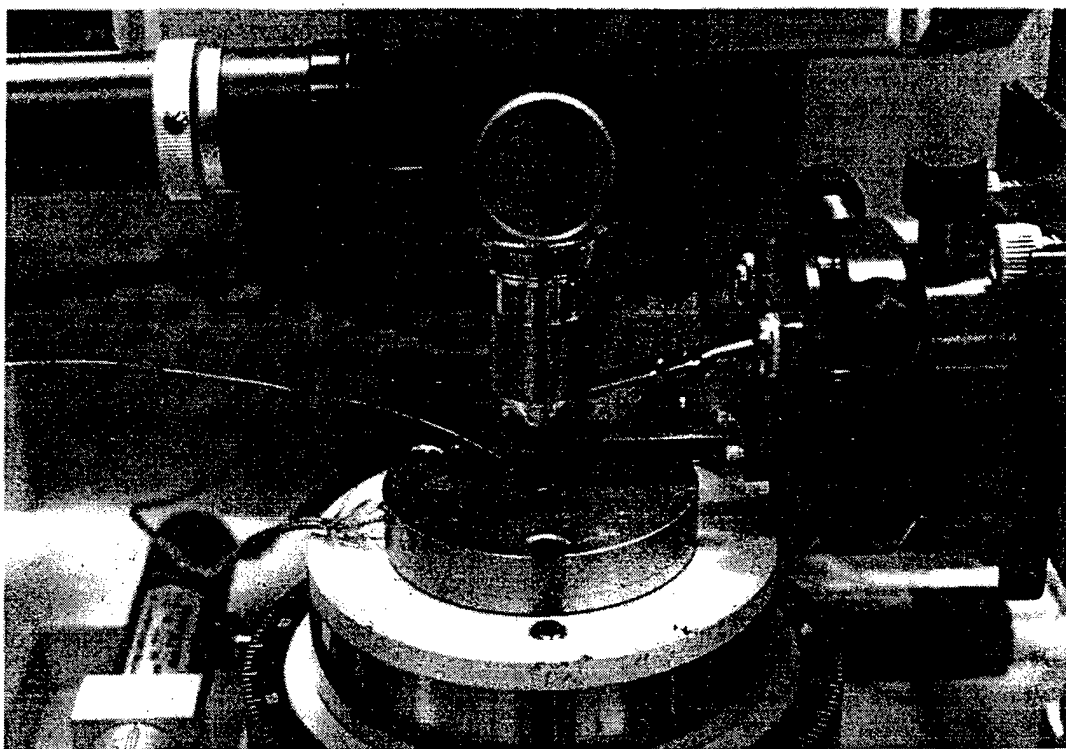


Fig. 4.5 A photograph showing the heated stage, the cone-shaped adapter, the bonding wire which is connected to a voltage source, and the pin-chuck for fine manipulation of the top component.

anodically. Next, a silicon chip with a 100 μm diameter hole (the anode) is aligned and bonded to the extractor. Finally, another Pyrex glass chip is bonded followed by a silicon chip with a single 2.5 μm hole (the limiting aperture) is aligned to the anode and then bonded. Figure 4.7 is a photograph of a fully functional source assembled as described above. The U-shaped Pyrex glass chips in the source improves the vacuum by an order magnitude compared to previous source using square Pyrex glass chips.

2.4.1.3.4 Einzel lens Assembly

Assembling the einzel lens requires a different approach in order to form the center electrode which is essentially a 100 to 200 μm diameter hole etched through a 1-1.5 μm thick free standing silicon membrane. Previously this involved handling mechanically thinned down, free standing silicon films.^{4,10} As shown in Fig. 4.6(b), the current approach starts with a wafer containing an array of 10 \times 10 mm membranes formed by wet etching. A 100 to 200 μm hole is etched through the center of each membrane using the same process depicted in Fig. 4.2. A 7.5 \times 8.5 mm Pyrex glass chip is placed on the back surface of the membrane and then bonded anodically. The membrane is then broken from the wafer and is trimmed along the edges of the Pyrex glass chip. A 7.5 \times 7.5 mm Pyrex glass chip is positioned on the the free membrane surface and bonded anodically. The mismatch in the Pyrex glass chips' sizes allows electrical connection to the protruding center electrode later. The final assembly steps involve aligning and bonding two 100 to 200 μm diameter silicon microelectrodes onto opposite surfaces of the center electrode sub-assembly. This approach offers the advantages of simplicity and reliability since handling of free standing thin silicon films is avoided. Moreover, the silicon membrane formed by wet etching is of higher quality than mechanically polished silicon films in terms of electrical properties and surface smoothness.

2.4.1.4 Summary

We have developed an all dry process for building high aspect ratio multilayer microstructures. Central to this is the development of multilayer anodic bonding of silicon and Pyrex glass, and the use of optical microscope for alignment between layers with an accuracy of the order of 1 μm . This technique is used routinely for building fully functional microlenses for electron-beam microcolumns. Currently, we are able to obtain sub-40 nm resolution in our microcolumn experiments.

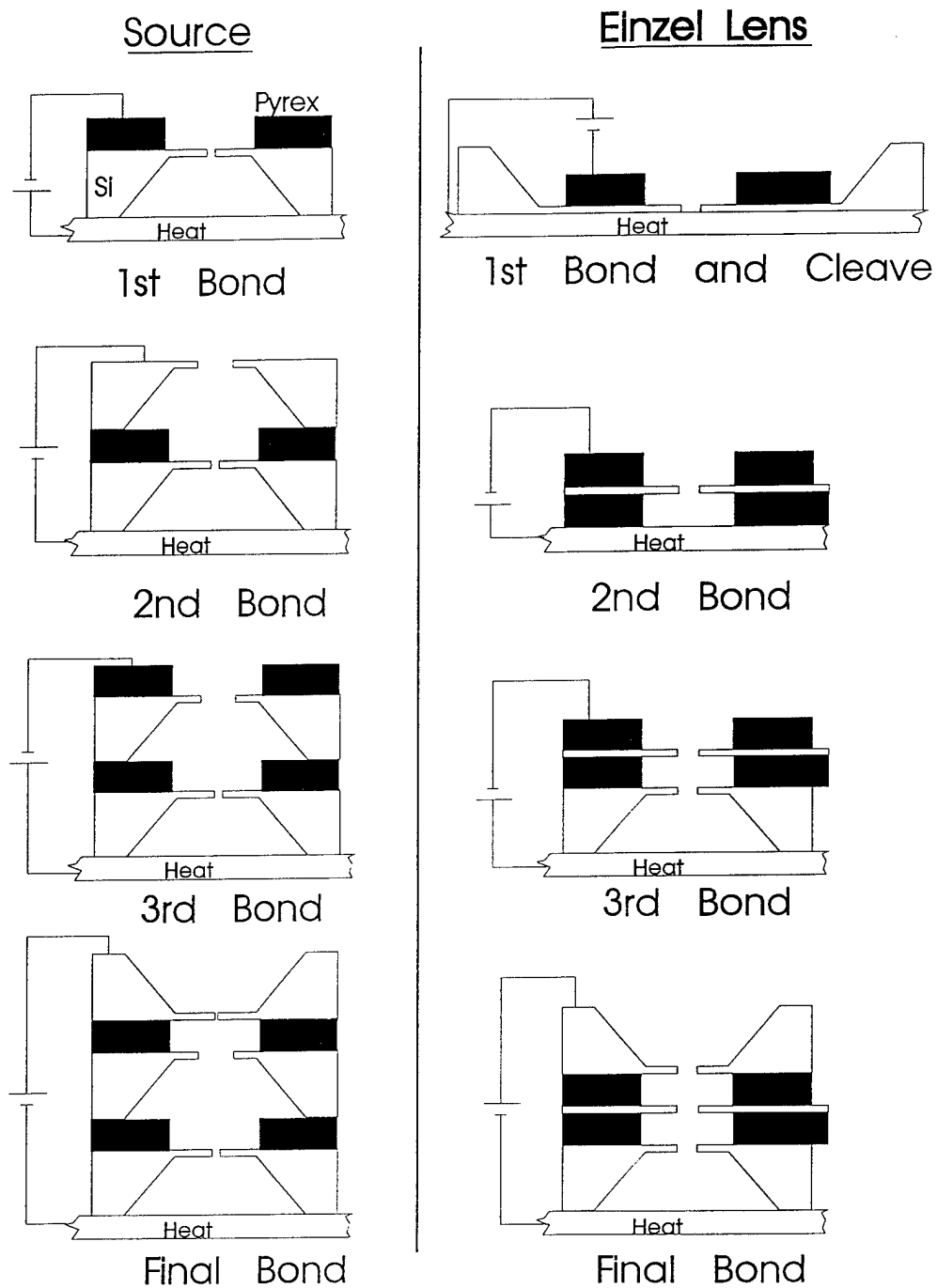


Fig. 4.6 Flow diagrams showing the assembly of (a) a source and (b) an einzel lens.

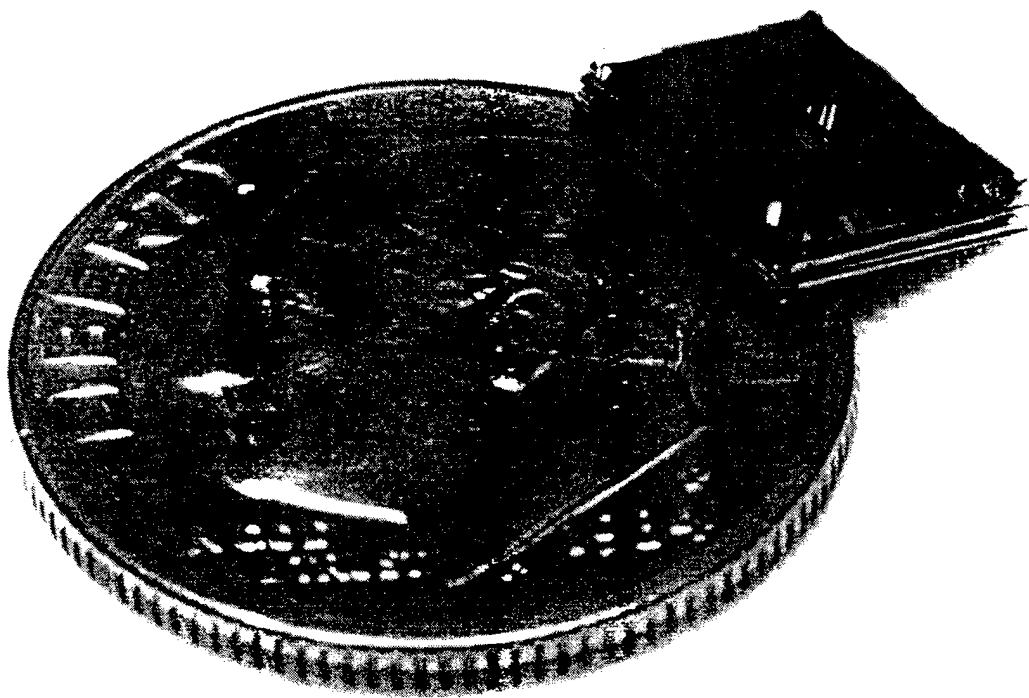


Fig. 4.7 Photograph of a source on a US dime. The two Pyrex glass chips sandwiched between three silicon chips are clearly discernible.

2.4.2 Micromachining applications of a high resolution ultra-thick photoresist

2.4.2.1 Introduction

High aspect ratio lithography on ultra-thick ($> 50\text{ }\mu\text{m}$) resist adds a new dimension and flexibility in the building of tall, high aspect ratio microstructures. An example of this is the LIGA (Lithographie, Galvano- formung, Abformung) process in which very high aspect ratio microstructures are built by electro-plating in a very thick PMMA template ($\approx 1\text{ mm}$) patterned by synchrotron X-ray lithography.^{4,11} Here, we present a new epoxy-based photoresist, SU-8, for near UV lithography capable of similar aspect ratio in up to $200\text{ }\mu\text{m}$ thick layers. Methods for fabricating high aspect ratio microstructures by through silicon wafer etching and metal plating using SU-8 templates are demonstrated. As an example, we describe the fabrication of micro-octupole deflectors for electron microcolumns.

2.4.2.2 SU-8 Properties and Process

SU-8 is a negative tone photoresist consisting of EPON SU-8 resin (from Shell Chemical) and is photosensitized with triaryl sulfonium salt (e.g. Cyracure UVI from Union Carbide).^{4,12,4,13} The resist has two important properties suited for ultra-thick applications. Firstly, its low molecular weight allows dissolution in a variety of organic solvents to form very high concentration mixtures (72-85% solids by weight). Secondly, the layer has very low optical absorption in the near UV spectrum. At 365 nm , UV transmission through $100\text{ }\mu\text{m}$ thick layer is 46% as shown in Fig. 4.8.

For films of up to $200\text{ }\mu\text{m}$ thick, the appropriate amount of the SU-8 resin is dissolved in GBL (γ -butyrolactate) to form a solution with a concentration of 85% by weight. To this solution is added 5% by weight of the triaryl sulfonium salt. The resist is applied by spinning, and up to $200\text{ }\mu\text{m}$ thick layers can be obtained with a single coat. The resist is baked on a hotplate at $90\text{-}95^\circ\text{C}$ for 15 minutes. Lithography is carried out on a contact aligner with a broadband near UV source (G, H, and I lines). The exposure dose is between $300\text{-}1200\text{ mJ/cm}^2$, depending on the resist thickness. The exposed resist is subjected to a 15 minute post exposure bake on a hotplate at $90\text{-}95^\circ\text{C}$ and then developed in either PGMEA (propylene glycol methyl ether acetate) or GBL.

Using the above process, resist images with 10:1 aspect ratio and smooth vertical sidewalls are routinely achieved in $20\text{-}200\text{ }\mu\text{m}$ thick layers, i.e. $2\text{ }\mu\text{m}$ and $20\text{ }\mu\text{m}$ resolution in $20\text{ }\mu\text{m}$ and $200\text{ }\mu\text{m}$ thick layers respectively. Figure 4.9 shows SEM micrographs of

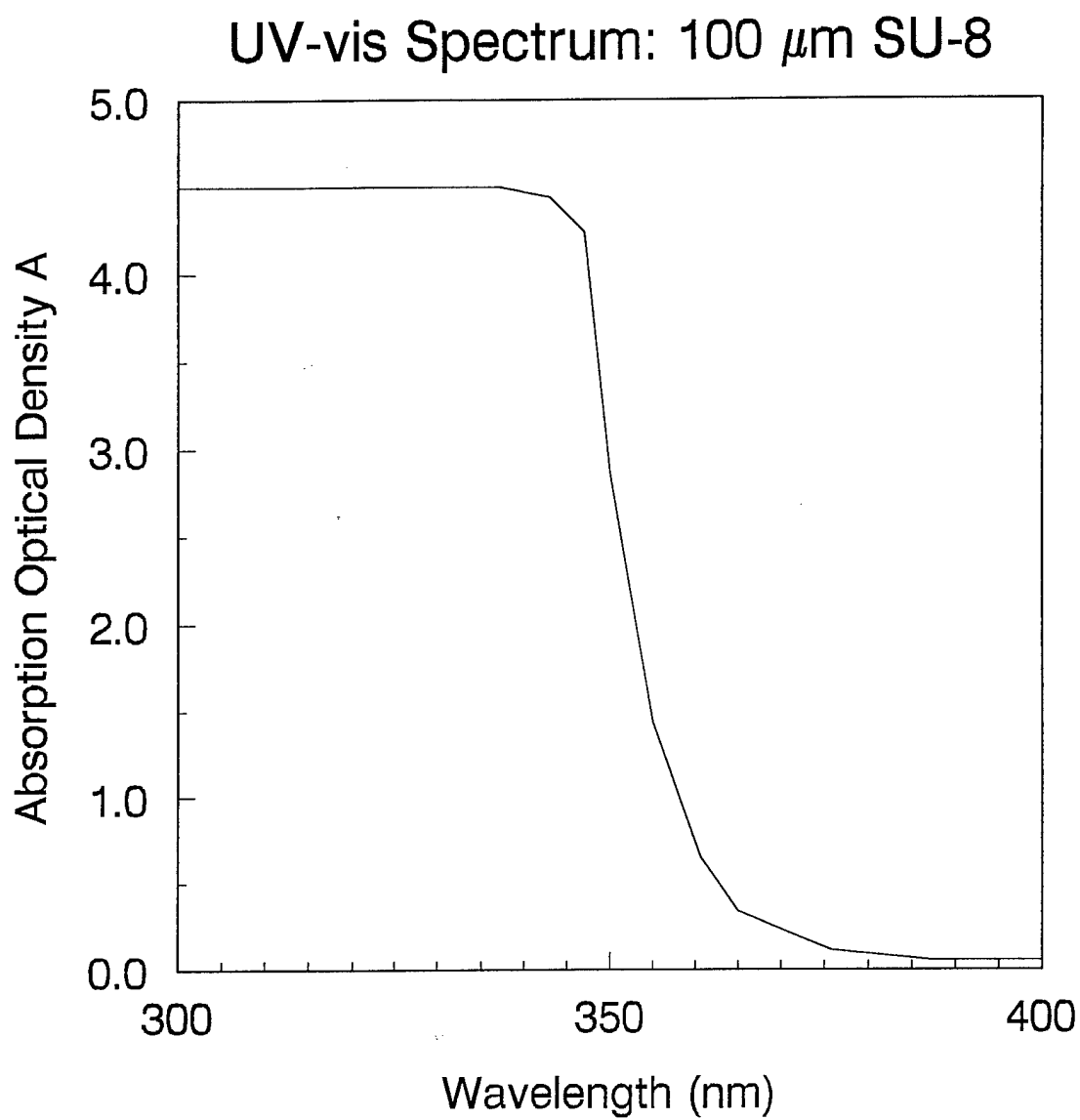


Fig. 4.8 UV absorption spectrum for a 100 μm thick SU-8 film

160 μm thick SU-8 structures with 16 μm minimum feature size. We have also achieved sub-0.1 μm resolution in 100-130 nm thick layer using high resolution electron-beam lithography.

2.4.2.3 Micromachining Applications

Two approaches utilizing ultra-thick SU-8 for fabricating tall high aspect ratio microstructures for MEMs (micro electro mechanical structures) and packaging applications are described here. In the first approach patterned SU-8 is used as a mask for etching through a silicon wafer while the second involves very thick metal plating using SU-8 stencils. The fabrication methods of silicon and gold micro-octupole scanners for electron microcolumns using both approaches are described here. The micro scanners are designed for the IBM electron microcolumn; the desired electrode widths are between 50 and 200 μm with deflector bores of between 200 and 800 μm , and are a few hundred microns thick (up to 500 μm). The electrodes are required to have smooth sidewalls with near vertical profile. The use of photolithography for the fabrication of these scanners provides the advantages of miniaturization (thus lowering scan voltage) and precision (low distortion).

2.4.2.4 Deep Silicon Etching

Silicon micro-scanners are of great interest to us as these are fully compatible with the microlenses used in our microcolumns which consist of anodically bonded layers of silicon and Pyrex.^{4,14} A silicon micro scanner can be easily aligned and anodically bonded to the micro-lenses to form a fully integrated electron microcolumn.

The starting material is a n+ silicon wafer which is slightly over 200 μm thick. A 200 μm thick SU-8 is then coated on the wafer and then exposed optically with the scanner patterns which have electrode widths of 100 and 200 μm . After development, the resist is cured in a 200°C oven for 30 minutes.

The wafer is then reactive-ion etched in a conventional system using a gas mixture of SF_6 and CBrF_3 . The inherent high thermal stability of SU-8 (glass transition temperature $T_g \approx 200^\circ\text{C}$, and degradation temperature $T_d \approx 380^\circ\text{C}$ when fully cured) and its high aspect ratio patterning capability in ultra-thick resist layer makes it an ideal mask for prolonged reactive-ion etching (RIE). Etch selectivity between silicon and SU-8 of greater than 3:1 is achieved. As shown by the SEM micrographs in Fig. 4.10, very smooth and near vertical sidewalls are obtained. It can be also be seen that the resist

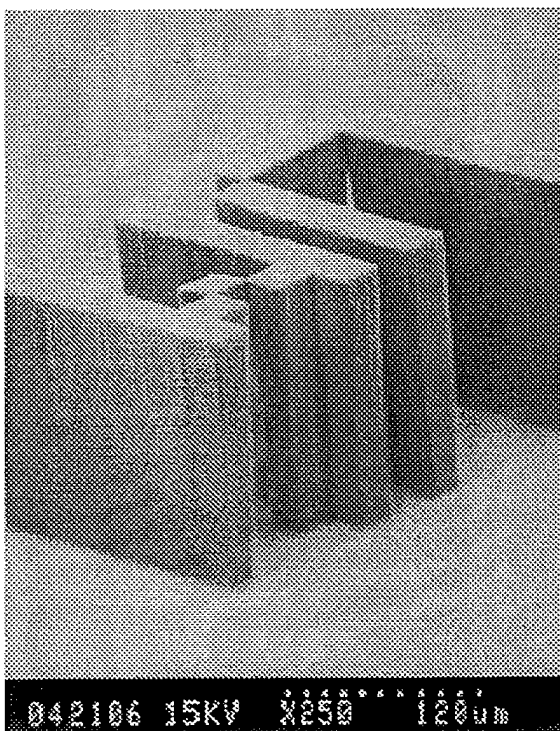
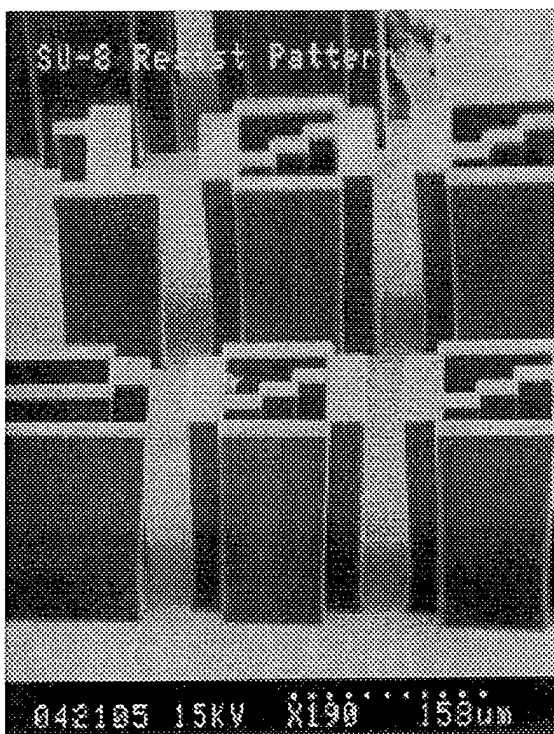
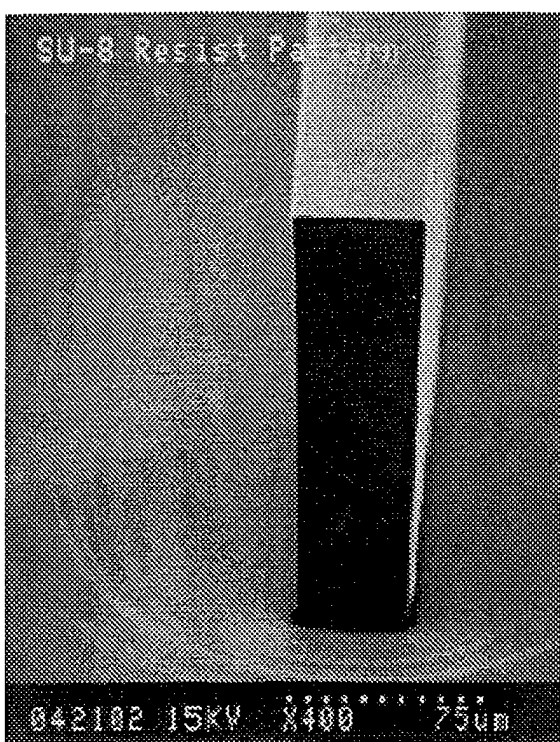
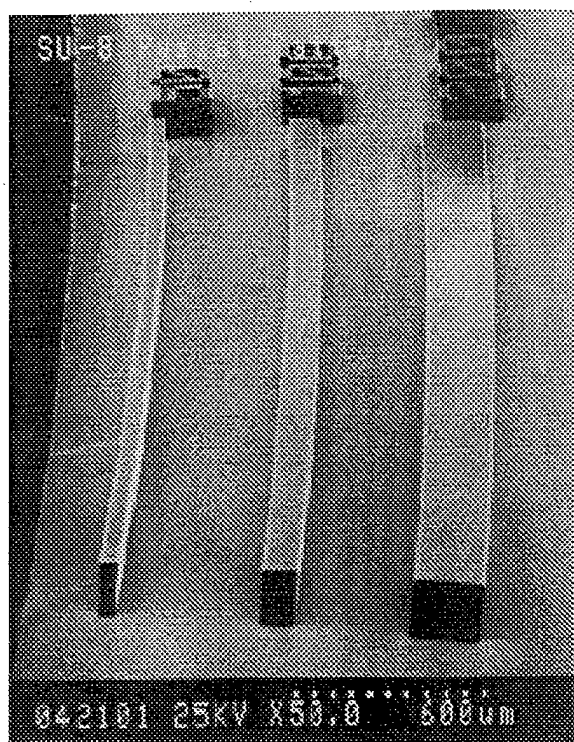


Fig. 4.9 SEM micrographs of SU-8 resist structures formed by near UV photolithography. Minimum feature size of 16 μm is resolved in 160 μm thick SU-8.

retains its integrity and straight sidewalls for different linewidths even after tens of hours of etching.

Silicon RIE using a gas mixture of SF_6 , CHF_3 and O_2 has also been carried out. This process yields a faster etch rate (≈ 500 nm per minute) but has lower etch selectivity ($< 2:1$) due to the presence of O_2 . The black silicon method as described by Jansen *et al.*^{4,15} is used to vary the etched profile. This involves interplaying the flow rates of the three gases, the pressure and the power. In general, higher SF_6 flow rate reduces anisotropy, higher O_2 causes a positive taper and higher CHF_3 causes more negative taper. As shown in Fig. 4.11, the undercut profile is eliminated by reducing SF_6 flow rate.

We find that with a conventional RIE system, deep silicon RIE using $\text{SF}_6/\text{CBrF}_3$ gas mixture is superior to that using $\text{SF}_6/\text{CHF}_3/\text{O}_2$ in terms of etched profile and etch selectivity but has the disadvantage of a very slow etch rate. The latter RIE process has ten times faster etch rate but requires further process optimization. Fabrication of silicon micro octupole scanners by deep etching using the $\text{SF}_6/\text{CBrF}_3$ RIE process at various stages is shown in Fig. 4.12. We are able to etch through the silicon wafer i.e. > 200 μm at an etch rate of 50 nm per minute. The silicon micro scanners are anodically bonded to Pyrex substrates in the final steps as shown in micrographs in Fig. 4.13.

For deep silicon etching a better approach may be by low temperature RIE in a high density plasma which has been shown to be anisotropic, fast (etch rate of up to 5 μm per minute), and highly selective.^{4,16,4.17} This will be evaluated using SU-8 mask.

2.4.2.5 Electroplating

An alternative means for building tall high aspect ratio microstructures is by electro-plating using ultra-thick SU-8 stencils. Preliminary work is focused on fabricating the micro-octupole scanners by gold plating. The first step involves deposition of a plating base consisting of 10 nm of gold on 5 nm Ni on a silicon substrate. A 170 μm thick SU-8 is then coated on the substrate and the scanner patterns exposed. The developed resist is then used as the stencil for gold plating. Gold thickness of up to 130 μm has been obtained so far with a plating rate of 100 nm per minute. The SU-8 stencil is stripped using an organic solvent. Figure 4.14 are SEM micrographs showing a gold micro scanner with 200 μm wide electrodes. Very vertical sidewalls are obtained.

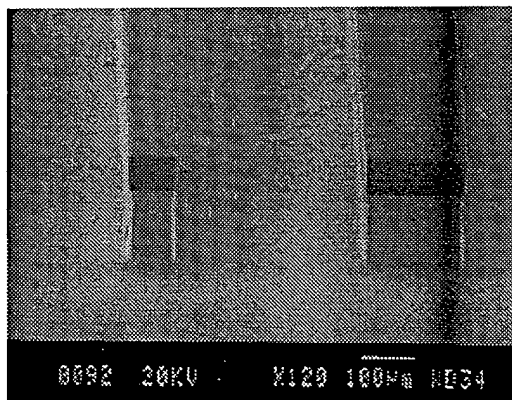
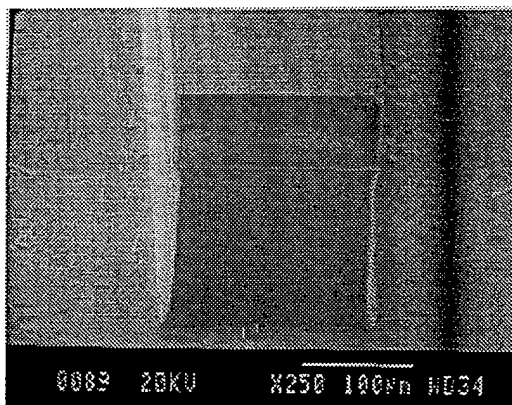
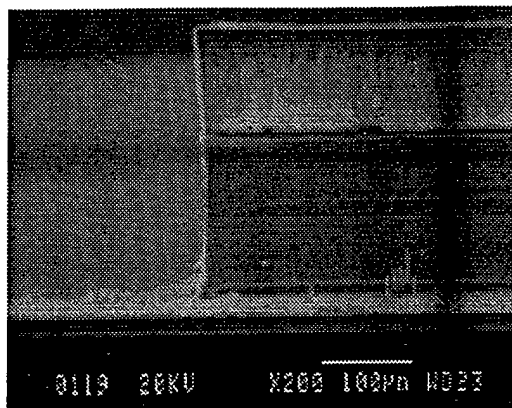


Fig. 4.10 SEM micrographs of silicon structures with very vertical sidewalls formed by $\text{SF}_6/\text{CBrF}_3$ RIE using SU-8 mask. The etched depth in silicon is over 150 μm . About 50-100 μm thick SU-8 remains at this stage. It can be seen that the resist retains its integrity and vertical profile.

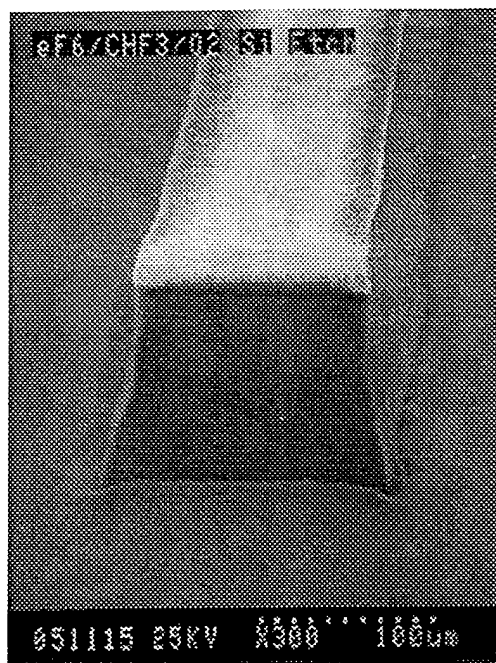
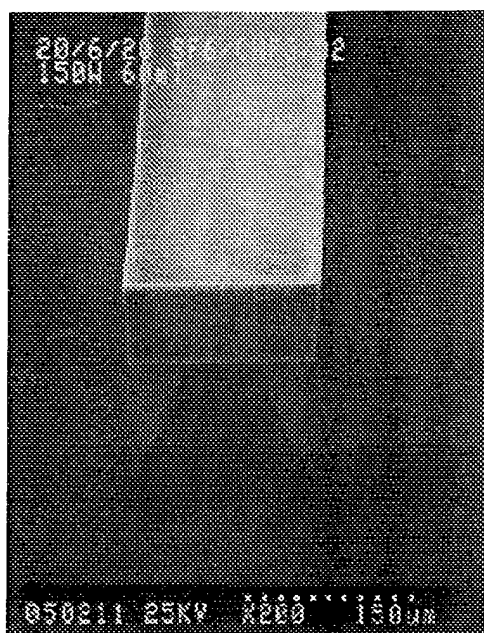
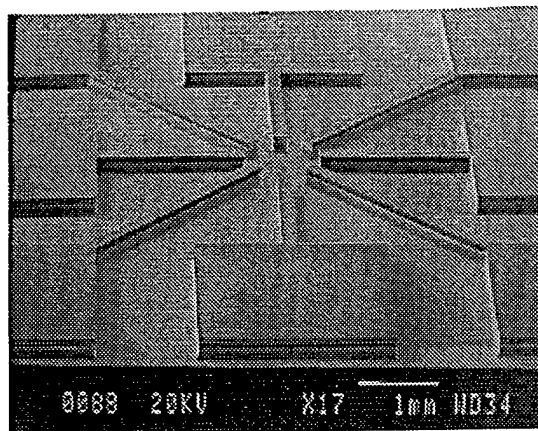
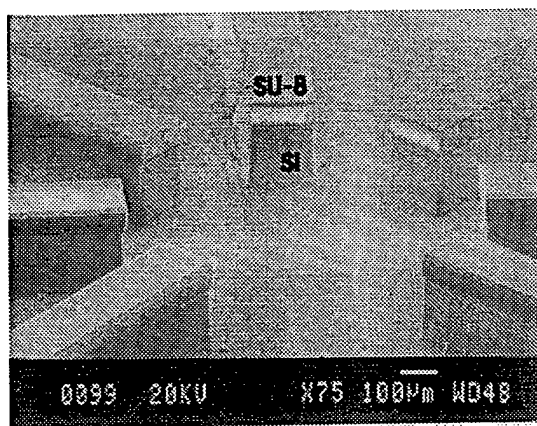


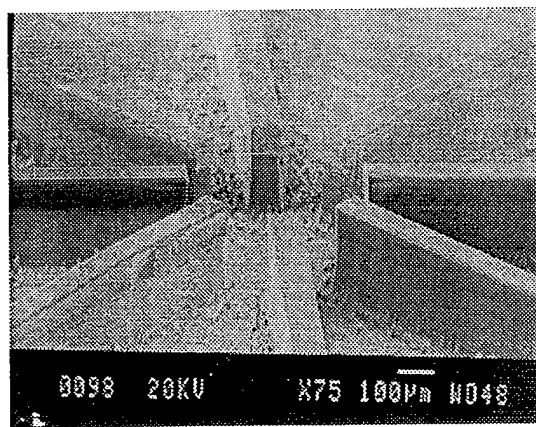
Fig. 4.11 SEM micrographs of 100 μm thick silicon structures formed by $\text{SF}_6/\text{CHF}_3/\text{O}_2$ RIE. By reducing SF_6 flow, the etched profile changed from (a) undercut profile to (b) slight positive taper.



(a)

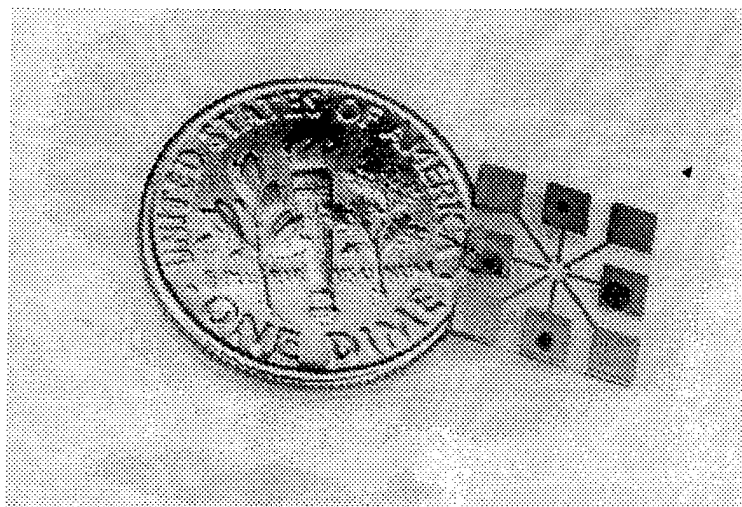


(b)

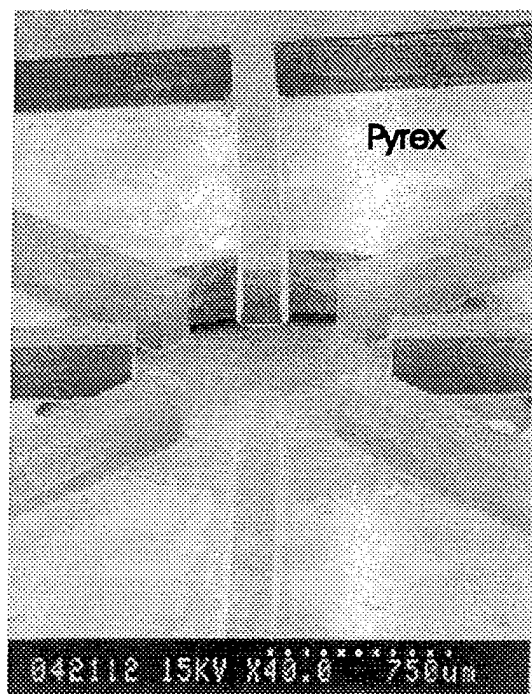


(c)

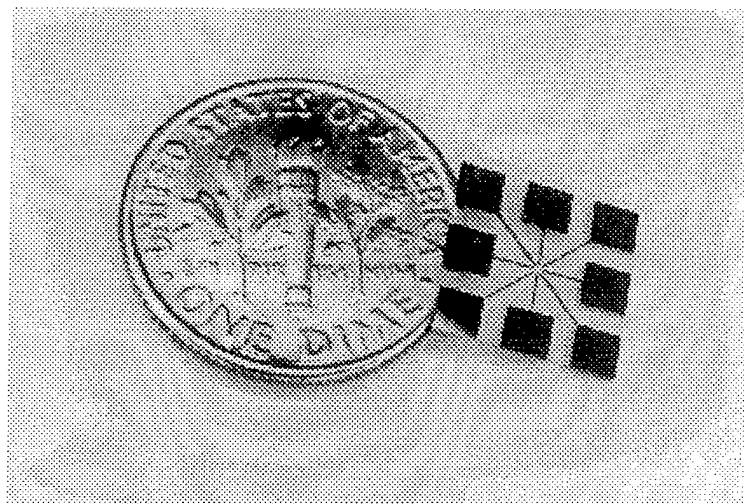
Fig. 4.12 SEM micrographs showing partially etched silicon micro octupole scanner. An overview of the scanner is shown in (a) and close-up views of 200 μm wide and 100 μm wide electrodes are shown in (b) and (c) respectively. The etched depth is 150 μm in (a) and 200 μm in (b) and (c).



(a)

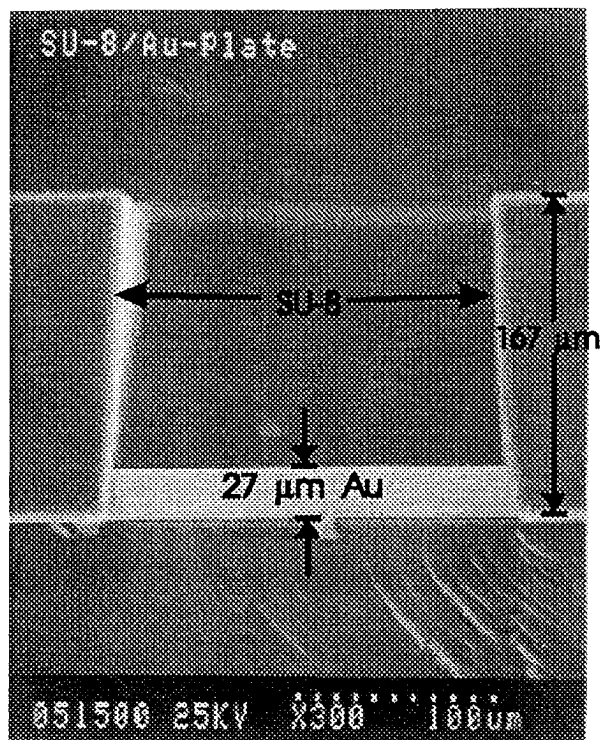


(c)

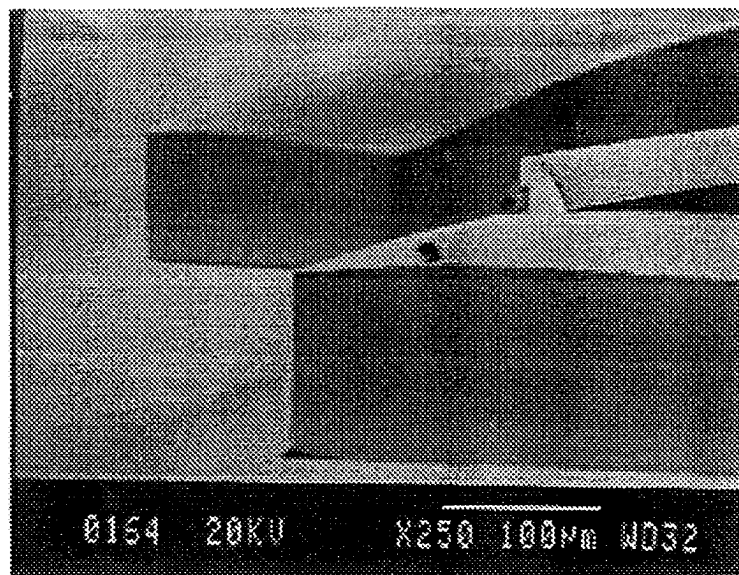


(b)

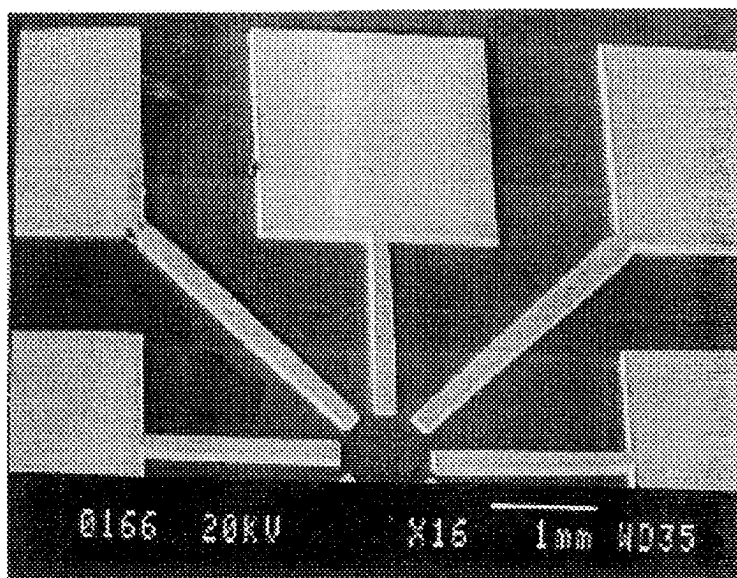
Fig. 4.13 Micrographs of completed silicon micro scanners which have been bonded anodically to Pyrex substrates. 200 μm wide and 100 μm wide deflectors are shown in (a) and (b) respectively, while a close-up view of 200 μm wide electrodes is shown in (c). It can be seen in all the micrographs that the electrodes extend over the through holes in the Pyrex substrates (i.e. the ends are free standing).



(a)



(c)



(b)

Fig. 4.14 SEM micrographs showing (a) 27 μm thick gold plated in 167 μm thick SU-8, (b) overview of gold micro scanner with 200 μm wide and 130 μm thick electrodes, and (c) close-up side view of the gold electrodes showing vertical sidewalls which are 130 μm thick.

The above process is similar to the LIGA process. Compared to this process, the use of SU-8 offers the advantages of low cost and faster turn around time. Both processes give similar aspect ratio patterning except that the SU-8 thickness is limited by the film application process to 200 μm currently. However, photolithography on up to 500 μm thick SU-8 is anticipated in the near future.

2.4.2.6 Conclusions

We have demonstrated high aspect ratio and high resolution near UV photolithography on ultra-thick SU-8 resist films. The process is simple and can resolve 20 μm features in 200 μm films. The resist shows very high thermal and chemical stability and is thus suitable for prolonged plasma etching and metal plating. Application of this resist for fabricating micro-octupole scanners for electron microcolumns has been demonstrated. Silicon micro-octupole scanners bonded anodically to Pyrex substrates have been fabricated by through wafer etching ($> 200 \mu\text{m}$) using SU-8 mask. Tall high aspect ratio structures can also be obtained by very thick metal plating using SU-8 stencils. We have built 130 μm thick gold structures with vertical sidewalls. The results show that the plating process using SU-8 can be a cost effective alternative to the LIGA process. Another potential application is the fabrication of LIGA masks.

(3) Acknowledgments

This report has been prepared with contributions from

- Mr. Brian Hussey
- Dr. Hoseob Kim
- Dr. Ernst Kratschmer
- Dr. Kim Y. Lee
- Dr. Stephen A. Rishton
- Dr. Michael G.R. Thomson
- Dr. Ming L. Yu
- Mr. Shervin Zolgharnain

(4) References

- 1.1. T.H.P. Chang, L.P. Muray, U. Staufer, M.A. McCord and D.P. Kern, SPIE Institutes for Advanced Optical Technologies IS10, 127 (1993)
- 1.2. T.H.P. Chang, D.P. Kern, and M.A. McCord, J. Vac. Sci. Technol. B 7, 1855 (1989)
- 1.3. T.H.P. Chang, D.P. Kern, and L.P. Muray, J. Vac. Sci. Technol. B 8, 1698 (1990)
- 1.4. K.Y. Lee, S.A. Rishton, and T.H.P. Chang, J. Vac. Sci. Technol. B 12, 3425 (1994)
- 1.5. L.P. Muray, U. Staufer, D.P. Kern, and T.H.P. Chang, J. Vac. Sci. Technol. B 10, 2749 (1992)
- 1.6. E. Kratschmer, H.S. Kim, M.G.R Thomson, K.Y. Lee, S.A. Rishton, M.L. Yu, and T.H.P. Chang, J. Vac. Sci. Technol. B12, 3503 (1994)
- 1.7. M.L. Yu, B.W. Hussey, and T.H.P. Chang, W.A. Mackie, paper Q2 presented at the 39th Intl. Conf. on Electron, Ion and Photon Beam Technol. and Nanofabrication 1995, Scottsdale, AZ, May 30 - June 2, 1995
- 1.8. J. Kelly, T. Groves, and H. P. Kuo, J. Vac. Sci. Technol. 19, 936 (1981)
- 1.9. D.W. Tuggle and L.W. Swanson, J. Vac. Sci. Technol. B3, 220 (1985)
- 1.10. K. Gamo, K. Yamashita, F. Emoto, and S. Namba, N. Samoto and R. Shimizu, J. Vac. Sci. Technol. B3, 117 (1985)
- 1.11. H.S. Kim, E. Kratschmer, M.L. Yu, M.G.R. Thomson, and T.H.P. Chang, J. Vac. Sci. Technol. B12, 3413 (1994)
- 1.12. H.S. Kim, M.L. Yu, E. Kratschmer, B.W. Hussey, M.G.R. Thomson and T.H.P. Chang, paper C26 presented at the 39th Intl. Conf. on Electron, Ion and Photon Beam Technol. and Nanofabrication 1995, Scottsdale, AZ, May 30 - June 2, 1995

- 1.13. K.Y. Lee, S.A. Rishton, and T.H.P. Chang, J. Vac. Sci. Technol. B 12, 3425 (1994)
- 1.14. Ted Pella Inc., Redding, CA
- 1.15. H.S. Kim, M.L. Yu, E. Kratschmer, B.W. Hussey, M.G.R. Thomson and T.H.P. Chang, J. Vac. Sci. Technol. B 13, 2468 (1995)
- 1.16. S. Kleindiek, H.S. Kim, E. Kratschmer, and T.H.P. Chang, J. Vac. Sci. Technol. B 13, 2653 (1995)
- 1.17. E. Kratschmer, H.S. Kim, M.G.R Thomson, K.Y. Lee, S.A. Rishton, M.L. Yu, and T.H.P. Chang, J. Vac. Sci. Technol. B 13, 2498 (1995)
- 1.18. D.A. Gedcke, J.B. Ayers, and P.B. DeNee, Scanning Electron Microsc. I, 581 (1978)
- 1.19. P.E. Russel and J.F. Mancuso, J. of Microscopy, 140, 323 (1985)
- 1.20. G.D. Meier, F.E. Prins and D.P. Kern, paper F2, 40th Intl. Conf. on Electron, Ion and Photon Beam Technology and Nanofabrication 1996, Atlanta, GA, May 28-31, 1996
- 1.21. S. Zolgharnain, K.Y. Lee, S.A. Rishton, D. Kisker, and T.H.P. Chang, J. Vac. Sci. Technol. B 13, 2556 (1995)
- 1.22. Galileo Electro-Optics Corp., Sturbridge, MA
- 2.1. T. H. P. Chang, D. P. Kern, and L. P. Muray, J. Vac. Sci. Technol. B 8, 1698 (1990).
- 2.2. E. Kratschmer, H. S. Kim, M. G. R. Thomson, K. Y. Lee, S. A. Rishton, M. L. Yu, and T. H. P. Chang, J. Vac. Sci. Technol. B 13, 2498 (1995).
- 2.3. See, for example, P. Grivet, *Electron Optics* (Pergamon, New York, 1965).
- 2.4. The programs including source code were obtained from *Munro's Electron Beam Software, Ltd.*, London, England.

- 2.5. M. Szilagyi and J. Szép, IEEE Trans. Electron Devices **ED-34**, 2634 (1987).
- 2.6. M. Szilagyi and H. Cho, J. Vac. Sci. Technol. B **13**, 142 (1995).
- 2.7. W. Ziegler and D. P. Kern, *Proceedings of the 13th International Congress on Electron Microscopy*, (Les Editions de Physique, Les Ulis, 1994), Vol. 1, pp. 185-186.
- 2.8. P. E. Gill, W. Murray, M. A. Saunders, and M. H. Wright, ACM Trans. Math. Software **10**, 282 (1984).
- 2.9. Available from *The Numerical Algorithms Group, Inc.*, Downers Grove, IL.
- 2.10. Dieter P. Kern, J. Vac. Sci. Technol. **16**, 1686 (1979).
- 2.11. H. Ohiwa, E. Goto, and A. Ono, Electron. Commun. Jpn. **54-B**, 44 (1971).
- 2.12. P. W. Hawkes and E. Kasper, *Principles of Electron Optics* (Academic, New York, 1989) Vol 2, Section 40.3.
- 2.13. M. G. R. Thomson, J. Vac. Sci. Technol. B (in press).
- 2.14. T. T. Tang and C. Y. Sheng, J. Vac. Sci. Technol. B **5**, 165 (1987).
- 2.15. K. Y. Lee, N. LaBianca, S. A. Rishton, S. Zolgharnain, J. D. Gelorme, J. Shaw, and T. H. -P. Chang, J. Vac. Sci. Technol. B **13** 3012 (1995).
- 2.16. L. Reimer, *Scanning Electron Microscopy*, Springer Series in Optical Sciences Vol. 45, edited by P. W. Hawkes (Springer, Berlin, 1985), Sec. 4.2.1.
- 2.17. R. D. Heidenreich, L. F. Thompson, E. D. Feit, and C. M. Melliar-Smith, J. Appl. Phys. **44** 4039 (1973).
- 2.18. G. H. Jansen, *Coulomb Interactions in Particle Beams*, Advances in Electronics and Electron Physics Suppl 21 (Academic, New York, 1990).
- 2.19. H. Boersch, Z. Phy. **139**, 115 (1954).

- 2.20. P. W. Hawkes and E. Kasper, *Principles of Electron Optics* (Academic, New York, 1989), Vol. 2, Chap. 49.
- 2.21. K. H. Loeffler and R. H. Hudgin, *Microscopie Électronique 1970*, edited by P. Favard (Société Française de Microscopie Électronique, Paris, 1970), Vol. 2 pp. 77 and 381.
- 2.22. T. Groves, D. L. Hammond, and H. Kuo, *J. Vac. Sci. Technol.* **16**, 1680 (1979).
- 2.23. N. K. Kang, D. Tuggle, and L. W. Swanson, *Optik* **63**, 313 (1983).
- 2.24. L. R. Danielson and L. W. Swanson, *Surf. Sci.* **88**, 14 (1979).
- 2.25. P. W. Hawkes and E. Kasper, *Principles of Electron Optics* (Academic, New York, 1989), Vol. 2, Chap. 44.
- 2.26. A. E. Bell and L. W. Swanson, *Phys. Rev. B* **19**, 3353 (1979).
- 2.27. J. C. Wiesner and T. E. Everhart, *J. Appl. Phys.* **44**, 2140 (1973).
- 2.28. The "EMECH" program package supplied by *Munro's Electron Beam Software, Ltd.*, London.
- 3.1. U. Staufer, L.P. Murray, D.P. Kern, and T.H.P. Chang, *J. Vac. Sci. Technol. B* **9**, 2962 (1991).
- 3.2. H.S. Kim, M.L. Yu, U. Staufer, L.P. Murray, D.P. Kern, and T.H.P. Chang, *J. Vac. Sci. Technol. B* **11**, 2327 (1991).
- 3.3. M.L. Yu, B.W. Hussey, H.S. Kim and T.H.P. Chang, *J. Vac. Sci. Technol. B* **12**, 3431 (1994).
- 3.4. E. Kratschmer, H.S. Kim, M.G.R. Thomson, K.Y. Lee, S.A. Rishton, M.L. Yu and T.H.P. Chang, *J. Vac. Sci. Technol. B* **12**, 3503 (1994).
- 3.5. L.W. Swanson and N. A. Martin. *J. Appl. Phys.* **46** (5) 2029 (1975).
- 3.6. J. Orloff and L.W. Swanson, *J. Appl. Phys.* **50**, 2494 (1979).

- 3.7. D.W. Tuggle and L.W. Swanson, J. Vac. Sci. Technol. B **3**, 220 (1985).
- 3.8. D.W. Tuggle, J.Z. Li and L.W. Swanson, J. Micro. **140**, 293 (1985).
- 3.9. M. Gesley J. Appl. Phys. **65**, 914 (1989).
- 3.10. M.G.R. Thomson, J. Vac. Sci. Technol. B **12**, 3498 (1994).
- 3.11. A.E. Bell and L.W. Swanson, Phys. Rev. B **19**, 3353 (1979);
- 3.12. The data were provided FEI Company, 19500 N.W. Gibbs Drive, Beaverton, Oregon.
- 3.13. Vu Thien Binh, A. Piquet, H. Roux, R. Uzan, and M. Drechsler, J. Phys. E (Sci. Instr.), **9**, 377 (1976).
- 3.14. Vu Thien Binh, R. Uzan, and M. Drechsler, Surf. Sci. **60**, 13 (1976); Vu Thien Binh and R. Uzan, Surf. Sci. **179**, 540 (1987).
- 3.15. D.A. King T. E. Madey, and J.T. Yates, J. Chem. Phys. **55**, 3236 (1971).
- 3.16. R. Gomer, *Field emission and Field ionization*, (Harvard University Press, Cambridge, 1961).
- 3.17. A.V. Crewe, D.N. Eggenberger, J. Wall, and L.M. Welter, Rev. Sci. Instr. **39** 576 (1968).
- 3.18. T.H.P Chang, D.P. Kern, M.A. McCord, and L.P. Muray, J. Vac. Sci. Technol. B **9**, 438 (1991).
- 3.19. L.E. Toth, *Transition Metal Carbides and Nitrides*, (Academic Press, New York, 1971).
- 3.20. F.H. Plomp, in Proceedings of the Fifth European Congress on Electron Microscopy, 1972, edited by V.E. Cossett (Institute of Physics, Bristol, 1972), p.2.
- 3.21. H. Adachi, Scanning Microsc. **1**, 919 (1987).

- 3.22. M.L. Yu, B.W. Hussey, and T.H.P. Chang, J. Vac. Sci. Technol. B **13**, 2436 (1995).
- 3.23. Y. Ishizawa, T. Aizawa, and S. Otani, Appl. Surf. Sci. **67**, 36 (1993).
- 3.24. Vu Thien Binh, J. Microsc. **152**, 355 (1988).
- 3.25. J.P. Barbour, F.M. Charbonnier, W.W. Donald, W.P. Dyke, E.E. Martin, and L.K. Trolan, Phys. Rev. **117**, 1452 (1960).
- 3.26. Vu Thien Binh, S.T. Purcell, N. Garcia, and J. Doglioni, Phys. Rev. Lett. **69**, 2527 (1992).
- 3.27. M.L. Yu, N.D. Lang, B.W. Hussey, T.H.P. Chang, and W.A. Machie, Phys. Rev. Lett. **77**, 1636 (1996).
- 3.28. E. Kratschmer, H.S. Kim, M.G.R. Thomson, K.Y. Lee, S.A. Rishton, M.L. Yu and T.H.P. Chang, J. Vac. Sci. Technol. B **13**, 2498 (1995).
- 3.29. Papers from the Eighth International Vacuum Microelectronics Conference, J. Vac. Sci. Technol. B **14**, 1883 (1996).
- 3.30. N.S. Xu, Y. Tzeng, and R.V. Latham, J. Phys. D: Appl. Phys. **27**, 1988 (1994).
- 3.31. J.C. Angus, A. Argoitia, R. Gat, Z. Li, M. Sunkara, L. Wang, and Y. Wang, Phil. Trans. R. Soc. Lond. A **342**, 195 (1993).
- 3.32. P-O. Joffreau, R. Haubner, and B. Lux, Int. J. Refractory and Hard Metals, **7**, 186 (1988).
- 3.33. N.S. Xu, Y. Tzeng, and R.V. Latham, J. Phys. D: Appl. Phys. **26**, 1776 (1993).
- 3.34. W. Zhu, G.P. Kochanski, S. Jin, and L. Seibles, J. Appl. Phys. **78**, 2707 (1995).
- 3.35. D.D. Koleske, S.M. Gates, B.D. Thoms, J.N. Russell, Jr., and J.E. Butler, J. Chem. Phys. **102**, 992 (1995).
- 3.36. M.W. Geis and M.A. Tamor, *Diamond and Diamondlike Carbon*, Encyclopedia of Applied Physics, Vol 5, 1 (1993).

- 3.37. M.K. Miller and G.D.W. Smith, *Atom Probe Microanalysis*, (Materials Research Society, Pittsburgh, 1989).
- 3.38. W.B. Choi, J.J. Cuomo, V.V. Zhirnov, A.F. Myers, and J.J. Hren, *Appl. Phys. Lett.* **68**, 720 (1996).
- 3.39. S. Kleindiek, H.S. Kim, E. Kratschmer, and T.H.P. Chang, *J. Vac. Sci. Technol. B* **13**, 2653 (1995).
- 3.40. L.W. Swanson, *J. Vac. Sci. Technol.* **12**, 1228 (1975).
- 3.41. L.W. Swanson, and L.C. Crouser, *Phys. Rev.*, **163**, 622 (1967).
- 3.42. L.W. Swanson, and L.C. Crouser, *Phys. Rev. Lett.*, **19**, 1179 (1967).
- 3.43. J.W. Gadzuk, E.W. Plummer, *Rev. Modern, Phys.*, **45**, 487 (1973); L.W. Swanson, and A.E. Bell, *Adv. Electron. Phys.* **32**, 193 (1973).
- 3.44. W.K. Lo, M. Skvarla, C.W. Lo, H.G. Graighead, and M.S. Isaacson, *J. Vac. Sci. Technol. B* **13**, 2441 (1995).
- 3.45. M.L. Yu, H.S. Kim, B.W. Hussey, T.H.P. Chang, and W.A. Mackie, *J. Vac. Sci. Technol. B* **14**, in press (1996).
- 3.46. L.W. Swanson, and N.A. Martin, *J. Appl. Phys.*, **46**, 2029 (1975).
- 3.47. P. Zinzindohoue, *Optik* **74**, 131 (1986).
- 3.48. H.S. Kim, M.L. Yu, E. Kratschmer, B.W. Hussey, M.G.R. Thomson, and T.H.P. Chang, *J. Vac. Sci. Technol. B* **13**, 2468 (1995).
- 3.49. N. Samoto, R. Shimizu, H. Hashimoto, N. Tamura, K. Gamo, and S. Namba, *J. App. Phys.* **24**, 766 (1985).
- 3.50. H.S. Kim, M.L. Yu, E. Kratschmer, M.G.R. Thomson, and T.H.P. Chang, *J. Vac. Sci. Technol. B* **12**, 3413 (1994).
- 3.51. P.W. Hawkes and E. Kasper, *Principles of Electron Optics* (Academic, New York, 1989), vol. 2.

- 3.52. J.W. Gadzuk, and E.W. Plummer, Phys. Rev. B **3**, 2125 (1971).
- 3.53. A.B. El-Kareh, J.C. Wolfe, and J.E. Wolfe, J. Appl. Phys. **48** (11), 4749 (1977).
- 3.54. A. Modinos, *Field, Thermionic, and Secondary Electron Emission Spectroscopy* (Plenum Press, New York, 1984).
- 4.1. PyrexTM is a registered trademark of Corning Glass Works.
- 4.2. E. Bassous, IEEE Trans Electron Devices, **ED-25**, 1178 (1978).
- 4.3. P. E. Mauger, A. R. Shimkunas, and J. J. Yen, U. S. Patent No. 4 919 749.
- 4.4. K. Y. Lee and W. S. Huang, J. Vac. Sci. Technol. B **11**, 2807 (1993).
- 4.5. L. P. Muray, U. Staufer, E. Bassous, D. P. Kern, and T. H. P. Chang, J. Vac. Sci. Technol. B **9**, 2955 (1991).
- 4.6. G. Wallis and D. I. Pomerantz, J. Appl. Phys. **40** 3946 (1969).
- 4.7. P. B. DeNee,, J. Appl. Phys. **40** 5396 (1969).
- 4.8. K. B. Albaugh, J. Electrochem. Soc. **138** 3089 (1992).
- 4.9. K. B. Albaugh, Mater. Lett. **4** 465 (1986).
- 4.10. L. P. Muray, U. Staufer, D. P. Kern, and T. H. P. Chang, J. Vac. Sci. Technol. B **10**, 2749 (1992).
- 4.11. E. W. Becker, W. Ehrfeld, P. Hagmann, A. Maner, and D. Munchmeyer, Microelectron. Eng. **4**, 35 (1986).
- 4.12. N. C. LaBianca and J. D. Gelorme, presented at the SPE Ellenville Conference, Nov. 1994.
- 4.13. U. S. Patent No. 4 882 245 (1989).
- 4.14. K. Y. Lee, S. A. Rishton, and T. H. P. Chang, J. Vac. Sci. Technol. B **12**, 3425 (1994).

- 4.15. H. Jansen, M. D. Boer, J. Burger, R. Legtenberg, and M. Elwenspoek, Microelectron. Eng. **27** 475 (1995).
- 4.16. J. W. Bartha, J. Greschner, M. Puech, and P. Maquin, Microelectron. Eng. **27** 453 (1995).
- 4.17. J. W. Rangelow and P. Hudek, Microelectron. Eng. **27** 471 (1995).